The search for strangeonium resonances: Partial wave analysis of polarised photoproduction reaction $\gamma p \longrightarrow \eta\phi p$ at the GlueX experiment

Darius Darulis

Submitted in fulfilment of the requirements for the
Degree of Doctor of Philosophy

School of Physics and Astronomy
College of Science and Engineering
University of Glasgow

September 2025

Abstract

The strong force gives rise to a large hadron spectrum, many areas of which are still not well understood. Progress in mapping out these regions is vital for building better models of the strong force and verifying the predictions of its quantum field theory, Quantum Chromodynamics. This thesis focuses on the study of the so-called strangeonium states, which are mesons with $s\bar{s}$ quark content, and in particular on members of the ϕ meson series $\phi(1680)$ and $\phi_3(1850)$. The former is a radially excited vector that has been seen by both e^+e^- collider and photoproduction experiments, but whose reported mass does not match between the two, with observations from photoproduction being systematically higher; the latter is a tensor that has not been measured since the 1980s and never in experiments with high statistical power.

The data analysed in this thesis was collected at the GlueX experiment, which has produced the world's largest photoproduction dataset to date since starting to run in 2016. A 9 GeV linearly polarised photon beam incident on a liquid hydrogen target was used to produce a variety of mesonic and baryonic resonances. The GlueX spectrometer allows both neutral and charged final states to be exclusively reconstructed with good resolution and angular acceptance. Results from the partial wave analysis of decay channel $\gamma p \to \eta\phi p \to K^+K^-\gamma\gamma p$ are presented.

After signal was isolated from background using a combination of event selection criteria and statistical subtraction via the sPlot method, an extended maximum likelihood fit to angular decay distributions allowed the extraction of partial wave amplitudes. A partial wave consistent with the $\phi(1680)$ was observed, but no clear evidence of a $\phi_3(1850)$ was found. The obtained amplitudes indicated a preference for natural parity exchange. A fit to the intensity of the wave identified as the $\phi(1680)$ resulted in a Breit-Wigner mass more compatible with the e^+e^- measurements. A cross-section was also calculated, allowing an order-of-magnitude estimate that matched the existing predictions.

The results provide evidence against the additional vector meson states that have been previously hypothesised to explain the higher observed mass of the $\phi(1680)$ in photoproduction. They should also aid the development of models of the strangeonium spectrum.

Contents

List of Tables

List of Figures

Acknowledgements

The following 120-odd pages are written in an impersonal passive voice a PR consultancy could be jealous of and which, for better or worse, hides the real material conditions of producing research. None of this work would have been possible without the scientific and/or moral support of the many colleagues and friends that have had to remain behind the scenes. Within the traditional format of the PhD thesis, yours truly can only provide the following brief acknowledgements.

I would first like to thank my supervisors, Peter Hurck and David Ireland, and other staff members of the Glasgow group, especially Derek Glazier, for their help in seeing this project through. It is only because of their guidance and feedback that the results you are to see at the end of this text are anything near convincing.

I would also like to thank the GlueX collaboration in general, without which the data used in this thesis would not exist – the third Chapter, though only about 20 pages in length, describes an experiment that took multiple decades to come to fruition. More presently, the advice received from the Vector-Pseudoscalar Working Group was hugely helpful in getting the partial wave analysis to function.

Turning the focus back to Glasgow, I salute the brave troops in the Nuclear and Hadron Physics PhD trenches. Although their impact on my productivity could only be described as ”mixed”, their contributions to me maintaining some semblance of emotional stability are undeniable. The same goes for my friends at large, who have been around to remind me that activities outside the academia do still exist.

Finally, I may never have made it to a PhD at all without my wonderful partner, Freya, and my mother, Violeta. Without their continuing support, I probably would not have made it through it, either. Unfortunately, I do not have the space to thank them properly here, so I will only say – how lucky one can be!

Declaration

The work in this thesis is based on research carried out at the Nuclear and Hadron Physics Group, School of Physics & Astronomy, University of Glasgow, UK. No part of this thesis has been submitted elsewhere for any other degree or qualification and it is all my own work unless referenced to the contrary in the text.

Chapter 1

Introduction

1.1 Hadrons and their structure

Nuclear and particle physics has been a century long effort of trying to understand the structure of matter. Modern atomic theory took its first steps in the 19th century, when evidence from chemistry and statistical mechanics began to lead physicists into accepting the view that matter was composed of particles called atoms [1]. Although these were first thought to be indivisible, the discovery of the electron by J.J. Thomson in 1897 [2] complicated matters. He went on to propose his famous plum pudding model in 1904 [3], in which the atom was described as a positively charged nucleus with negatively charged electrons embedded in it. However, this picture's failure to explain phenomena like alpha scattering [4] led Rutherford to create his own namesake model: the atom was now a compact central nucleus which was surrounded by electrons [5]. A modified version of it with additions by Niels Bohr [6] made a big impact on the field – now electrons were orbiting the nucleus on discrete orbits, and, importantly, these orbits were quantised in energy. This view, alongside similar semi-classical ideas of the time, pointed the way to modern quantum mechanics.

The fundamentals of nuclear structure began to be understood around the same time. The proton was discovered by Rutherford in 1918 [7] and the neutron by James Chadwick in 1932 [8], which led to the formulation of multiple models of the nucleus [9, 10]. Confirmation of nuclear fission and the ability to produce various nucleii followed soon after in the late 1930s [11, 12]. The practical applications in warfare and energy engineering became obvious in the 1940s with the development of the nuclear bomb and the nuclear reactor.

A large number of particles were to be discovered over the coming decades. Early particle detectors, such as Wilson's cloud chambers, were used to detect naturally occurring cosmic rays [13]. This research saw the positron and the muon join the ranks of experimentally confirmed particles [14, 15], both first discovered by Carl D. Anderson. Also amongst the discoveries of the mid-century period were particles that would eventually come to be known as kaons [16] and hyperons [17, 18]. Both had considerably longer than expected lifetimes. Gell-Mann [19],

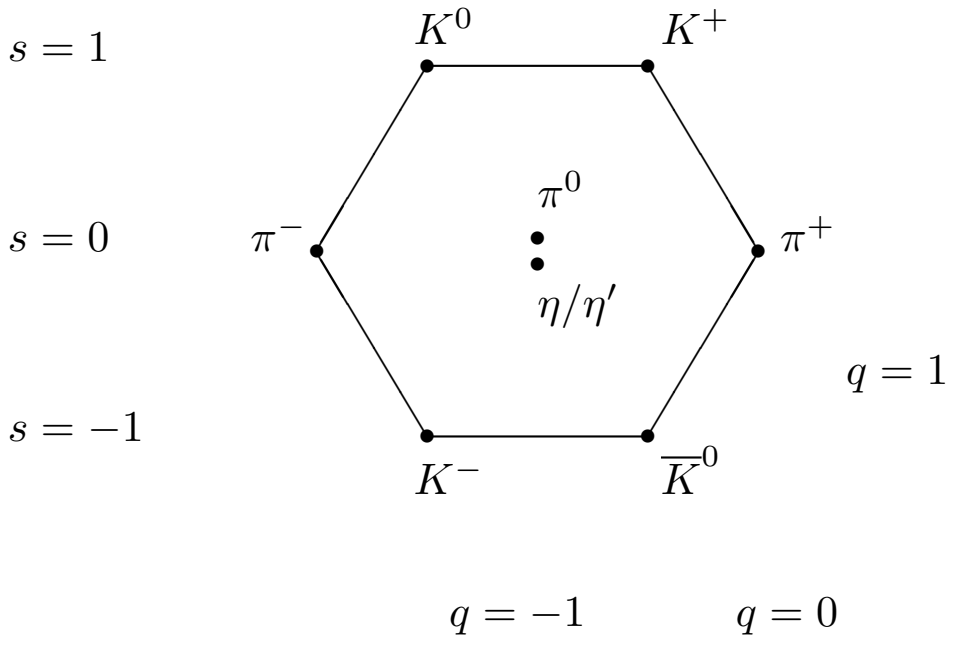

Figure 1.1: The meson octet and η' singlet in the Eightfold Way model. The mesons are arranged according to their electric charge and strangeness. Adapted from [27].

Pais [20], Takano, and Nishijima [21] proposed a new quantum number, called strangeness, that was conserved during electromagnetic and strong interactions to explain this.

Many hadronic states remained to be found in artificial production. The first major particle accelerators started being built in the 1950s, beginning with the early proton synchotrons like the Cosmotron at Brookhaven and the Bevatron at Berkeley [22] that were capable of reaching GeV scale energies. The latter is notable for having provided experimental evidence for nucleonic anti-matter [23]. These were followed by the more powerful Alternating Gradient Synchotron, also at Brookhaven, and Stanford Linear Accelerator (SLAC) [24] in the 1960s. Experimental efforts at these facilities led to a deluge of new particles being named. At this point in time, all new particles were considered to be elementary with no internal structure. This state of affairs was famously termed the 'particle zoo' [25]. The fact that so many of them existed was considered to be a sign that some underlying regularity was not yet discovered. In 1961, Murray Gell-Mann proposed a model which became known as the Eightfold Way [26]. The then-known particles were organised by grouping them according to charge and strangeness. Mesons and baryons formed symmetric patterns when this was done. The mesons formed an octet and a singlet, as visualised in Figure 1.1, while the baryons formed a nonet and a decuplet.

In 1964, Gell-Mann and Zweig developed the quark model [28, 29]. Baryons and mesons were no longer fundamental, but were formed of constituent particles called quarks and their

anti-matter counterparts. The SU(3) symmetry encoded by the Eightfold Way was seen as a result of the particles being comprised of three flavours of quark - up, down, and strange. Mesons are particles formed from a quark-antiquark pair, while baryons are composed of three quarks. The group theoretic decomposition of the SU(3) symmetry group naturally explains to the octet + singlet meson grouping. The existence of constituent quarks was confirmed experimentally at SLAC in 1969 [30]. Experimental work over subsequent decades eventually led to the discoveries of three more quark flavours – charm [31, 32], bottom [33], and top [34, 35]. The up and down quarks are often grouped together as the light sector, having masses on the order of a few MeV, while the charm, bottom, and top form the heavy sector with masses in the GeV range. The strange quark lies in-between at a mass of 95 MeV.

The majority of known states are consistent with having internal structure of qqq or $q\bar{q}$, but nothing in the classic constituent quark model prohibits particles with a larger number of quarks. Indeed, the original paper on the Eightfold Way [26] already allowed for any odd numbered quark configuration of baryons and any even numbered quark-anti-quark configuration for mesons. The hunt for such states has taken place at various facilities [36, 37]. Recent decades have seen results that seem to confirm the existence of tetraquarks. In particular, one can look at the so-called X, Y, and Z states [36, 38] claimed by collaborations like BESIII and LHCb, amongst others, that seem to strongly suggest a four quark composition.

There are other classes of states that are not forbidden – particles could contain valent gluonic content which contributes to their quantum number, or be composed entirely of gluons. This is because gluons, the carriers of the strong force, can themselves participate in strong interactions. The former class of particle is called hybrid, while the latter class is the glueball. It is not entirely clear how the glue would function in either type of state – competing phenomenological models exist [39, 40].

There is positive evidence for these states. States in the light meson spectrum that are surplus to the traditional octets are observed – these supernumerary states indicate that physics beyond the constituent quark model may be contributing [38]. This could indicate the presence of the glue-rich states. In addition, some states are thought to possess quantum numbers, as described in Section 1.3, that indicate gluonic contributions [26].

1.2 The strong force and Quantum Chromodynamics

The physics described in the previous section is governed by Quantum Chromodynamics (QCD), the quantum field theory of the strong force [41]. The strong force is the fundamental force that mediates interactions between quarks. Its force carrier is the gluon, which is a spin-1 gauge boson. The strong force acts on particles that have colour, which is the charge of the strong force. Colour comes in three flavours, which are canonically called red, green, and blue. There are three corresponding types of anti-colour – anti-red, anti-green, and anti-blue. A combination of

all three colours, all three anti-colours, or of a colour and its anti-colour combine to form a colour neutral, or colourless, state. The corresponding $SU(3)_c$ colour symmetry is the fundamental symmetry of QCD.

The Lagrangian that describes the dynamics of QCD is given by:

$$\mathscr{L} = \sum_q (\bar{\psi}_{qi} i\gamma^\mu [\delta_{ij}\partial_\mu + ig(A^\alpha_\mu t_\alpha)_{ij}]\psi_{qj} - m_q \bar{\psi}_{qi}\psi_{qi}) - \frac{1}{4} G^\alpha_{\mu\nu} G^{\mu\nu}_\alpha \tag{1.1}$$

The ψ terms represent quark fields with index i running from 1 to 3, corresponding to the three colour charges, while m_q are the quark masses. The expression in the square brackets is the gauge covariant derivative that couples the quark fields, via infinitesimal SU(3) generators t_α, with coupling strength g to the gluon fields. The latter are contained in the gauge invariant gluon field strength tensor $G^\alpha_{\mu\nu}$:

$$G^\alpha_{\mu\nu} = \partial_\mu \mathscr{A}^\alpha_\nu - \partial_\nu \mathscr{A}^\alpha_\mu + g f^{abc} \mathscr{A}^b_\mu \mathscr{A}^c_\nu \tag{1.2}$$

The gluon fields are denoted by $\mathscr{A}^a_\mu$, indexed by a,b,c running from 1 to 8. The f^{abc} terms are structure constants of SU(3). Finally, γ^μ are the canonical Dirac gamma matrices. The Lagrangian is non-linear and difficult to solve. Unlike in the case of Quantum Electrodynamics that governs electromagnetic interactions, where the mediating photon is neutral, the gluon carries colour charge and itself participates in strong interactions, including self-interactions. Although they may not be apparent from reading Eq. (1.1), QCD exhibits some surprising features not seen in QED. The first, colour confinement [42], means that colour carrying particles are not seen individually except for exotic states of matter such as quark-gluon plasmas. As these particles are drawn apart, they will eventually reach a point where it is energetically favourable to spontaneously produce a quark-antiquark pair and form colour-neutral hadrons. This process is usually called hadronisation. It has not been analytically proven for QCD or equivalent theories, but has remained a robust experimental finding [43].

Another important feature of QCD is called asymptotic freedom [44]. Asymptotically free theories contain interactions that become increasingly weaker as the energy scale increases, or equivalently the length scale decreases. This can be modelled as the effect of virtual particles on a charge. A charge effectively polarizes the vacuum around it, causing virtual particles of opposite charges to be attracted to it. In QED, this results in the charge becoming weaker. In QCD, where the gluon is also a colour charge, it results in the opposite effect and the colour charge is augmented. As one moves closer toward a colour charge, this effect diminishes and the strong interaction strength decreases. This can be analysed in terms of the strong coupling constant's dependence on the energy scale:

$$\alpha_s(Q) \simeq \frac{1}{\beta_0 \ln(\frac{Q}{\Lambda})} \tag{1.3}$$

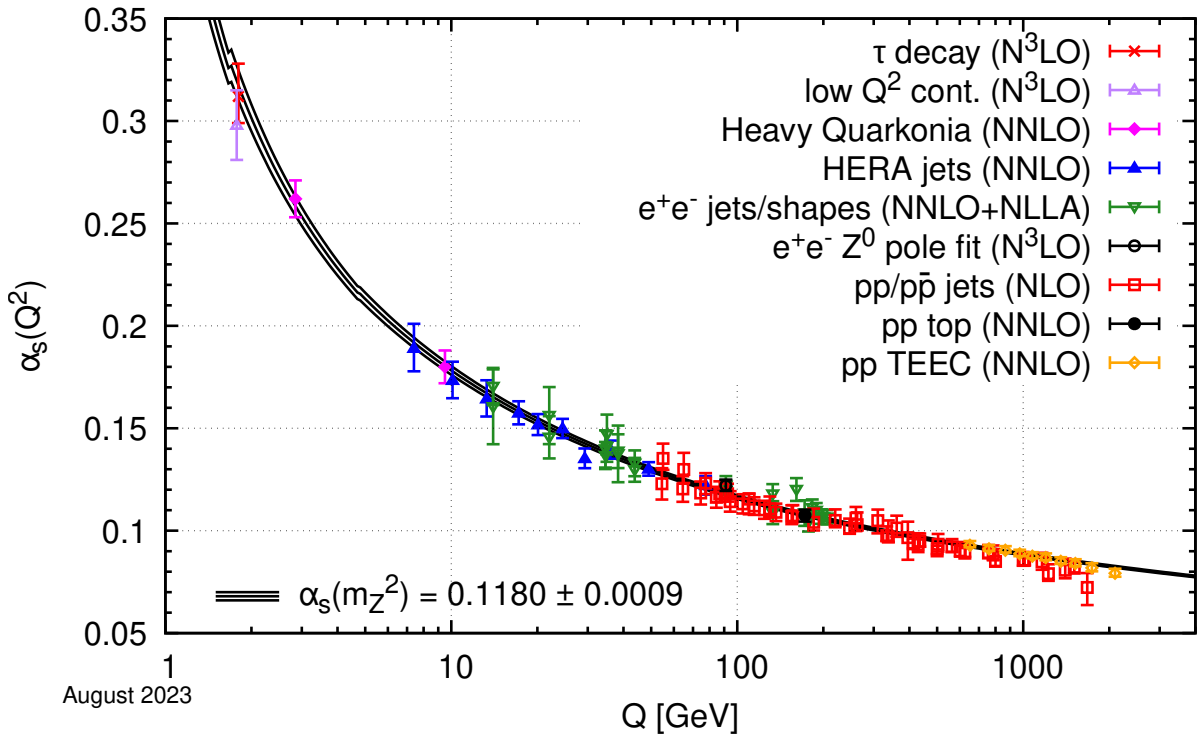

Figure 1.2: The dependence of the strong coupling constant on the energy scale Q. The figure shows the logarithmic relationship that leads to asymptotic freedom in QCD with the strong coupling becoming asymptotically weak at high energies. Taken from the Particle Data Group review [45].

The value Λ is called the QCD scale, with β_0 a constant. A plot of this relationship is shown in Figure 1.2. At high energies, strong interactions between particles become asymptotically weak. As a result of asymptotic freedom in QCD, the quarks inside hadrons can behave as if they were free particles.

1.3 Meson spectroscopy

Spectroscopic experiments are a major driver of progress in particle and hadron physics. Evidence for and against theories can be measured in how well they can reproduce the properties of already known particles and how well they predict as of yet unseen states. One obvious parameter is the mass of the particle – short-lived states also have a natural width, related to their lifetime, that can be measured. Another important quantity to measure is the fraction of resonances decaying to specific particle combinations – these branching fractions are required for computing cross sections.

A defining attribute of hadrons is the set of quantum numbers denoted as J^{PC}. In this notation J stands for the total angular momentum of the state, while P and C denote the parity and charge conjugation parity respectively. The parity operator P performs a mirror reflection on the spatial component of a wavefunction, such that for a given wavefunction $\psi(x)$:

$$P\psi(x) = e^{\frac{i\phi}{2}}\psi(-x) \tag{1.4}$$

The operator has eigenvalues of ± 1. For a diquark state with orbital angular momentum L, the parity value is given by:

$$P = (-1)^{L+1} \tag{1.5}$$

When classifying particles it is also common to separate them into the natural and unnatural parity series, depending on whether their P follows the relation $(-1)^J$ or $-(-1)^J$ respectively.

The charge conjugation operator C transforms a particle $|\psi>$ into its own antiparticle:

$$C|\psi> = |\bar{\psi}> \tag{1.6}$$

If the particle is its own anti-particle, e.g. π^0, it takes on eigenvalues of ± 1 like parity. The charge conjugation parity is equal to the product of the individual parities in a system of free particles, while for a system of two bound quarks it is given by:

$$C = (-1)^L \tag{1.7}$$

These quantum numbers can provide evidence for particles outside the constituent quark model. In the case of mesons, not all J^{PC} combinations are possible if only a quark-anti-quark pair is present – for example, such a pair cannot form a 1^{-+} state.

An interesting region of the hadron spectrum is composed of states collectively dubbed 'strangeonium', which are mesons comprised of $s\bar{s}$ pairs. Their spectrum is an intermediate region between the light and heavy quark sectors. This makes it an interesting testing ground for theorists, as the approaches used in those cases can face difficulties when applied to strangeonium [46].

The strangeonium spectrum is also interesting on experimental grounds. There are over 20 states predicted to be $s\bar{s}$ [47]. Figure 1.3 shows them laid out according to predicted invariant mass and quantum number. Some of these states have never been seen; some have only seen limited evidence; some have seen inconsistent measurements stretching back decades; some states are seen often, but have no consensus regarding their interpretation, including hybrid meson candidates [48]. This is typified by the ϕ mesons – strangeonium states that are thought to be part of the 1^{--} meson spectrum. The following Section describes previous research on these states in detail.

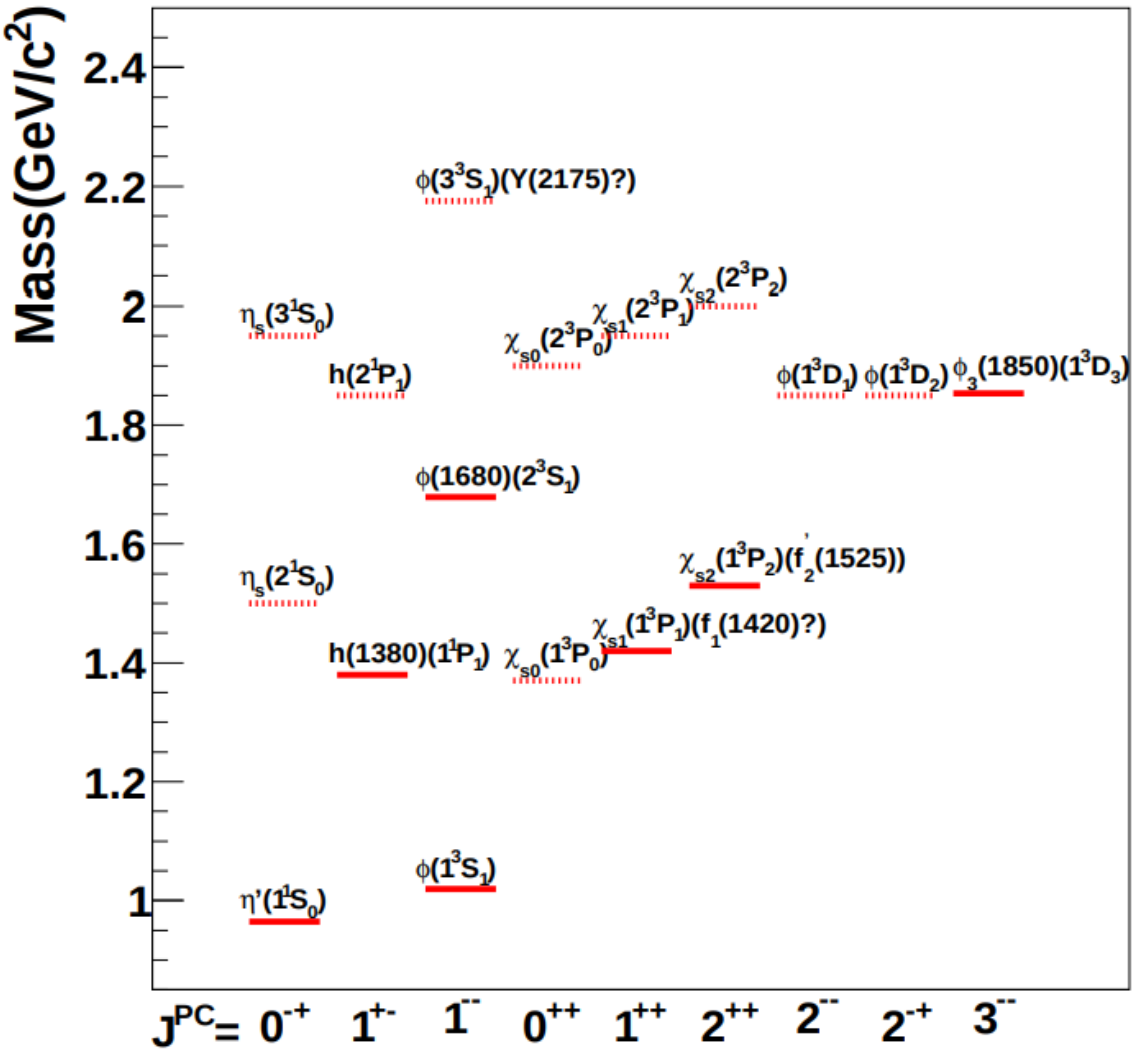

Figure 1.3: A possible variant of the $s\bar{s}$ meson spectrum according to their mass and J^{PC} quantum numbers predicted using the $^3P_0$ model. States underlined in bold red were considered established in the PDG tables, while the lightly underlined states were not as of 2015. Figure taken from [46].

1.4 The experimental status of the ϕ meson spectrum

There are currently four attested states assigned the ϕ label – $\phi(1020)$, $\phi(1680)$, $\phi_3(1850)$, and $\phi(2170)$ (also sometimes known as the Y(2175)). The first of these is the ground level 1^{--} vector meson, while the $\phi(1680)$ and the $\phi_3(1850)$ are identified as potential excited states with orbital angular momentum L = 1 and L = 3 respectively with quantum numbers 1^{--} and 3^{--}. The $\phi(2170)$ is especially controversial, having interpretations ranging from normal meson [49] to hexaquark molecular state [50]. All four states are thought to be $s\bar{s}$ because of their decay to final states with high strangeness content. Numeric results are taken from the Particle Data Group listings if not otherwise stated.

1.4.1 The $\phi(1020)$

The lowest energy member of the ϕ meson spectrum is experimentally well established. It was first proposed in 1962 by Sakurai [51] and was experimentally confirmed a year later at the Alternating Gradient Synchrotron in Brookhaven [52] using kaon - proton collision reactions. It is an almost pure $s\bar{s}$ state. Its wavefunction can be written as follows [45]:

$$\phi = \frac{1}{\sqrt{2}}(u\bar{u} + d\bar{d})\cos(54.7^\circ + \theta) - s\bar{s}\sin(54.7^\circ + \theta) \tag{1.8}$$

The mixing angle θ is an experimentally measured parameter. If it was exactly 35.3°, maximum mixing would be achieved and Eq. (1.8) would become just $s\bar{s}$. In reality, it is known to be equal to a slightly lower value of 35°, with a small $u\bar{u} + d\bar{d}$ component still present.

The $\phi(1020)$ decays predominantly into two kaons, with measured branching fractions of 48.9% for decays into K^+K^- and 34.2% into $K^0_S K^0_L$. The other decay channel with a branching fraction above the 1% level is the decay into combinations of the ρ meson and pions at 15.2%. Although one may have expected the dominant decays to have been into the three pion state, this is suppressed by the OZI rule [53, 54, 55]. The rule is a dynamic selection rule that states the following: any strongly interacting process will be suppressed if its Feynmann diagram can be split into two disconnected diagrams by the removal of internal gluon lines. The diagram of the decay into three pions fits this category, as seen in Figure 1.4.

Since its discovery the $\phi(1020)$ has been measured at a number of experiments. It is a very narrow state – the global fits for the resonance parameters in the PDG put it at 1019.46 ± 0.02 MeV with a width of 4.26 ± 0.04 MeV. Most of the published measurements used for the global averages come from e^+e^- colliders, which can measure 1^{--} states without hadronic backgrounds being present, allowing for the high precision of the computed central values. These measurements agree well across final states, including both dominant kaon channels and less common final states like $\eta\gamma$. Other measurements not included in the PDG averages have also been performed with techniques like kaon scattering [58]. Although these fall outside the current

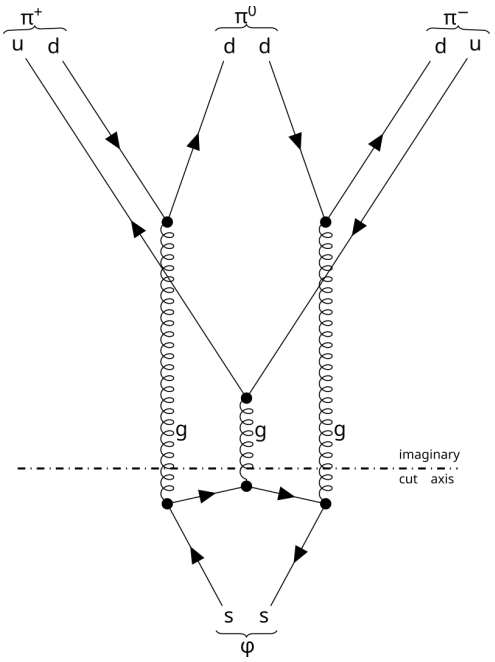

Figure 1.4: A Feynmann diagram of the $\phi \to 3\pi$ decay. The diagram can be split into two disconnected graphs if internal gluon lines are removed, meaning it is suppressed in nature despite being more energetically favourable than the $\phi \to KK$ process. Diagram is a reproduction from [56] taken from Wikipedia [57].

global uncertainty on the resonance parameters, they are still quite close on the peak position. The reported width values are more variable.

1.4.2 The $\phi(1680)$

The first excited member of the ϕ spectrum is the $\phi(1680)$. It has generally been identified as a radially excited state 1^{--} of the $\phi(1020)$ with orbital angular momentum L = 1. It was first observed in 1971 using a bubble chamber at the Argonne National Laboratory in pion-deuterium scattering [59]. The oldest measurement still used by the PDG comes from the 1982 paper by the DM1 experiment [60], where the $\phi(1680)$ was seen as an enhancement in the cross-section of multiple final states. A large number of measurements are available from e^+e^- experiments performed since. A plot showing some of their mass dependent cross-sections results is given in Figure 1.5. Although variability in reported central values is present, most of these experiments agree on it being a 1^{--} resonance with a peak below 1.7 GeV. The status of the resonance width measurements is unclear, with the PDG only giving an 'educated guess' on the global average.

However, a puzzle appears when the previous results are compared to measurements from photoproduction facilities. The latter put the potential resonance much higher in invariant mass. There are four such results historically collated by the PDG [61, 62, 63, 64], though they have been removed from the 2022 edition onwards. These analyses see peaking structures around or above 1.7 GeV in decays into K^+K^-. This structure is interpreted in three of the papers as

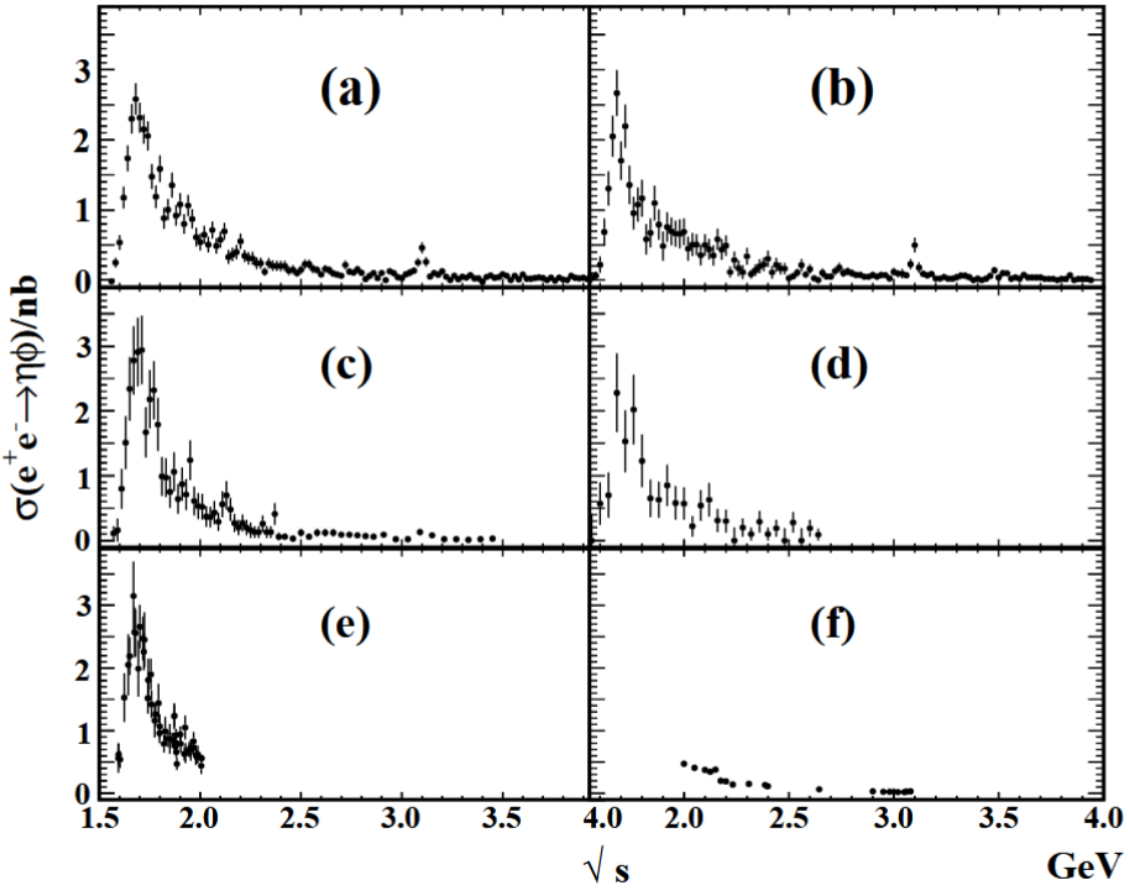

Figure 1.5: Mass dependent cross-sections for e^+e^- decays into $\eta\phi$ final states from different experiments. a) $\eta \to \gamma\gamma$ at Belle. b) $\eta \to \pi^+\pi^-\pi^0$ at Belle. c) $\eta \to \gamma\gamma$ at BaBar. d) $\eta \to \pi^+\pi^-\pi^0$ at BaBar. e) $\eta \to \gamma\gamma$ at CMD-3. f) $\eta \to \gamma\gamma$ at BESIII. Subplots a) through e) contain clear enhancements corresponding to the $\phi(1680)$. Reproduced from [66].

the $\phi(1680)$ despite the mass discrepancy [61, 62, 63]. The possibility of interference from other vector states are discussed to explain the differences between the two production modes, but no definitive statements are made. The newer FOCUS analysis [64] concludes that was seen is instead a different 1^{--} state called X(1750). Furthermore, unlike previous work in electroproduction, a recent measurement from BESIII [65] claimed to see both in the same partial wave fit to data from $\psi(3686) \to K^+K^-\eta$ decays, implying two distinct states. The effects of vectors like $\rho(1700)$ are again not excluded. It is not apparent why this enhancement is not seen in the other published e^+e^- data.

Other physics quantities related to the state are not properly understood either. The branching ratios for $\phi(1680)$ are reported for few channels, though an analysis of BELLE data [67] and a combined fit to the e^+e^- measurements shown in Figure 1.5 [66] put $\mathscr{B}(\phi(1680) \to \eta\phi)$ at around 20%. The total cross-sections that are available are hard to compare – because reliable branching ratios are not available, any reported values will be specific to the final state under study. They also come from experiments with highly variable beam energies, which has a major impact on the magnitude of the results. Theory predictions for photoproduction cross-section

exist [68] but additional experimental data will be required.

1.4.3 The $\phi_3(1850)$

The second excited ϕ state in the PDG is the $\phi_3(1850)$, which is identified as a 3^{--} state. The existing literature is sparse with only three kaon scattering results available. It was first observed by a CERN hydrogen bubble chamber experiment in 1981 [69] in final states of the channel $K\bar{K}\Lambda$. Another paper from the OMEGA collaboration in 1982 [70] and a later measurement at SLAC [71] in 1988 confirmed the results. The first two analyses report the resonance parameters from a simple Breit-Wigner fit to the final state invariant mass spectrum, as shown in Figure 1.6, with the second paper also containing a moments analysis that was claimed to indicate a 3^{--} state. The SLAC measurement also performed a similar moments analysis that agreed with this J^{PC} determination, but extracted the Breit-Wigner parameters from fits to partial wave intensities computed from the moments rather than the invariant mass spectrum.

It should be noted all of the existing measurements were based on low statistics samples. The fits from the bubble chamber analysis gives a yield of about 120 events for the observed state, while the two moments analyses contained approximately 2500 and 1350 events within the mass range of interest for the $\phi_3(1850)$ respectively. Although describing something as 'low' or 'high' statistics can only be done in relative terms, considering the number of free parameters and degrees of freedom involved, moments-based methods like the ones just mentioned would benefit from having more events to solidify the inferences made. The uncertainties reported on the peak and the width of the state are fairly low, but some doubt is probably warranted regarding the J^{PC} numbers. Branching ratios are not known and no photoproduction results have been published.

1.4.4 The $\phi(2170)$

The $\phi(2170)$ is perhaps the most controversial state in the ϕ spectrum. It has been seen repeatedly by experiments in e^+e^- facilities. It was observed by the BaBar experiment in 2006 [72] in an initial state radiation measurement of final state $\phi f_0(980)$. This measurement was confirmed by BELLE using the same technique and channel [73], while also being seen at BESII [74] in $J/\psi \to \phi f_0(980)\eta$ decays. A number of additional results for different reactions have followed from BESIII [75, 76, 77, 78, 79, 80]. Most of these e^+e^- measurements place the state at around 2.2 GeV with a width of about 100 MeV, though uncertainties on both values are on the order of 100 MeV. No previous photoproductions results are available, but there is an ongoing GlueX analysis aiming to measure the $\phi(2170)$ using the $\phi\pi^+\pi^-$ final state [81] with preliminary results that do not agree with the averages reported by the PDG. It is generally accepted that the state is a 1^{--} vector.

The $\phi(2170)$ has been a source of lively discussion in the theory community with many

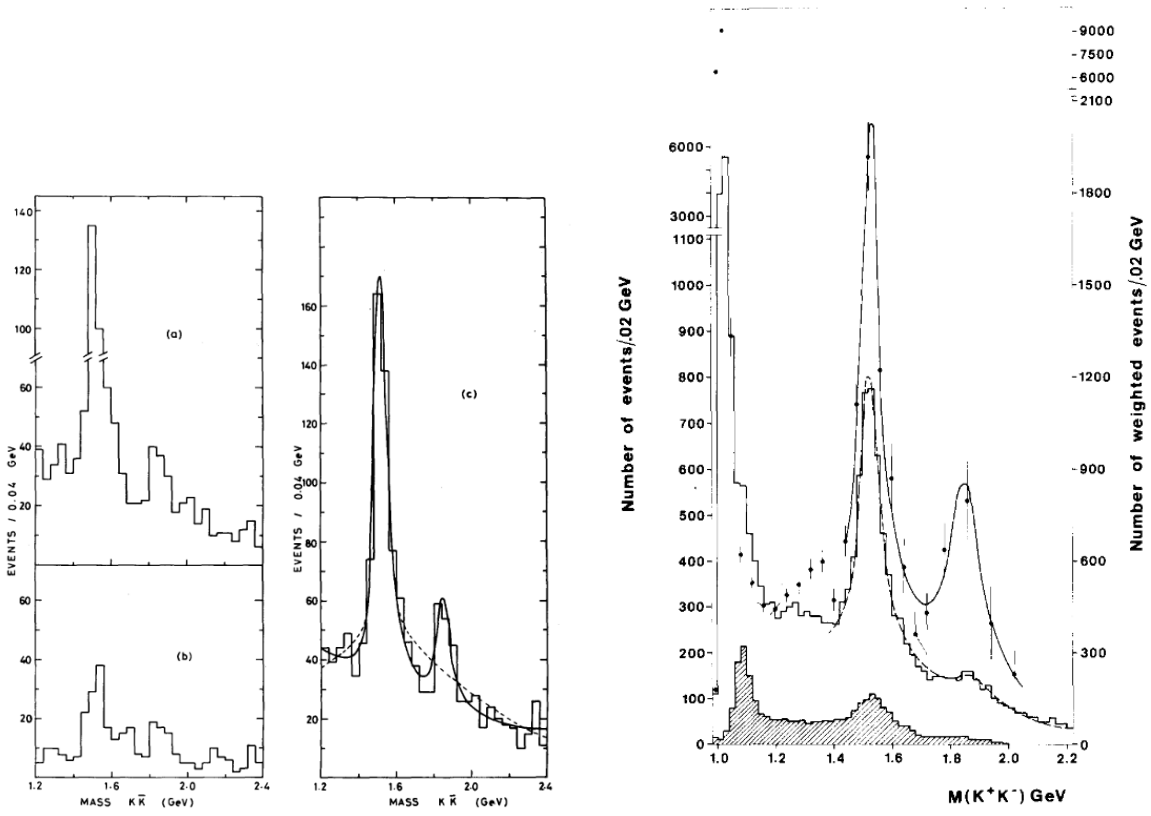

(a) (b)

Figure 1.6: Invariant mass spectra taken from the CERN HBC collaboration's measurements in 1981 (1.6a) and the OMEGA collaboration's measurement in 1982 (1.6b) of the $\phi_3(1850)$. In Subfigure 1.6a, the subplots in the left column represent the invariant masses of the $K^+K^-\Lambda$ and $K^0_S K^0\Lambda$ final states with the right column showing their sum and the associated Breit-Wigner fit curves. Subfigure 1.6b shows the raw counts after event selection in the unshaded histogram, a background component in the shaded histogram, and the acceptance corrected data with dots with the associated Breit-Wigner fits using the $K^+K^-(\Lambda/\Sigma_0)$ final states. Reproduced from [69] and [70] respectively.

papers published about its nature. The range of interpretations is wide: excited ϕ state [82, 83], hybrid meson [84, 85], a tetraquark [86, 87], molecules [88, 89], or as a dynamically generated state [90, 91], but no consensus exists. The available phenomenological models can generate predicted partial widths for $\phi(2170)$'s decays, which generally differ based on the proposed structure of the state [49]. This provides a way to experimentally distinguish between them. In some cases, the models predict that specific decay channels may become dominant – for example, the $\eta\phi$ and $\eta'\phi$ modes could be dominant if the state is a tetraquark [48]. Conversely, in a hybrid interpretation, the dominance of $K_1(1270)K$ and $K_1(1400)K$ channels is predicted.

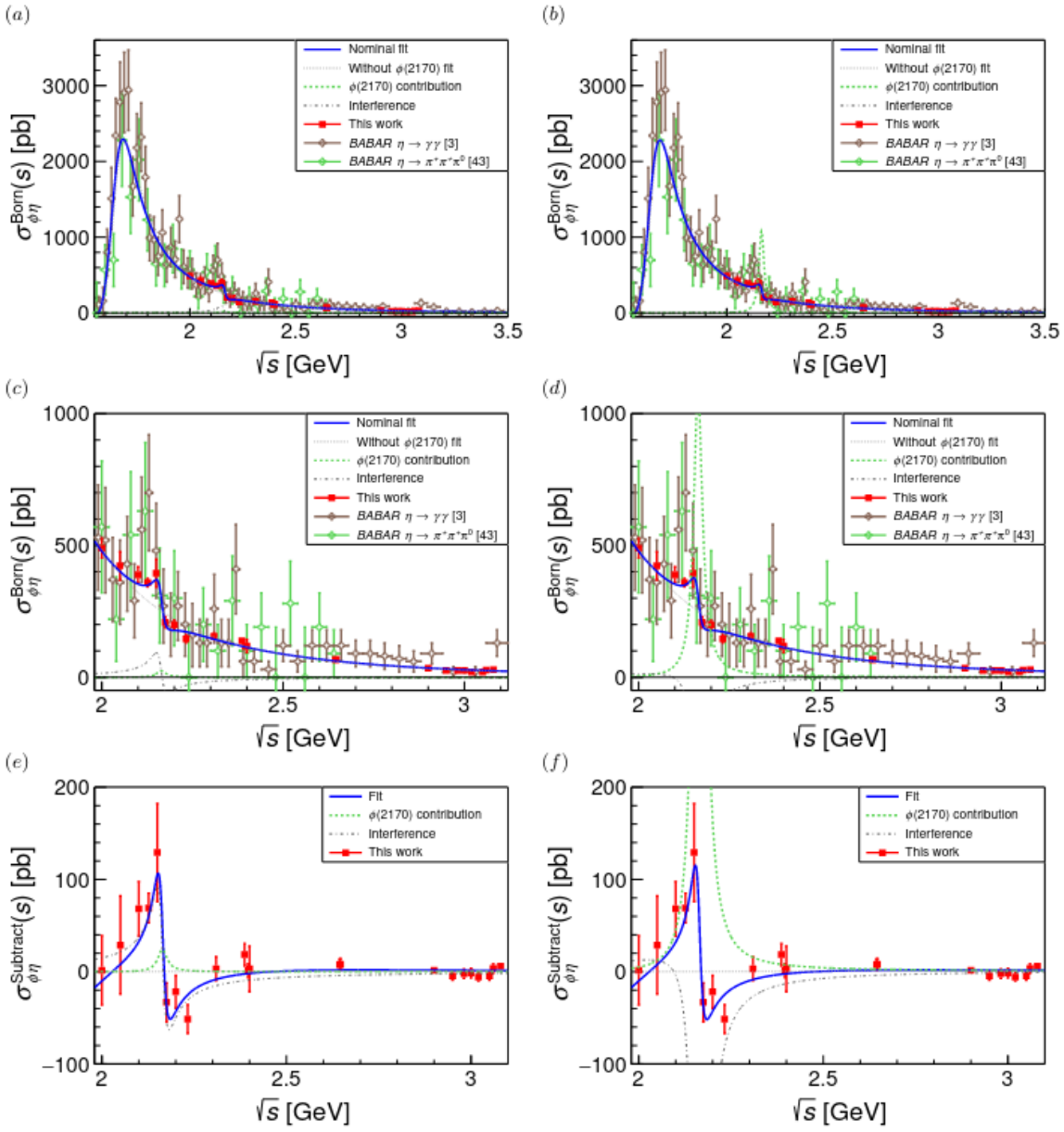

Figure 1.7: BESIII results for reaction $e^+e^- \to \eta\phi$ using initial state radiation measurements. Two equally likely solutions are shown in subplots a,c and b,d. The second row presents the same data with a more zoomed in view. The final row presents the data after subtracting fit components excluding the $\phi(2170)$. Reproduced from [78] .

1.5 Accessing ϕ states through $\eta\phi$ decays at GlueX

A number of open issues in the spectroscopy of the strangeonium spectrum have been laid out. The ϕ meson series has a number of states that require more experimental evidence, especially in photoproduction, to resolve outstanding questions concerning their properties and structure. The present thesis will aim to use linearly polarised photoproduction data from the GlueX experiment at the Thomas Jefferson National Accelerator Facility to contribute to this effort. A partial wave approach, described in Section 2.2, will be used.

Several channels were possible as options for the analysis. Strong decays conserve quark flavour – assuming the ϕ states are indeed strangeonium, the best channels to look into were ones that contain high strange content. The decay into $\eta\phi$ was chosen. As mentioned previously, the $\phi(1020)$ is an almost pure $s\bar{s}$ vector state, while the η meson also mixes strongly with strangeness with its full wavefunction being:

$$\eta = \frac{1}{\sqrt{6}}(u\bar{u} + d\bar{d} - 2s\bar{s}) \tag{1.9}$$

This channel is also of interest for the phenomenological models of the $\phi(2170)$. It is suggested that the partial widths of the $\eta\phi$ and $\eta'\phi$ channels [48], as well as their relative branching ratios [92], can discriminate between different interpretations of the state. Finally, no previous photoproduction measurements have used the $\eta\phi$ channel for measurements of the $\phi(1680)$ or $\phi_3(1850)$, meaning this analysis can fill a gap in the literature.

The final states to be actually analysed also had to be picked. The PDG list of branching fractions for the η and the ϕ mesons gives a number of possibilities. The ϕ, as already mentioned, decays predominantly into two kaons, but the K^+K^- and the $K^0_S K^0_L$ cases have comparable branching fractions. The η also has multiple decays with significant branching fractions. The neutral decay modes are dominated by the decay into two photons with a branching fraction of around 39%, but it can also decay to three π^0 with a branching fraction of 32.57%. The charged decay modes are rarer, but the decay into $\pi^+\pi^-\pi^0$ is comparable at a branching fraction of 23%. Ignoring all the decay modes that have sub-5% branching fractions gives 6 reasonable final states to look at.

Ideally, all six could be included in a coupled fit. However, this analysis focuses on the reaction $\gamma p \longrightarrow \eta\phi p \longrightarrow K^+K^-\gamma\gamma p$. This is both due to problems of scope, as the event selection and data processing required for all of these final states would require different treatment, and complexity, as this final state is among the less complicated available. It is also the final state with the highest combined branching ratio, allowing us to maximise the available statistics while sticking with one final state.

The analysis will provide preliminary results of a state that is identified as the $\phi(1680)$. Fits to a partial wave model allow the extraction of the state's J^{PC} quantum numbers, peak parameters, and a final state specific mass-dependent cross-section. The invariant mass region

around 1.8 GeV will be found to contain a peaking structure that could be the $\phi_3(1850)$, but the partial wave results to be inconclusive when trying to describe this structure. This, combined with possible baryon contamination, precludes extraction of reliable numerical results but no qualitative evidence will be found to support the 3^{--} interpretation found in the PDG. The status of the $\phi(2170)$ will be briefly discussed.

The thesis is structured as follows[1]. Chapter 2 describes the partial wave technique that will be used to extract the results. Chapter 3 will describe the facilities at Jefferson Lab and the experimental setup used by the GlueX experiment. Chapter 4 lists the event selection criteria and discusses the background subtraction techniques used to select signal events. Chapter 5 contains some considerations about the partial wave analysis and waveset selection. Chapter 6 presents the primary results. Chapter 7 describes a number of studies used to measure systematic uncertainties. The thesis concludes with a discussion of the interpretation of the results, their place in the literature, and future work in Chapter 8. An appendix for material that did not fit the main body of the text will be provided.

[1]Throughout the thesis, the natural unit convention is used. In particular this means that, because $c = 1$, mass and momentum are expressed in terms of GeV.

Chapter 2

Partial wave analysis

The classic approach for discovering resonances, sometimes known as "bump-hunting", involves finding peaking structures in invariant mass spectra of the final state under study and fitting them using an explicitly parameterised model. The models are generally built using a combination of relativistic Breit-Wigner terms and functional background shapes. Quality of fit is assessed using a χ^2 metric. The χ^2 metric is also used as the figure of merit when comparing multiple such models, such as when trying to infer whether features of the spectrum can be better explained by introducing additional states.

However, interpreting the results of this approach is not straightforward and can easily lead to incorrect conclusions. Non-resonant processes can produce invariant mass peaks; conversely, resonant processes do not always result in visible peaks [93]. Additionally, in the more complicated cases where a resonance is thought to lie under a significant non-removable background, the results may be very sensitive to choice of model. All of these factors contribute to making final inferences from such fits difficult. Beyond such challenges, not all physics quantities of interest can be obtained by direct fitting of invariant mass spectra. One of the main properties of a hadronic state is its quantum numbers. The importance and use of the quantum numbers in spectroscopy has been described in Section 1.3. There is no direct way to extract them from an invariant mass fit – other techniques must be used.

One way to determine a state's quantum numbers is by constraining what their values can be in a given reaction. An obvious example is experiments that use an e^+e^- collider – the annihilation process results in the creation of a photon, which possesses the J^{PC} numbers 1^{--}. Due to conservation laws it is guaranteed that any resonances produced this way will also have these same quantum numbers, and no further work is required to obtain them – examples include measurements of particles in the $c\bar{c}$ charmonium spectrum like the J/ψ [94]. Photoproduction, meanwhile, does not place such constraints on produced resonances. This enables the search for the many states that have J^{PC} numbers other than 1^{--}, but means that the quantum numbers have to be taken into account explicitly when building models. This is usually done using an approach called partial wave analysis.

The wavefunctions of particles in scattering interactions can be decomposed into sums of basis functions dependent on their spins, angular momenta, angular decay distributions, and, in cases where it is relevant, polarisation. Introductions to the method for generic scattering in the presence of simple potentials are given in various quantum physics textbooks, see e.g. [95, 96]. Briefly, elastic interactions are modelled as an incoming plane wave interacting with a spherical potential $V(r)$ that produces an outgoing spherical wave. If $V(r) = 0$, then the plane wave can be shown to be expressible as the sum of spherical waves over angular momentum l. It turns out that assuming $V(r)$ is non-zero only modifies the terms in the derived expressions by a so-called phase shift factor – in fact, this is a consequence of probability conservation. The end result of these derivations is the following scattering amplitude:

$$f(\theta) = \sum_{l=0}^{\infty} (2l+1) f_l(k) P_l(\cos(\theta) \tag{2.1}$$

Following [95], k is the momentum of the particle, θ is the scattering angle, l is the angular momentum, P_l is the standard associated Legendre polynomial, and $f_l(k)$ is a term called the partial wave amplitude. The modulus squared of the scattering amplitude in Eq. (2.1) is the cross-section of the reaction. Applying this expansion to real decays, due to conservation of angular momentum it is possible to determine the spin of the parent particle based on the decay angular distribution of the products.

In general, partial wave models can be much more complicated than the example above. Unsurprisingly, since the reaction being studied in this thesis involves both a polarised beam and higher spin objects, a more elaborate model is required. This Chapter introduces the partial wave formalism used in the present analysis. The reference frames and angular distributions utilised in the formalism are described in Section 2.1. The derivation of the formalism for the particular case of vector-pseudoscalar systems using a linearly polarised photon beam is sketched out in Section 2.2 starting with the two pseudoscalar model given in [97] and concluding with the expression that is practically implemented in software to perform the partial wave fits.

2.1 Reference frames

The partial wave analysis presented in this thesis is done in the so-called helicity reference frames of the resonance and the vector meson ϕ. A diagram of the frames can be seen in Figure 2.1. In total five angular variables are used – angles (θ, φ) are the polar and azimuthal angles of the ϕ meson in the resonance frame, while angles (θ_h, φ_h) are the polar and azimuthal angles of the K^+ meson in the ϕ meson frame. In addition, the angle Φ is calculated between the photon polarisation vector and the production plane of the resonance.

The coordinate systems for the reference frames are constructed as follows. For the $\eta\phi$ helicity frame the z-axis is defined as the direction of travel of the $\eta\phi$ resonance in the γp

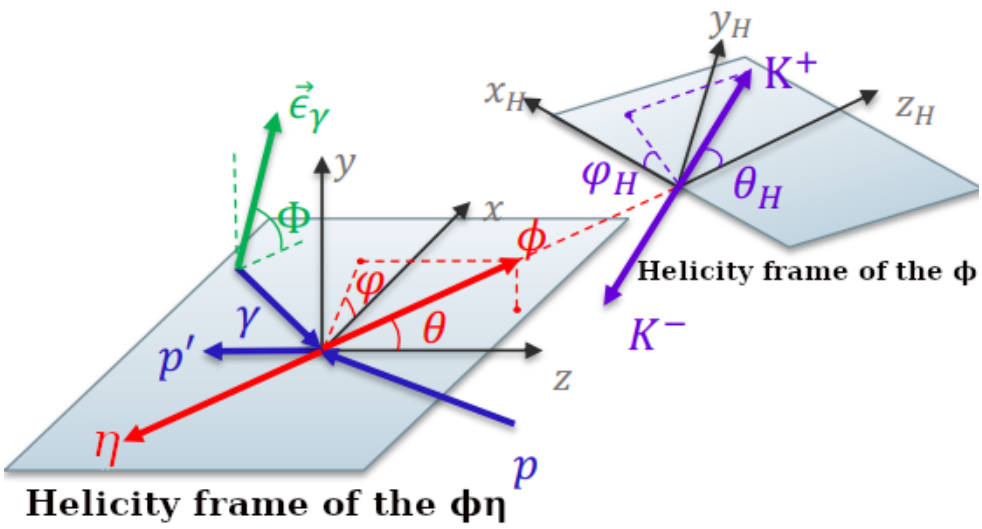

Figure 2.1: A diagram of the helicity frames used in the partial wave analysis.

centre-of-mass frame. After boosting along this axis to the $\eta\phi$ rest frame, denoted CM, the y-axis is then defined as being normal to the production plane of the resonance which is spanned by the directions of the incident photon and the resonance. The x-axis is given as the cross-product of the unit vectors along the z and y axes to produce a right-handed coordinate system. In symbolic terms, if we write the relevant unit vectors as $\hat{\mathbf{x}}, \hat{\mathbf{y}}, \hat{\mathbf{z}}$, then:

$$\hat{\mathbf{z}} = \frac{\mathbf{p}_{\eta\phi,\mathrm{CM}}}{|\mathbf{p}_{\eta\phi,\mathrm{CM}}|} \tag{2.2}$$

$$\hat{\mathbf{y}} = \frac{\mathbf{p}_\gamma \times \hat{\mathbf{z}}}{|\mathbf{p}_\gamma \times \hat{\mathbf{z}}|} \tag{2.3}$$

$$\hat{\mathbf{x}} = \hat{\mathbf{y}} \times \hat{\mathbf{z}}, \tag{2.4}$$

where $\mathbf{p}_{\eta\phi}, \mathbf{p}_\gamma$ are the 3-momenta vectors of the resonance in the CM frame of the $\eta\phi$ system and the beam photon respectively.

The coordinate system for the ϕ helicity frame is constructed similarly. After performing a Lorentz boost from the $\eta\phi$ helicity frame to the ϕ CM frame, the new z-axis is taken as the direction of travel of the ϕ meson in the $\eta\phi$ helicity frame. The y-axis is now defined to be normal to a plane formed by this z-axis and the z-axis of the previous frame; the x-axis is again obtained by taking the cross product of unit vectors along the other two axes to form a right-handed coordinate system. If the unit vectors are notated as $\hat{\mathbf{x}}_\mathbf{h}, \hat{\mathbf{y}}_\mathbf{h}, \hat{\mathbf{z}}_\mathbf{h}$ then symbolically:

$$\hat{\mathbf{z}}_\mathbf{h} = \frac{\mathbf{p}_{\phi,\mathrm{CM}_{\eta\phi}}}{|\mathbf{p}_{\phi,\mathrm{CM}_{\eta\phi}}|} \tag{2.5}$$

$$\hat{\mathbf{y}}_\mathbf{h} = \frac{\hat{\mathbf{z}} \times \hat{\mathbf{z}}_\mathbf{h}}{|\hat{\mathbf{z}} \times \hat{\mathbf{z}}_\mathbf{h}|} \tag{2.6}$$

$$\hat{\mathbf{x}}_\mathbf{h} = \hat{\mathbf{y}}_\mathbf{h} \times \hat{\mathbf{z}}_\mathbf{h} \tag{2.7}$$

In these coordinate systems the polar and azimuthal angles can computed in the usual way:

$$\cos(\theta) = \frac{\mathbf{p}_{\phi,\eta\phi\mathbf{CM}} \cdot \hat{\mathbf{z}}}{|\mathbf{p}_{\phi,\eta\phi\mathbf{CM}}|} \tag{2.8}$$

$$\phi = \tan^{-1}\left(\frac{\mathbf{p}_{\phi,\eta\phi\mathbf{CM}} \cdot \hat{\mathbf{y}}}{\mathbf{p}_{\phi,\eta\phi\mathbf{CM}} \cdot \hat{\mathbf{x}}}\right) \tag{2.9}$$

$$\cos(\theta_h) = \frac{\mathbf{p}_{\mathbf{K}^+,\phi\mathbf{CM}} \cdot \hat{\mathbf{z}}_\mathbf{h}}{|\mathbf{p}_{\mathbf{K}^+,\phi\mathbf{CM}}|} \tag{2.10}$$

$$\phi_h = \tan^{-1}\left(\frac{\mathbf{p}_{\mathbf{K}^+,\phi\mathbf{CM}} \cdot \hat{\mathbf{y}}_\mathbf{h}}{\mathbf{p}_{\mathbf{K}^+,\phi\mathbf{CM}} \cdot \hat{\mathbf{x}}_\mathbf{h}}\right) \tag{2.11}$$

Finally, the angle Φ is defined. The beam polarisation vector in the lab frame is required and is given as:

$$\hat{\varepsilon}_\gamma = \begin{bmatrix} \cos(\phi_{pol}) \\ \sin(\phi_{pol}) \\ 0 \end{bmatrix}, \tag{2.12}$$

where ϕ_{pol} is the polarisation angle of the beam determined by the orientation of the diamond radiator. The expression for Φ is then:

$$\Phi = \tan^{-1}\left(\frac{\frac{p_{\gamma,CM}}{|p_{\gamma,CM}|} \cdot (\varepsilon_\gamma \times \hat{y})}{\hat{y} \cdot \varepsilon_\gamma}\right), \tag{2.13}$$

with $p_{\gamma,CM}$ being the 3-momentum of the beam photon in the $\eta\phi$ CM frame.

2.2 Reflectivity formalism for vector-pseudoscalar systems

Like in the simple example at the start of this Chapter, the goal of this Section is to expand the wavefunction of a resonance by using angular momentum dependent partial waves. The following formalism is able to handle reactions with intermediate non-0 spin states. The exposition will begin in the helicity basis, where helicity is defined as the projection of a particle's spin onto its momentum vector:

$$h = \hat{\mathbf{s}} \cdot \hat{\mathbf{p}} \tag{2.14}$$

The helicity basis has been used for writing out scattering and decay amplitudes since its development by Jacob and Wick in 1959 [98] to account for difficulties encountered in the canonical spin-orbital angular momentum scheme. In this scheme, the relevant operators are defined in reference frames that are not at rest with respect to each other – the spin operator is applied in the rest frames of the individual particles while the orbital angular momentum is applied in the system's centre of mass frame [99]. Although this does not make formulating the amplitudes impossible, the algebra required may be complicated and require switching between different state representations [98].

In contrast, because helicity is invariant with respect to rotations these challenges can be avoided – multi-particle states with a definite total angular momentum and helicities for all particles can always be defined [98, 99]. Helicity is also defined in the same way for both massive and massless particles, avoiding the need for special cases which arise in the canonical scheme. In the end, the resulting amplitudes are simpler in form. Full derivations demonstrating this can be found in [98] and [99].

The following outline is a sketch starting from the two pseudoscalar partial wave formalism described in [97] together with preliminaries from [93]. The scattering cross section for a resonance X is proportional to the squared modulus of the Lorentz-invariant transition amplitude, such that:

$$\frac{d\sigma}{dE_\gamma dt dM d\Omega} = \frac{1}{\text{Flux}_{\text{beam}}} \sum_{\text{ext.spins}} |\mathscr{M}|^2 d\rho \tag{2.15}$$

Here $\mathscr{M}$ is the Lorentz invariant transition amplitude, $d\rho$ is the Lorentz invariant phase space element, E_γ is the beam energy, t is the Mandelstam t, M is the invariant mass of the $\eta\phi$ system, and Ω are the angular distributions in the helicity frames described in Section 2.1. The transition amplitude is itself a representation of the scattering operator T, given as:

$$\mathscr{M} = < out|T|in >, \tag{2.16}$$

where $< out$ and $in >$ are the bra and ket of the outgoing and the incoming particle waves respectively. If it is assumed that the analysis is performed in fixed bins of E_γ, t, and M, then the cross section relationship only depends on angular distributions and spins up to a constant factor. An intensity can be defined, which gives the density of events over the appropriate phase space. It is written as:

$$I(\Omega, \Omega_h) = \frac{d\sigma}{d\Omega} = \kappa \cdot \sum_{\text{ext.spins}} |\mathscr{M}|^2 \tag{2.17}$$

The κ denotes any relevant dynamic factors. The linearly polarised photon beam allows us to introduce a spin-density matrix ρ and incorporate polarisation into the model. The intensity can now be rewritten in terms of amplitudes $A(\Omega, \Omega_h)$, such that:

$$I(\Omega,\Omega_h)=\frac{d\sigma}{d\Omega}=\kappa\cdot\sum_{\lambda,\lambda',\lambda_1,\lambda_2}A_{\lambda,\lambda_1,\lambda_2}(\Omega)\rho^{\gamma}_{\lambda\lambda'}(\Phi)A^*(\Omega)_{\lambda'\lambda_1\lambda_2} \tag{2.18}$$

The individual amplitudes are defined as follows:

$$A_{\lambda;\lambda_1\lambda_2}(\Omega)=\sum_{lm}T^l_{\lambda m;\lambda_1\lambda_2}Y^l_m(\Omega) \tag{2.19}$$

The symbols $\lambda,\lambda_1,\lambda_2$ represent the helicities of the beam, target nucleon, and recoil nucleon respectively. Y^l_m are the Laplace spherical harmonics for angular momentum l, and $T^l_{\lambda m;\lambda_1\lambda_2}$ are the partial waves, which will be free complex parameters in the model.

The intensity can explicitly be written out as:

$$I(\Omega,\Omega_h,\Phi)=I^0(\Omega)-P_\gamma I^1(\Omega)\cos(2\Phi)-P_\gamma I^2(\Omega)\sin(2\Phi) \tag{2.20}$$

The quantity P_γ is the magnitude of the photon beam polarisation, bounded between 0 and 1. The intensity components I^0,I^1,I^2 are given as:

$$I^0(\Omega,\Omega_h)=\frac{\kappa}{2}\sum_{\lambda;\lambda_1\lambda_2}A_{\lambda;\lambda_1\lambda_2}(\Omega)A^*_{\lambda;\lambda_1\lambda_2}(\Omega) \tag{2.21}$$

$$I^1(\Omega,\Omega_h)=\frac{\kappa}{2}\sum_{\lambda;\lambda_1\lambda_2}A_{-\lambda;\lambda_1\lambda_2}(\Omega)A^*_{\lambda;\lambda_1,\lambda_2}(\Omega) \tag{2.22}$$

$$I^2(\Omega,\Omega_h)=i\frac{\kappa}{2}\sum_{\lambda;\lambda_1\lambda_2}A_{-\lambda;\lambda_1\lambda_2}(\Omega)A^*_{\lambda;\lambda_1\lambda_2}(\Omega) \tag{2.23}$$

The beam helicity λ takes on values ±1 and the helicities of the initial and recoil nucleons λ_1,λ_2 take on values $\pm\frac{1}{2}$. The baryon helicities are dropped from the following derivations and will be reintroduced at the end without loss of generality.

First, to extend the model to vector-pseudoscalar channels, multi-particle decays must be modelled. The vector meson ϕ is not detected directly, but reconstructed from its products – two kaons. The isobar approach is used, where the full reaction being treated as two sequential two-body decays that can be factored together and that ultimately produce three spinless particles; the intermediate particle that decays is called an isobar. Figure 2.2 shows a sketch of the process. The term that describes these interactions, previously $Y^l_m(\Omega)$, becomes dependent not only on the angular variables in the resonance frame but also on the angular variables of the isobar decay. In terms of the defined amplitudes, following the derivation in [93] the expression in Eq. (2.19) can be modified to obtain:

$$X^l_m(\Omega,\Omega_h)=\sum_{\lambda_{isobar}}D^{J_i*}_{m,\lambda}(\Omega)F^i_\lambda D^{1*}_{\lambda,0}(\Omega_h) \tag{2.24}$$

This is usually referred to as the decay amplitude. Certain correction factors are omitted for

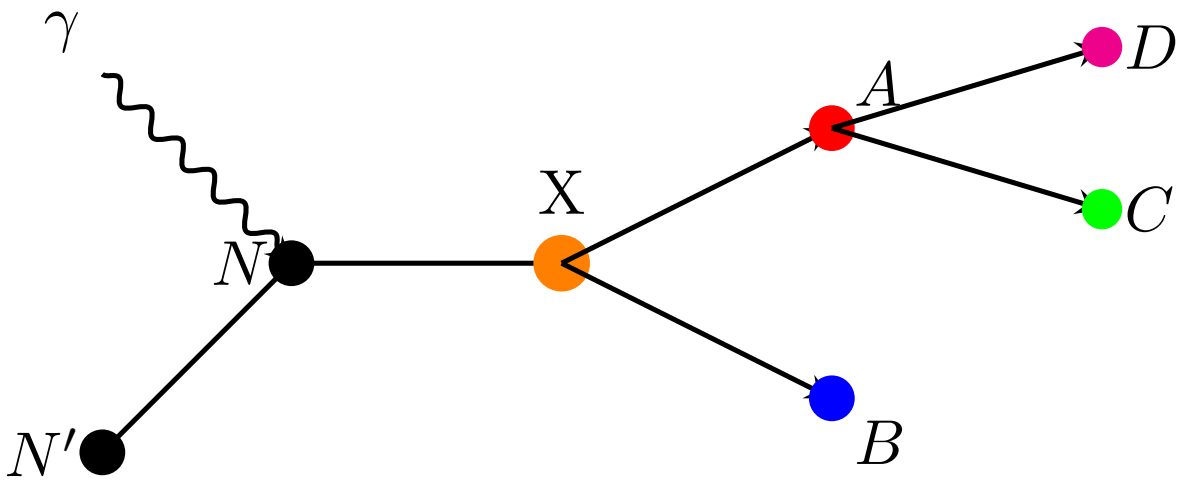

Figure 2.2: A sketch of an isobar decay. An interaction produces a resonance X that decays into two particles A and B, where A, also called the isobar, decays again. The full decay is modelled as a product of all intermediate isobars – in principle, an arbitrary number of intermediate decays can be accommodated.

clarity and will be mentioned later in the Section. The sum runs over the helicity of the isobar ϕ while the D terms are elements of Wigner-D matrices which are computed using formulae given in [100]. These terms encode the information about complex rotations performed when changing basis from the reference frame of the resonance to the reference frame of the isobar. F^i_λ is a function containing the Clebsch-Gordan coefficients required for the proper normalisation of the change in basis.

The modifications required to incorporate vector mesons into this model are described in GlueX technical notes [101, 102]. Starting once again with the definition of amplitudes A in the isobar model:

$$A_{\lambda,m}(\Omega,\Omega_h) = \sum_{i=1,2\ldots} \sum_{m=-J_i\ldots J_i} T^i_{\lambda,m} X^i_m(\Omega,\Omega_h) \tag{2.25}$$

The sums run over all contributing resonances indexed by i; the projection of a resonance's total angular momentum onto the chosen axis is indexed by m. The decay amplitude X^i_m has the same form as in (2.24), with the Clebsch-Gordan term given as:

$$F^i_{\lambda_\phi} = \sum_l < J_i \lambda_\phi | l 0, 1 \lambda_\phi > C^i_l \tag{2.26}$$

The helicity of the isobar ϕ meson can take values $-1, 0, 1$. Finally returning to the original intensity definition in (2.20), the expressions (2.21) to (2.23) can be substituted in to get the following, with the beam helicities explicitly notated:

$$I(\Omega,\Omega_h,\Phi) = \frac{\kappa}{2}[A_-(\Omega,\Omega_h)A_-^*(\Omega,\Omega_h) + A_+A_+^*(\Omega,\Omega_h) - P_\gamma(A_-(\Omega,\Omega_h)A_+^*(\Omega,\Omega_h) + A_+(\Omega,\Omega_h)A_-^*(\Omega,\Omega_h))e^{i2\Phi}] \quad (2.27)$$

If rotated amplitudes are defined as:

$$\widetilde{A}_\pm = e^{i\Phi}A_\pm(\Omega,\Omega_h) \quad (2.28)$$

The intensity can again be rewritten as:

$$I(\Omega,\Omega_h,\Phi) = \frac{\kappa}{4}[(1-P_\gamma)|\widetilde{A}_+(\Omega,\Omega_h) + \widetilde{A}_-(\Omega,\Omega_h)|^2 + (1+P_\gamma)|\widetilde{A}_+(\Omega,\Omega_h) + \widetilde{A}_-(\Omega,\Omega_h)|^2] \quad (2.29)$$

Helicity, which is the basis in which the formalism has been expressed, is not an eigenstate of parity. As the partial wave analysis aims to determine this quantum number, a transformation to a basis which is an eigenstate of parity is required. The reflectivity basis is one such option. Reflectivity is a quantum number associated with the reflectivity operator. The operator performs a rotation around a chosen axis (usually taken to be the normal to the production plane) followed by a parity operator. Like helicity it will take on values of either + or -. This basis is useful in a few ways. The reflectivity can be defined as the product of the parities of the resonance and the exchange particle that was involved in its production. Comparing amplitudes for different reflectivities thus allows access to information about the production mechanism. It also brings benefits in terms of the algebra, as partial waves with different reflectivities cannot interfere with each other.

Care has to be taken to account for both of the parities when defining the reflectivity amplitudes. The transition to the new basis can be done by using the following relations:

$$T^i_{+,m} = {}^+T^i_m + {}^-T^i_m \quad (2.30)$$

$$T^i_{-,m} = \tau_i(-1)^m({}^+T^i_{-m} - {}^-T^i_{-m}) \quad (2.31)$$

As previously, $T^i_{\pm,m}$ are the helicity amplitudes, while ${}^\pm T^i_m$ are the reflectivity amplitudes. From this it follows that $A_\pm$ become:

$$A_+ = \sum_{l,m}({}^+T^i_m + {}^-T^i_m)X^i_m(\Omega,\Omega_h) \quad (2.32)$$

$$A_- = \sum_{i,m} ({}^+T^i_{-m} - {}^-T^i_{-m})\tau_i(-1)^m X^i_{-m}(\Omega,\Omega_h) = \sum_{i,m} ({}^+T^i_{-m} - {}^-T^i_{-m}) X^{*i}_m(\Omega,\Omega_h) \tag{2.33}$$

In Eq. (2.33) the following parity relation from [102] is used:

$$-\tau_i(-1)^m X^i_{-m}(\Omega,\Omega_h) = X^{*i}_m(\Omega,\Omega_h) \tag{2.34}$$

For further convenience, a rotated decay amplitude can also be defined:

$$Z^i_m(\Omega,\Omega_h) = e^{-i\Phi} X^i_m(\Omega,\Omega_h) \tag{2.35}$$

The final step is to rewrite the intensity in a form required by the fitting tools used in the analysis, described in detail in Chapter 5. In particular, we have to recast it in terms of a series of coherent sums. If we write out the sum and difference of the amplitudes $\widetilde{A}_+, \widetilde{A}_-$ as:

$$\widetilde{A}_+ + \widetilde{A}_- = 2\sum_{i,m} i^- T^i_m Im(Z^i_m) + {}^+T^i_m Re(Z^i_m) \tag{2.36}$$

$$\widetilde{A}_+ - \widetilde{A}_- = 2\sum_{i,m} i^+ T^i_m Im(Z^i_m) + {}^-T^i_m Re(Z^i_m) \tag{2.37}$$

These sums and differences can be plugged into (2.29) to get:

$$I(\Omega,\Omega_h,\Phi) = \sum_{\lambda_1,\lambda_2} \{(1-P_\gamma|\sum_{i,m} |i^- T^i_m Im(Z^i_m) + {}^+T^i_m Re(Z^i_m)|^2 + (1+P_\gamma)|i^+ T^i_m Im(Z^i_m) + {}^-T^i_m Re(Z^i_m)|^2\} \tag{2.38}$$

The previously dropped indices over the baryon helicities λ_1, λ_2 have been reintroduced. To achieve the final form of the intensity, this is rewritten as a sum over baryon spin flip/non-flip amplitudes. Since parity invariance gives us the following:

$${}^\varepsilon T^i_{m;\lambda_1-\lambda_2} = \varepsilon(-1)^{\lambda_1-\lambda_2} {}^\varepsilon T^i_{m;\lambda_1\lambda_2}, \tag{2.39}$$

Defining complex parameters of the model as:

$$[J_i]^\varepsilon_{m,0} = {}^\varepsilon T^i_{m;+-} \tag{2.40}$$

$$[J_i]^\varepsilon_{m,1} = {}^\varepsilon T^i_{m;++} \tag{2.41}$$

Replacing the sum over baryon helicities with:

$$\sum_{\lambda_1\lambda_2} {}^{\varepsilon}T^{i}_{m;\lambda_1\lambda_2}\,{}^{\varepsilon}T^{i}_{m';\lambda_1\lambda_2} = (1+\varepsilon\varepsilon')\sum_{k}[J_i]^{\varepsilon}_{m;k}[J'_i]^{\varepsilon'*}_{m';k'} \tag{2.42}$$

We can write the final form of the intensity that is used in the fit as:

$$I(\Omega,\Omega_h,\Phi) = 2\sum_{k}\Big\{(1-P_\gamma)[|\sum_{i,m}[J_i]^{-}_{m,k}Im(Z^i_m)|^2+|\sum_{i,m}[J_i]^{+}_{m,k}Re(Z^i_m)|^2] + (1+P_\gamma)[|\sum_{i,m}[J_i]^{+}_{m,k}Im(Z^i_m)|^2+|\sum_{i,m}[J_i]^{-}_{m,k}Re(Z^i_m)|^2]\Big\} \tag{2.43}$$

The complex model parameters $[J_i]^{\varepsilon}_{m,k}$ represent the production amplitudes of the reflectivity amplitudes of the partial waves and are obtained through numerical fitting techniques. Although this final form of the intensity may not appear the most natural, it is required by the software tools that are used to implement the amplitudes – see Section 5.1. As a benefit, it does emphasise that partial waves of different reflectivities can only add incoherently. It has to be noted that though the intensity involves a sum over baryon spin configurations k, this cannot be measured in GlueX. It is assumed that this only matters up to a multiplicative constant and so is not considered in the actual fitting procedure.

The separation of reflectivities into separate sums also enables the partial wave analysis to provide information about the mechanisms involved in producing the resonance. Mesons at GlueX are expected to be produced in t-channel exchanges – see Subsection 4.4.2 for more detail – with a virtual particle being exchanged between the beam photon and the target proton. The exchange particle can be either natural or unnatural parity, and in the kinematic regime relevant for the analysis in this thesis the reflectivity is assumed to be equal to the naturality. Hence, if positive reflectivity amplitudes dominate it can be assumed that mesons are produced primarily via exchange of natural particles like pomerons [103], while negative reflectivity amplitudes would indicate unnatural particles like pions.

Finally, the sketch just given has omitted the spin dependent centrifugal barrier correction factors $F_l(q)$. The angular momentum of the decaying resonance has an effect on its shape, especially near threshold, and this effect must be accounted for. The factors are inserted inside the sums in Eq. (2.19). The full derivation can be found in [93] and its references, but the relevant terms for the partial waves used are provided in Appendix A.

The full partial wave formalism in reflectivity basis for vector-pseudoscalar decays produced with a polarised beam has been presented. It can be used to extract the parity and angular momentum quantum numbers that characterise a resonance by performing a fit to the angular variables of the data, as well as to compute the yields and in turn the mass dependent cross-sections of those resonances. The next two Chapters will describe the experimental setup, event reconstruction, and event selection procedures required to collect said data at the GlueX experiment.

The thesis will return to the formalism in Chapter 5, where the application of the intensity given in Eq. (5.1) in extended maximum likelihood fits and practical considerations relating to the ability of the model to obtain the partial wave amplitudes will be discussed.

Chapter 3

The GlueX experiment

The GlueX experiment is located in experimental Hall D of the Thomas Jefferson National Accelerator Facility (JLab), Newport News, Virginia. GlueX uses a tagged linearly polarised photon beam incident upon a liquid hydrogen target to study a variety of photoproduction reactions. Particles produced in interactions with the target are detected inside the GlueX detector system. The system is comprised of superconducting magnets, drift chambers, electromagnetic calorimeters, and scintillating detectors, achieving almost full azimuthal coverage. Both charged and neutral particles can be detected and reconstructed with good resolution. The experiment aims to map out the light and strange hadron spectrum, with a particular focus on states that may contain gluonic contributions to their quantum numbers. This Chapter describes the experimental setup inside Hall D and the facilities used to produce the photon beam.

3.1 Continuous Electron Beam Accelerator Facility

The Continuous Electron Beam Accelerator Facility (CEBAF) is a continuous wave electron accelerator within JLab [104]. It produces an electron beam with energies of up to 12 GeV that is served to the four experimental halls. Experiments in different halls are able to run concurrently – each may receive the beam at different currents and energies without interfering with the other halls. The CEBAF is laid out in a so-called racetrack setup whose diagram can be seen in Figure 3.1. Two linear accelerators (linacs), which increase the energy of passing electrons using superconducting radio frequency cavities, are connected together at both ends of the facility with recirculation arcs. These arcs contain magnets that focus and steer the beam, allowing multiple passes through the linacs. When provided to Hall D the beam undergoes 5.5 passes, allowing it to reach the full 12 GeV energy limit.

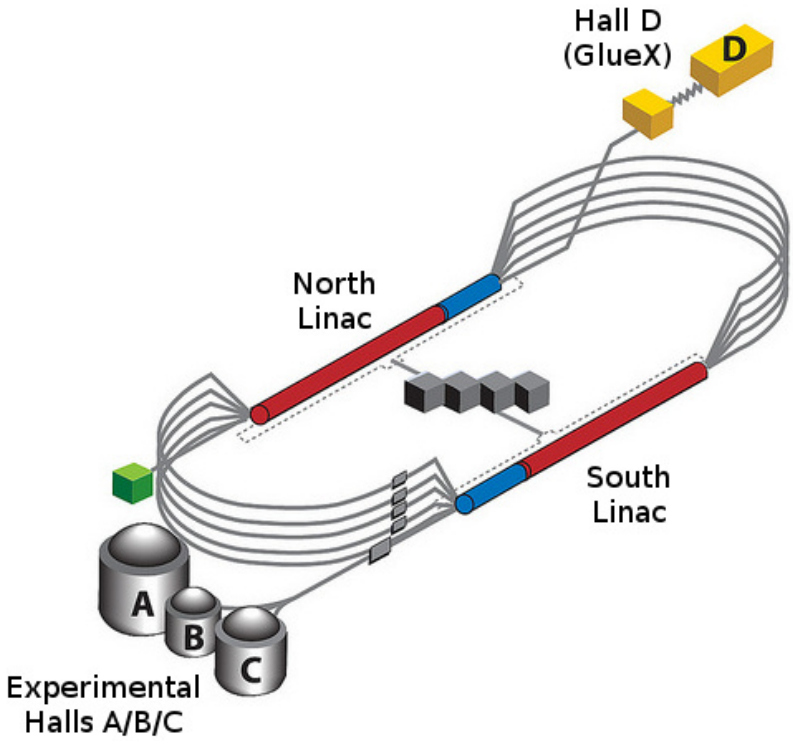

Figure 3.1: A diagram of the CEBAF accelerator. The two linear accelerators and entry points to the experimental halls are highlighted. Diagram taken from the GlueX diagram repository [105].

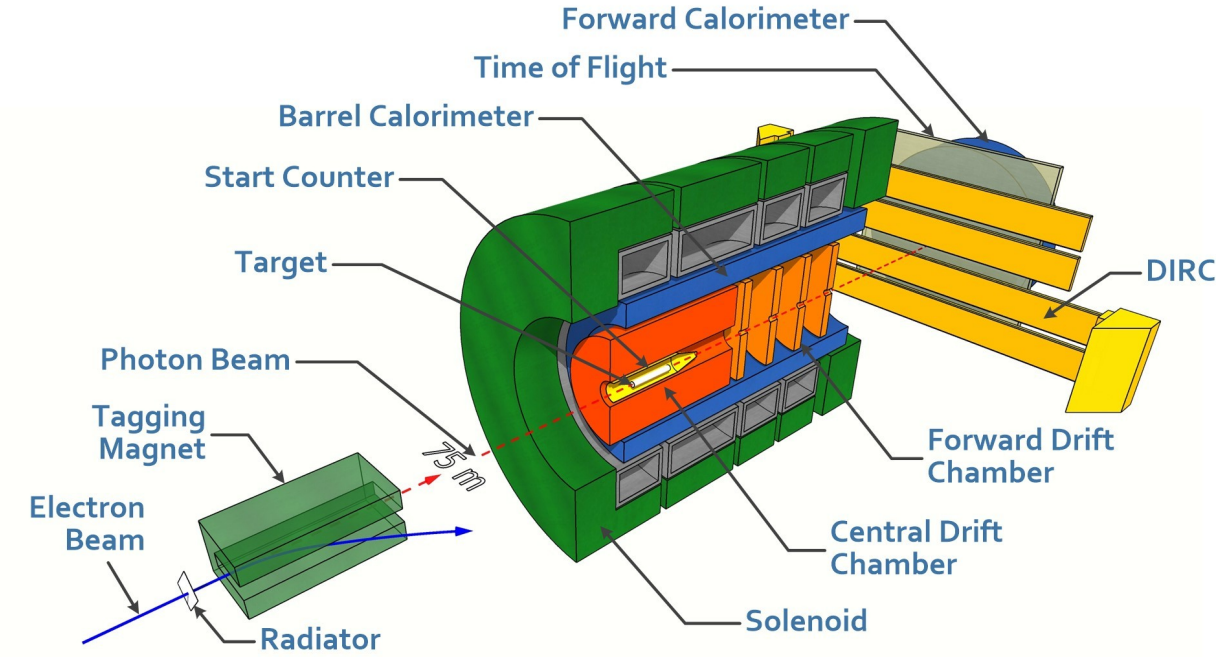

Figure 3.2: A diagram of the Hall D complex with main detector systems labelled. Diagram not to scale. Diagram taken from the GlueX diagram repository [105].

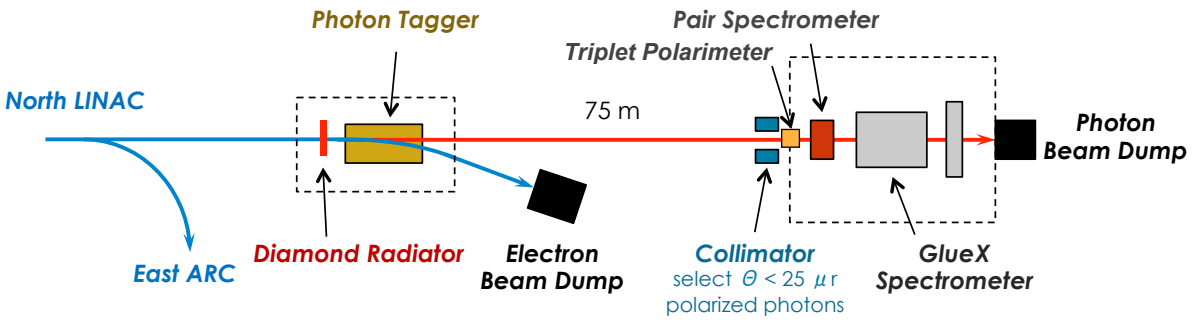

Figure 3.3: A diagram of the photon beamline throughout the Hall D complex. The radiator and tagger system are located in the tagger hall, which is 75m away from the detector hall that contains the detector system, here denoted as the GlueX Spectrometer. Diagram taken from the GlueX diagram repository [105].

3.2 Tagger hall

The Hall D experimental facility is comprised of two separate halls – the tagger hall and the detector hall. A diagram of the setup can be seen in Figure 3.2. As GlueX is a photoproduction experiment, the CEBAF electron beam has to be converted to a photon beam. This is done inside the tagger hall using a diamond radiator, which is an approximately 50 µm thick diamond crystal. Electrons that hit it scatter and produce photons that are sent 75 m forward into the detector hall. These electrons travel to two tagging detectors where their energy, and therefore the energy of the corresponding photons, is determined. The remaining electrons are directed into a beam dump by a magnet. A diagram of the photon beamline can be seen in Figure 3.3.

3.2.1 Photon beam

When electrons scatter off the diamond radiator, a process called coherent brehmsstrahlung occurs. This produces photons that are linearly polarised. This can be observed as an enhancement in collimated intensity above a bremsstrahlung spectrum produced by an amorphous aluminium radiator, as seen in Figure 3.4. The energy of this enhancement – usually called the coherent peak – as well as the polarisation value and its direction can be tuned by changing the orientation of the radiator with respect to the electron beam. All radiators are positioned on a multi-axis goniometer that allows for precise movement in all three dimensions. The coherent peak can go as high as the energy of the electron beam, but the level of achievable polarisation decreases as the energy increases. Taking the various physics objectives that GlueX aims for into account, the peak was optimised to be between 8 and 9 GeV. The exact value varies between data taking periods; linear polarisation in the peak reaches around 40%.

Knowing the energy of beam photons is desirable when performing reaction identification. It can be computed as

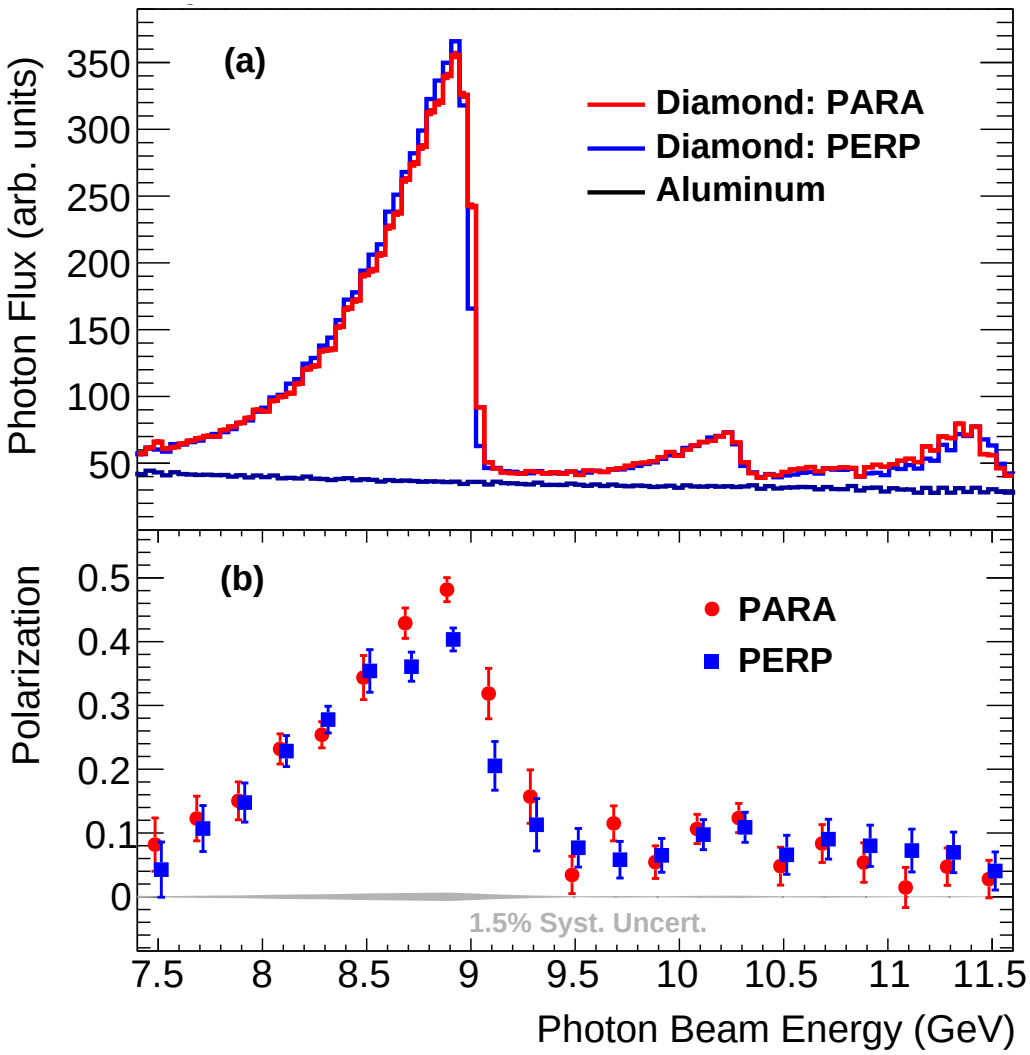

Figure 3.4: (a) Flux of the photon beam as measured using the Pair Spectrometer for different diamond radiator orientations in red/blue and the aluminium radiator in black, in bins of photon energy. An enhancement at the coherent edge can be seen when compared to the aluminium radiator spectrum. (b) Polarisation of the photon beam in bins of photon energy for different diamond radiator orientations. Figure taken from [106].

$$E_\gamma = E_{e^-}^{beam} - E_{e^-}^{scattered}, \tag{3.1}$$

where $E_{e^-}^{beam}$ is the energy of the CEBAF beam electron incident on the radiator and $E_{e^-}^{scattered}$ is its energy after scattering off the radiator. The former is known to high precision, while the latter is measured with a magnet and a pair of scintillating detectors, see Subsections 3.2.3 to 3.2.5.

3.2.2 Radiator

GlueX uses a 50 μm thick diamond as a radiator. Diamond is well suited to coherent brehmsstrahlung production [107] – it possesses a high coherent scattering probability owing to the low atomic

number of carbon and its crystal lattice properties. Diamond also has great thermal conductivity and radiation hardness, making it suitable for use in a high beam intensity environment [107]. The diamond crystals used were produced using a chemical vapour deposition (CVD) process [108]. The thickness of the radiator had to be less than a 100 μm to minimise the effects of multiple Coulomb scattering, which would widen the coherent peak and decrease polarisation [106]. However, radiation damage limits radiator thinness – thinner crystals experienced buckling after relatively short periods of beam time, seemingly caused by differential expansion of the crystal at the location where electrons were incident. This also caused the peak to widen and would have necessitated frequent changes of the crystal in use. Perhaps due to increased stiffness, a thickness of 50 μm was sufficient to prevent the physical deformation and so this value was chosen as a good compromise [106].

3.2.3 Tagger dipole magnet

The tagger hall dipole magnet is an 80 ton room temperature magnet [109]. It operates at a normal field strength of 1.5T, with a maximum strength of 1.75T. The magnet deflects electrons scattered off the radiator. Electron deflection angle depends on their energy – electrons that lose little or no energy go straight towards a beam dump, while other are aimed towards the tagger detector system. Magnetic field integrals along relevant electron trajectories are known to 0.1%.

3.2.4 Tagger Hodoscope

The Tagger Hodoscope [106] is a detector composed of 222 scintillation counters, which are sheets of EJ-228 plastic [110]. They are 6mm thick and 40mm high with widths that vary across the length of the detector. Each counter is coupled to a photo-multiplier tube (PMT) with an acrylic light guide. A diagram of the tagger setup can be seen in Figure 3.5. Once the scattered beam electrons hit the hodoscope their position on an imaginary focal plane is determined based on which counter produces scintillating light. The Hodoscope counters are placed in three rows slightly downstream of the plane, with their faces normal to the electron trajectory. Because electrons with different energies are bent at different trajectories by the tagger magnet, they also hit the hodoscope by crossing different points on the plane. In effect, if the magnetic field, and in turn the paths of bent particles, is well known and it is possible to determine where on the hodoscope an electron of a given energy would land, measuring the position allows the indirect measurement of the electron energy. Additionally, the detected electron can be matched to the photon that it produces if the hodoscope hit timing is recorded. This is made possible due to the detector's high temporal resolution of 200 ps. The matching allows for the determination of the photon's energy in turn as per Eq. (3.1).

As mentioned in Subsection 3.2.3 the magnetic field is indeed well understood, allowing the electron and photon energy determinations to be made. The hodoscope is designed to tag

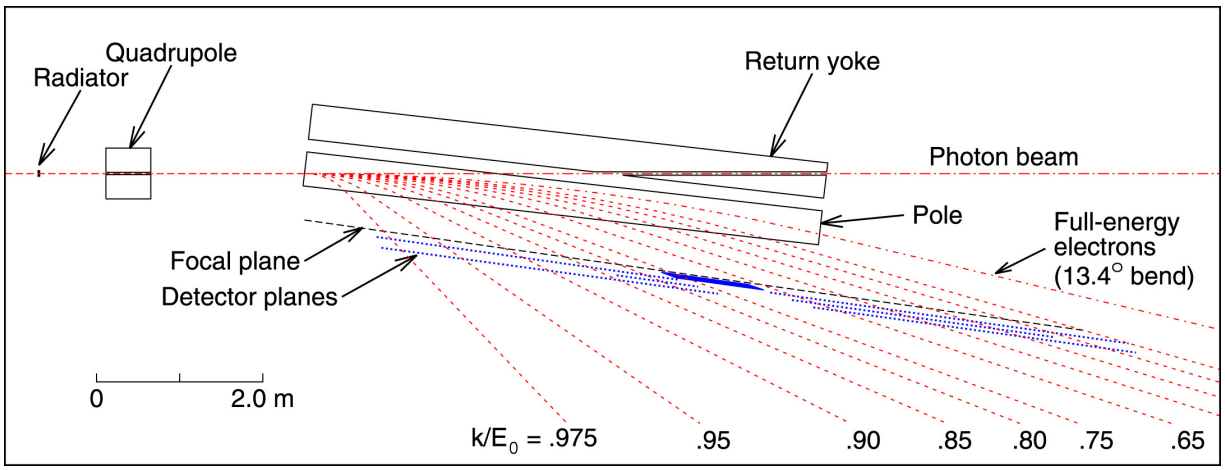

Figure 3.5: A diagram of the full tagger setup. The electrons are bent by the tagger magnet and travel along energy-dependent trajectories. The energies corresponding to tracks in the diagram are given in ratios of electron energy to produced beam photon energy. Electrons that have lost sufficient energy to the radiator intersect the two tagging detectors along the focal plane, which allows their energy to be measured. Taken from [106].

energies of electrons corresponding to 25% to 97% of the beam photon energy range. It covers 100% of the coherent peak region and above, but coverage below 60% of the maximum beam energy is worse and significant gaps in measurable energy between counters exist. An intentional hole in the middle of the detector is left to accommodate the high resolution tagging microscope, see Subsection 3.2.5 below.

3.2.5 Tagger Microscope

The Tagger Microscope [111] is a high resolution hodoscope that detects deflected electrons in the coherent peak energy region. The microscope consists of 510 scintillating fibres of BCF-20 plastic [112] that are fused at the downstream end to a clear light guide. They are tightly packed in a 102x5 formation, with 102 fibres horizontally in 5 vertical rows. Each fibre has a 2x2 mm^2 transverse profile and is orientated at an angle to the focal plane such that it is parallel to the electron trajectory – this maximises detector response. The crossing angle β varies slightly over the span of the detector volume, resulting in the fibres needing to be staggered along the electron dispersion axis. The light guide directs produced scintillation light to a shielded silicon photomultiplier (SiPM).

Like the Tagger Hodoscope, measuring the position the beam electron hits the microscope allows the electron's and the corresponding beam photon's energy to be determined. The timing resolution is similar at around 230 ps, meaning that matching the appropriate beam photon is possible like with the hodoscope. The higher density of the scintillating counters in the microscope means the resolution on the energy computation is better. The microscope is movable to account for the fact that the coherent peak energy may be changed.

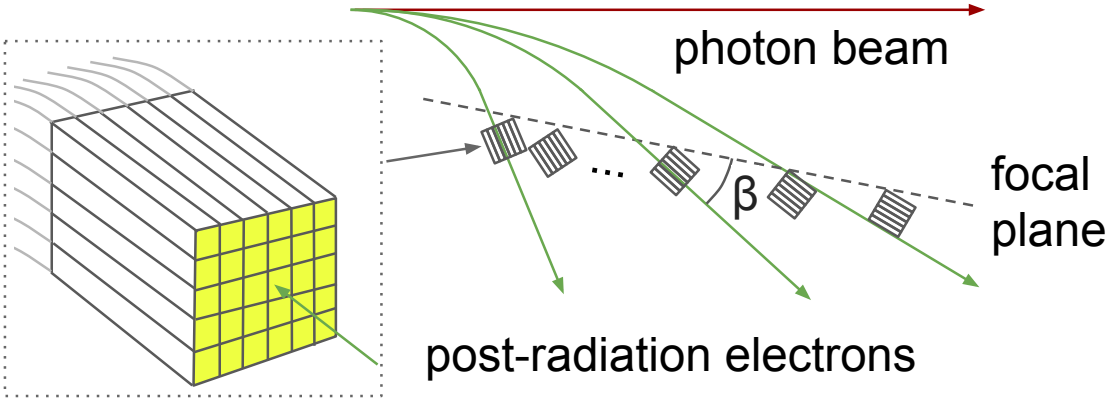

Figure 3.6: A more detailed diagram of the Tagger Microscope. The scintillating fibres are at a non-constant angle β with respect to the focal plane in order to have scattered electron trajectories be parallel to the fibre axis. Taken from [106].

3.3 Detector hall

The rest of the Chapter describes the primary GlueX detector system and target, which are housed in a hall 75m downstream from the tagger hall. Upon entering the hall, the photon beam is first collimated using the active collimator. It then travels through a set of detectors designed to measure beam-related quantities required for physics analyses, such as beam flux and polarisation, before finally hitting the target cell. Particles produced by interactions with the target or subsequent secondary decays are detected by a number of detector subsystems. These include calorimeters, tracking detectors, and various scintillating detectors. The data from the detector systems that passes the appropriate triggers is recorded by the Data Acquisiton System (DAQ) and stored on disk. The low-level detector information is used to reconstruct objects such as particle 4-vectors which can subsequently be used in physics analyses; both charged and neutral particles can be reconstructed. This process is described in more detail in Chapter 4.

3.3.1 Solenoid

GlueX tracking detectors and forward calorimeter are surrounded by a superconducting solenoid magnet [113] which produces a 2T magnetic field. The field is used to curve charged particle trajectories inside the detector, allowing the measurement of particle momentum. The magnetic field is mapped out throughout the hall and its contributions to momentum uncertainty is less than a percent – negligible compared to detector uncertainties.

3.3.2 Active Collimator and beam monitoring

The bremsstrahlung produced by the diamond radiator contains both coherent and incoherent components. The former is correlated with a more forward photon angular distribution. By removing photons with larger emission angles the polarisation of the beam can be enhanced due to suppression of the incoherent component. The beam undergoes passive collimation during its travel down the tunnel from the tagger hall, which is one of the reasons for the long distance between the two parts of the Hall D complex.

Upon entering the detector hall the beam goes through the Active Collimator, a system based on a similar device previously used at SLAC [114]. A set of tungsten pins are attached via circular baseplates to the primary collimator, which is itself a tungsten block with a 5mm aperture. If the beam hits the baseplates, currents are induced in the collimator and the pins. These currents can be used to deduce the displacement of the beam from its nominal centre. This information is fed back into the electron beam steering system, allowing the beam position to remain stable throughout active running.

3.3.3 Triplet Polarimeter

The Triplet Polarimeter (TPOL) [115] is used to measure the degree of linear polarisation of the photon beam. Many physics observables, like the partial wave amplitudes extracted in this thesis, depend on this quantity. After travelling through the collimator the beam hits a beryllium foil converter, which causes e^+e^- pairs to be produced off an atomic electron [115]. The azimuthal angular distribution of the recoil electron is proportional to the polarisation of the incident photon if the energy and trajectory of the pair are known. In particular, the cross section for triplet photoproduction using a linearly polarised photon beam can be written as [115]:

$$\sigma_t = \sigma_0[1 - P\Sigma\cos(2\varphi)], \tag{3.2}$$

where σ_0 is the unpolarised triplet cross section, P is the polarisation of the photon, Σ is the beam asymmetry, and φ is the azimuthal angle of the recoil electron with respect to the plane of polarisation of the incident photon beam. The recoil electron is detected by a silicon strip detector housed within a vacuum chamber.

The azimuthal angular distribution is fit to a function of the form [115]:

$$\mathrm{I}(\varphi) = A[1 - B\cos(2\varphi)], \tag{3.3}$$

where A and B are parameters of the fit and $B = P\Sigma$. Σ is a function of the beam energy, converter thickness, and the geometry of the setup that has been measured for GlueX. Assuming that Σ is known, the polarisation P can be extracted once the fit to φ is performed. The produced e^+e^- pair and beam photons that did not interact with the TPOL proceed in the evacuated beam-

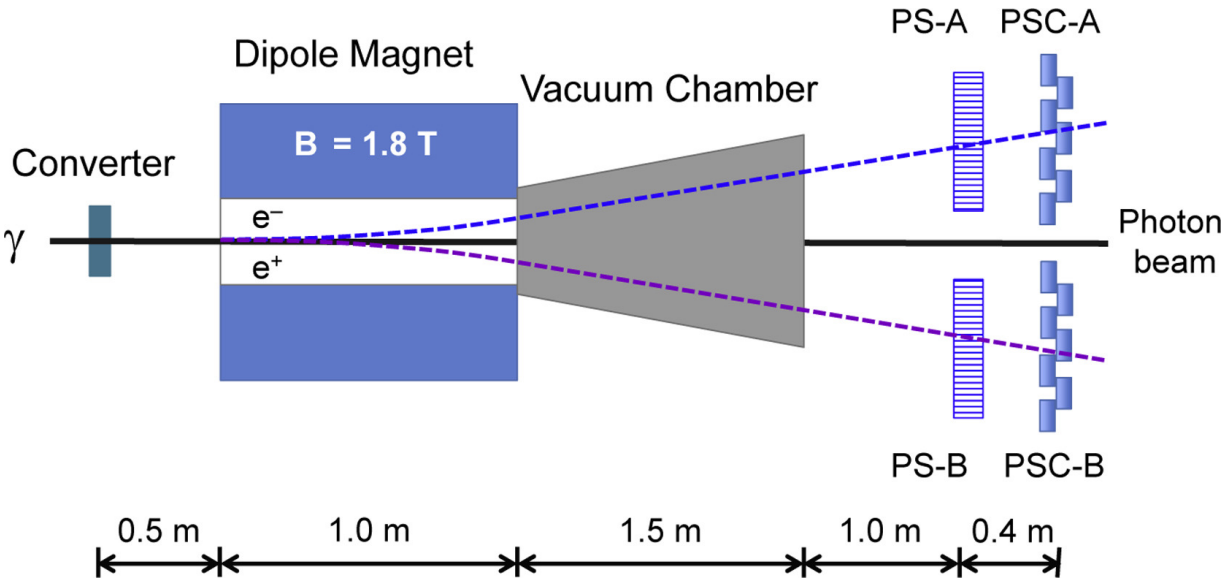

Figure 3.7: A diagram of the Pair Spectrometer. The beam photons scatter off an atomic electron in the converter foil and produce lepton pairs. The dipole magnet separates these along energy dependent trajectories that cross the two arms of the Spectrometer. Taken from [116].

line. The pair ends up entering the magnetic field and vacuum chamber of the Pair Spectrometer described in Subsection 3.3.4, while the photons go towards the GlueX target region.

3.3.4 Pair Spectrometer

The Pair Spectrometer (PS) [116] is used to determine both the photon beam flux, required for cross-section calculations, and measure the fraction of polarised photons present in the coherent peak region. The PS operates by detecting e^+e^- pairs produced in a converter material after an interaction with a beam photon, allowing its energy to be reconstructed. These pairs are usually the ones produced inside the TPOL using the beryllium foil, but additional converters can be inserted. The PS contains two detector layers - a high granularity hodoscope and a set of coarser scintillators, called PS and PSC counters respectively. These are split into two arms, situated symmetrically on either side of the beam line. Each arm covers an $e^{\pm}$ energy range of 3.0 to 6.2 GeV, corresponding to reconstructed beam photon energies of 6.2 to 12.4 GeV [106]. The PS has a trigger separate from the main GlueX trigger that is used in parallel. Like in the tagger detectors described in Subsections 3.2.4 and 3.2.5, the energy of the detected leptons can be determined with the help of a magnet. In this case, a dedicated dipole magnet with a nominal field strength of 1.8 T is used. A diagram can be seen in Figure 3.7. The calibration required to perform total flux determination with the PS is performed using the Total Absorption Counter, see Subsection 3.3.5.

3.3.5 Total Absorption Counter

The Total Absorption Counter (TAC) is a high efficiency lead-glass calorimeter that is used for the determination of the total normalisation of the photon beam flux. It was originally designed for the CLAS experiment in Jefferson Lab's Hall B [117]. Similar to the Forward Calorimeter described in Subsection 3.3.13, the TAC measures Cherenkov radiation caused by particles entering the lead-glass. The radiation is read out using PMTs. The TAC is designed to detect all beam photons above a given energy threshold. The Counter, which is otherwise retracted, is inserted immediately upstream of the photon beam dump during dedicated low intensity calibration runs and all hits coincident with hits in the tagging detectors are measured. Running at normal intensities would significantly increase the systematic uncertainty on the TAC measurements due to overlapping photon hits. Coincidences with pairs detected in the PS are also measured – this allows for the determination of the ratio of PS hits to tagger counter hits, which is used during normal running to convert the PS pair detection rate to a flux.

3.3.6 Target

GlueX uses a liquid hydrogen target due its high proton density. The hydrogen is contained in a 30 cm long conical cell that decreases from a diameter of 2.42 cm to 1.56 cm over its span. The cell is cooled by a cryogenics system such that it maintains an operating temperature of approximately 20 K at a pressure of 1.31 bar.

3.3.7 Start Counter

The Start Counter (SC) is a cylindrical scintillation detector made up of 30 paddles that surround the target cell [118]. The paddles are made out of EJ-200 scintillating plastics [110], while the produced scintillating light is detected using SiPM detector modules. A diagram can be seen in Figure 3.8. The primary task of the SC is to match the particles produced by an interaction in the GlueX target to the corresponding beam photon. Correct beam bunch matching is necessary for various techniques used in signal selection, e.g. when using 4-momentum conservation as a constraint in kinematic fits – see Subsection 4.1.3. For this to be achievable temporal resolution high enough to resolve the RF structure of the beam is required. In practice this resolution depends on which section of the SC charged particles interact with. In the nose section that comprises the end of the detector past the target cell, where the majority of the charged tracks intersect with the SC, the resolution is 450 ps. This is sufficient to distinguish the 4 ns wide beam bunches. Besides recording timing, the Start Counter can also be used when performing particle identification. Particles that trigger scintillation in the paddles will lose some of their energy with energy deposit profiles that will vary as a function of particle type and momentum. In particular, protons can be distinguished from other positively charged particles up to 0.9 GeV.

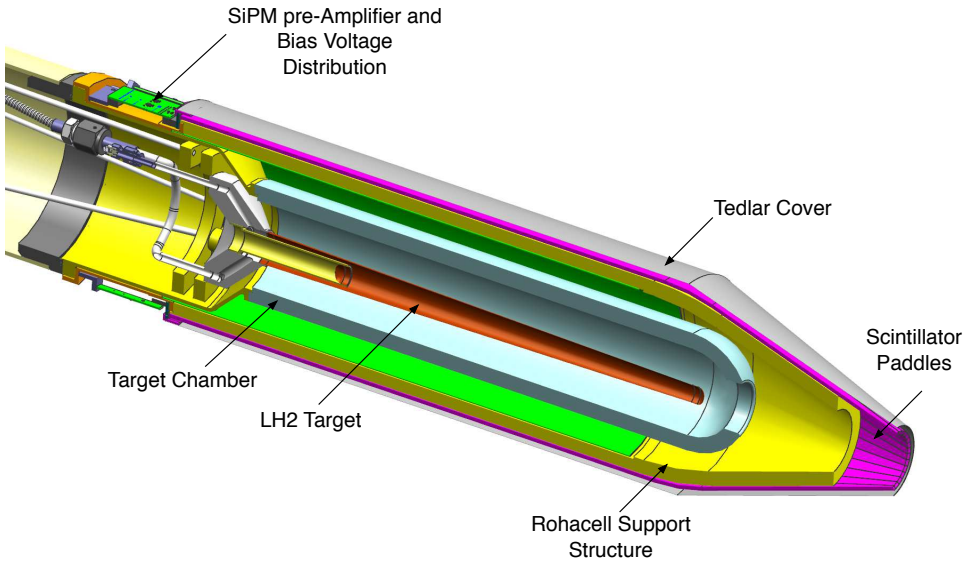

Figure 3.8: A diagram of the Start Counter. The detector surrounds the liquid hydrogen target and tapers to a narrower 'nose' section in the beam direction. Different regions of the SC exhibit different timing resolutions. Taken from [106].

3.3.8 Central Drift Chamber

Reconstruction of charged particles requires their trajectories to be known to a high level of accuracy. GlueX achieves this primarily through the use of two Drift Chambers. The first is the Central Drift Chamber (CDC) [119], a tracking detector located within the Barrel Calorimeter surrounding the target cell and the Start Counter. The CDC is a straw-tube drift chamber, comprised of 3522 gold-plated tungsten anode wires in Mylar sheaths arranged in a cylindrical volume. The Drift Chamber is pumped with a 50:50 CO2:Ar gas mixture. When charged particles travel through the CDC, the gas is ionised and the resulting free electrons are attracted to the anodes close to the ionisation path. The electrons themselves cause further ionisation – this avalanche produces a signal in the wires. If a model for the propagation of the avalanches can be assumed, locations of wires that registered an electric signal can used to determine the particle's trajectory. It is also possible to determine dE/dx energy loss and timing information from the CDC. The former, like in the case of the SC, allows for effective identification of low momentum particles. The Central Drift Chamber covers the region of 6° - 168° in the polar angle, with optimum coverage between 29° - 132°. The tubes are arranged in 28 layers, with 12 being axial and 16 being offset at stereo angles of $\pm$ 6° to provide additional spatial information along the beam direction. This arrangement is depicted from the upstream end of the detector in Figure 3.9.

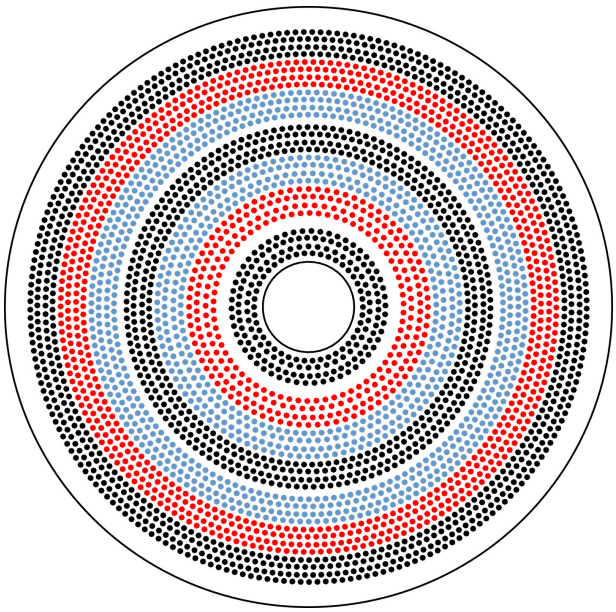

Figure 3.9: Upstream view of the CDC straw layout. The axial straws are pictured in black, while the stereo straws are red (+6°) and light blue (-6°). Taken from [119].

3.3.9 Forward Drift Chamber

The second Drift chamber is the Forward Drift Chamber (FDC) [120]. It is a wire tracking detector designed to handle high density charged tracks in the forward region of the GlueX detector. In general, the forward angular region contains most particles produced in meson resonances and so requires additional attention. The FDC has full coverage between 1° - 10° in the polar angle with partial coverage up to 20°. The FDC is built up from 24 1 m diameter planar drift chambers. These are combined into 4 packages of 6 chambers each. Each chamber in a package is rotated 60° to the previous and contains a wire plane and a cathode plane, split into thin strips, on either side. The components of the chamber are held together in a fiberglass insulated frame. A sketch can be seen in Figure 3.10. The chambers are separated by a ground plane of thin aluminised Mylar. The FDC is filled with a mixture of CO2 and Ar gas at a 60:40 ratio, which reduces the impact of the magnetic field on the tracking measurements compared to the 50:50 mix [106]. Like in the case of CDC described in Subsection 3.3.8, charged particles cause ionisation in the FDC gas such that free electrons are attracted to the anode wires. The density of charged tracks in the forward region is higher than at angles covered by the CDC, meaning that good track separation and position resolution is required. This is achieved with the use of the two sets of cathode strips as discussed in [120].

3.3.10 Time of Flight detector

Good particle identification capability is necessary to successfully reconstruct desired final states. One informative quantity that can be used for this purpose is the Time of Flight (TOF) of

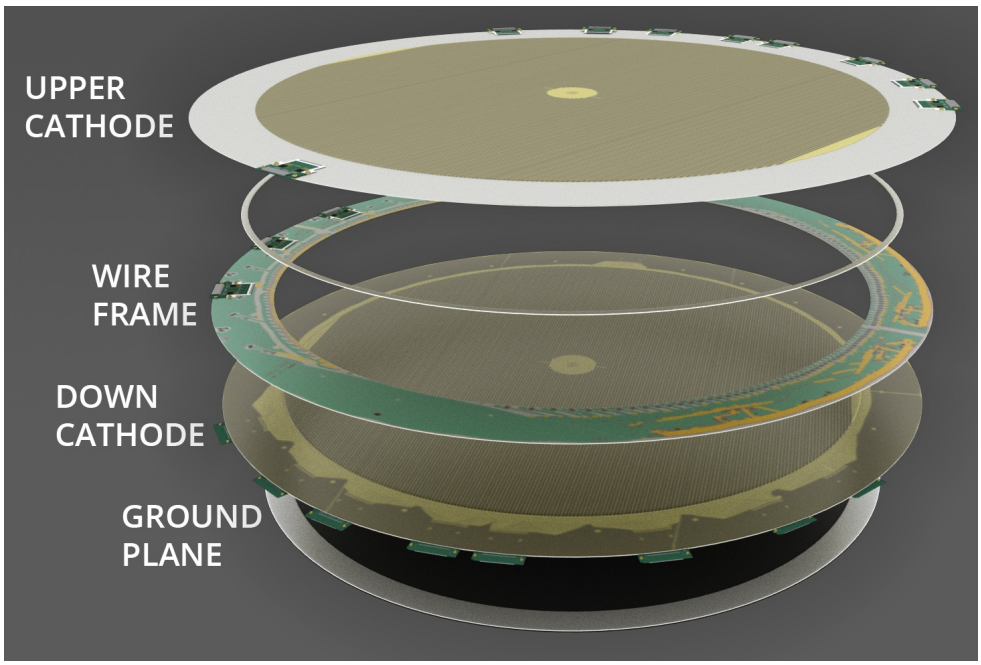

Figure 3.10: An artist's rendition of an FDC chamber. Taken from [106].

a particle, which is defined as the time necessary to traverse the distance from its initial vertex in the target to a dedicated detector. This time can be related to the mass and momentum of the particle [121]. As the momentum for charged tracks can be measured using the GlueX solenoid magnet, knowing the TOF allows us to predict the mass. The Time of Flight detector is a scintillator detector located 5.5 m downstream of the target cell in front of the FCAL [106]. It is made from two stacked planes of EJ-200 scintillator paddles. A small hole is left in the middle of the detector to allow the photon beam to pass through and the paddles immediately surrounding this hole are shorter. The TOF provides fast timing signals with a resolution of 100 ps. The Time of Flight is obtained by combining the timing data from the Start Counter, see Subsection 3.3.7 and the TOF detector hit, where the former provides the start time and the latter the end time of the particle's travel.

A common plot used for PID is the 2D histogram of particle velocity, expressed as $\beta = \frac{v}{c}$, against particle momentum; the velocity can be computed from the Time of Flight in the usual way. An example of this plot using the GlueX TOF detector can be seen in Figure 3.11. As expected, different particle species form distinct bands based on their mass. The TOF shows good PID performance for pion/kaon discrimination up to 2 GeV, where separation at 4σ is achievable. Unfortunately the two particle types become increasingly indistinguishable when momentum increases, though protons remain easily separable throughout.

3.3.11 Detector of internally reflected Cherenkov radiation

GlueX PID detectors cannot reliably distinguish particles like kaons and pions past approximately 2 GeV, e.g. see the TOF performance in Subsection 3.3.10. Extending the viable mo-

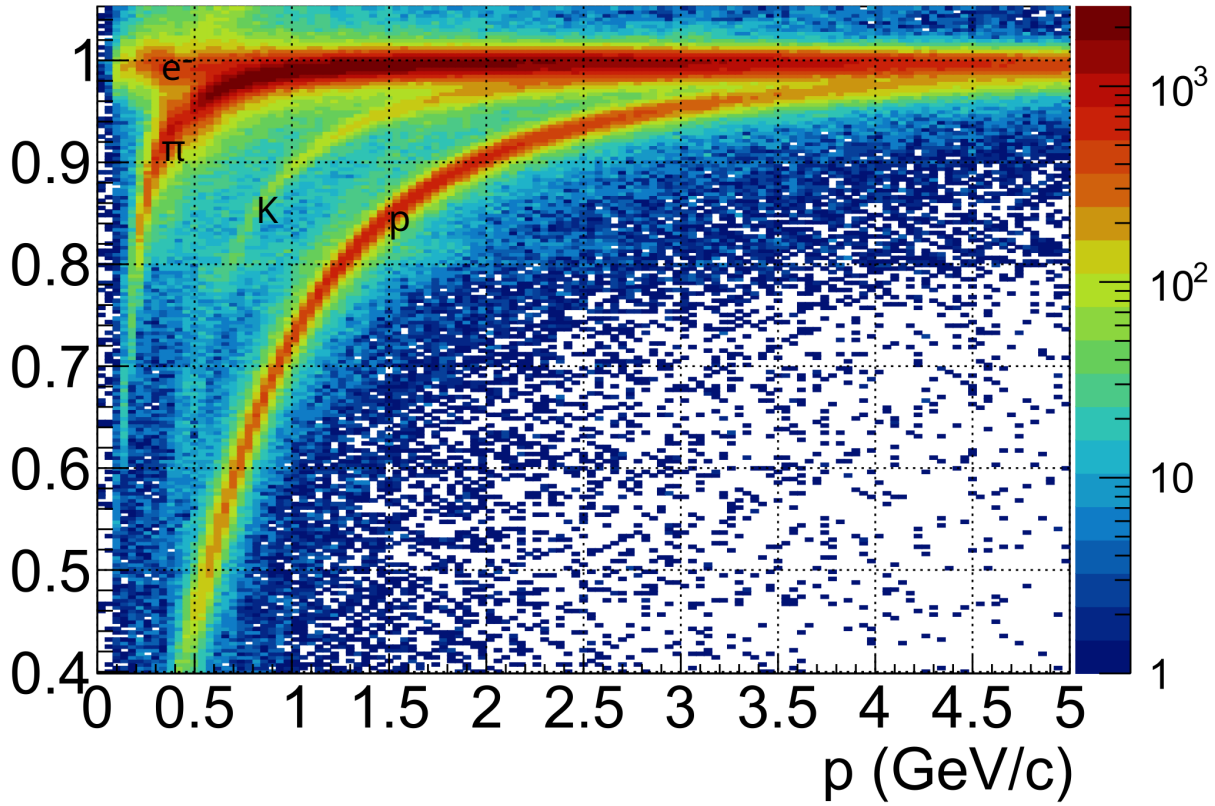

Figure 3.11: Factor $\beta = \frac{v}{c}$ against particle momentum. Colour map is on a logarithmic scale. Distinct bands can be seen for charged kaons, pions, electrons, and protons and are notated on the plot. The separation between bands means the Time of Flight detector can be used for particle identification. Protons are easily separable from other particle species throughout the momentum range, but pions and kaons begin to become indistinguishable past 2 GeV. Taken from [106].

mentum range in which pion/kaon separation can be performed could be helpful for reactions where higher average particle momenta is expected. In general it would also allow GlueX analyses to maximise available statistics. To this end, the Detector of internally reflected Cherenkov radiation (DIRC) [122] was commissioned for data-taking runs starting in late 2019. It is the newest addition to the GlueX detector, designed to extend PID capabilities to 2.5 GeV - 3 GeV in particle momentum [122]. Commissioning studies indicate that pion/kaon separation can reach 3σ accuracy in some angular regions [123].

It is made out of 48 fused silica glass bars arranged in 4 boxes. Particles that travel through the glass bars move faster than the local speed of light in the medium, producing Cherenkov radiation. The produced photons are internally reflected inside the glass tubes using mirrors until they eventually hit a PMT array. The angle of Cherenkov photons emitted in the bars is a direct measure of the particle's β and allows the DIRC to be used for PID, similar to the TOF. The angles can be reconstructed via a number of methods [124], including deep learning algorithms, but the standard approach is to use pre-calculated lookup tables [124]. Because the DIRC is a relatively new addition to the GlueX system, studies on its performance with real data

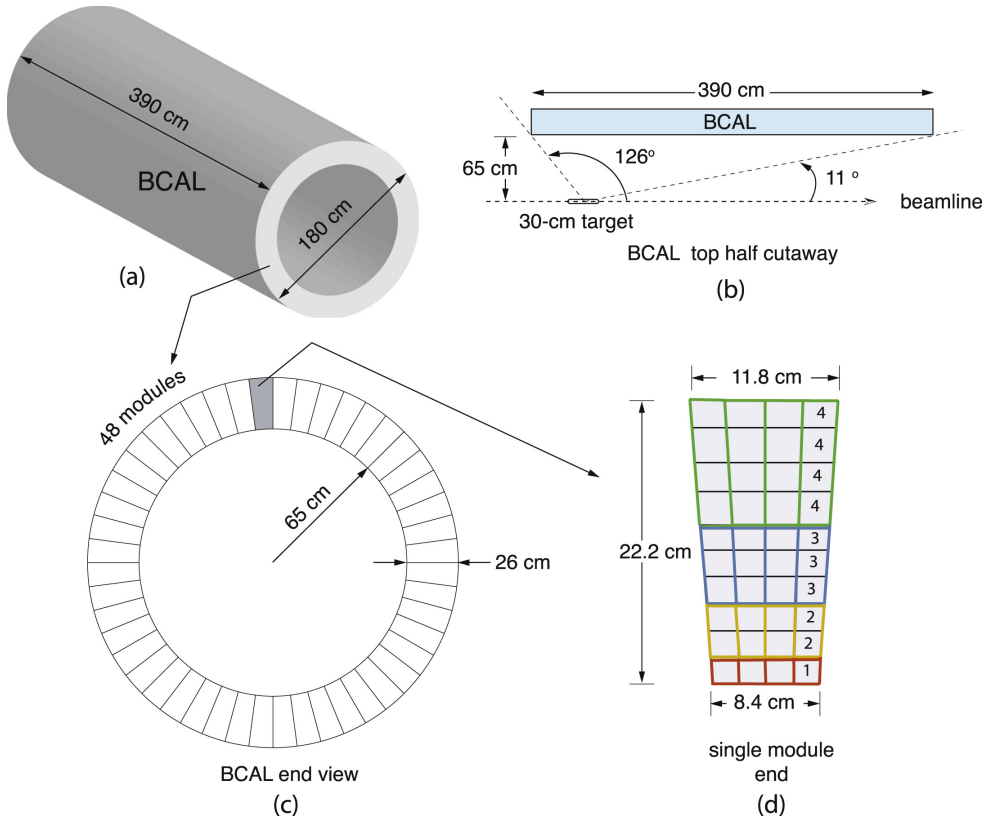

Figure 3.12: Schematics of the BCAL. a) A general view of the BCAL. b) A cutaway that shows the polar angle coverage of the BCAL. c) The end view of the BCAL that demonstrates how the detector is segmented. d) A matrix of the readout electronics. Taken from [125].

are still ongoing and it was not used in the analysis presented in this thesis.

3.3.12 Barrel Calorimeter

Tracking and scintillator detectors are capable of detecting charged particles, but calorimetry systems are necessary for the neutrals that do not cause ionisation. As in the case of the Drift Chambers, GlueX uses two calorimeter detectors to achieve high angular coverage and resolutions. The first is the Barrel Calorimeter (BCAL), an electromagnetic calorimeter that surrounds the target cell area in an open-ended cylinder shape; the target is located in the backwards region of the BCAL. The calorimeter is made out of alternating layers of lead sheets and scintillating fibres made from Kuraray SCSF-78MJ plastic [126]. The calorimeter is split into 48 optically isolated modules with the scintillating fibres running parallel to the cylinder axis. Schematics showing various angles of the BCAL are given in Figure 3.12. A particle – whether neutral or charged – hitting the lead will interact, causing an electromagnetic cascade that leads to scintillating light being produced in the fibres. The light is collected with waveguides at the end of each module and relayed to SiPM readout detectors. This can be used to determine the energy deposition and the position of the particle hit in the BCAL – the latter is obtained by a clustering algorithm on the BCAL cells that were activated by a hit [125]. The Barrel Calorimeter covers

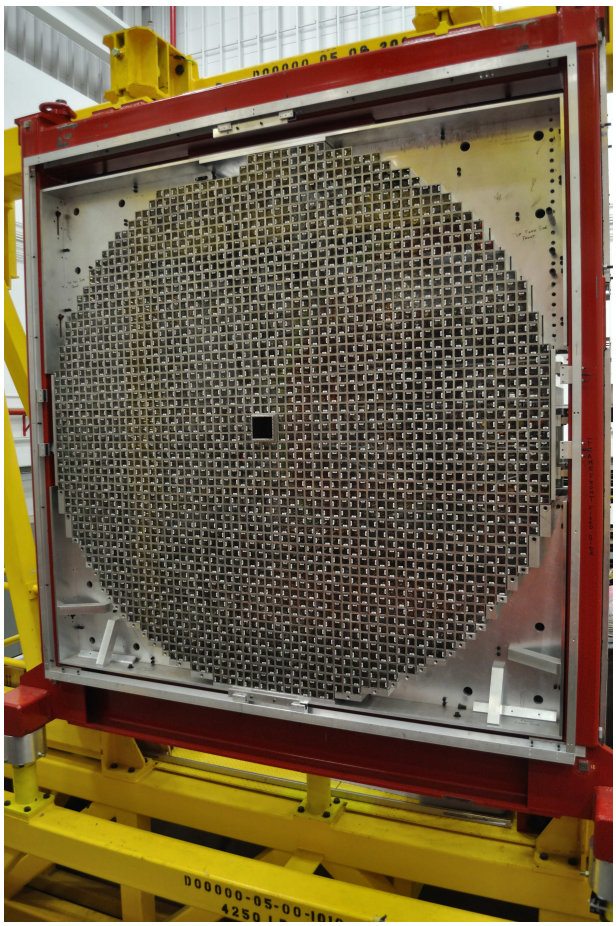

Figure 3.13: A frontal view of the Forward Calorimeter inside the detector hall. The beam hole can be seen in the middle of the detector. Taken from the GlueX photo collection [127].

polar angles of 11° - 126° with full azimuthal angle coverage and has an energy resolution of $\sigma_e/E = \frac{5.2\%}{\sqrt{E(GeV)}} \oplus 3.6\%$ [125]. It also has a temporal resolution of 100 ps - 200 ps depending on particle energy [125]. This is low enough to make the BCAL a viable timing detector as the resolution is comparable to the dedicated TOF.

3.3.13 Forward Calorimeter

As mentioned when discussing charged particle detection in Subsection 3.3.9, the forward angular region requires extra attention to properly reconstruct the particles produced by meson resonances. The Forward Calorimeter (FCAL) [106] is an electromagnetic calorimeter that covers the forward region with polar angle coverage of 1°-11°. It is located 5.6 m downstream of the GlueX target, behind the TOF detector, and is made out of 2800 stacked 4x4x45cm lead-glass blocks arranged in a circular array. A hole in the middle of the calorimeter allows beam passthrough. Figure 3.13 shows a frontal view of the detector. The electromagnetic cascades caused by particles incident on the FCAL blocks produce particles that move at relativistic speeds and emit Cherenkov radiation inside the lead-glass. The radiation is collected using

PMTs and read out using fast ADC electronics. The intensity of the Cherenkov light is proportional to the particle's energy. The calorimeter can detect particles up to energies of a few GeV with a resolution of $\sigma_e/E = \frac{6.2\%}{\sqrt{E(GeV)}} \oplus 4.7\%$ [106]. The fast readouts enable the high density of particles in the forward region to be detected with high efficiency. In addition to the energy measurements, the position of the hit can also be reconstructed using clustering like in the BCAL.

3.3.14 Trigger and data acquisition system

GlueX collects detector data continuously, but it is only saved for longterm storage if certain physics conditions, or triggers, are satisfied. Triggers are used to filter out data that is highly likely to be low quality, i.e. not suitable for accurate particle reconstruction or unlikely to yield interesting events. GlueX uses a relaxed trigger based on energy deposition in the two calorimeters. It consists of the following conditions:

1. $2E_{FCAL} + E_{BCAL} > 1$ GeV, $E_{FCAL} > 0$ GeV
2. $E_{BCAL} > 1.2GeV$

The first condition is the primary trigger, as most physics events from meson resonance decays will be produced in the forward direction. The second condition is used to capture events from certain processes that release a high amount of transverse energy. Alternative triggers can be used for calibration and detector study purposes. Signals from the calorimeters are digitised using Flash Analog-to-Digital Converters (fADCs) at a sampling rate of 250 MHz. Energy deposition calculations sum these digitised signals on FPGA boards. If trigger conditions are met, signals to all relevant data readout crates (ROCs) are sent and detector data is streamed into the Data Acquisition System (DAQ). In addition, a parallel random 100 Hz trigger is run to collect events for more realistic simulation backgrounds. A number of dedicated computer nodes collate the data streams and write them out to data storage.

Once data is stored, it is available to be used for reconstruction and subsequent data analysis. Reconstruction, data skimming, and signal event selection of the GlueX data used in this thesis are covered in the following Chapter. The dataset obtained from these steps is used in the partial wave analysis which is presented in Chapters 5 and 6.

Chapter 4

Event selection

The motivation for analysing the $\eta\phi$ channel and the necessary preliminaries for doing so have been laid out. This Chapter describes the data sets used in the analysis, the reconstruction of the data to physics objects and the full event selection procedure performed to pick out signal. Section 4.1 presents the GlueX data and simulation production pipelines. Sections 4.2, 4.3, and 4.4 describe the various types of selection criteria, commonly called 'cuts', applied to the data to eliminate background, while Section 4.5 is dedicated to the question of combinatoric backgrounds. A statistical subtraction procedure described in Section 4.6 attempts to remove remaining background components from the post-selection sample. Diagnostic plots show that the most significant sources of background are removed, or are outwith the kinematic region which the analysis focuses on, although some residual baryon contamination is possible as shown in Section 4.7.

4.1 GlueX datasets

4.1.1 GlueX data acquisition and reconstruction

The full available GlueX dataset is split by data-taking period. There are currently four such periods making up two distinct phases of the experiment, GlueX-I and GlueX-II, with the latter still ongoing. The periods are further split into runs that generally span a few hours of data acquisition – this is done to account for changes in experimental conditions over time and simplify later data calibrations. Table 4.1 summarises the integrated luminosities of all periods. The primary data used in this thesis was taken during the 2019-11 run from GlueX-II. As seen from the table, it contains statistics roughly equivalent to the entirety of GlueX-I dataset.

There are some notable difference between GlueX-I and GlueX-II beam times. Like mentioned in Subsection 3.3.11, the DIRC detector was added for GlueX-II running. The beam energy ranges for the coherent peak also differ – in GlueX-I it is between 8.2 GeV and 8.8 GeV, while for GlueX-II it was set between 8.0 GeV and 8.6 GeV. Figure 4.1 shows the photon beam

Table 4.1: Integrated luminosities for the coherent peak region for each GlueX data-taking period. Coherent peak ranges differ between GlueX-I and GlueX-II data.

Run period	Integrated coherent peak luminosity	Phase
2017-11	$21.8\,\mathrm{pb}^{-1}$	GlueX-I
2018-01	$63.0\,\mathrm{pb}^{-1}$	GlueX-I
2018-08	$40.1\,\mathrm{pb}^{-1}$	GlueX-I
2019-11	$132.4\,\mathrm{pb}^{-1}$	GlueX-II

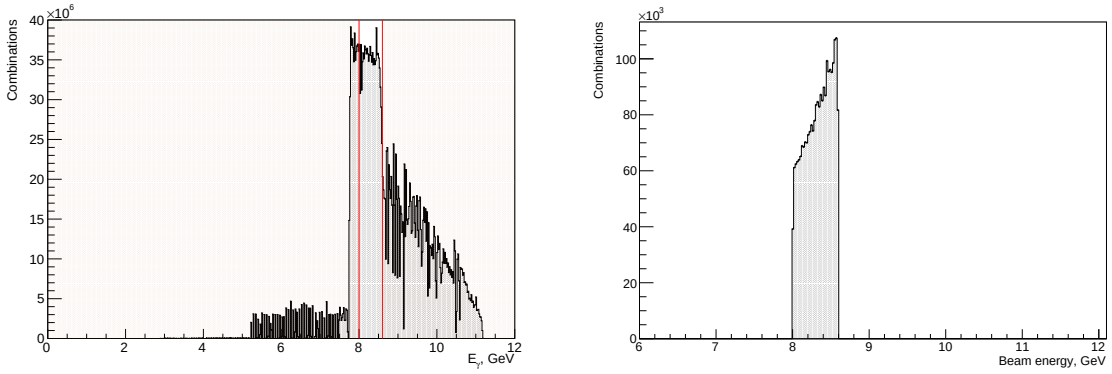

(a) Data.

(b) Monte Carlo.

Figure 4.1: Distributions of the photon beam energy for data with no cuts or accidental subtraction applied (4.1a) and signal simulation (4.1b). The rising edge of the coherent peak can be seen around 8.0 GeV. The red lines indicate the coherent peak cuts with removed regions shaded.

energy distribution for the GlueX-II data used.

Data collected during the experiment undergoes a number of processing steps before it is presented for physics analysis. When data is collected it is first stored in the EVIO file format [128] by the DAQ system. Files in this format contain low level information such as signals produced in the detector subsystems. EVIO files are processed using the halld_recon software suite [129] and reconstruction is performed, see Subsection 4.1.2. Detector calibration constants required for reconstruction are applied on a per-run basis – they are stored in a database called CCDB and can be retrieved using SQL queries. The output of the reconstruction is stored as REST files in the hddm format [130] which only contain higher level objects like particle tracks and calorimeter showers.

The final set of steps in this pipeline involves constructing candidate events according to the decay channel under study. Conversion of REST data into reaction specific datasets is done in centrally launched batches called Analysis Launches. GlueX researchers submit reactions that they wish to analyse using a web form; once a sufficient number of requests are logged the Launches are run on the central JLab batch farm. The halld_recon suite is used again alongside a plugin called the ReactionFilter to construct candidate events matching the requested final state.

This is also the stage at which the Kinematic Fit described in Subsection 4.1.3 is performed. Some preliminary event selection criteria are applied during the Launches, which are discussed in more detail in Section 4.2. The final output in this chain are ROOT trees usually referred to as Analysis Trees. The trees store the 4-vectors of the final state particles together with a large number of detector and beam level quantities. The Analysis Trees are processed using the DSelector library [131]. Depending on the analysis, the output of the DSelector can either be a set of final result histograms or additional ROOT trees to be used with other frameworks for further processing.

4.1.2 Track and cluster reconstruction

In order to convert detector data into physical observables, the 4-vectors of final state particles have to be reconstructed. Neutral particles are identified from calorimeter showers, which are reconstructed by clustering activated calorimeter cells. The clustering algorithms for the FCAL [132] and the BCAL [125] are similar. In both cases the cell with the highest energy deposit for a given event is selected as the 'seed' block of the initial cluster given that it is above a certain energy threshold – this is 90 MeV for the FCAL and 15 MeV for the BCAL [106]. All activated cells in geometrical proximity to this 'seed' are iteratively added to the cluster, with the total shower energy and centroid position being recomputed at each step. After this procedure is complete, it is repeated with the remaining activated cells until they have all been added to a cluster or no more 'seeds' above the threshold can be found. The BCAL algorithm finishes with an additional step, where neighbouring clusters may either be fully merged into one or individual cells reassigned between them. These decisions are made using predicted shower sizes and deposited energies in the cells relative to the total shower energies. The shower position resolutions of the two calorimeters are approximately 1.1 cm and 2.5 cm for the FCAL and BCAL respectively [106], allowing differentiation of relatively close photon hits.

In the case of charged particles, hits in drift chambers, calorimeters, and scintillator detectors are matched up to determine particle trajectories. The hits in the drift chambers must be linked up to form track segments – this is a 3 stage process. First, candidate track segments are determined in both the FDC and the CDC. For the former, each package that contains hits is analysed starting from the most upstream plane. Charged particles in a solenoidal magnetic field will travel in a helical pattern, meaning that hits within each detector plane will be contained on a circle in the X-Y coordinate plane. A segment is formed if at least three planes in a package contain hits within 2 cm of each other radially [133]. For each successfully formed segment, a fit based on a hyperbolic projection of the X-Y plane is performed to extract initial track parameters [134] under the assumption that it starts at the centre of the target. The segments are then projected through the subsequent packages; the positions of the projection and the actual segment in a given package should also lie on a circle if they belong to the same track – if they are sufficiently close the segments are linked. A metric dependent on the circle radius is used to

determine whether this is the case [133].

For the CDC, the drift times in each straw-tube containing a hit are computed and converted to a distance between the location of the initial ionisation and the anode wire [135]. This distance can then be used as a radius to define a circle around the wire. If a given particle caused a hit in a straw-tube, its trajectory must be tangent to the corresponding circle. A fit can thus be performed to reconstruct a track that is tangent to the circles around every activated wire subject to resolutions effects – see Figure 4.2 for a geometric sketch. The combined track segments from both detectors are then joined together if they originate in the target and pass through both Drift Chambers within the 5° to 20° polar angle range [106]. Knowledge of the magnetic field mapping in the detector allows calculation of particle momenta from the trajectory's curvature.

The second step uses a Kalman filter [136, 137] to start finding the final track parameters. The fit proceeds from the furthest hit associated with the track and moves towards the closest approach of the track to the beam line. The filter takes into account magnetic field information and multiple re-scattering interactions. At this stage the filter assumes that all tracks are from pions, unless they have momentum below 0.8 GeV, in which case they are identified as protons. During the final stage a Kalman filter is used to perform another fit, this time incorporating information about drift times and candidate particle masses. Initial timing information for calculating drift times is collected from matching a track to the SC, TOF, BCAL, or FCAL. Specific particle identifications are assigned at the end. Tracks are reconstructed well, with momentum and polar angle resolutions varying from 1 % to 10 % and from 0.1 % to 1.5 % respectively based on particle type and momentum [106].

4.1.3 Kinematic fitter

The final step of the reconstruction in most GlueX analyses is the use of a software tool called the Kinematic Fitter. Its primary goal is to improve the resolution on variables of interest by using information about detector uncertainties and physical conservation laws. The Kinematic Fitter performs a constrained least-squares fit that can be expressed by the following matrix equation:

$$\chi^2 = \varepsilon^T \hat{V}^{-1} \varepsilon + 2\lambda^T F, \tag{4.1}$$

where ε is a vector of residuals between fit and directly measured variables $x^i_{j,fit} - x^i_{j,meas.}$, for variable i in for the j-th combination of final state particles; $\hat{V}$ is a covariance matrix encoding the uncertainties between variables used in the fit; λ is a free fit parameter, and F is a physics constraint. The present analysis uses a constraint on overall 4-momentum conservation and position of the initial vertex, such that the interaction must have begun inside the target cell.

Potential physics events are usually only saved if this fit converges. Measures of fit quality, such as number of degrees of freedom over the computed χ^2, can be used to further refine

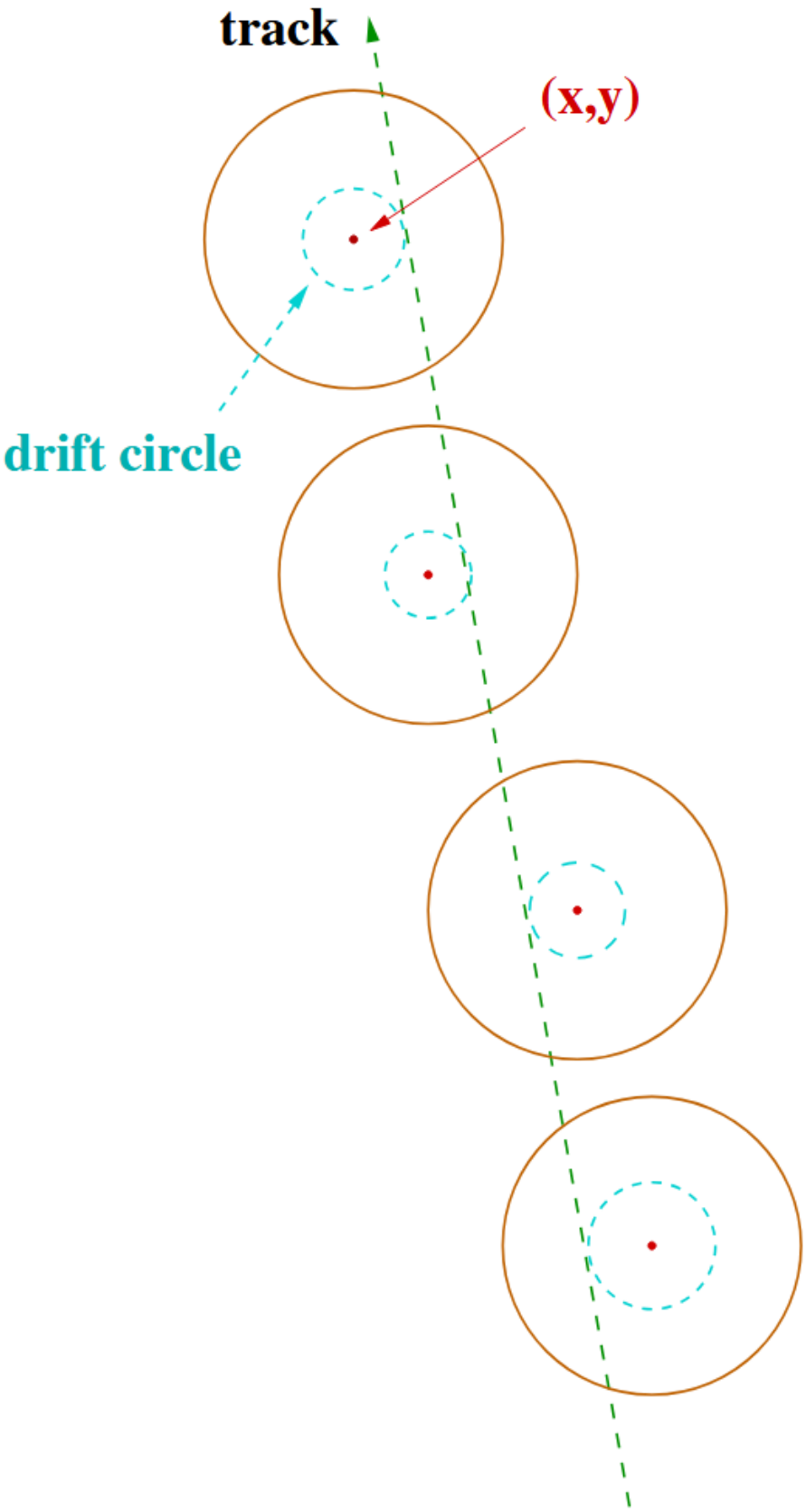

Figure 4.2: A diagrammatic sketch of track reconstruction in the Central Drift Chamber. A track that caused hits within CDC straw-tubes must pass tangent to circles centred around the anode wires, with a radius equal to the distance of the initial ionisation from the wire. Taken from [135].

Table 4.2: Resolutions of relevant invariant masses and angular distributions when using measured and kinematically fit variables. The kinematic fit systematically improves resolutions, which manifests visually as sharper distributions. A particular improvement is seen in the η invariant mass.

	m(ϕ)	m(η)	m($\eta\phi$)	θ	ϕ	Φ	θ_h	ϕ_h
Measured	8 MeV	35 MeV	58 MeV	0.07 rad	0.09 rad	0.09 rad	0.09 rad	0.09 rad
Kin. fit	4 MeV	20 MeV	18 MeV	0.03 rad	0.04 rad	0.04 rad	0.08 rad	0.08 rad

signal selection. Kinematically fit variables have, in general, better resolutions compared to the original measured variables. A comparison of invariant mass distributions before and after the kinematic fit for the ϕ and η mesons in simulated data can be seen in Fig. 4.3. In some cases, like the η invariant mass shown in the Figure, where the peak width is driven almost entirely by detector resolutions, the improvement is large. A full list of resolutions for invariant masses and angular distributions can be found in Table 4.2.

4.1.4 GlueX simulations

Simulated data, often referred to as Monte Carlo (MC) data, is required for various stages of the analysis. Simulations are required to determine detector resolutions, calculate acceptance corrections, to perform background subtraction, analyse the systematic effects of event selection, and more. Simulated data in GlueX is created in four steps. First, a generator produces particle 4-vectors for a given reaction according to a physics model. A variety of generators are available, but the two used in this analysis are the gen_vec_ps generator [138] for producing phase space and signal data, and the bggen generator [139], which is a general purpose PYTHIA-based [140] hadronic background generator used by the collaboration. The generators generally produce hddm files as outputs.

These 4-vectors are then put through a fully modelled GEANT4 [141] simulation of the GlueX detector. Some particles, like η mesons, have their decays simulated at this point. A plugin called evtgen [142] may be used in order to specify branching fractions for these decays instead of relying on the inbuilt experimental tables. This increases the efficiency of the simulation if only specific final states are of interest. The third step uses a tool called mcsmear to apply corrections that emulate detector resolutions to make the simulation look closer to real data, including the folding in of random triggers to simulate random detector background. Finally, the same reconstruction chain used for real data is used to produce Analysis Trees with the ReactionFilter plugin. These trees can then be analysed as normal with DSelectors, although the stored information differs slightly from real data trees.

A number of MC datasets were produced for the present analysis. A set of signal samples that were generated according to partial wave models were produced for use in studies of the partial wave fit performance. These are described in detail in Section 5.3. Besides these, 125M

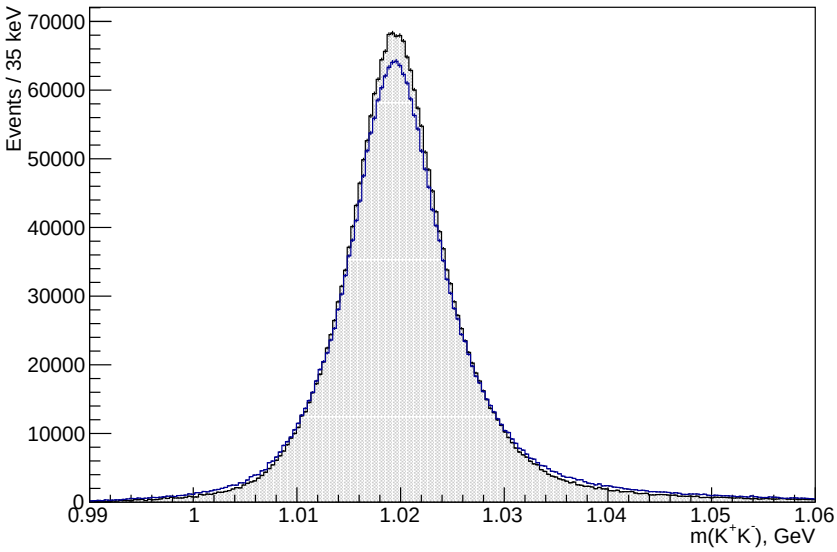

(a) K^+K^- mass

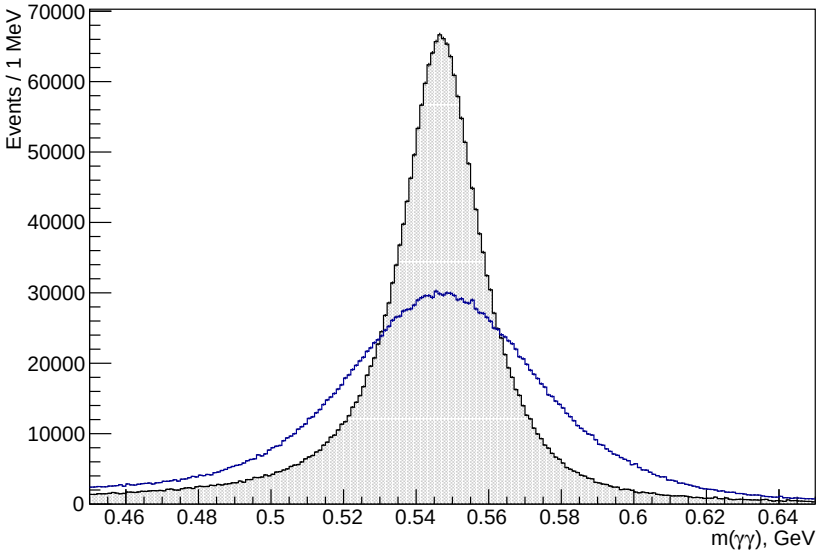

(b) $\gamma\gamma$ mass

Figure 4.3: A comparison of invariant mass distributions with and without the kinematic fit in simulated data for the ϕ (4.3a) and η (4.3b) mesons. In both cases the kinematically fit variables are plotted in the gray-fill histogram, while the measured variables are in the unfilled blue histograms. The kinematic fitter especially improves the resolution noticeably in the η case.

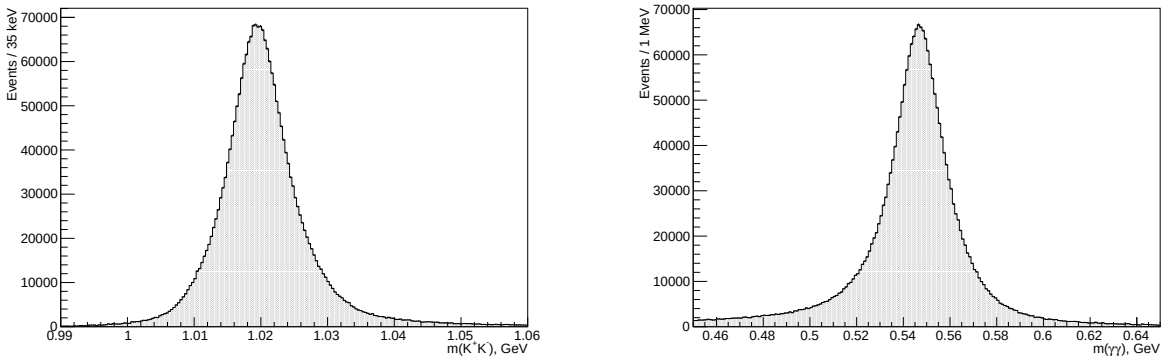

(a) K^+K^- mass (b) $\gamma\gamma$ mass

Figure 4.4: The invariant mass distributions of the ϕ (4.4a) and η (4.4b) meson decay candidates from phase space simulations with a loose confidence level cut. Beam accidentals are subtracted.

events were generated according to a phase space distribution. The phase space events have flat angular decay distributions. phase space data is required to compute the integrals involved in the partial wave fit likelihood calculations discussed in Section 2.2 and the acceptance correction factors needed for cross-section calculations. This dataset is also used to provide the invariant mass distribution templates used in the background subtraction fits in Section 4.6. Distributions of the ϕ and η invariant masses from the phase space samples are shown in Figure 4.4.

4.2 Preliminary selections

Several types of preliminary selections, sometimes called 'skim' cuts, are applied during the Analysis Launches. Because the GlueX physics trigger does not impose very strict conditions on events, these cuts are necessary to cut down on the number of events unlikely to be signal that make it to the analysers. The first set of skim cuts removes events that were only detected in some subsystems. Charged tracks are removed if they do not have at least one hit in either the BCAL, FCAL, ToF, or SC. Showers caused by neutral particles must have an energy of at least 100 MeV. If the shower was caused in the BCAL, it also must have triggered at least two separate cells.

Next, a number of particle specific timing cuts listed in Table 4.3 are applied based on what detectors reported hits. Specifically, selection is done on the following time difference:

$$\Delta T = t_{track} - \left(t_{RF} + \frac{z_{track} - z_{target}}{c} \right) \tag{4.2}$$

In this expression t_{track} is the time of a track at its origin computed assuming a specific particle type, z_{track} and z_{target} are the z-positions of the measured track's origin and target respectively, and t_{RF} is the event reference time. Assuming correct particle identification and perfect detector resolutions, ΔT should be 0.

Table 4.3: The timing cuts applied during during reconstruction. All cuts are based on ΔT of the respective detector system as calculated using (4.2).

Particle type	BCAL	ToF	FCAL	SC
$K^{\pm}$	± 0.75 ns	$\pm$ 0.3 ns	$\pm$ 2.5 ns	$\pm$ 2.5 ns
$\pi^{\pm}$	$\pm$ 1.0 ns	$\pm$ 0.5 ns	$\pm$ 2.0 ns	$\pm$ 2.5 ns
p	$\pm$ 1.0 ns	$\pm$ 0.6 ns	$\pm$ 2.0 ns	$\pm$ 2.5 ns
γ	$\pm$ 1.5 ns	N/A	$\pm$ 2.5 ns	N/A

Table 4.4: Skim cuts on the deposited energy in the CDC.

Particle type	CDC $\frac{dE}{dx}$
$K^{\pm}, \pi^{\pm}$	$e^{-7.0p+3.0} + 6.2$
p	$e^{-4.0p+2.25} + 1.0$

Priority is given to timing information from detectors with better temporal resolution, which gives the ordering BCAL $>$ ToF $>$ FCAL $>$ SC. For example, if a hit is reported in both the TOF and the FCAL, a cut is only placed on the TOF timing. If a potential event does not report a hit in any of these detectors it automatically survives this cut unless it's a kaon, in which case it is cut if it also does not have sufficient hits in the CDC to compute the deposited energy. Additionally, if the Start Counter is the only timing detector with a hit, a cut is only applied if exactly one hit is reported to account for ghost tracks. The timing cuts are re-computed after the kinematic fit is performed with the updated timing and vertex variables. If a fit was not performed, then the cuts are made looser for detached vertices.

Loose cuts are placed on lost energy reported in the CDC. Some particle types have additional cuts on lost energy from other detectors, but they are not relevant to the final state used in this analysis. Finally, some cuts are performed on the masses of the particles. For directly detected particles, the cut is on their missing mass. The missing mass is defined as

$$\mathrm{MM}^2 = (P_{\gamma,beam} + P_{target} - \sum P_i)^2, \tag{4.3}$$

where P_i denote 4-momenta of particles in the final state. Because all final state particles are measured in GlueX, conservation laws should result in MM^2 being equal to $0\,\mathrm{GeV}^2$. However, due to the limited detector resolutions in a real experimental setting, a distribution peaking around this value will be observed instead. This is demonstrated in Figure 4.6.

For particles detected from secondary decays, like the η, the cut is placed on the invariant mass of their decay products. In some cases like the π^0 both are performed. Tables 4.4 and 4.5 list the deposited energy and mass cuts for relevant particle types. The final consideration to note is that if a Kinematic Fit was performed, the events are only saved if the fit converges.

Table 4.5: Skim cuts on particle invariant mass and missing mass squared.

Particle type	Missing mass squared	Invariant mass
$\pi^{\pm}$	$-1.0\,\mathrm{GeV}^2 < MM^2 < 1.0\,\mathrm{GeV}^2$	None
$K^{\pm}$	$-1.0\,\mathrm{GeV}^2 < MM^2 < 1.0\,\mathrm{GeV}^2$	None
γ	$-0.1\,\mathrm{GeV}^2 < MM^2 < 0.1\,\mathrm{GeV}^2$	None
p	$-0.5\,\mathrm{GeV}^2 < MM^2 < 4.41\,\mathrm{GeV}^2$	None
ϕ	None	$0.8\,\mathrm{GeV} < M < 1.2\,\mathrm{GeV}$
η	None	$0.35\,\mathrm{GeV} < M < 0.75\,\mathrm{GeV}$

4.3 Fiducial cuts

It is expected that some areas of the detector will see a low signal-to-noise ratio. This may be caused by differences in angular distributions characteristic to the interactions producing signal events and backgrounds. Some areas of the detector may also be less well represented by simulated Monte Carlo data than required for analysis. It is standard practice to eliminate these areas from data entirely. The GlueX collaboration has organised multiple working groups to standardise a set of such cuts. The primary fiducial cuts involve cuts on regions of both of the calorimeters and the reconstructed vertex of the event in the target cell. As an example, Figure 4.5 shows the fiducial cut applied on the target Z position. An additional cut removes the innermost 16 channels of the FCAL around the beam hole. The list of all cuts, including fiducial, is given in Table 4.7.

4.4 Exclusivity cuts

A set of cuts are applied to select events from the photoproduction of $\eta\phi$ decaying into a $\mathrm{K^+K^-}\gamma\gamma$ final state. The first set of cuts are loose cuts on the reconstructed invariant masses of the $\mathrm{K^+K^-}$ and the $\gamma\gamma$ subsystems, the combined invariant mass of the candidate $\eta\phi$ system, and the missing mass squared of the system. These cuts are very loose and are aimed primarily at reducing the number of events that have to be stored for further analysis. Two additional cuts have a particularly strong impact. These are the cut on the Confidence Level of the Kinematic Fitter and the cut on the momentum transfer to the recoil proton squared.

4.4.1 Confidence level

The confidence level is the name used by GlueX for the probability obtained from integrating the χ^2 distribution of the kinematic fit. It is similar as a measure of fit to $\frac{\chi^2}{NDF}$ but is more commonly seen within the collaboration. The quality of the fit is best when close to 1 and worse when close to 0. Cutting on the Confidence Level removes events that are less consistent with the conservation law constraints imposed during the Kinematic Fit. Figure 4.7 shows the

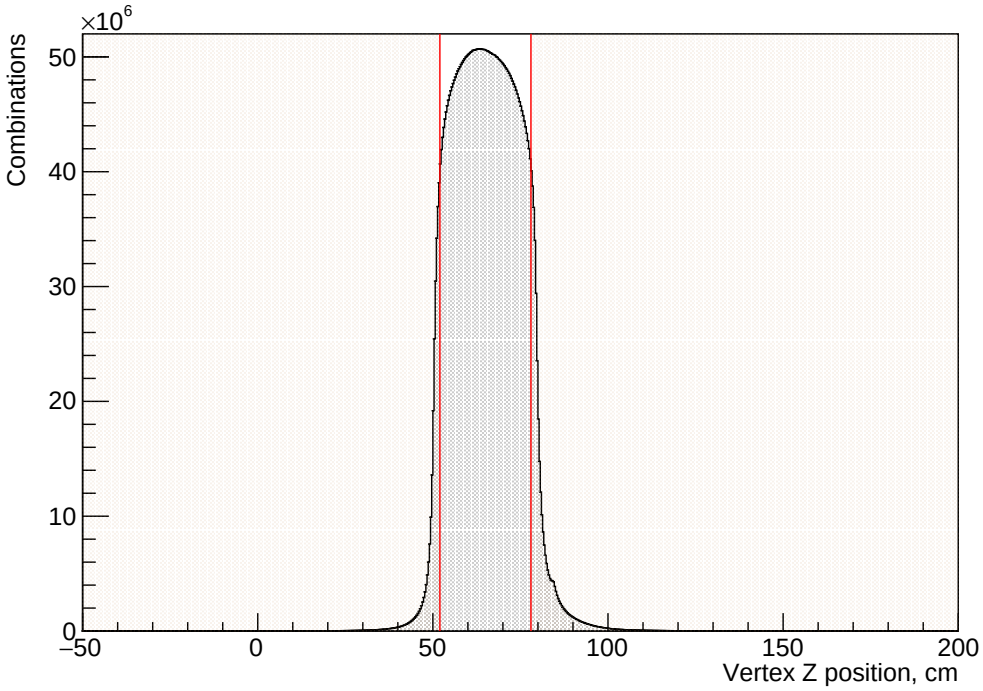

Figure 4.5: The distribution of the decay vertex Z position in the target cell. The fiducial cuts eliminate events on the periphery of the target, which are much more likely to have been background and cause poorer agreement between data and simulation.

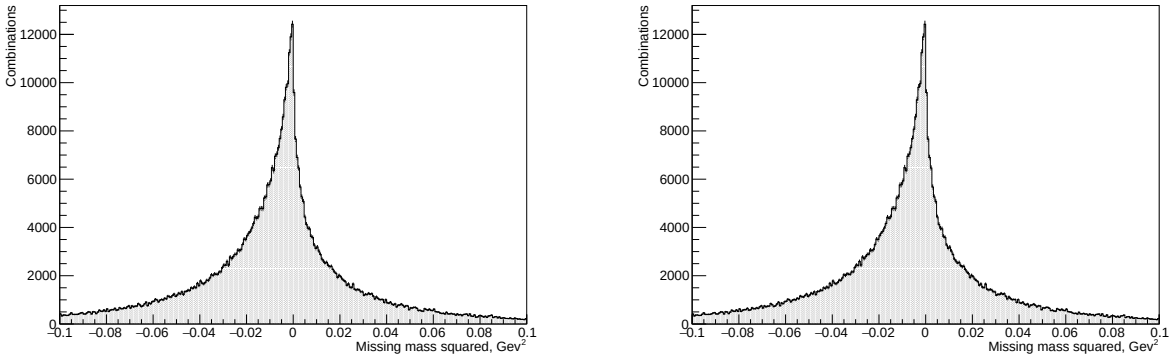

(a) Data. (b) Monte Carlo.

Figure 4.6: Distributions of the missing mass squared for data (4.6a) and simulated phase space (4.6b).

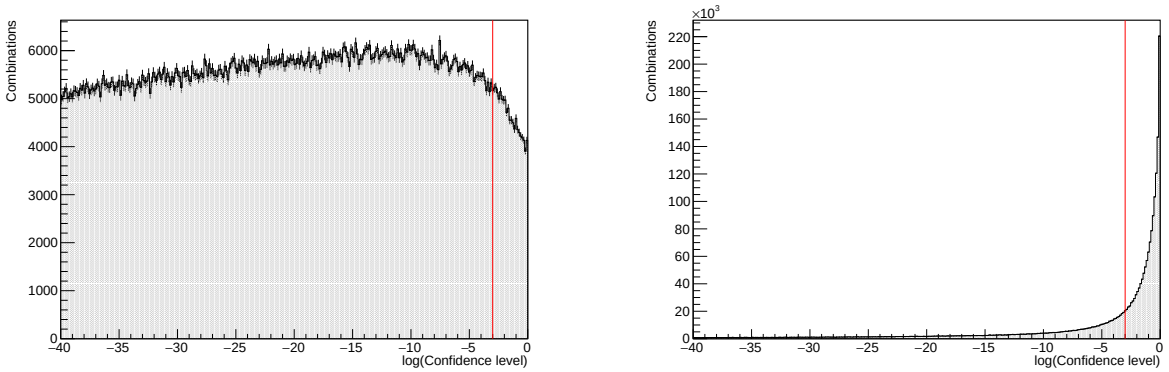

(a) Data. (b) Monte Carlo.

Figure 4.7: Distributions of the kinematic fitter Confidence Level for data (4.7a) and simulated signal (4.7b) samples. The red line shows the value of the event selection cut used.

confidence level distributions for data and phase space MC samples while the effects of varying the Confidence Level cut on the ϕ and η candidate invariant mass spectra are shown in Figure 4.8. As this cut is the most important for enforcing exclusivity out of the ones used in the analysis, a study to pick an approximately optimal value was performed. To evaluate the effects of the cut, the following figure of merit (FoM) was considered:

$$\text{FoM} = \frac{N_S}{\sqrt{N_S + N_B}} \tag{4.4}$$

The N_S and N_B represent the signal and background yields respectively. This statistic is commonly used in particle physics when the signal yield is to be estimated accurately, see Chapter 40 in [45]. To calculate the required yields the full event selection and sPlot background subtraction procedure – see Section 4.6 – was repeated for a range confidence level cut values in the $\eta\phi$ mass region from 1.5 GeV to 2.02 GeV using the same binning as in the rest of the analysis. This is the part of the mass spectrum that was expected to contain the two primary resonances under study. In addition, as discussed in Section 4.7, the region above 2 GeV is more likely to contain background not removed by the sPlot and so the higher mass bins were not considered.

The cut values were spaced out widely for low values of Confidence Level for efficiency considerations – any cut below 10^{-10} would usually be considered too lax, leaving too many background events in the dataset to feasibly handle when performing later fits. The plot in Figure 4.9a shows the change in signal and background yields over the tested cut values, while Figure 4.9b shows the change in the Figure of Merit. The purity of the signal keeps increasing as the cut is made tighter because the background yields decrease faster, but the FoM reaches an optimum value. The Figure of Merit does not change significantly after a confidence level value cut of 10^{-4}, but the optimum value is found to be at 10^{-2} which is therefore chosen for this analysis. The relative larger drop in signal yield going from 10^{-2} to 10^{-1} is what results in the latter cut having a lower Figure of Merit value. The numeric values of the yields and the

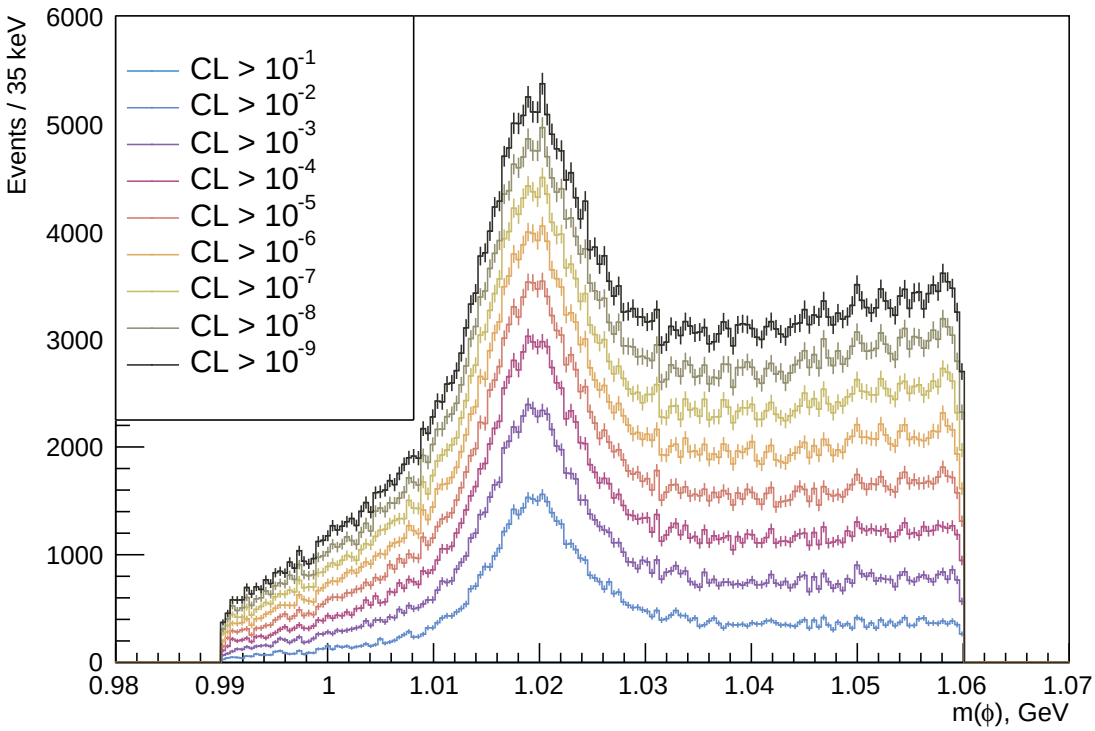

(a) K^+K^- mass.

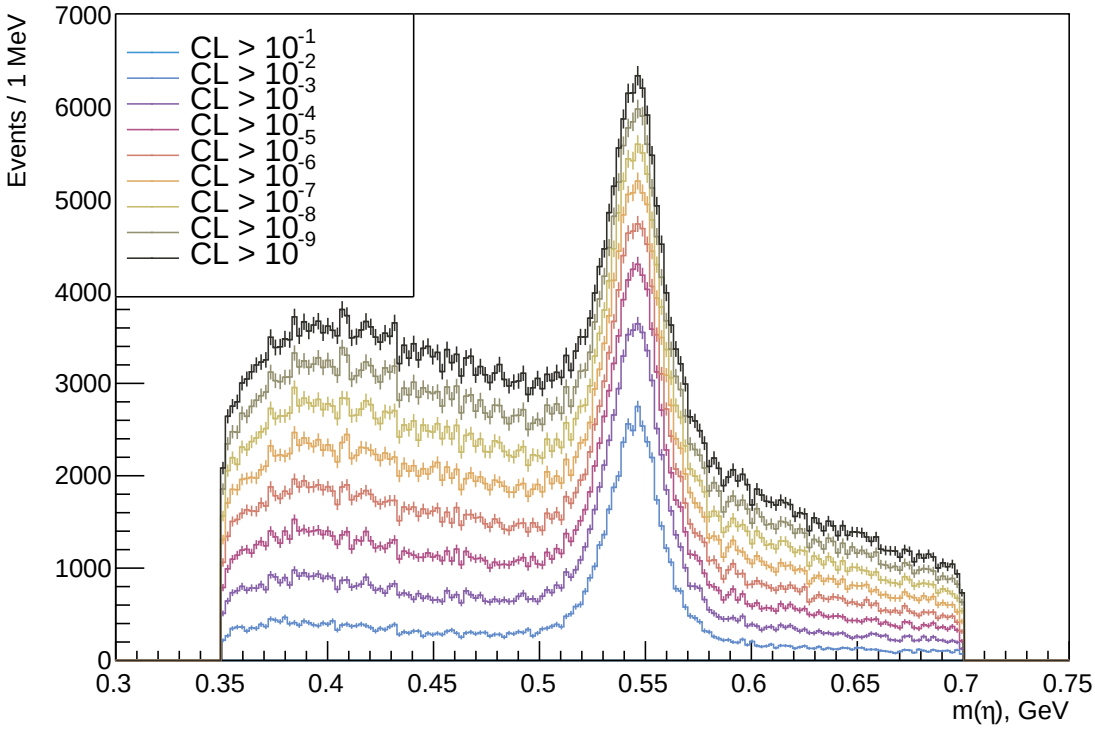

(b) $\gamma\gamma$ mass.

Figure 4.8: The ϕ (4.8a) and η (4.8b) candidate invariant mass spectra for different values of confidence level cut after fiducial cuts and accidental subtraction. More stringent cuts remove more of the background below the peaks but never entirely eliminate it by themselves.

Table 4.6: A table of $\eta\phi$ yields, background yields, their ratio (signal purity), and the Figure of Merit for various values of the confidence level cut. The variation in the FoM becomes small after 10^{-4}, but the optimal value is found at 10^{-2}.

CL cuts	$\eta\phi$ yield	Bkg. yield	$\eta\phi$ signal purity	FoM
10^{-39}	31852	370345	0.09	50.22
10^{-29}	28537	319934	0.09	48.34
10^{-19}	30130	227392	0.13	59.37
10^{-9}	24425	111588	0.22	66.23
10^{-8}	23424	98663	0.24	67.04
10^{-7}	23093	84990	0.27	70.24
10^{-6}	22151	72293	0.31	72.08
10^{-5}	21099	59238	0.36	74.44
10^{-4}	20254	46222	0.44	78.56
10^{-3}	19088	33533	0.57	83.21
10^{-2}	16698	21172	0.79	85.81
10^{-1}	12375	10156	1.22	82.45

FoM are noted for each cut value in Table 4.6.

4.4.2 Mandelstam t

The 4-momentum transfer squared, where the momentum transfer happens from the beam photon to the target proton, is equivalent to the Mandelstam variable t, which is one of three dynamical variables first defined by Stanley Mandelstam [143]. In natural units it is defined as:

$$t = (p_1 - p_3)^2 = (p_4 - p_2)^2 \tag{4.5}$$

Here p_1 is the 4-momentum of the beam photon, p_2 is the 4-momentum of the target proton, p_3 is the 4-momentum of the produced resonance, and p_4 is the 4-momentum of the recoil proton.

The choice of cut on t heavily influences the dominant production mechanisms of the observed resonances. The interactions that are expected for meson spectroscopy in GlueX data are the so-called t-channel exchanges, where a virtual particle with energy equivalent to the variable t is produced by the photon scattering off the target nucleon. A pseudo-Feynmann diagram representing t-channel production is shown in Figure 4.10. These interactions are expected in low t regions. Conversely, as one moves higher in t other processes, for example the beam photon exciting the target nucleon instead of producing a meson resonance, become more common. These interactions can prove to be sizeable background contributions – see Section 4.7. Placing a fiducial cut to select the t region appropriately therefore becomes important.

The t distributions for data and MC are shown in Figure 4.11. They are modelled with functions proportional to an exponential e^{bt} where b is a parameter called the t-slope, which has to

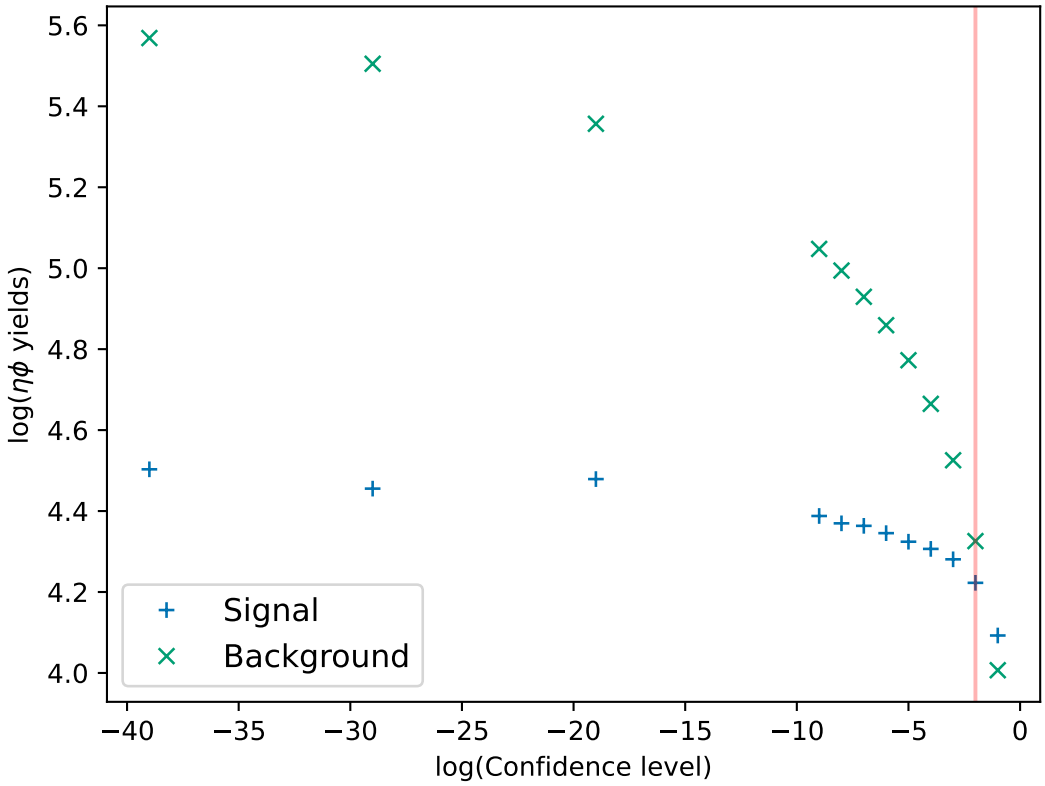

(a) Background and $\eta\phi$ signal yields over $\eta\phi$ invariant mass range from 1.5 GeV to 2.02 GeV after sPlot background subtraction for different values of Confidence Level cut. Both axes are logarithmic.

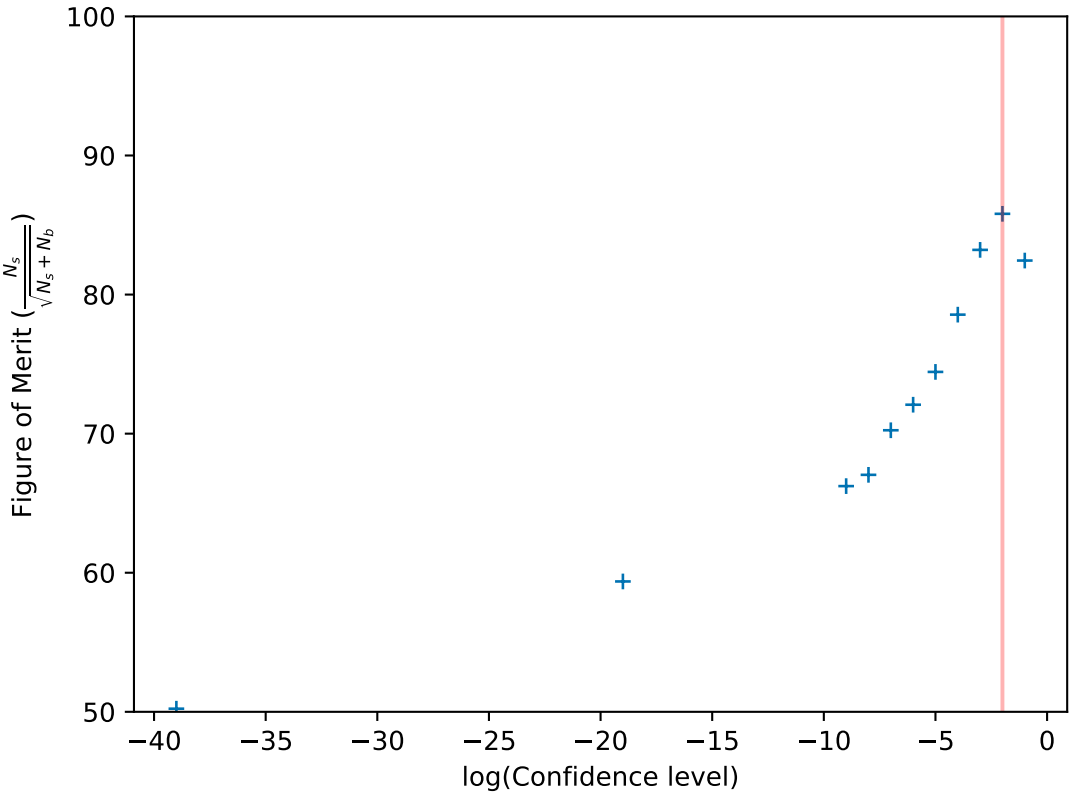

(b) The Figure of Merit for different values of confidence level cut. The x axis is logarithmic.

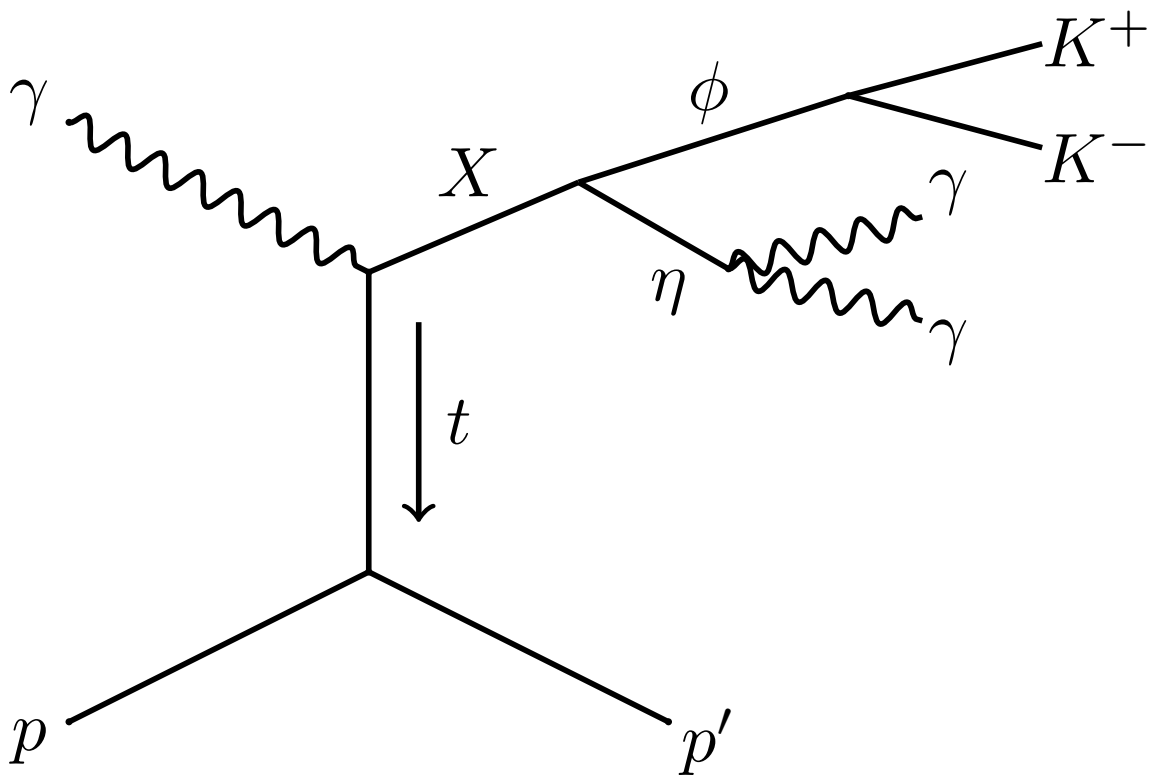

Figure 4.10: A pseudo-Feynmann diagram for the t-channel production picture expected for the channel in the current analysis. X denotes the resonance that is produced by the photon scattering. The energy of the virtual interacting particle is equal to t, which is the square of the 4-momentum transferred to the target proton.

be estimated from data when performing simulations. In the case that sufficient statistics are available, it would be preferable to bin in terms of t to track the t-dependence of the results. However, the current analysis is statistically limited and cannot sustain binning in multiple variables. Common practice within the collaboration in such cases is to place a single cut at or below $-1\,\text{GeV}$, as this has often proven to be sufficiently selective for t-channel interactions. The impact of varying the t cut on the background subtracted yields are shown in Figure 4.12. Changes in the cut values seem to have a mostly systematic effect on the yields below 2 GeV. As this indicates no reason to make the t selection stricter, the conventional value of $-1\,\text{GeV}$ was chosen to maximise the statistics available for partial wave fits. The full table of applied cuts is given in Table 4.7.

4.5 Photon accidental and combinatorial backgrounds

The reconstruction algorithms often cannot assign a unique combination of initial and final state particles for a given event. There are three primary reasons for having more than one possible combination:

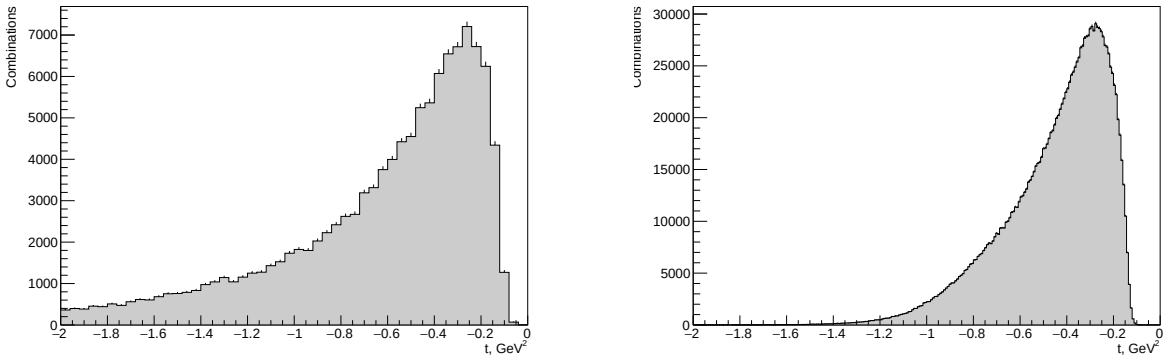

(a) Data. (b) Monte Carlo.

Figure 4.11: The Mandelstam t distributions for data (4.11a) and simulated signal (4.11b). Both distributions follow an exponential distribution. The so-called t-slope parameter for simulated data was chosen to roughly match the slope observed in data.

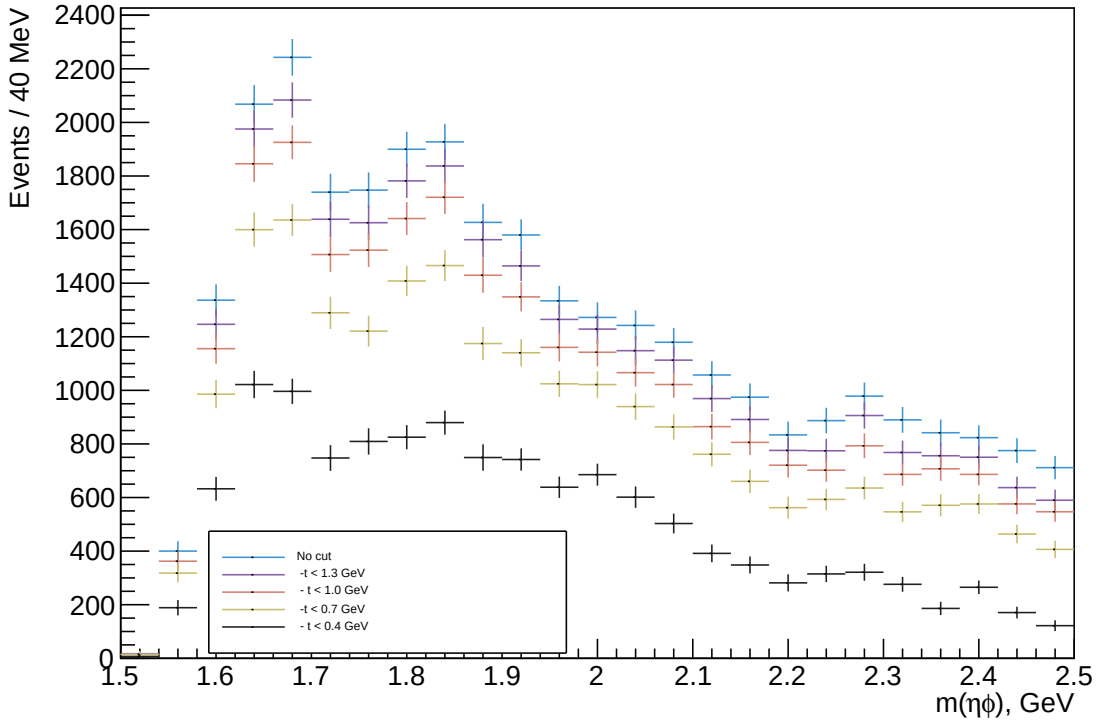

Figure 4.12: Comparisons of the background subtracted $\eta\phi$ invariant mass spectrum for varying values of cut on Mandelstam t. More stringent cuts systematically lower the yield throughout the mass range.

Table 4.7: The full set of selection cuts applied to the data. Cuts are denoted by type.

Cut	Value	Type
E_γ	8.0 GeV - 8.6 GeV	Coherent peak
-t	< 1 GeV	Fiducial
Confidence level	$> 10^{-2}$	Exclusivity
η invariant mass	0.35 GeV - 0.7 GeV	Exclusivity
ϕ invariant mass	0.996 GeV - 1.06 GeV	Exclusivity
$\eta\phi$ invariant mass	1.5 GeV - 2.9 GeV	Exclusivity
Missing mass	-0.1 GeV - 0.1 GeV	Exclusivity
Vertex z position	52 cm - 78 cm	Fiducial
BCAL shower z position	-100 cm - 393 cm	Fiducial
FCAL shower position (radius)	25 cm - 105.5 cm	Fiducial

- GlueX is a high luminosity experiment. One negative side effect of high luminosity is that it can be hard to determine which photon beam bunch caused the event due to finite temporal resolution. The extraneous beam photons that could be involved in the reaction are called photon accidentals.

- It is likely that the number of charged tracks or clusters that could be part of a recorded event is higher than the number of charged or neutral particles in the final state. This means that e.g. three feasible charged tracks are present for an event where two charged particles should be reconstructed.

- Even if the exact number of tracks and clusters is present, in states that contain multiple charged particles with the same charge or multiple neutral particles it can be hard to determine which hits in the detectors belong to which particles.

These cause a type of background labelled combinatoric. The photon accidental background is removed using a technique called accidental sideband subtraction. If the time difference between the RF clock and the tagger time is histogrammed, a plot like Figure 4.13 is produced. A number of peaks to either side of the central peak, which is called the prompt peak, are selected. Events in the side peaks contain the accidental out-of-time photons, while the prompt peak should contain the in-time beam bunches. Every event is then assigned a weight of 1 if it's within the prompt peak or a weight of $-\frac{1}{N_{bunches}}$ if it's within the sidebands. For this calculation the first peak in either sideband is usually ignored, as photons from the prompt peak may leak into them. The sidebands in the present analysis use three beam bunches on either side, not counting the skipped bunch. A further scaling factor is retrieved from a central database and applied multiplicatively to account for changes in the instantaneous beam rate. This is required for proper normalisation. Applying these weights when fitting and plotting removes the effects of photon accidental background.

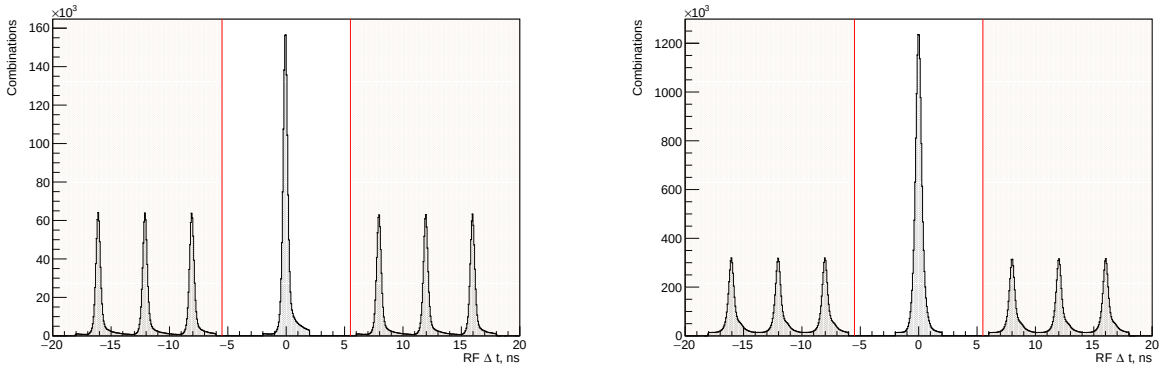

(a) Data.

(b) Monte Carlo.

Figure 4.13: Plots of the time difference between the RF clock and SC times for data (4.13a) and simulated signal (4.13b) without accidental subtraction. The sidebands are shaded. The beam bunches immediately next to the prompt peak are cut.

The combinatorial background arising from multiple possible track/cluster combinations is not dealt with separately, but is assumed to be taken care of by the sPlot background subtraction procedure detailed in Section 4.6. The first plot in Figure 4.14 shows the particles in the final state responsible for the presence of multiple combinations before any event selection cuts. The second plot demonstrates that the combination of cuts and sPlot subtraction seem effective in removing any present combinatorial backgrounds with the number of events that are associated with more than one combination at less than 1% of the total yield.

4.6 Background subtraction

The cuts and accidental removal described above are not able to completely remove the background from the event sample. The $\eta\phi$ invariant mass spectrum on the bottom of Figure 4.16 contains structures that may correspond to the desired resonant decays, but the individual η and ϕ invariant mass spectra in Figure 4.15 both clearly show a background component underneath the respective peaks. The backgrounds are also visible when these invariant masses are plotted against each other as in the top plot of Figure 4.16 An additional background subtraction procedure was performed using the sPlot method [144]. It has previously been successfully used at collaborations like LHCb [145] and CMS [146], as well as within other GlueX analyses [147]. An extended maximum likelihood fit is performed using a model that consists of a sum of probability density functions (PDFs) corresponding to different data sources. A set of discriminating variables must be selected as the independent variables of the PDFs. The selected variables should allow the signal and background components to be separated, i.e. the respective PDFs should have different shapes.

In this case the sources are signal and background, although models can in principle be composed of as many data classes as desired. The fit aims to produce a set of per-event weights

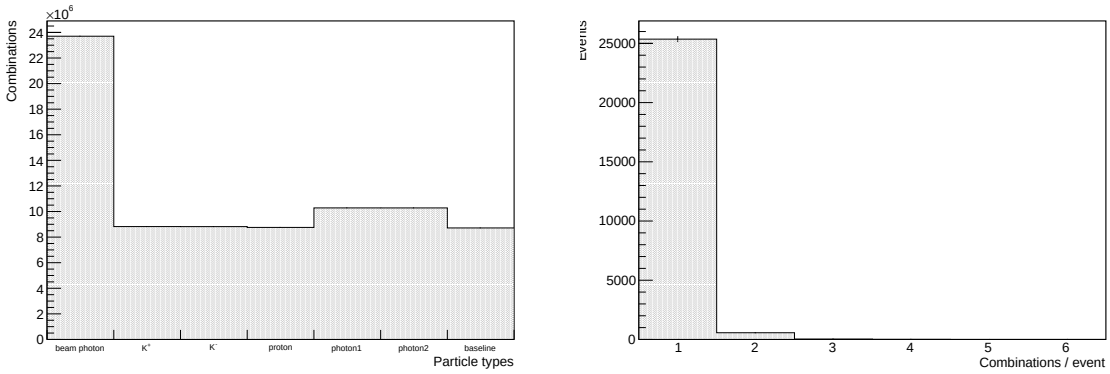

(a) (b)

Figure 4.14: Subfigure 4.14a shows the particles that cause additional combinations to be formed for a candidate event. The baseline bin shows the number of combinations if there was only one combination per event. Most additional combinations are caused by beam accidentals. Subfigure 4.14b shows the number of events associated with more than one combination after background subtraction. The number of such events remaining is negligible.

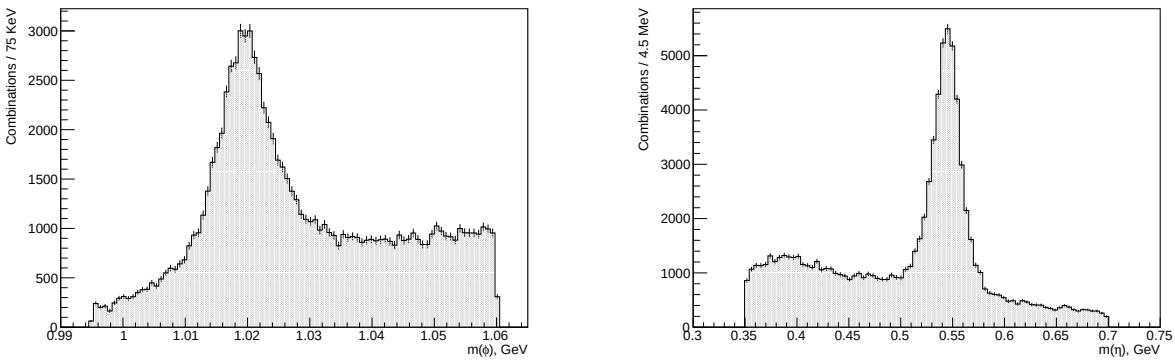

(a) K^+K^- mass. (b) $\gamma\gamma$ mass.

Figure 4.15: The ϕ (4.15a) and η candidate (4.15b) invariant masses after cuts and accidental subtraction. Peaks are clearly present around in the expected positions of the spectra, but a background on the order of approximately 20% can be seen under the peaks.

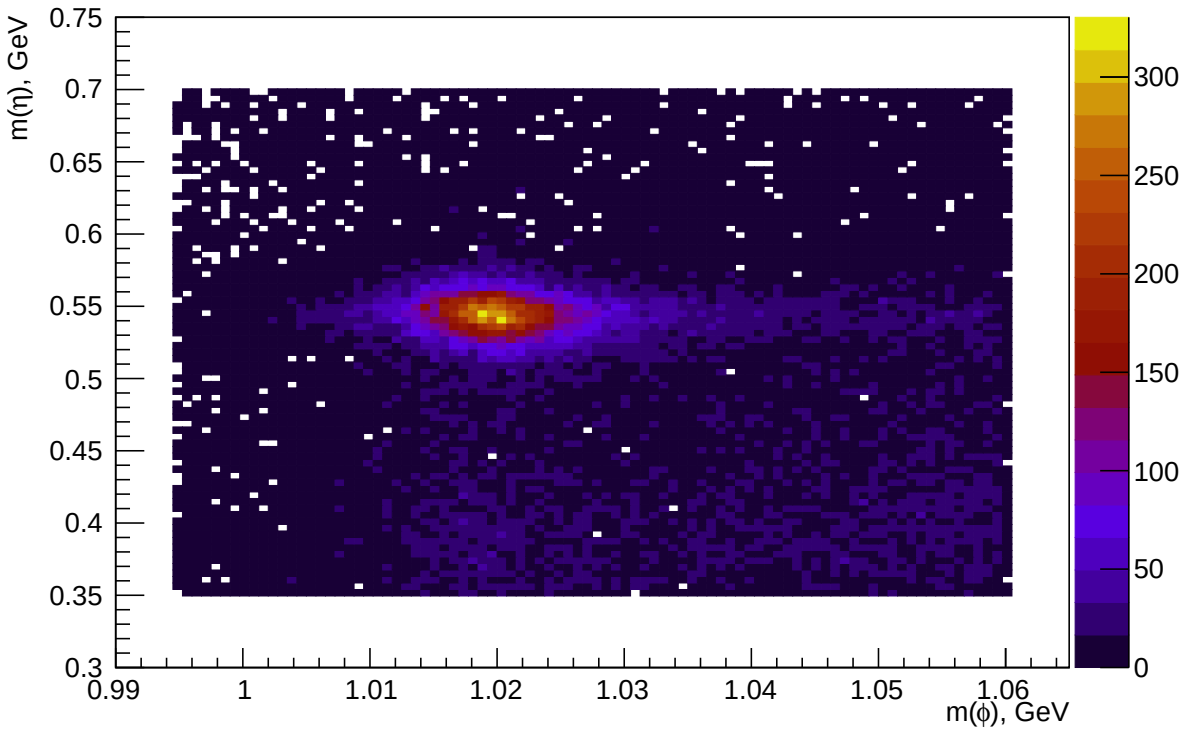

(a)

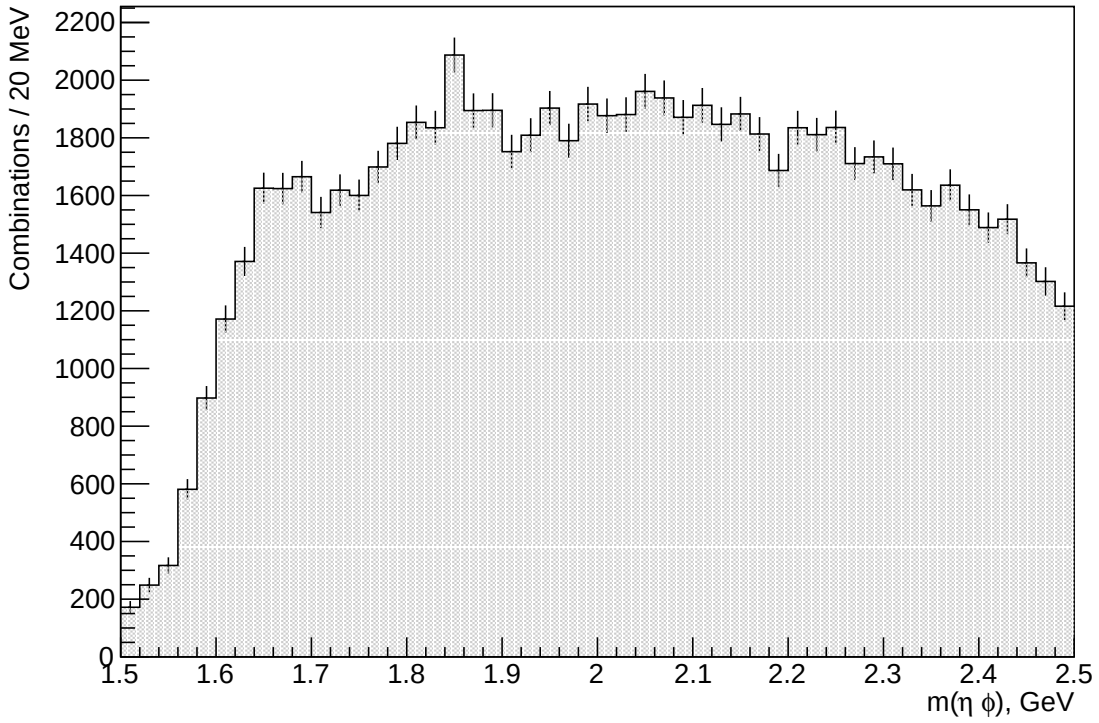

(b)

Figure 4.16: Subfigure 4.16a shows a 2D histogram of the ϕ and η invariant masses while Subfigure 4.16b shows the $\eta\phi$ invariant mass spectrum after cuts and accidental subtraction.

for each data class, such that if the data is histogrammed or fit using a given class' weights, that component is projected out. It is assumed that the discriminatory variables and the projected variables are uncorrelated. The full derivation of the formulas can be found in the original paper [144], but the master equation for obtaining the sPlot weights is the following:

$$ {}_sP_n(y_e) = \frac{\sum_{j=1}^{N_S} \mathbf{V_{nj}} \mathbf{f_j}(\mathbf{y_e})}{\sum_{k=1}^{N_s} N_k f_k(y_e)} \tag{4.6} $$

Here y_e is the set of discriminatory variables, f_i are the probability density functions for the i-th data class, $f_i(y_e)$ are the values of those density functions for variables y_e associated with event e, N is the total number of events in the data sample, N_i is the number of events expected for data class i, N_s is the number of data classes, V_{nj} is the covariance matrix between species n and j, and ${}_sP_n(y_e)$ is the produced weight.

Invariant masses of the intermediate ϕ and η mesons were chosen as the discriminatory variables. For a background to be indistinguishable from signal, it would have to take on a peaking distribution with relatively close peak parameters to the decaying particle when reconstructed, which is not common. This is especially true when the decay distributions are narrow. Visual inspection confirms that the backgrounds do appear to take on a polynomial shape in these discriminatory variables. A 2nd order Chebyshev polynomial was chosen as the functional form – these polynomials exhibit a smooth and continuous shape, and have well-constrained parameters that make for well-behaved numeric optimisation.

Two general approaches are possible to pick the shape for the signal component. One is to select a functional form as done for the background. Common choices are the relativistic Breit-Wigner function and the Gaussian function. A second option is to model the distributions by simulating their shape using Monte Carlo data – this is the approach chosen in the present analysis. The invariant mass distributions from phase space Monte Carlo were presented in Figure 4.4. To extract them for the fits, the distributions are used to fill a densely binned histogram which is then smoothed using a first degree polynomial. This smoothed curve is used to interpolate the distribution during the fit.

The fit was performed using the brufit framework [148], which is built on ROOT's RooFit library [149]. The fit was done in two steps, as a subtraction must be performed for the backgrounds under the ϕ and the η peaks separately. One of the properties of the weights provided by the sPlot is that they are multiplicative, allowing them to be used in consecutive fits – taking the weights resulting from the first fit and applying them during the second fit allows a combined signal weight to be obtained. The first fit can itself be supplied the photon accidental subtraction weights to incorporate this into the background subtraction.

The sPlot fits are performed in bins of invariant mass of the $\eta\phi$ system. The binning scheme picks 25 bins of equal width in the invariant mass range 1.5 GeV to 2.5 GeV, resulting in 40 MeV wide bins. This width was chosen to allow sufficient statistics in each bin for the partial wave

fits. It was also observed that convergence started to pose problems during the sPlot fits if the binning was too fine.

Three parameters were used in the fits alongside the free parameters describing the background polynomial and the signal. These are given in the legends as alpha, offset, and scale. The former is the width of a Gaussian that is convoluted with the combined PDF used in the fit, while offset and scale describe a translation and scaling of the x-axis of the signal component. These parameters are used to account for any variations in the signal shape that may arise from discrepancies between MC and data. In the ideal case they would be equal to 0, 0, and 1 respectively.

The sPlot fit results for a representative mass bin from 1.66 GeV to 1.7 GeV are given in Figure 4.17, with fits in the other bins being available in Appendix B. The results are shown for both the ϕ and η together with their residuals and pull distributions. In this case pull is defined as the difference between the model and the data divided by the statistical uncertainty of the data. If the fit is robust, pulls should follow a normal distribution with a mean of 0 and a standard deviation of 1. In general, the fits appear to describe the data well. The alpha, offset, and scale parameters are compatible with their expected values and the pulls appear well behaved. Most of the background seems to be removed by the first round of fits, causing some numerical instability on the reported yield uncertainties in certain bins when performing the η fits.

The $\eta\phi$ invariant mass spectrum after background subtraction can be seen in Figure 4.18. The plot shows both the signal and background components projected using their respective sets of weights. Peaking structures around 1.68 GeV and 1.85 GeV, which were still mostly hidden by the background after cuts, are now visible in the signal spectrum. These appear to be in the locations expected for potential $\phi(1680)$ and $\phi_3(1850)$ resonances based off their parameters reported in the PDG. No clear peaks are present in the mass region above 2 GeV, although as discussed in Section 4.7 this region suffers from likely baryon contamination.

The order of the sPlot fits should not matter – the underlying data remains the same, so there is in principle no difference in whether the ϕ or the η backgrounds are subtracted first. In practice the maximum likelihood fits used to obtain the weights are not deterministic and some variation may occur. This was tested by doing the background subtraction both ways. As expected, Figure 4.19 shows that the difference in yields is not significant. The rest of the thesis will use the ϕ-first order.

4.7 Hadronic backgrounds

All particle physics analyses must contend with the presence of possible backgrounds in the data. Many processes can result in the same final states despite undergoing different intermediate processes. It can also be hard to differentiate particles like high momentum pions and kaons

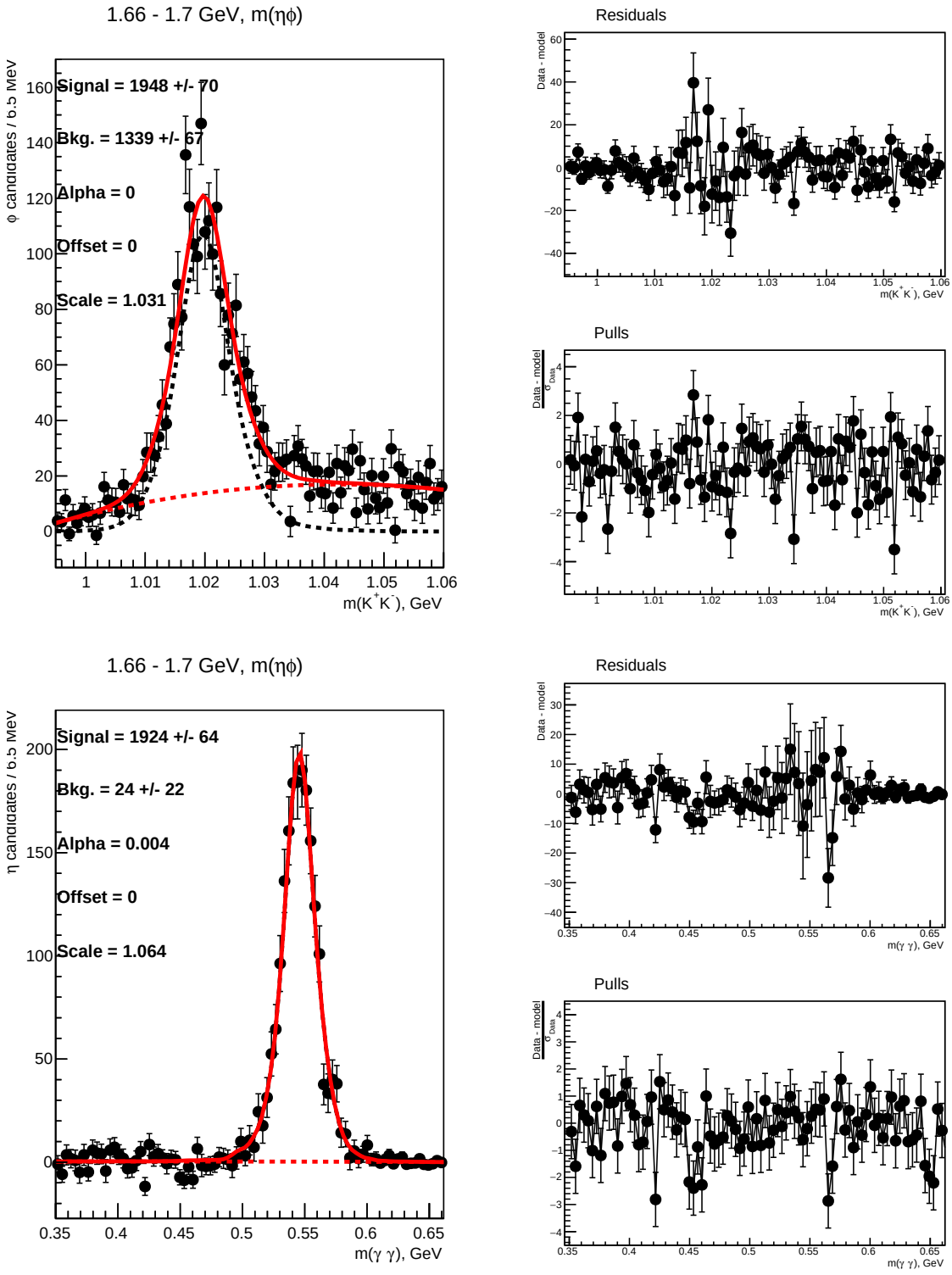

Figure 4.17: The sPlot fits for the 1.66 GeV to 1.7 GeV $\eta\phi$ invariant mass bin. Fits to the η invariant mass are performed using weights from the ϕ fit.

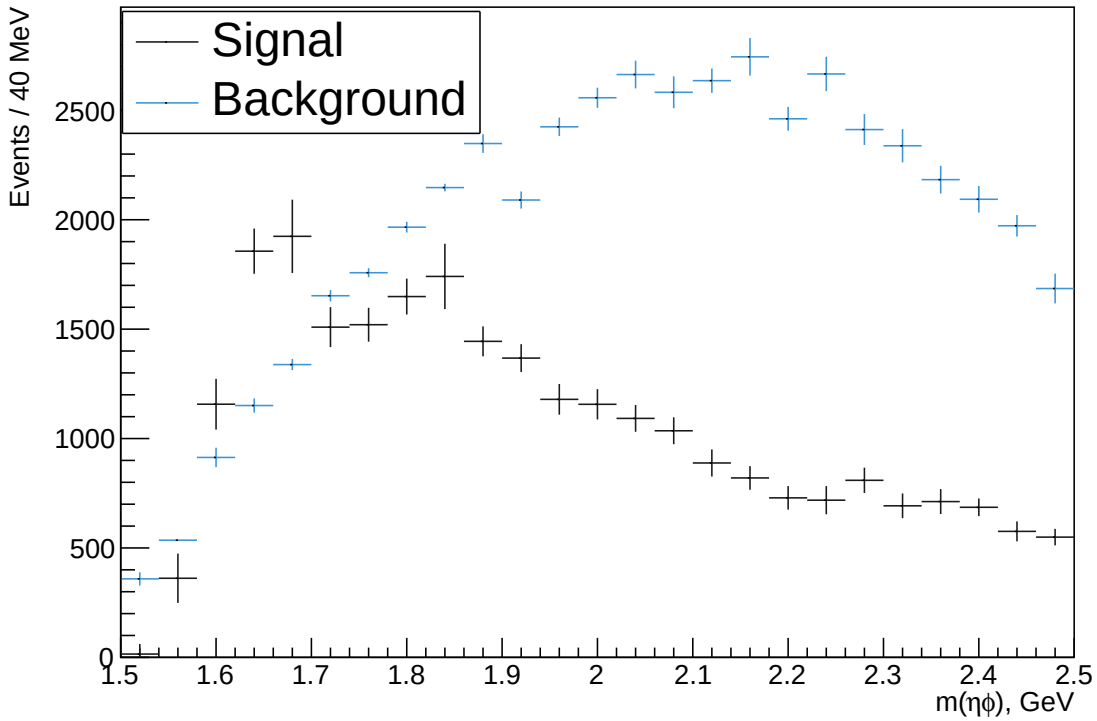

Figure 4.18: The $\eta\phi$ invariant mass spectrum after sPlot fits showing both signal and background components. The background shows a mostly smooth rise with invariant mass.

from each other, resulting in misidentification. For example, a large bump in the raw K^+K^- invariant mass spectrum in Figure 4.20 can be seen around 1.25 GeV. This is likely the $\pi^+\pi^-$ decay of the $\rho(770)$ meson. The ρ has a much higher production cross section than the $\phi(1020)$ – as a result, even a small fraction of pions being misidentified as one of the constituents in the K^+K^- subsystem can result in it becoming a large background component. The mass differences between kaons and pions see the ρ peak shifted to higher observed invariant mass.

The effect of the event selection cuts is evaluated on simulated data. A 2 billion event sample produced using bggen is put through the same reconstruction and event selection as the real data. None of the numerous final state configurations generated by bggen survive the cuts with significant yields, with only two background topologies retaining more than 200 combinations. These are the $K^+K^-\gamma\gamma p$ with non-resonant kaon production and the $\pi^+\pi^-4\gamma$ channels. Combined with a small number of other pion-rich final states, 1096 combinations pass the selection in total. The resulting invariant mass spectrum is shown in Figure 4.21. The effectiveness of the cuts in removing bggen events lends confidence to the performance of the event selection on real data – however, backgrounds that the PYTHIA-based physics model may not reproduce sufficiently well still have to be considered.

A common source of hadronic backgrounds in GlueX data are baryon resonances. Instead of producing a meson via particle exchange, a photon may instead provide energy to the target

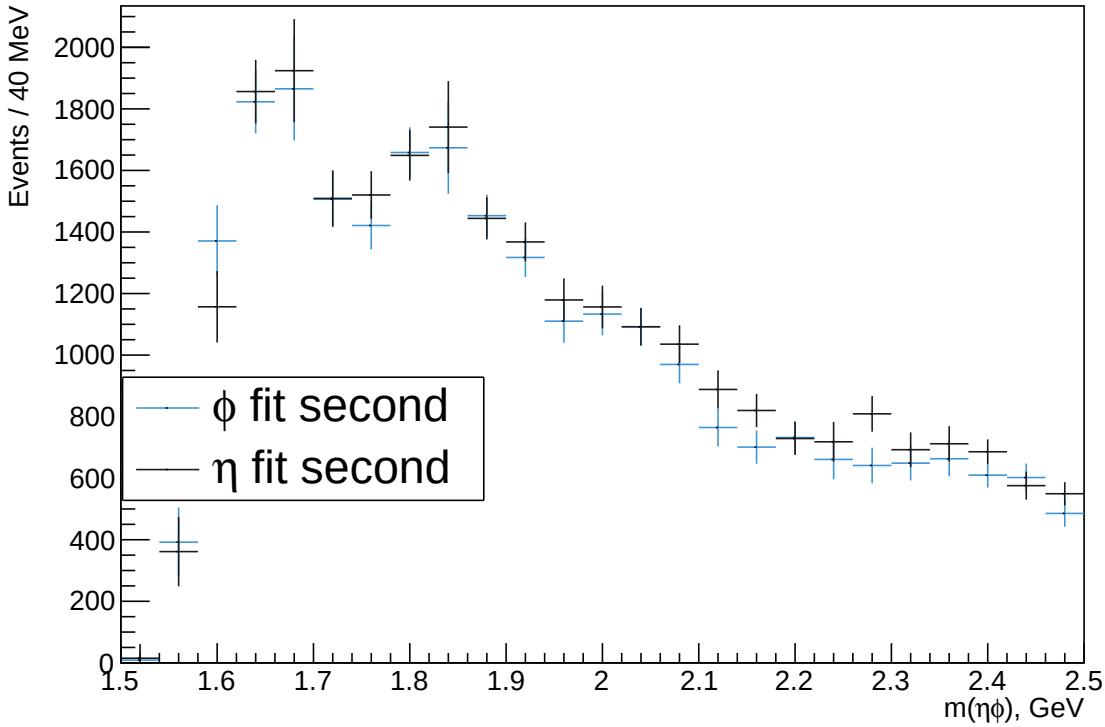

Figure 4.19: A comparison of $\eta\phi$ invariant mass spectra after performing the sPlot background subtraction by doing the fits in both orders: ϕ then η and η then ϕ. The results are within statistical uncertainty of each other throughout the mass range.

nucleon and excite it. This process increases with higher Mandelstam t. In particular, looking at the ηp invariant mass spectrum before background subtraction, an obvious peak corresponding to N^* resonances around 1.6 GeV can be seen. This is caused by the resonances decaying to a $N\eta$ final state, which can be misreconstructed as the ηp subsystem.

This background is still present in the data after full event selection. Figure 4.22 shows ηp invariant mass after background subtraction. A definite peaking structure can still be seen around 1.6 GeV, albeit smaller. However, the 2D histogram of $\eta\phi$ invariant mass against ηp invariant mass in Figure 4.23 shows that the 1.6 GeV peak is only relevant at $\eta\phi$ masses considerably higher than 2 GeV and so this background should not have an effect on the analysis of $\phi(1680)$ and $\phi_3(1850)$ candidates.

It is possible that higher mass baryon resonances are also contributing, though there are no obvious corresponding peaking structures in the ηp spectrum. These would intersect with the relevant region of $\eta\phi$ mass of below 2 GeV, but a simple cut on ηp mass that could prevent this turns out to be undesirable. Cutting out events above 2.4 GeV in ηp would significantly decrease the available statistics. For this to be worthwhile would require a big increase in signal purity to offset the effects of the increased statistical uncertainty on partial wave fits. It would also distort the angular decay distributions – Figure 4.24 shows that ηp invariant mass has a

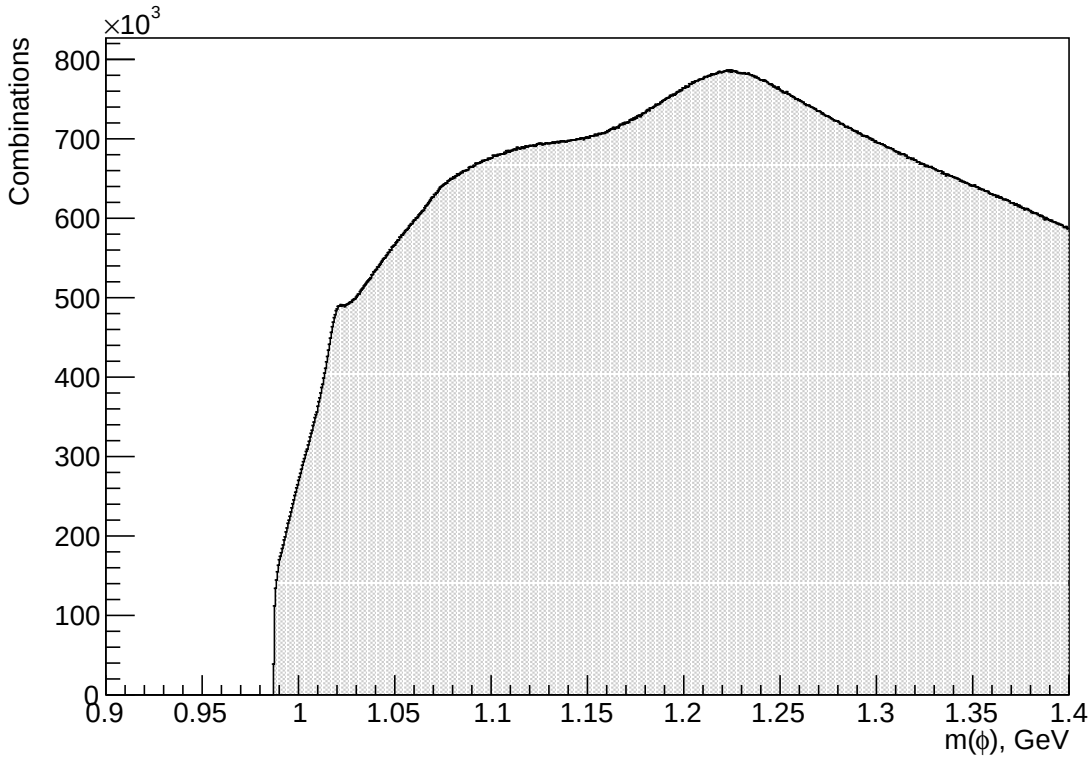

Figure 4.20: The invariant mass distribution of K^+K^- candidates before cuts. The desired $\phi(1020)$ peak can be seen as the small shoulder feature slightly above 1 GeV. A large bump around 1.25 GeV can be seen, which is caused by decays of the $\rho(770)$ meson to two pions being misidentified as kaons.

strong correlation with the θ angle in the ϕ helicity frame. The cut on ηp mass would thus place a hard cut on this angle and significantly affect the reliability of the fits.

A possible alternative that could ameliorate this effect on θ would be to use a mass dependent approach, such as a Van Howe angle analysis presented in [150]. Ultimately the decision was made not to perform any explicit baryon removal cuts in this thesis. As discussed later, the final results in Chapter 6 focus on the $\phi(1680)$ resonance because the situation of the potential $\phi(1850)$ remains unclear in the partial wave fits. This could be an outcome of baryon contamination around the $\eta\phi$ peak at 1.8 GeV, as suggested by Figure 4.23; however, initial tests did not indicate that baryon cuts greatly improved the stability of the fits in this region. They were hence not implemented on the basis that, all other things considered, having fewer selection criteria is preferable.

All the elements necessary to perform a partial wave analysis, which is going to be the focus of the remainder of the thesis, have been presented. In the next Chapter, a number of studies on the behaviour of the model using both real and simulated data will be shown. The results of the studies will guide the waveset selection, one of the main steps of a partial wave analysis before numerical results can be extracted.

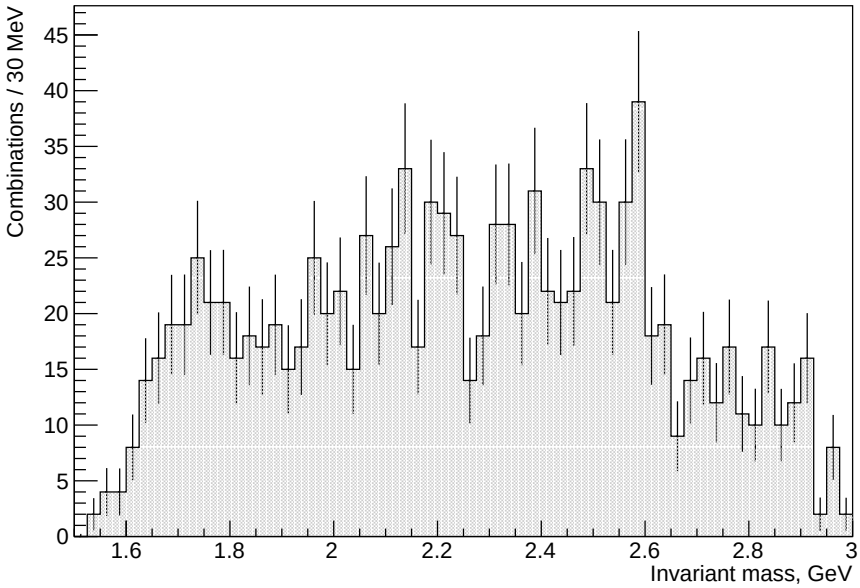

Figure 4.21: The invariant mass spectrum of background channels simulated using bggen that survive the event selection procedure. Of the 2 billion generated events, 1096 surviving combinations are left after cuts and accidental subtraction. Primary background channels are non-resonant kaon production and misidentified pion final states.

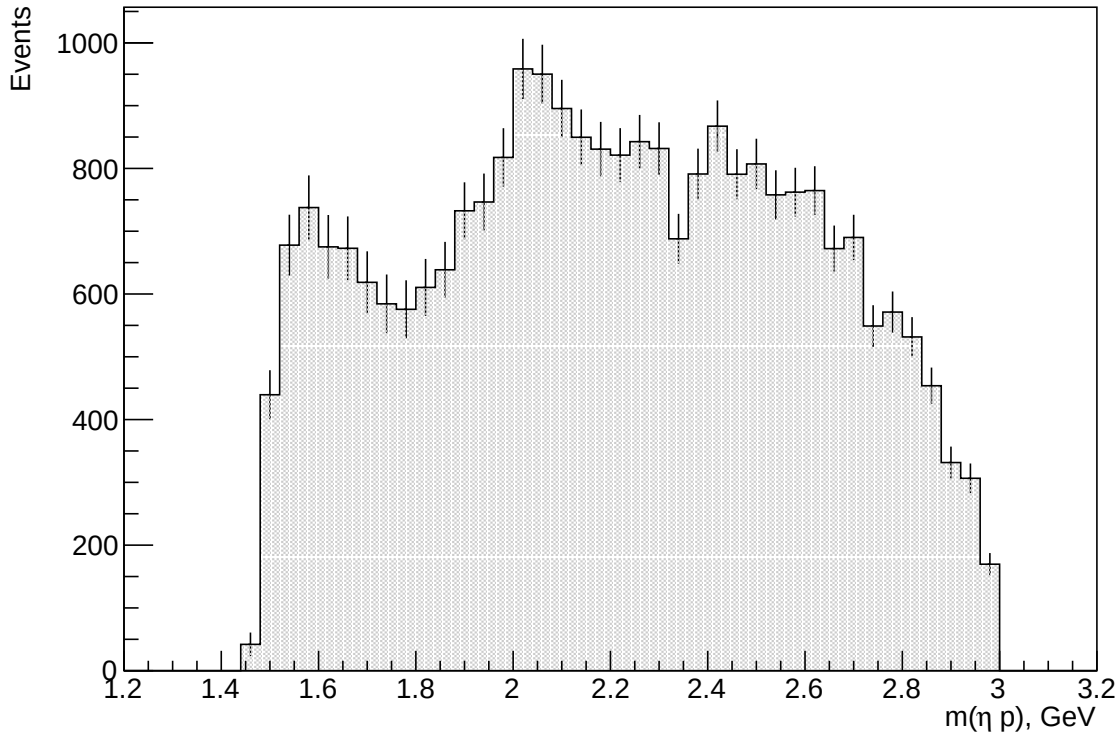

Figure 4.22: The invariant mass spectrum of the ηp subsystem after full background subtraction. A peaking structure can be seen around 1.6 GeV which is likely caused by a N* resonance.

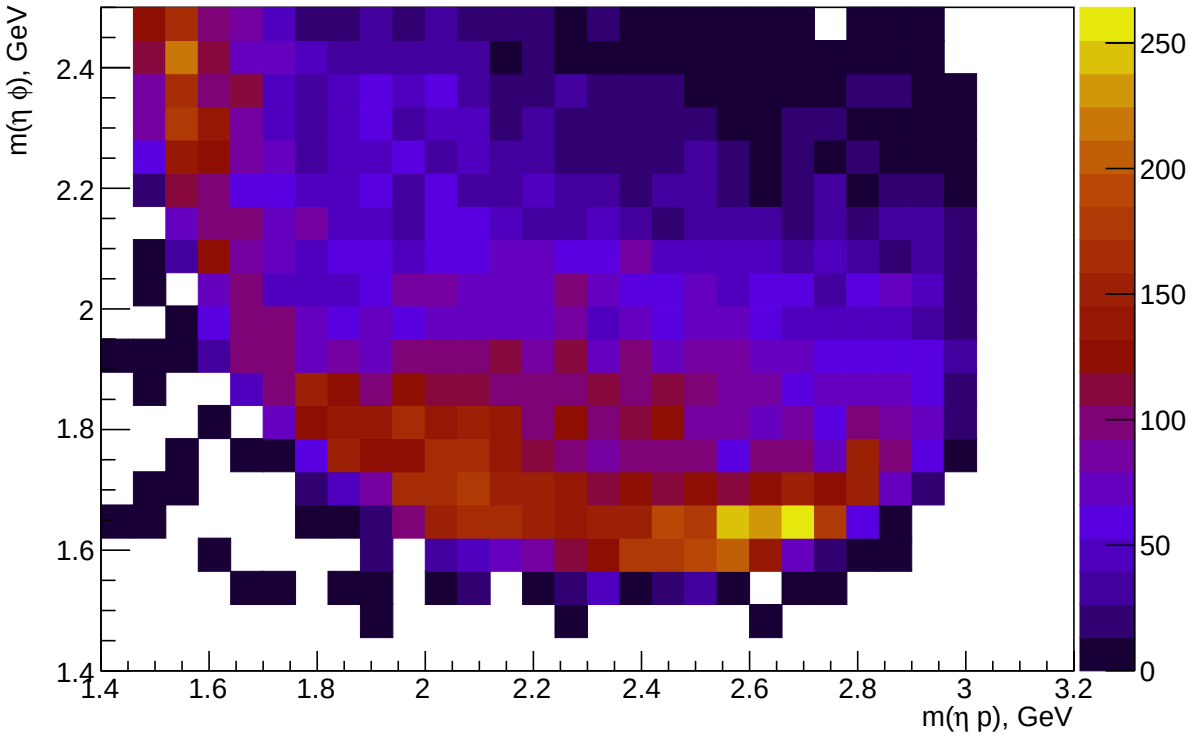

Figure 4.23: Histogram of ηp invariant mass against $\eta\phi$ invariant mass. It can be seen that the peak seen in the 1D ηp spectrum is only present at high $\eta\phi$ masses and will not influence the analysis of lower mass resonances. Possible baryon contamination may still be present at higher ηp masses.

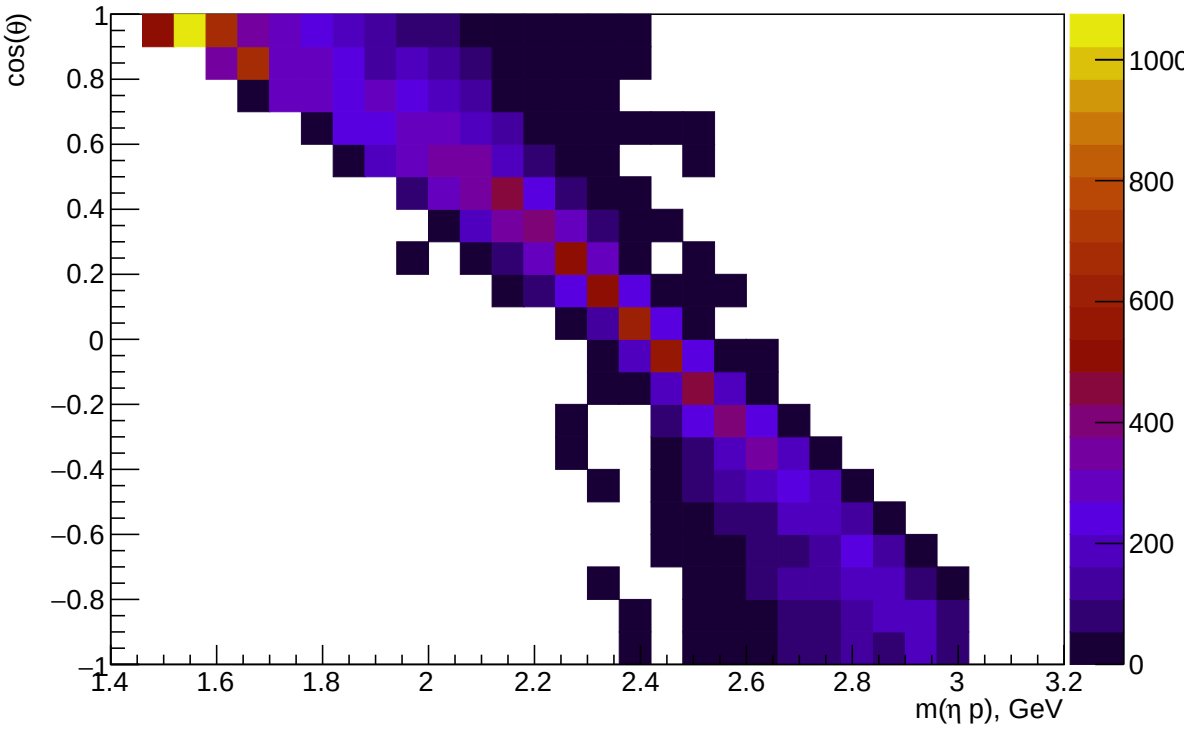

Figure 4.24: A plot of ηp invariant mass and the θ decay angle in the ϕ helicity frame. A strong correlation can be observed. Placing a cut on ηp thus imposes a cut on the θ angles – placing it at around 2.4 GeV would cut all events below 0 rad.

Chapter 5

Studies of partial wave fit behaviour

This Chapter considers various aspects of the partial wave analysis performed using the formalism described in Chapter 2. Section 5.1 briefly introduces the software framework used in the fitting and certain aspects of how its configuration affects fitting in practice. Section 5.2 presents a discussion of some of the typical behaviour observed for both hybrid and mass independent fit types, as well as statistical methods for model selection, allowing a nominal waveset to be picked. The Chapter concludes with an input-output study performed on simulated data in Section 5.3.

5.1 AmpTools

The software framework used to perform the partial wave analysis is called AmpTools [151]. It was designed to serve as a general purpose tool for such analyses at GlueX, allowing the users to perform extended maximum likelihood fits with custom amplitude definitions. Its utility libraries also serve as a backbone to a large number of Monte Carlo generators used by the collaboration, like gen_vec_ps.

AmpTools constructs an intensity function as an incoherent sum of coherent sums. Each coherent sum represents a quantum mechanically distinct physics process. Each coherent sum is modelled as a product of terms alongside their production coefficients, which are complex parameters in the fit, and any constant scale factors that may be present. The amplitudes themselves are assumed to be factorisable into products and may possess free parameters. In other words, the full intensity is given as:

$$I(x) = \sum_{\sigma} \left| \sum_{\alpha} s_{\sigma,\alpha} V_{\sigma,\alpha} A_{\sigma,\alpha}(x) \right|^2 \tag{5.1}$$

The σ indexes the coherent sums in the intensity and α indexes the terms within a coherent sum. $s_{\sigma,\alpha}, V_{\sigma,\alpha}, A_{\sigma,\alpha}(x)$ are respectively the constant scale factors that may be included to e.g. force two amplitudes to be a strict multiple of one another; the free complex parameters

representing the strength of the partial wave amplitudes and which are obtained by fitting, called production coefficients; and the partial wave amplitudes.

The terms are assumed to be of the following form:

$$A_{\sigma,\alpha} = \prod_{\gamma=1}^{\eta_{\sigma,\alpha}} a_{\sigma,\alpha,\gamma}(x) \tag{5.2}$$

The $\eta_{\sigma,\alpha}$ are the number of factors for a given term. The form assumed for the intensity is the reason why Eq. (2.20) is the final formulation of the vector-pseudoscalar model. The factors $a_{\sigma,\alpha,\gamma}(x)$ are defined by the user as a C++ class. AmpTools uses the standard C++ interface of the Minuit [152] optimiser to perform the likelihood fits.

In particular, AmpTools performs extended maximum likelihood fits [153]. Like in all maximum likelihood estimation (MLE) techniques the aim is to maximise a likelihood function $\mathscr{L}$, or equivalently minimise $-\mathscr{L}$, by iterative optimisation. The likelihood is a function that gives the probability of observing a data sample with the given parameters for some model. It is standard to minimise the logarithm of the negative likelihood due to the desirable numerical properties of logarithms. Compared to 'standard' MLE, the extended maximum likelihood modifies $\mathscr{L}$ to account for the fact that the expected number of observed events in a particle physics experiment should follow Poisson statistics, i.e. it is itself a random variable, turning it into a model parameter. The general form of the extended likelihood can be written as:

$$\mathscr{L}(\xi) = \frac{\mathbf{e}^{-\mu}\mu^{\mathbf{N}}}{\mathbf{N}!}\prod_{\mathbf{i=1}}^{\mathbf{N}}\mathbf{P}(\mathbf{x_i},\xi) \tag{5.3}$$

In the above expression, N is the number of events in the data sample, P is a probability density distribution, ξ is the set of parameters of the fit model, and μ is the expected number of events. Of course, μ and P can be written out in terms of the intensity model constructed previously, such that:

$$\mu = \int I(x_i,\xi)\eta(x)dx \tag{5.4}$$

$$P(x_i,\xi) = \frac{1}{\mu}I(x_i,\xi)\eta(x) \tag{5.5}$$

Here $\eta(x)$ describes the efficiency, which is the probability that a given event is detected by the detector and passes all subsequent reconstruction and event selection steps. As mentioned, it is often more convenient to work with the negative log likelihood, which is given by:

$$-2ln\mathscr{L}(\xi) = -\mathbf{2}\left(\sum_{\mathbf{i=1}}^{\mathbf{N}}\mathbf{lnI}(\mathbf{x_i};\xi) - \int \mathbf{I}(\mathbf{x_i};\xi)\eta(\mathbf{x})\mathbf{dx}\right) + \mathbf{c} \tag{5.6}$$

The constant c collects all terms that are not functions of the parameters ξ.

The probability density shown in 5.5 requires the intensity to be normalised by the integral in 5.4. This integral is not analytically computable, as the efficiency $\eta(x)$ does not generally have a closed form. This means it must be computed numerically with Monte Carlo techniques. If a simulated event sample that populates the phase space region of interest is produced, then it is possible to get the expected value of the integral as:

$$< I(x;\xi)\eta(x) >= \frac{1}{N_{MC}} \sum_{i=1}^{N_\alpha} I(x_i;\xi), \tag{5.7}$$

where N_{MC} is the total number of events in the Monte Carlo sample and N_α is the number of events that pass the full reconstruction and event selection that was applied to the real data sample. This expected value is approximately equal to the integral only up to a scaling factor. However, the final effect of this factor is to provide a term not dependent on the parameters in the full likelihood expression, which means the minimisation procedure is not affected. The computed expected value also has some statistical uncertainty associated with it, as the Monte Carlo samples used have a finite size. It is assumed that for sufficiently large samples this uncertainty is negligible. Angular distributions for the phase space sample after acceptance effects have been applied are shown in Figure 5.1.

5.1.1 Partial wave analysis in AmpTools

This Subsection will clarify a few potentially confusing practical points that arise when discussing partial wave fits in AmpTools. The fits, regardless of the distinctions between different ways to parametrise the model that are mentioned below, are unbinned extended maximum likelihood fits in the five angular distributions of the partial wave formalism. The angular distributions will be binned whenever they are presented in histogram form, but this is an arbitrary choice for visualisation purposes – each event contributes to the likelihood in the fit individually. The data may, however, be binned in terms of other variables, which affects the way the fits have to be configured in software.

Two types of partial wave fits are performed at GlueX. The first type is called a mass independent fit. In this type of fit, the data is split into bins of kinematic variables of interest, usually invariant mass and/or Mandelstam t. Fits to the partial wave model are then performed independently in each bin. This allows fewer assumptions about the data to be made, as no functional form for the invariant mass distribution needs to be provided. It is important to stress that on the level of the numerical fitting, fits in one bin do not affect fits in other bins at all – in the case of the current analysis, there are essentially 25 separate datasets created by doing invariant mass binning. The fits within each bin are still unbinned in terms of the target angular distributions.

This has a few implications: first, since no mass dependent constraints on the structure of the waves are enforced, smoothness and continuity in wave intensities will point toward the presence of real physics; second, as the yields being constrained in the extended likelihood formulation

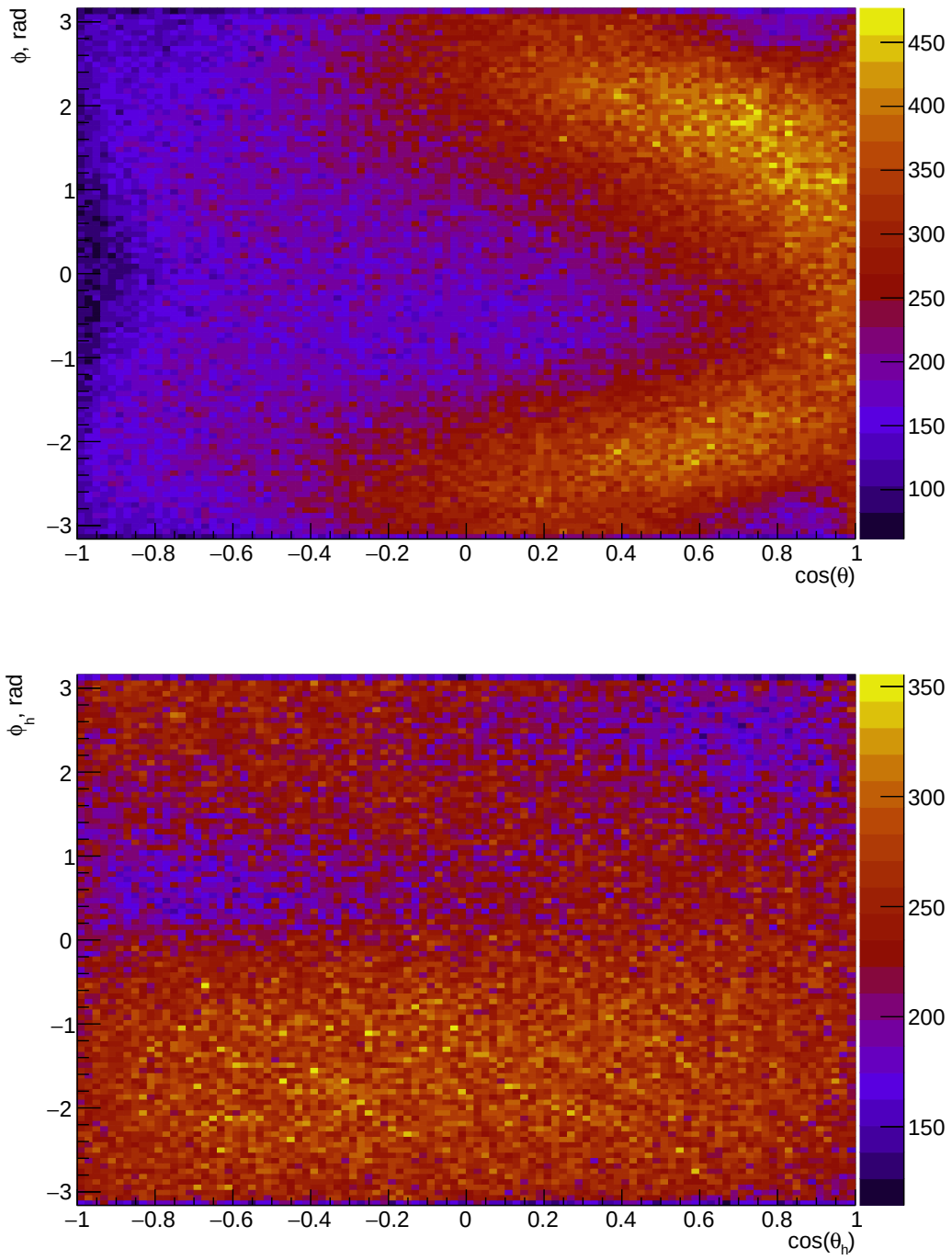

Figure 5.1: Angular distributions for simulated phase space data. The individual angular distributions, or the cosines thereof in the case of θ and θ_h, are flat in the generated samples. The shapes seen in the plots are induced by acceptance effects.

are the individual yields for each bin, the difference between the fit's reproduction of the $\eta\phi$ invariant mass spectrum and the data is not a meaningful way to determine goodness of fit.

The other type of fit is usually referred to as hybrid or semi-mass dependent. In this approach, select amplitudes thought to belong to a resonance are modelled as products of Breit-Wigner and vector-pseudoscalar reflectivity terms, introducing an explicit mass dependence into the fit. However, the remainder of the waves in the waveset remain described solely by the reflectivity amplitudes. This may have certain benefits – as will be discussed in the rest of the section, amplitudes in mass independent fits can suffer from large bin-to-bin variation due to factors like e.g. an insufficiently constrained solution space. Enforcing continuity of some waves by construction may thus help stabilise the rest of the fit. It can also act as a cross-check to the mass independent fits as, assuming the chosen resonances can indeed be reasonably modelled as a Breit-Wigner, the results in both cases should be similar.

The implications on the numerical details of the fitting should again be noted. The waves in the fit that are not being constrained by a Breit-Wigner shape must still have production coefficients that can be different for each mass bin, while the BW terms are dependent on all events in the dataset and only have one complex parameter per fit. In AmpTools practice this means that the former are implemented as so-called piecewise amplitudes, one for each mass bin, that return 0 for the intensity if an event does not fall within the mass range of the bin. All of this means that the fit must now be performed over the full dataset all at once. This makes the hybrid fit quite expensive computationally, as the number of free parameters in the fit is now multiplied by the number of bins and the computation is no longer as easily parallelisable.

Regardless of fit type, additional considerations must be made for the presence of local minima. Although in an ideal world there would only be the one global minima for a fit to converge to, this is not usually the case and multiple local minima may exist. One of the factors that can seriously affect which of these minima a fit will eventually reach is the set of starting parameters it is initialised with. To ameliorate this effect, all fits are performed a number of times with random initial parameters each iteration. As no particular amount of random starts would ensure that the global minima is included in the solution set, this number is an educated guess based on past analyses – unless stated otherwise it is assumed that each fit underwent a 100 iterations. Figure 5.8 shows the distribution of likelihoods for a selected waveset and bin. It can be seen that there is a spread of solutions, though as will be noted later most of these do not actually result in very qualitatively different results.

The final point of order are the uncertainties on partial wave parameters and the subsequently obtained intensities. By default the statistical errors output by Minuit are obtained by computing the matrix of second derivatives at the solution. It has been noted that these uncertainties are not reliable when weighted events are used [154], as is the case when sPlots are used to remove background from the data sample. On average they tend to be underestimated, and this appears to be the case here as the Minuit uncertainties on the partial wave amplitude parameters are

generally on the order of $< 1\%$ – clearly too low to be realistic. Instead, the bootstrap method [155] is used – the dataset is sampled with replacement to create 200 separate datasets of the same size as the original. This procedure is assumed to approximate the real data distribution. Although increasing the number of bootstraps will tend to increase the statistical power of the technique, 200 was chosen as a good compromise between performance and computational demands. Parameter extraction is performed on each of the bootstrapped datasets in the same way as for the original, which in this case means they undergo the event selection described in Chapter 4 and the partial wave fits presented above; the statistical uncertainty on quantities of interest is assumed to be the standard deviation of their values over the datasets. Errors on hybrid fits were not computed due to prohibitive computational cost, as they were not used when calculating the final results or systematic uncertainties.

5.2 Waveset selection

The data being analysed in this thesis is a product of various particle decay mechanisms. If the event selection procedure was successful, these mechanisms should be meson decays that can be described by the formalism from Chapter 2. There should thus be some unique combination of partial wave amplitudes that reflects the data generating process. In the literature the combination of waves used in a fit is usually referred to as the waveset. Consequently it is generally expected that a single reference waveset that provides the best match to the data is picked when reporting results. In the ideal case all that would be required to do this would be to pick some reasonable set of possible waves, run the partial wave fits, and see amplitudes not present in the data go to 0 within at least statistical uncertainty. Unfortunately, when dealing with real experimental data this rarely happens so easily – fits can often converge to different solutions depending on factors like initial parameters and in certain cases may describe the data comparably well.

Instead, waveset selection requires, study of the practical behaviour of the partial wave fits – even if automatically finding the best waveset may not be possible, varying them and comparing the fit results can support inferences about which waves are more likely to be dominant. Results of these exploratory data fits can then inform Monte Carlo studies of how the model fares when faced with pure signal, which in turn feed back into how the results of the fits are interpreted. Statistical metrics that may be usable when comparing model performance also exist and may be studied as an aid to the final scientific judgement. The remainder of this Chapter will discuss all of these issues, starting with observing trends in partial wave fits in Subsection 5.2.1 and concluding with input-output studies in Section 5.3.

Table 5.1: A table of a J^{PC} combinations allowed for a vector-pseudoscalar decay in terms of J and L. Particles with higher J and L values are technically possible, but are not predicted to be seen in the $\eta\phi$ channel. Resonances possessing numbers 0^{--} and 2^{+-} would be exotic mesons, as these cannot be obtained in a $q\bar{q}$ configuration.

	J = 0	J = 1	J = 2	J = 3
L = 0	-	1^{+-}	-	-
L = 1	0^{--}	1^{--}	2^{--}	-
L = 2	-	1^{+-}	2^{+-}	3^{+-}
L = 3	-	-	2^{--}	3^{--}

5.2.1 Exploratory data analysis

Waveset selection can be guided by results from earlier measurements. Previous analyses indicate that the $\phi(1680)$ and $\phi_3(1850)$, which are expected to be present in the data, should have the quantum numbers 1^{--} and 3^{--} respectively. Chapters 1 and 2 introduced the concept of the J^{PC} quantum numbers and their use in classifying hadron resonances but it is worthwhile tabulating what partial waves these correspond to. This is shown in Table 5.1 – the J = 1, L = 1 and J = 3, L = 3 waves are expected to dominate. There are no especially strong intuitions for which m-projections or reflectivities are expected to be stronger, which is to say there are no strong assumptions made about the resonances' production mechanism.

Each potential combination of J, L, M and reflectivity will contribute an amplitude, and thus a free complex parameter, to the model used in the fit. The results obtained from a partial wave analysis can be visualised in terms of the intensities for each of these amplitudes. However, as their number grows large, the share of intensity each amplitude contributes may grow quite small and make for difficult viewing. It is also often the case that one may be more interested in the behaviour of particular coherent sums of the amplitudes, e.g. such as correspond to intensities of a wave integrated over their m-projections and reflectivities. In the following plots, unless stated otherwise in the legend and caption, all waves denoted with their J^{PC} and L values will be integrated over the other quantum numbers.

The observed signal spectrum extracted in Chapter 4 contains two peak-like structures. Their locations are consistent with the masses reported for the two ϕ resonances in the PDG, so this is where the relevant partial waves would also be expected to peak. However, the possibility of interference from resonances with different J^{PC} combinations also cannot be ignored – a variety of such states have been proposed [156, 157]. As a first test, the angular distributions near the mass peaks can be inspected. If the two peak regions contain resonances with different quantum numbers, the distributions should be made up of distinct combinations of sine/cosine functions and be visually distinct. All five of the angular distributions used in the fit for the bins covering the reported peaks of the two resonances are shown in Figure 5.2. The angle Φ is flat independent of mass, which is expected when data is combined over all radiator settings, but

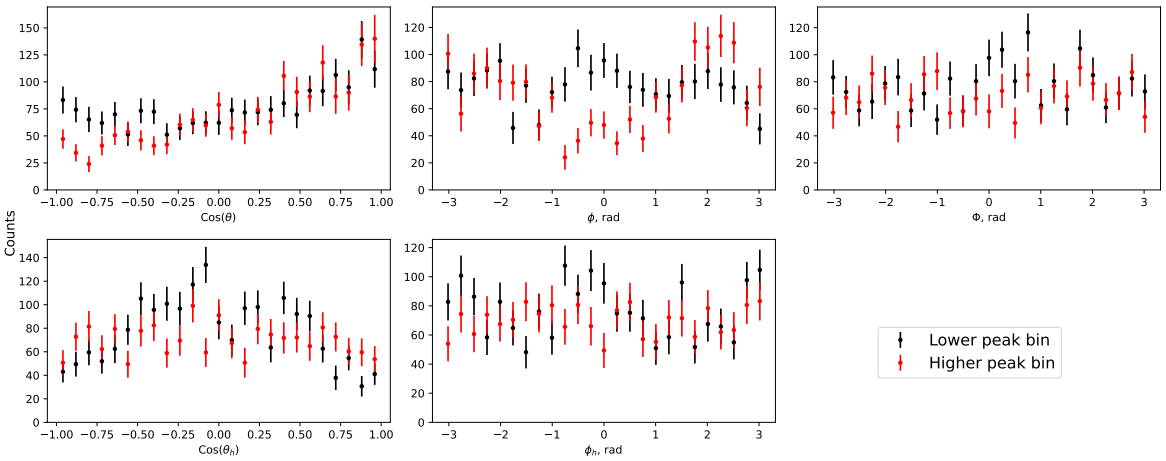

Figure 5.2: The five angular distributions for $\eta\phi$ invariant mass bins 1.66 GeV - 1.7 GeV and 1.82 GeV - 1.86 GeV denoted as lower and higher peak bins respectively in the legend. Some distributions cannot be distinguished within statistical uncertainty, but a divergence is clear in $\cos(\theta)$ and ϕ.

the θ and ϕ distributions look quite different even accounting for the relatively large statistical uncertainties.

If the one dimensional angular histograms do indicate multiple resonances in the data, this should be replicated in the projections of the partial wave fits. The projections are performed by using the amplitude parameters obtained from the fits and computing the intensity from each event in the accepted MC dataset, normalised by the number of MC events. These intensities can then be used to histogram the desired variables. If the projection is instead performed on the generated MC, i.e. the integral in Eq. (5.1) is changed such that the sum is over the generated MC events, the projections will be corrected for detector and reconstruction acceptance effects. Acceptance corrected plots for the nominal waveset will be shown in the next Chapter.

The angular distribution projections for a mass independent fit containing the 1^{--} and 3^{--} waves are shown in Figure 5.3 for the same two mass bins, now separated into different subplots. As previously, the 1^{--} wave is dominant in the lower mass bin while the latter wave is strong in the higher mass bin. The angles are reproduced fairly well overall in the first bin outside the very edges of the $\cos(\theta_h)$ distribution, but the fit fares worse at the higher mass peak, completely failing to capture that same distribution. As noted back in Chapter 1, the assignment of the $\phi_3(1850)$ quantum numbers is not on entirely stable ground. This means that a number of possible partial waves must be considered in the fits. For example, it is possible that 2^{--} states may be present and overlap with any existing 3^{--} resonance.

Indeed, even more waves should be considered for study. For example, it is possible that the long-tail of a broad 1^{+-} resonance could be seen in the data. The only relatively certain fact is that no states with J above 3 are expected, so the waveset can be truncated at J = 3. To explore how the waveset affects the results, a large number of fits with different combinations

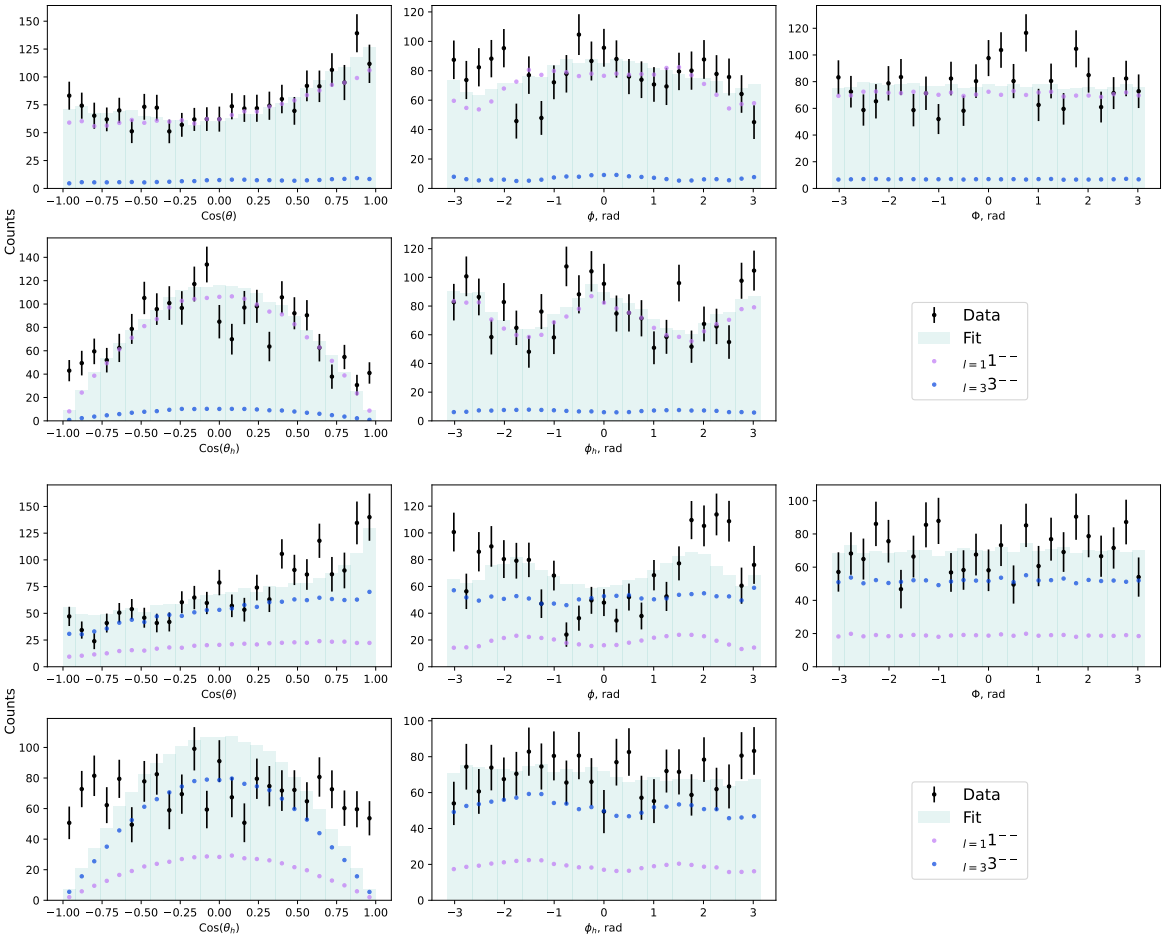

Figure 5.3: A fit with 1^{--} and 3^{--} waves to angular distributions in bins of $\eta\phi$ invariant mass. The top plots are from the bin 1.66 GeV - 1.7 GeV and the bottom plots are from the bin 1.85 GeV - 1.89 GeV. The lower mass bin is described well, but in the higher mass bin the fit completely fails to reproduce $\cos(\theta_h)$.

of partial waves were performed. To a first approximation, if an amplitude corresponds to a resonance, it would be expected to be continuous over the invariant mass spectrum and to peak in the appropriate location while non-resonant amplitudes should remain approximately flat. Some pruning of the waveset may be possible at this stage, as waves that consistently contribute little to the intensity can be dropped. Invariant mass projections for some of these fits are shown in Figure 5.4.

A few trends can be observed. Waves do not appear to reliably peak around 1.85 GeV, and the 3^{--} wave easily loses intensity to other waves in many fits. There is thus no unambiguous signal that can be identified with a $\phi_3(1850)$ resonance. A dominant 1^{--} component, however, is consistently present around the first peak, matching the hypothesis that the $\phi(1680)$ is present in the data. The intensity of the 1^{--} wave varies depending on waveset. This loss of intensity appears more pronounced when some waves are included – for example, the intensity of J = 2, L = 1 wave can often be of similar magnitude when both are in the fit. In the limit of a large number of waves, peaking behaviour is less pronounced; the last fit shown includes all eligible waves, and though the 1^{--} still forms a small peak, most waves individually make only small contributions to the total intensity in any given bin.

As mentioned previously the invariant mass projections, due to the way the extended likelihood is constructed, do not provide a direct way to assess how good the results from mass independent fits actually are. The first step to assessing their quality is to once again compare their projections to the angular distributions. Figure 5.5 shows angular projections when J = 2 waves are added to the PDG waveset. The results in the first peak bin do not change very much, though the 1^{--} wave loses intensity. The situation in the higher mass bin improves, which may indicate that regardless of whether a 3^{--} resonance is present other states may be needed to explain the higher mass structure. The invariant mass projections also indicate that the 1^{+-} S-wave component has significant intensity in the first few mass bins when it is included. It allows the fit to capture a rise at low $\cos(\theta)$ in the low mass region – in cases where the wave is not present, this angle is consistently poorly fit. This can be observed in the angular plots for the affected lower mass bins included in Appendix E.

The partial wave model used in the analysis is indexed not just by the angular momentum quantum numbers, but also the projection of J onto the helicity axis, notated by m, and their reflectivities. The dominance of certain reflectivities and combinations of m-projections would provide evidence for the resonances being produced via a particular mechanism. Figure 5.6 shows the partial waves of the m-projections for a selected fit. It is hard to draw any strong conclusions from the motion of the higher order waves. However, the 1^{+-} and 1^{--} components do show some structure. For both, the m = 1 and m = -1 amplitudes appear to be the most significant. The fit cannot reliably discriminate between the two projections, but the sum of their intensities remains relatively stable. The m = 0 projection is much weaker than the the m = $|1|$ component for the 1^{--} wave, but is of comparable magnitude for the 1^{+-} wave.

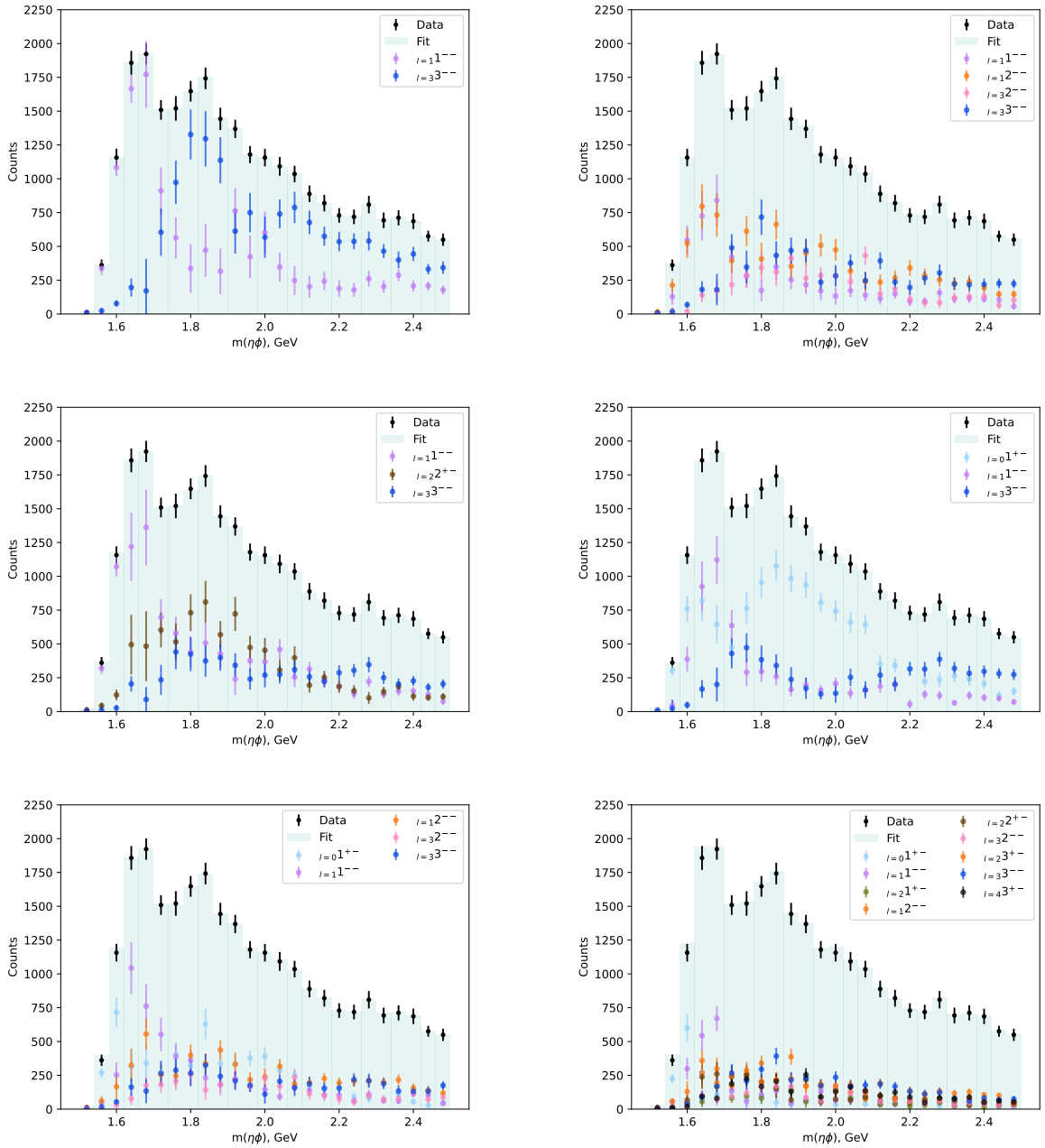

Figure 5.4: Invariant mass projections for a selection of mass independent fits. The first subplot in the top left corner shows a waveset that only includes waves corresponding to the J^{PC} assignments of the $\phi(1680)$ and the $\phi_3(1850)$. The last fit in the bottom right corner shows the results of including all waves up to J = 4. Most fits have the 1^{--} wave peaking around 1.68 GeV.

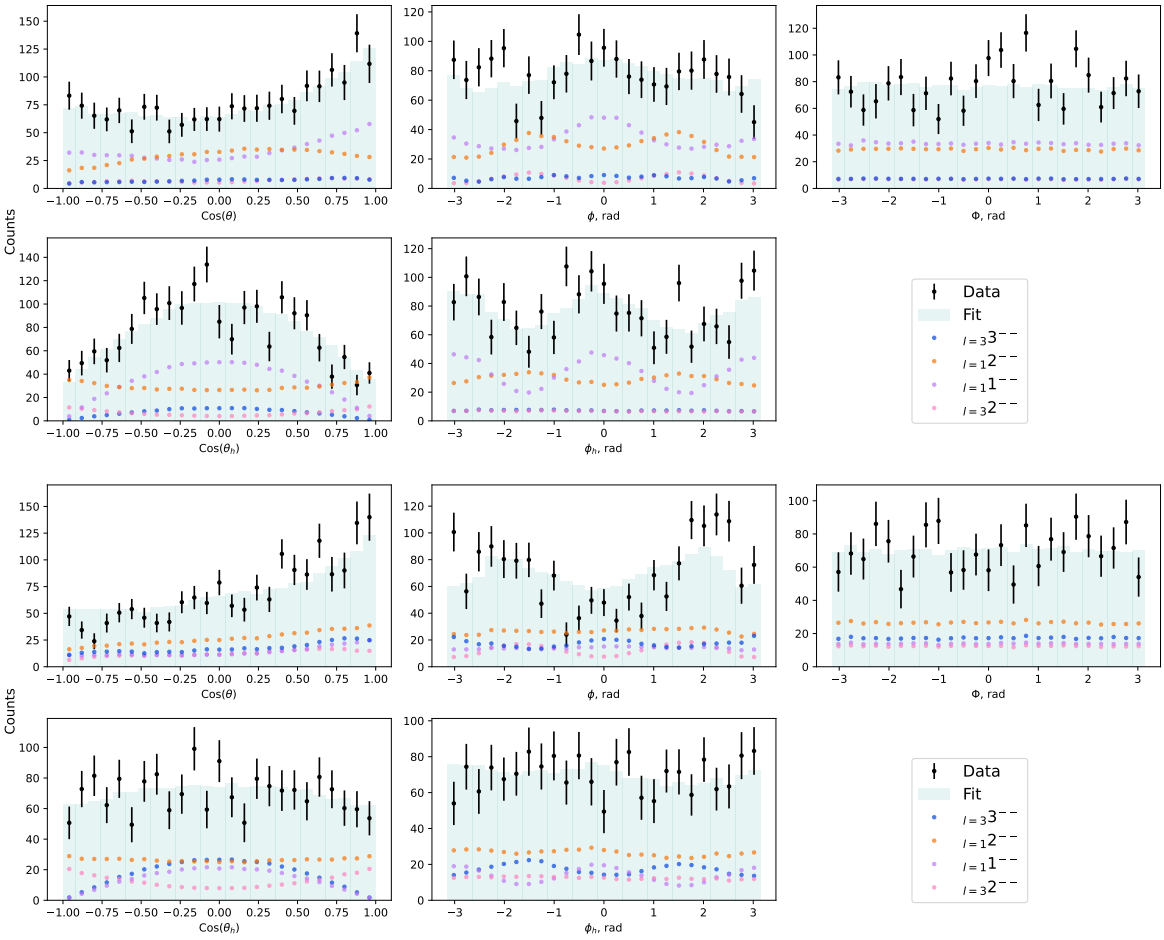

Figure 5.5: A fit with 1^{--}, 2^{--} and 3^{--} waves to angular distributions in bins of $\eta\phi$ invariant mass. The bins shown are for ranges 1.66 GeV - 1.7 GeV and 1.85 GeV - 1.89 GeV. The fit describes the data well in both bins, but lower in invariant mass an additional S-wave component is needed.

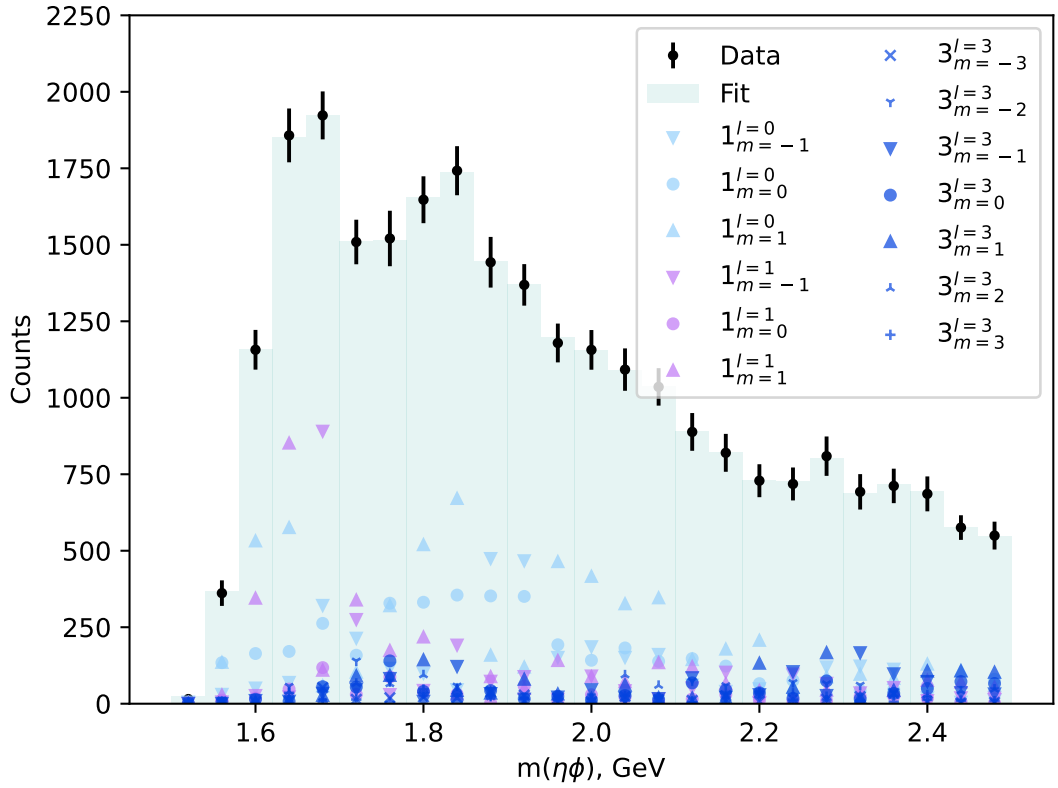

Figure 5.6: Invariant mass spectrum showing the individual m-projections for a waveset containing J = 1, L = 0, 1, and J = 3, L = 3 waves. For the first two waves, the m = |1| components dominate, though the fit cannot discriminate between the specific projections. The m = 0 projection is negligible for the J = 1, L = 1 wave, but is comparable to the other amplitudes for the J = 1, L = 0 wave.

Going back to plots integrated over the m-projections, invariant mass spectra separated by reflectivity for a few fits are shown in Figure 5.7. The positive reflectivity waves seem to be reliably stronger, though the ratio is not always constant. This also appears to be more pronounced for the 1^{--} wave. However, it is not sufficiently dominant to motivate entirely excluding the negative reflectivity amplitudes from the fit.

The fits discussed so far look reasonable, but their robustness has to be studied. It has been proven that certain choices of waveset lead to ambiguities [158]. By construction, any intensity model similar to the one used here will involve trivial discrete degeneracy caused by the fact that a valid solution can be generated by taking the complex conjugate of any solution. The ambiguities described in the cited talk are more complicated – they result from multiple minima with an exactly identical likelihood, meaning that they cannot be distinguished by the fit regardless of the available data. In fact, these ambiguities are continuous – if likelihoods are plotted as a function of the fit amplitude production coefficients, a surface of identical likelihood is formed.

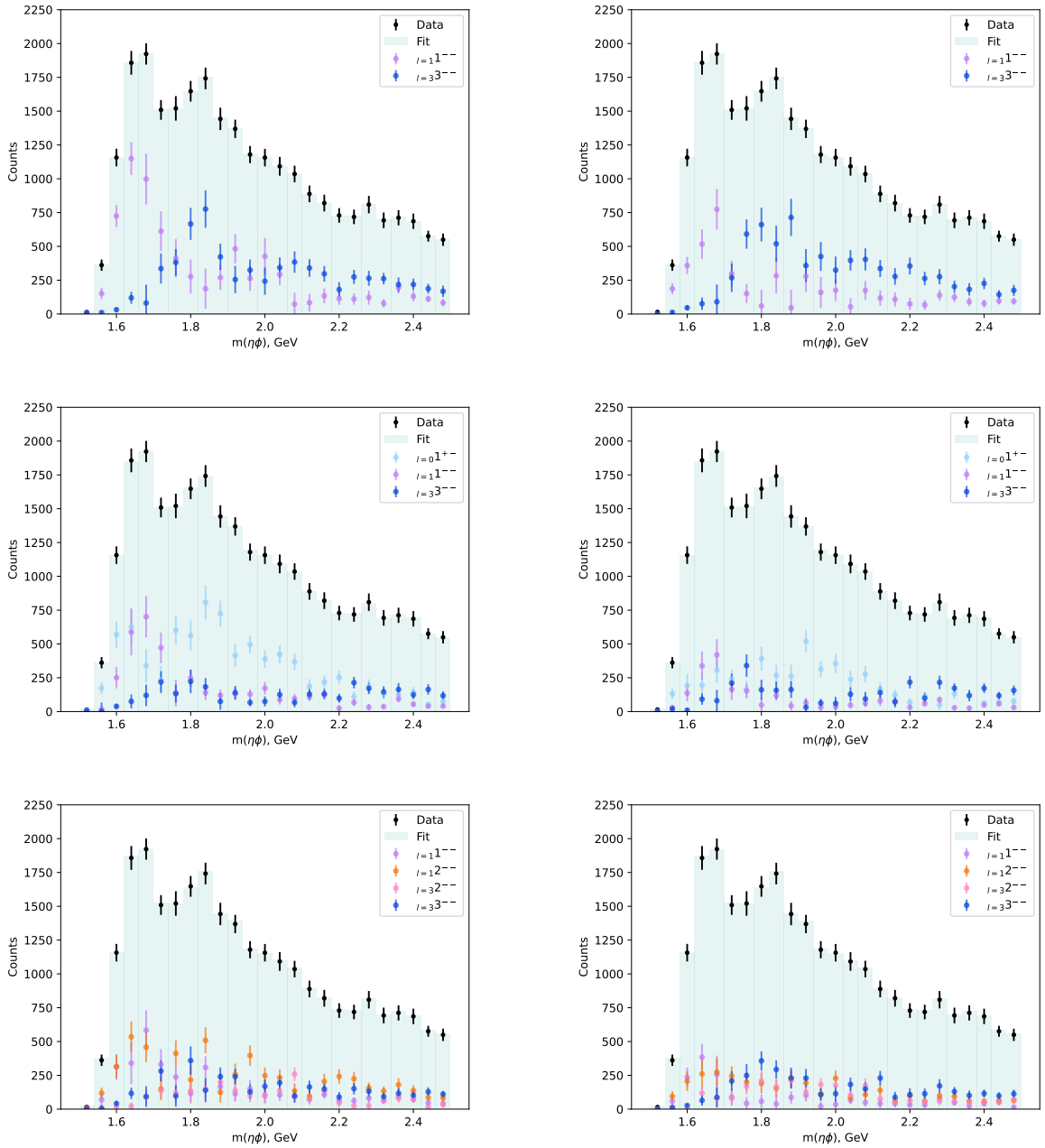

Figure 5.7: Invariant mass spectra for various fits according to reflectivity. The left column shows the positive reflectivity waves, while the right column shows the negative reflectivity waves. Positive reflectivity waves tend to be favoured, though the exact ratios can vary. This trend is consistent for the 1^{--} waves.

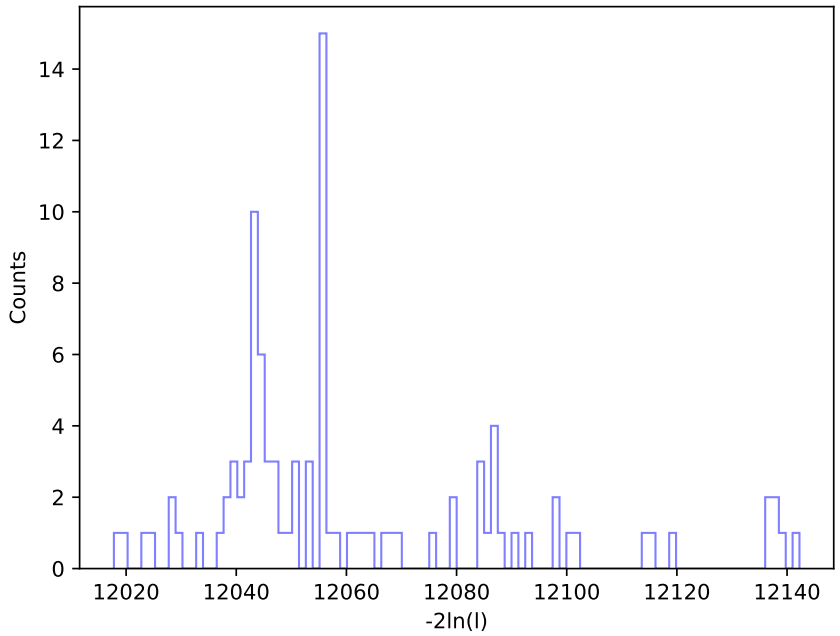

Figure 5.8: A histogram of likelihoods obtained from a 100 randomly re-initialised fits in the 1.66 GeV - 1.7 GeV bin for a waveset containing 1^{+-}, 1^{--}, and 3^{--} waves.

These continuous ambiguities are an inherent feature of the partial wave model, but are not present for all wavesets. The formal analysis cited above focused on the a particular set of cases where the $m = 0$ projection is almost zero and the m $= \pm 1$ projections are dominant for a 1^{--} wave in a waveset without higher J waves. It is clear that the m-projections for the 1^{--} wave in the current data do show this behaviour, but the presence of higher order waves may break these ambiguities. Comparing between results of randomly re-initialised fits does not show any instances of the likelihoods being exactly identical, though many can be within one arbitrary -2NLL unit of each other. A histogram of likelihoods for all 100 re-initialised fits for a sample bin is shown in Figure 5.8. This indicates that multiple solutions are more likely to arise from the existence of local minima in the fit rather than strict degeneracies in the model.

Despite this, results may not be strongly affected in practice. The variance of the intensities for each wave obtained from the top 10 fits by likelihood in each invariant mass bin is shown in Figure 5.9 for two wavesets. Some particular wavesets may see larger fit-to-fit variations, but the qualitative results remain quite similar – if a given J^{PC} component is dominant in the best fit, it will remain significant between fits. Looking at the same kind of plot for the separate m-projections in Figure 5.10 indicates that the local minima may often be caused primarily by fit-to-fit variations in these amplitudes. It has already been seen that the fit cannot distinguish different m-projections in the case of the 1^{--} amplitudes, so it is perhaps not surprising that this could be applicable for other waves as well.

The exploratory data analysis so far suggests that 1^{--} amplitudes describe the structure

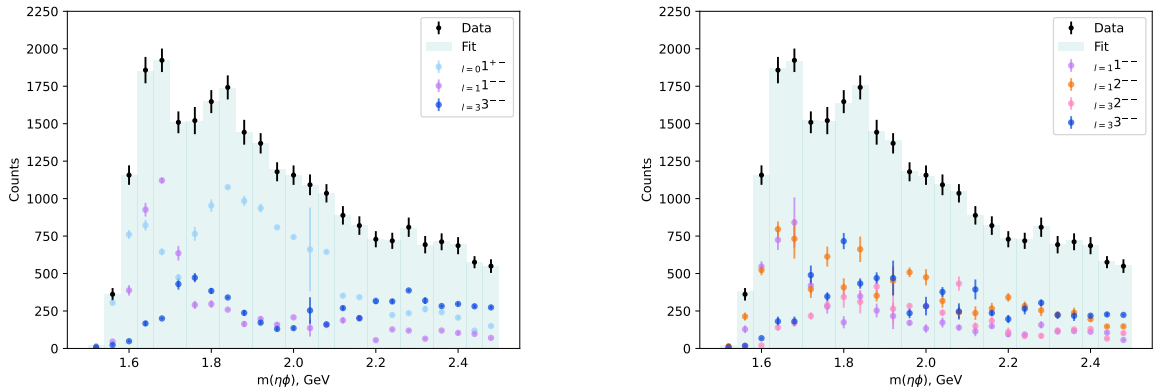

Figure 5.9: Invariant mass spectra for two selected wavesets. The error bars indicate variation in wave intensity in the top 10 fits by likelihood in each bin. The fit on the left sees little variation, but the fit on the right sees larger variation in bins where 1^{--} and 2^{--} waves are both strong.

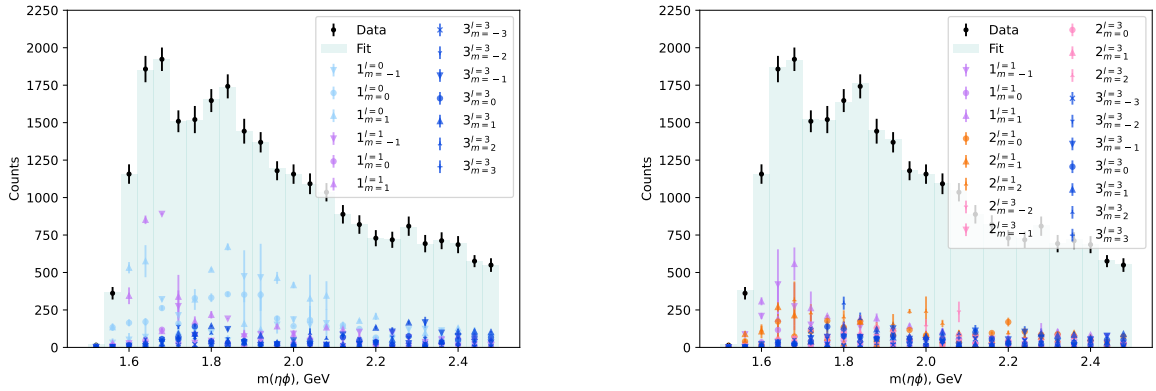

Figure 5.10: Invariant mass spectra for two selected wavesets by m-projection. The error bars indicate variation in wave intensity in the top 10 fits by likelihood in each bin. Both wavesets have significant variation in the m-projections, indicating that the local minima may be being caused by an inability to differentiate them during the fit.

around 1.68 GeV well, which is compatible with the presence of the expected $\phi(1680)$ resonance. The situation around the higher mass structure is not so clear. Waves other than the 1^{--} and the 3^{--} are required to describe this mass region well, but manual inspection of the angular distributions does not allow a definite determination of the best fit. In general, fits did not tend to remove waves from the waveset when additional amplitudes were added – whether this is because of intensity leakage between waves caused by difficulties in fit or genuine presence of many waves is not certain. The former is a serious possibility, especially taking into account the amount of parameters involved in the analysis. As each amplitude corresponding to a combination of J, L, m, and reflectivity contributes two real parameters to the fit, the number of free parameters grows quickly – even the PDG-based waveset will contain 39 if no m-projections are removed. The ability of the fit to discriminate between waves and to remain robust to phenomena like overfitting can be expected to decrease for the increasingly large wavesets. It may also be part of the reason why the fits seem to suffer from the presence of hard-to-distinguish local minima.

As neither the fit itself nor inspection of relevant histograms allow us to clearly pick one best waveset, goodness-of-fit metrics offer a way to perform model selection. A simple χ^2 metric that is commonly used in physics analyses is not possible in the case of the mass independent fits, as the observed bin-to-bin yields are already a free parameter in the extended likelihood fits. Any such metric would thus have to be performed on the angular distributions or other phase space variables. The model is naturally 5-dimensional which means comparing the data distributions to the fit results is not trivial, as χ^2 metrics are not easily constructable for high dimensional problems. Computing them for the individual distributions may allow a more quantitative statement to be made on how well these are reproduced by a fit, but combining them does not give a robust statistic.

A handful of likelihood based information theoretic metrics are often suggested for problems of this kind. The simplest is the likelihood ratio test, also known as the Wilks' test [159]. To perform parameter estimation, given that the parameters for the null hypothesis $\mathscr{H}_0$ are denoted ξ_0 and the parameters for the alternative hypothesis are denoted ξ, then the likelihood ratio is:

$$\lambda_{LR} = -2(\log(\mathscr{L}_0) - \log(\hat{\mathscr{L}})) \tag{5.8}$$

The $\mathscr{L}_0$ is the likelihood under the null hypothesis, while $\hat{\mathscr{L}}$ is the minimised likelihood of the model being fit. Wilks' theorem states that in the limit of infinite samples, the distribution of this statistic asymptotically reaches a χ^2 square distribution with degrees of freedom equal to the difference of the degrees of freedom of the two models being compared [159]. This allows a p-value to be computed to see if the differences between the models are statistically significant. For model selection purposes, one may also simply calculate the relative likelihood in Equation 5.8 and choose a model with the lower likelihood. This is often referred to as the Likelihood Ratio Test (LRT) and is a simple approach to model selection, but it has drawbacks. In particular, as the

test is only a function of the two likelihoods, comparing likelihoods may perform poorly when trying to select between models that have a large discrepancy in the number of free parameters – bigger models generally have more freedom in the fit, increasing the chances of overfitting and resulting in lower likelihoods by default. Some authors also argue that the LRT is only applicable when comparing nested models [160].

Two other metrics, the Akaike Information Criterion (AIC) [161] and the Bayesian Information Criterion (BIC) [162], are also widely used. Both metrics are similar in form:

$$\mathrm{AIC} = 2k - 2\ln(\hat{\mathscr{L}}) \tag{5.9}$$

$$\mathrm{BIC} = k\ln(n) - 2\ln(\hat{\mathscr{L}}) \tag{5.10}$$

As before, $\hat{\mathscr{L}}$ is the minimised likelihood of the models. In both cases, k is the number of free parameters in the fit and n is the number of data samples. Like in the relative likelihood case, model selection can be performed by selecting the model with the lower criterion value. No parametric constraints on the data or the statistics have to be satisfied, and it is not assumed that models have to be nested. It can be shown that in the asymptotic limit minimising the AIC or the BIC will trend toward the optimal solution [163], i.e. the model that best fits the given data, though debate exists on how this relates to the presence of the true model amongst available choices [164, 165]. Unlike the likelihood ratio test both the AIC and the BIC include terms that penalise the number of parameters. This aids in helping to reduce the potential issues with overfitting. For reasons of parsimony, it is also often preferred to reduce the number of contributing parameters if they are not expected a priori.

The penalty terms differ between the two criteria. The BIC term is a function of both sample and model size, which means that in situations where statistics are sufficiently high to ensure that $\ln(n) > k$, it penalizes the likelihood more strongly. In the case of the mass independent fits it also means that the BIC penalty term is not constant across the mass range, as fits performed in each bin will have different n. For both criteria it is assumed that the number of data samples is sufficiently higher than the number of free parameters in the fit. This is satisfied in the mass bins between 1.6 GeV and 2.02 GeV, though corrections for low sample cases exist [160].

These metrics provide a theoretical basis for finding the best fit, but they have to be calculated for each model under consideration. Due to the very large number of possible wave combinations, performing fits for all wavesets to complete an exhaustive search was not computationally tractable. To prune the search space, both reflectivities and all m-projections were kept in all the fits while varying the J and L of the included waves. The top three fits for each invariant mass bin are provided in Appendix C according to the AIC and the BIC statistics. As expected from the previous description of penalty terms, the criteria pick out different fits as top candidates. These candidate lists also vary over the mass range. The latter fact was to be ex-

pected – the patterns of wave motion in different wavesets and a visual inspection of the angular distributions suggests a preference for different waves at different parts of the spectrum.

Generally the AIC prefers more complicated wavesets while the BIC prefers smaller wavesets until quite high in invariant mass, a result of the statistics being high enough to make the BIC impose a stronger penalty on free parameters. Some trends that match the observations from the exploratory fits can be seen. With the exception of some AIC picks for the low statistics bins, all wavesets favoured up to 2 GeV include a 1^{--} wave. Although the AIC, as just mentioned, reliably selects combinations with a 3^{--} included, the top BIC choices only start including one or both of the similar $L = 3$ waves starting around 1.8 GeV. Inspecting the fits manually shows that the top candidates do not significantly differ in angular distributions.

Evaluating the performance of the AIC and the BIC is not trivial. During the input-output studies described in 5.3, both criteria were computed for fits using different wavesets to Monte Carlo datasets. If the metrics perform well, they should be able to at least select the true waveset used to generate the simulations. The studies seemed to show that both criteria are able to do this, though it is of course not clear how this directly translates to real data. The outcome of this model selection is thus equivocal. Further studies will have to be performed to decide whether the promised asymptotic guarantees obtain in this particular case, and if there are reasons to prefer one of these criteria over the other, or if more sophisticated modelling approaches should be pursued. These are outwith the scope of the present thesis.

In the end, none of the methods used are able to unambiguously determine a best fit. If a nominal waveset is desired, it must be picked by relying on the inferences made from the exploratory data analysis. A few features are consistent throughout the preliminary fits: an S-wave component in lower mass bins needed for a good fit; a peaking 1^{--} wave around 1.68 GeV; a non-1^{--} wave required for higher mass bins. Furthermore, some m-projections may be removed without reducing fit quality. Only one of the m = $|1|$ projections is required for the 1^{--} wave, so the m = -1 amplitudes can be left out. For the 3^{--} waves, the m > 2 waves are expected to be forbidden by decay selection rules and do not show any particularly interesting behaviour, so they can also be cut. Although the 3^{--} wave does not form an obvious resonance, it is kept in the waveset due to the existing PDG assignment, but 2^{--} waves are also included. There does not appear to be any a priori reason why other waves should be expected in the data, and they either consistently contribute little or act erratically. Finally, although the positive reflectivity is stronger in all attempted fits, it is not sufficiently dominant to remove the negative reflectivity amplitudes entirely. The final reference waveset is thus constructed as given in Table 5.2. Detailed plots and numerical results for fits using it are provided in the following Chapter.

Hybrid fits

Hybrid fits were performed as a cross-check to the mass independent fits. This approach should in principle be more stable due to enforcing continuity in the waves, though it is not obvious how

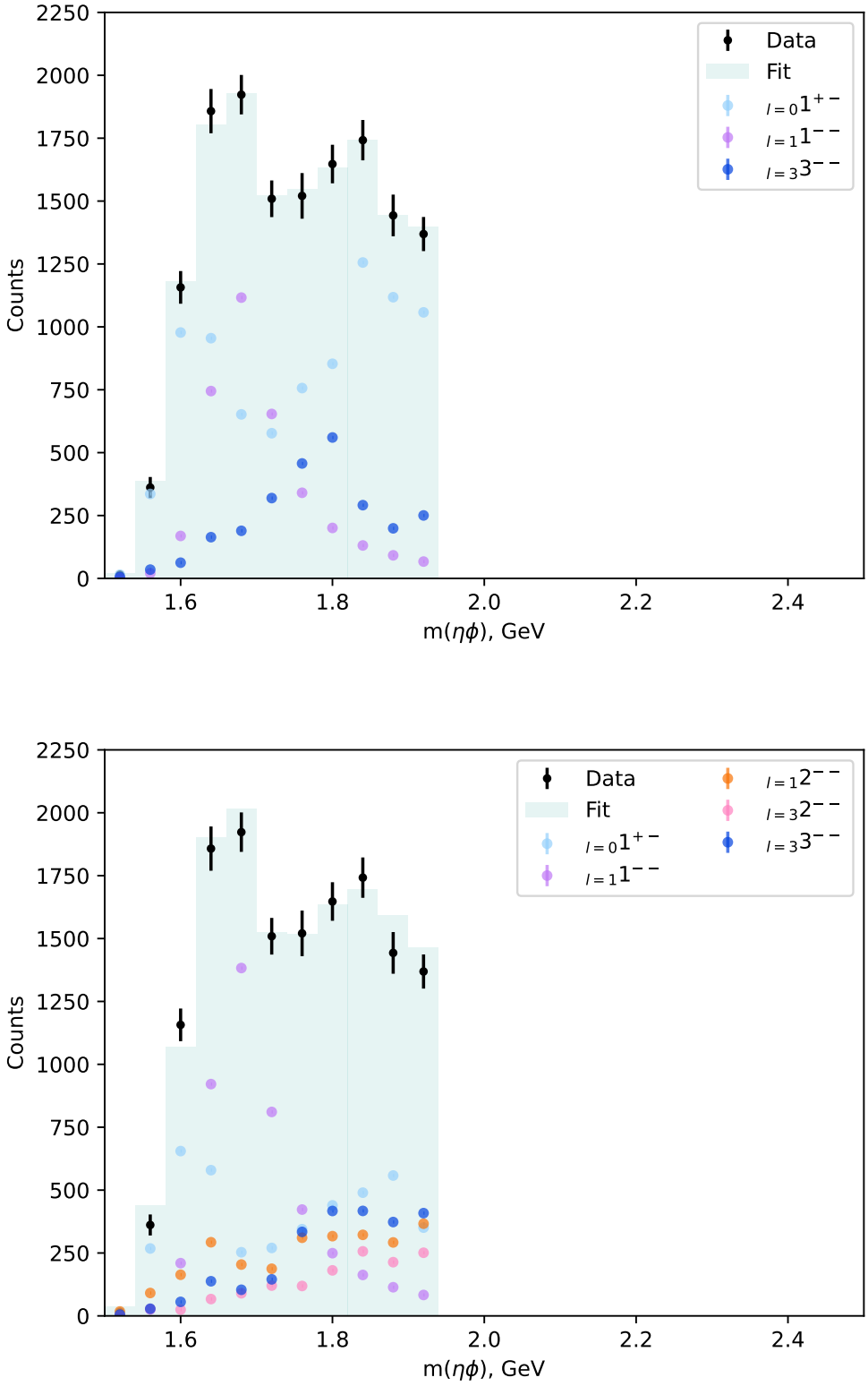

Figure 5.11: Invariant mass spectra for hybrid fits where the 1^{--} amplitudes are constrained with a Breit-Wigner term. The mass of the Breit-Wigners is fixed at 1.68 GeV with a width floating between the PDG uncertainty bounds. The overall results in the invariant mass range chosen look quite close to the mass independent fits qualitatively, though the intensities differ.

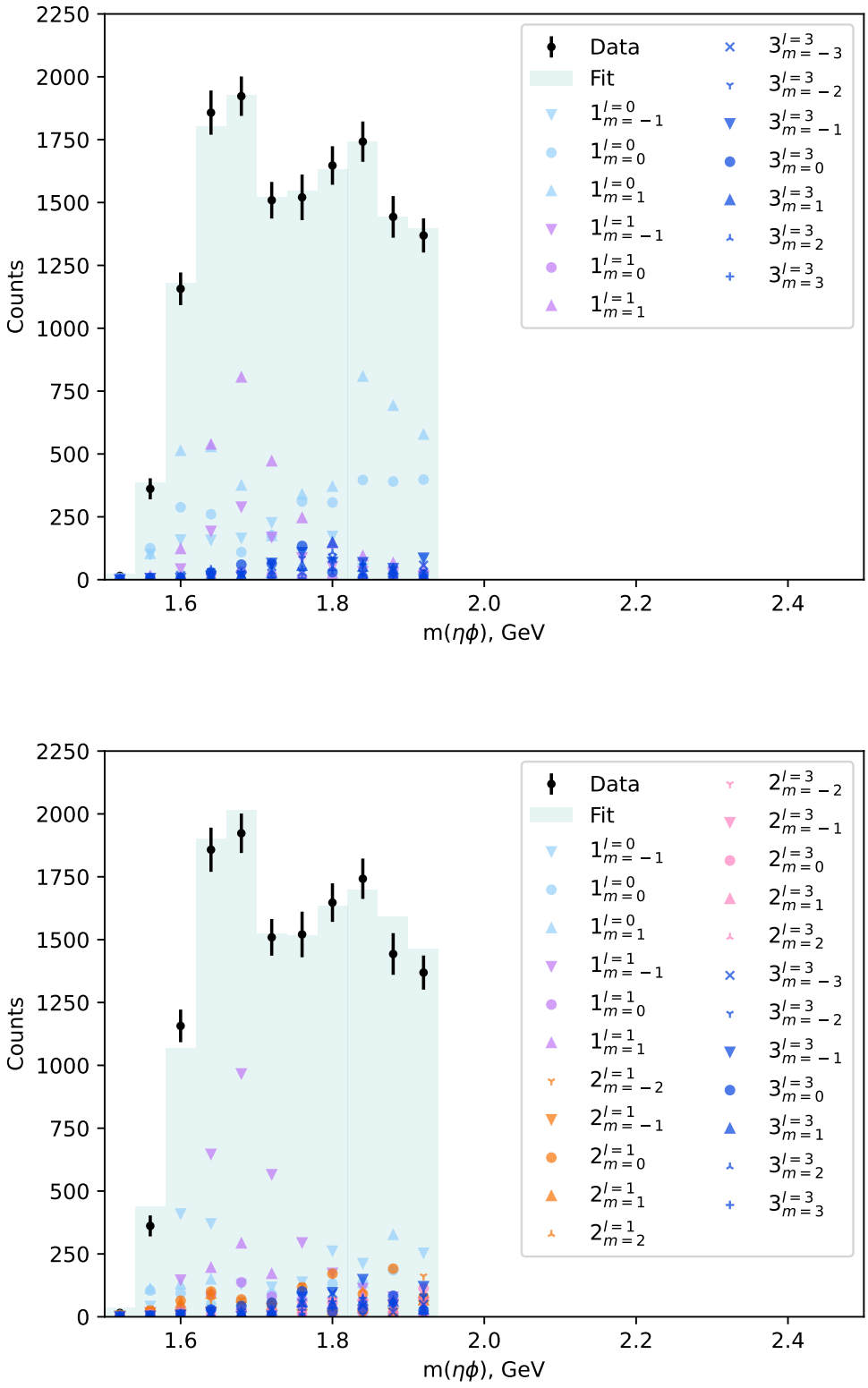

Figure 5.12: Invariant mass spectra for hybrid fits in terms of m-projections where the 1^{--} amplitudes are constrained with a Breit-Wigner term. The mass of the Breit-Wigners is fixed at 1.68 GeV with a width floating between the PDG uncertainty bounds. The overall results in the invariant mass range chosen look quite close to the mass independent fits qualitatively. Both fits feature relatively smooth m-projections.

Table 5.2: The reference waveset selected. Each cell contains the list of chosen m-projections for a given combination of J and L. Both reflectivities were included for all waves.

	J = 1	J = 2	J = 3
L = 0	m = -1, 0, 1	-	-
L = 1	m = 0, 1	m = -2, 1, 0, 1, 2	-
L = 2	-	-	-
L = 3	-	m = -2, 1, 0, 1, 2	m = -2, 1, 0, 1, 2

this is affected by the differences in the practical implementation of the two fit types. Regardless, agreement between the fits would lend credence to results of both and to the assumption that the features presented in the current Section are not spurious. Because they showed consistent signal in the mass independent fits, amplitudes corresponding to the 1^{--} wave are assumed to belong to the $\phi(1680)$ and constrained with Breit-Wigner terms as described previously.

The Breit-Wigner terms in the hybrid intensity may have one of their parameters fixed to further constrain the fit. Although the results for the parameters of the $\phi(1680)$ are equivocal in photoproduction, they are relatively well known for e^+e^- measurements. Based on the form of the invariant mass spectrum and the shape of the 1^{--} partial waves, it can be assumed that the state's mass reported in the PDG is compatible with the current data, and so the following fits have this parameter fixed with the width floating in the PDG's uncertainty range.

The invariant mass projections of the hybrid fits for some wavesets are shown in Figures 5.11 and 5.12. In addition to the fixed mass, the fits are constrained to the range between 1.5 GeV and 1.94 GeV – as the fit has to be performed to the whole data sample at once and the possibility of an interfering 1^{--} resonance in the higher mass region exists, the higher mass bins are excluded for both computational performance and interpretation considerations. Like previously noted the yield of the partial wave projections is no longer constrained on a per-bin basis, which allows the fit to deviate from the data in the invariant mass projections.

The shown projections generally agree with corresponding mass independent fits. The 1^{--} waves are dominant around the first peak, while the S-wave tends to rise in the low mass bins. No particular waves seem to reliably peak around the higher mass structure. The width of the Breit-Wigners varies between 0.1 GeV and 0.15 GeV. The 3^{--} still readily loses intensity to other waves. The m-projection stability appears increased, but this is dependent on the waveset chosen. In the first of the fits shown the projections are stable for all three waves, changing smoothly and continuously throughout the mass range. Larger hybrid wavesets still see some bin-to-bin variations in the S-wave around the second peak, although they are less pronounced than in the mass independent fits. Hybrid fits thus do not suggest any modifications to the nominal waveset selected with a mass independent analysis.

5.3 Input-output studies

Complex models, like the ones used for this partial wave analysis, can show unexpected behaviour when applied to real data. An important step in verifying the validity of the work is testing whether such behaviour also arises in studies of simulated data. One type of commonly performed study is the input-output test – Monte Carlo datasets are produced and treated as if they were real data to assess the performance of the partial wave fits. The basic idea is that if the simulation is produced using some set of partial waves with fixed parameters, then it should be possible to exactly extract those parameters in a fit. Although performing well in these studies is not a guarantee that the model and fitting techniques are fully robust, any issues that arise will flag up potential difficulties in the main analysis.

The expected $\phi(1680)$ and $\phi(1850)$ resonances were simulated. An angular dependence was imposed using the vector-pseudo-scalar amplitudes described in Section 2.2 with the assumption that the $\phi(1680)$ is in a 1^{--} P wave and the $\phi(1850)$ is in a 3^{--} F wave. The mass dependence was parametrised with the Blatt-Weisskopf corrected Breit-Wigner distributions. The Breit-Wigner parameters were taken from the global averages reported by the PDG, except for the width of the $\phi(1680)$ where the lower limit was chosen after comparing MC to data. Although there is some doubt about the precision of these values, the particular numbers chosen should not have a huge impact for the qualitative inferences made in this study. The same cuts as applied to the real data were used, and the photon accidental background is included and then subtracted using sidebands, again as in the real analysis.

The study used the reference waveset described in the previous Section. The generating partial wave parameters were tuned such that relative intensities of the two peaks were approximately equal, similar to the ratio seen in data. The strengths of the amplitudes were also chosen to roughly match the observed individual wave intensities: the 1^{--} m = 0 waves were set to be close to 0, while the 3^{--} amplitudes were all set to be equal to each other. The reflectivity split was chosen to be 50:50, as although positive reflectivity waves were stronger in the exploratory fits, it was not expected that this would have a strong impact on the studies.

The waveset was used to generate three datasets with differing statistics. It was expected that statistical uncertainty may have an effect on the performance of the fits, especially for wavesets with larger numbers of free parameters. The three chosen generated event sample sizes were 6M, 2M, and 200k. Once the full reconstruction and event selection criteria were applied, this corresponded to event sample sizes of approximately 150k, 50k, and 5k events respectively, or about 20x, 2x, and 0.5x the number of signal events below 2 GeV in the real data sample. The invariant mass spectra of the generated data for all the datasets can be seen in the left hand column of Figure 5.13.

Once the datasets were created, they were fit in the same way as the real data. The normalisation integrals were also computed using the same phase space sample as before. The fits were initialised to the nominal values used in the generation of the data where applicable. First, the

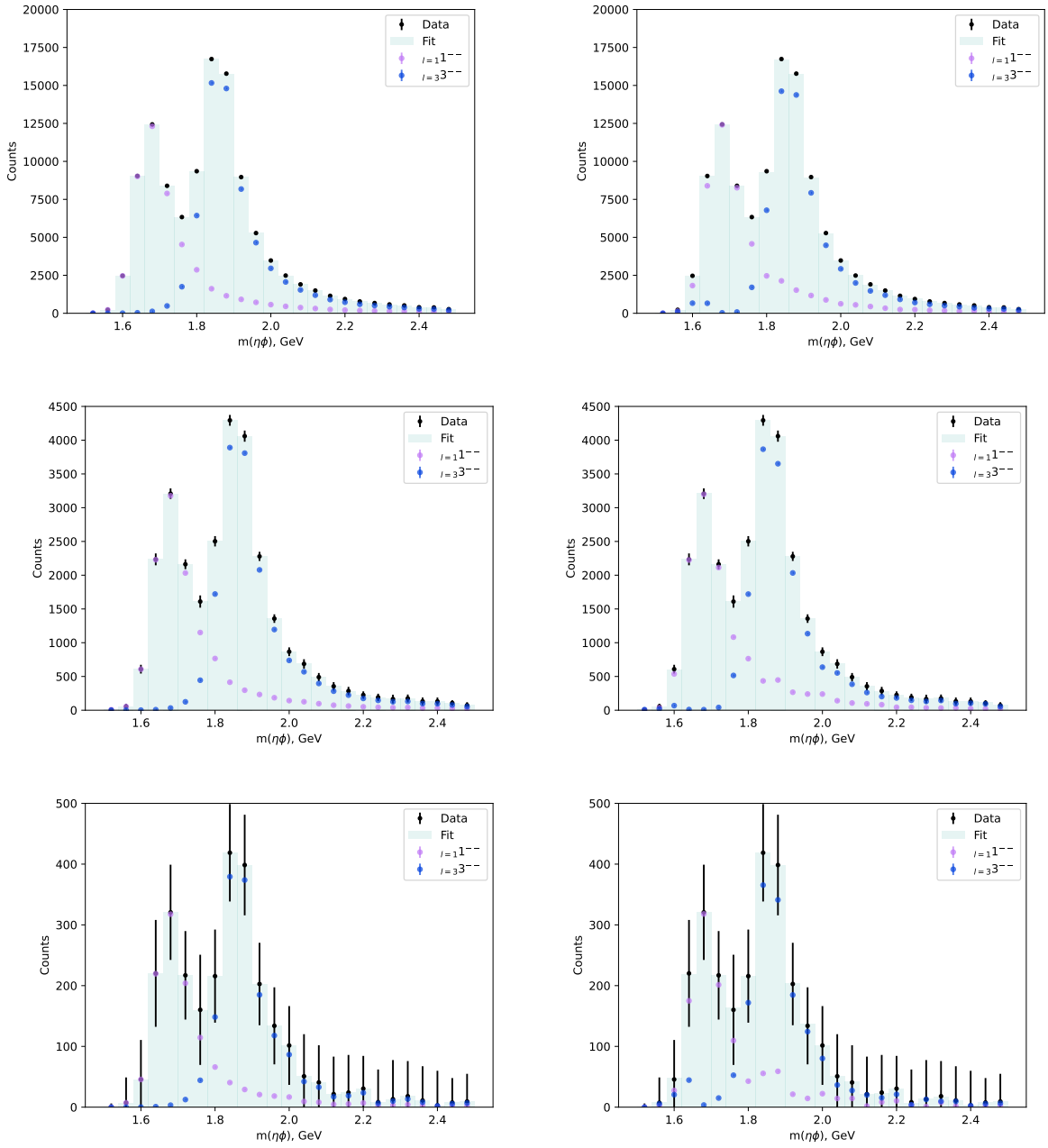

Figure 5.13: The left-hand column shows the invariant mass spectra of the three simulated datasets. All three were generated using the sample resonance parameters and partial wave content, with values taken from the PDG. The right-hand column shows mass independent partial wave fits to the datasets with exactly the true waveset used in the generation. The results show a good match, though it gets worse with decreasing sample size.

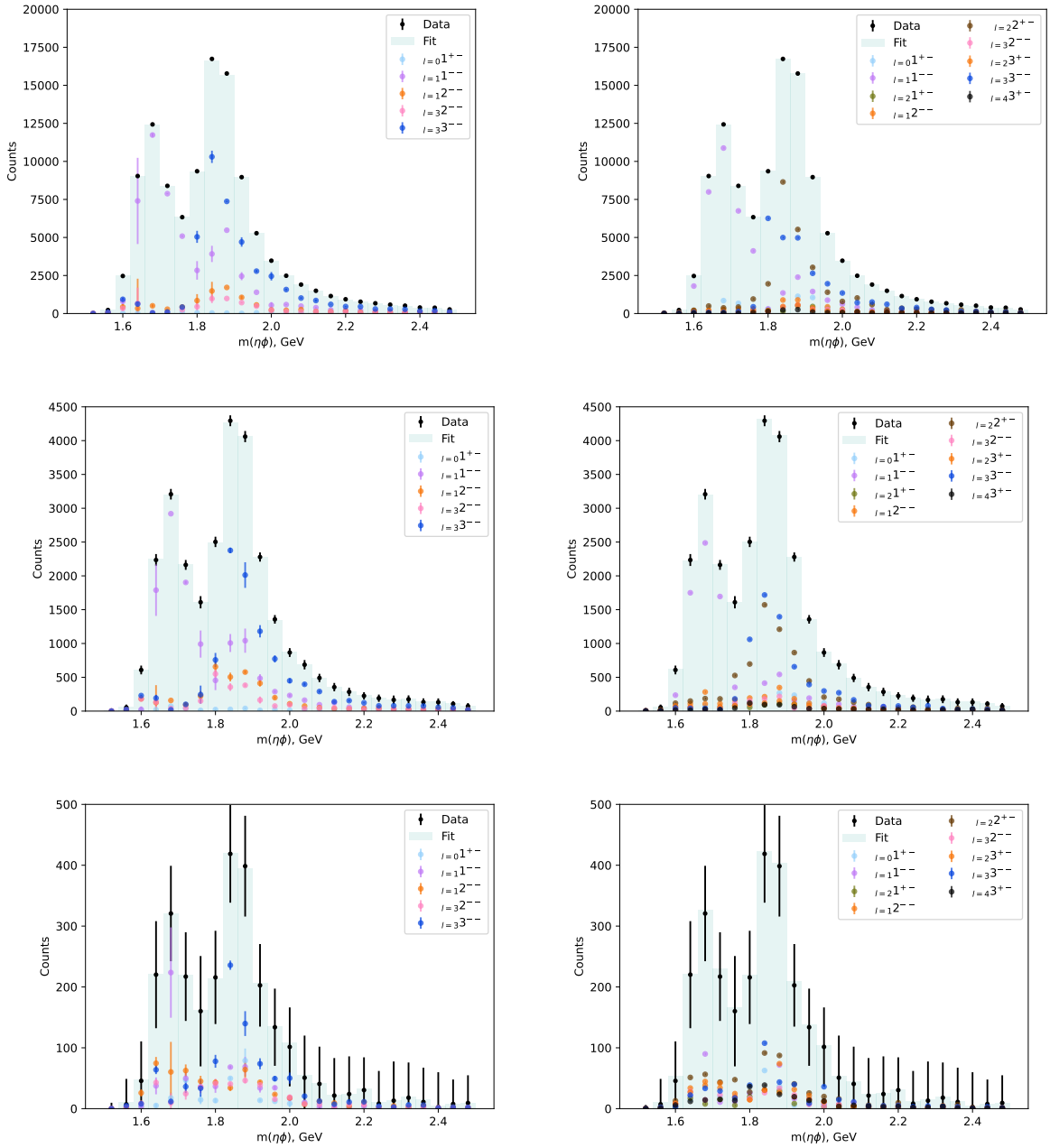

Figure 5.14: Mass independent partial wave fits to the simulated study data with two larger wavesets for all three datasets. The waveset in the left column, with the 1^{+-} and 2^{--} waves included in addition to the waves present in the data, recovers the 1^{--} wave relatively well, but the 3^{--} poorly regardless of statistics. The large waveset also fails the same way in the 3^{--} peak, but also fails to recover the 1^{--} when statistics are low. Error bars on partial waves indicate standard deviation of the top 10 solutions by likelihood.

true generating waveset was used. The right hand column of Figure 5.13 shows the fit results. As expected, wave intensities closely matching the generated MC were recovered for the first two datasets. The small sample size case performed worse, with some intensity from the 1^{--} wave leaking to the 3^{--} wave.

Fits with two larger wavesets are shown in Figure 5.14. The first of these is the reference waveset described in the previous Section, while the other includes all waves up to J = 4. The fits to the former, shown in the left hand column, still reproduced the 1^{--} peak but experienced large leakage from the 3^{--} wave. The fits on the right hand side using the large waveset consistently failed to recover the 3^{--} wave, though managed to do adequately in the first peak when statistics were sufficiently high.

Various amplitude projections were investigated. A comparison of the true waveset and the reference waveset with results separated by m-projections is shown in Figure 5.15. The correct ratios were approximately recovered for the true waveset, with the m = 1 projection dominating for the 1^{--} wave and the 3^{--} amplitudes being equal. The 1^{--} projections were also well recovered for the reference waveset, but the 3^{--} amplitudes deviated from their true values. Figure 5.16 further shows the reflectivity projections for the true waveset. The large and the small datasets saw the ratio of the reflectivities extracted close to the real 50:50 proportion, but the medium case saw higher variation, especially for the 3^{--} amplitudes.

To test whether local minima were present when fitting simulated signal, the standard deviation of the top 10 solutions by likelihood for each fit was computed. In most cases, the solutions were practically identical and would not produce visible differences. Some variation was noticeable when fitting using the reference waveset, visualised as error bars on the corresponding plots in Figures 5.14 and 5.15. This suggests that local minima, when present, are generally clustered closer together than in real data.

Hybrid fits were also performed. The true and reference wavesets were used with the large dataset. Their results are shown in Figure 5.17. Both reproduced the invariant mass spectrum reasonably well, with the reference waveset actually doing better in the first mass peak by filling in the highest statistics bin with the appropriate 1^{--} intensity. It also got considerably closer to the real resonance parameters – a mass of 1.686 GeV and width of 0.11 GeV compared to the true waveset's 1.697 GeV and 0.165 GeV respectively. It is not currently clear why the quality of the wavesets flips compared to the mass independent fits.

There was, however, more variation in local minima when using the reference waveset, as visualised with the error bars in Figure 5.17. This was also true of the Breit-Wigner parameters, with the mass in the reference waveset fit varying from 1.686 GeV to 1.703 GeV while the true waveset varied from 1.692 GeV to 1.697 GeV. The widths in both cases remained approximately constant between minima. The reflectivity and m-projection ratios were reproduced correctly in both cases.

Finally, the AIC and BIC metrics were computed and compared for the three wavesets used

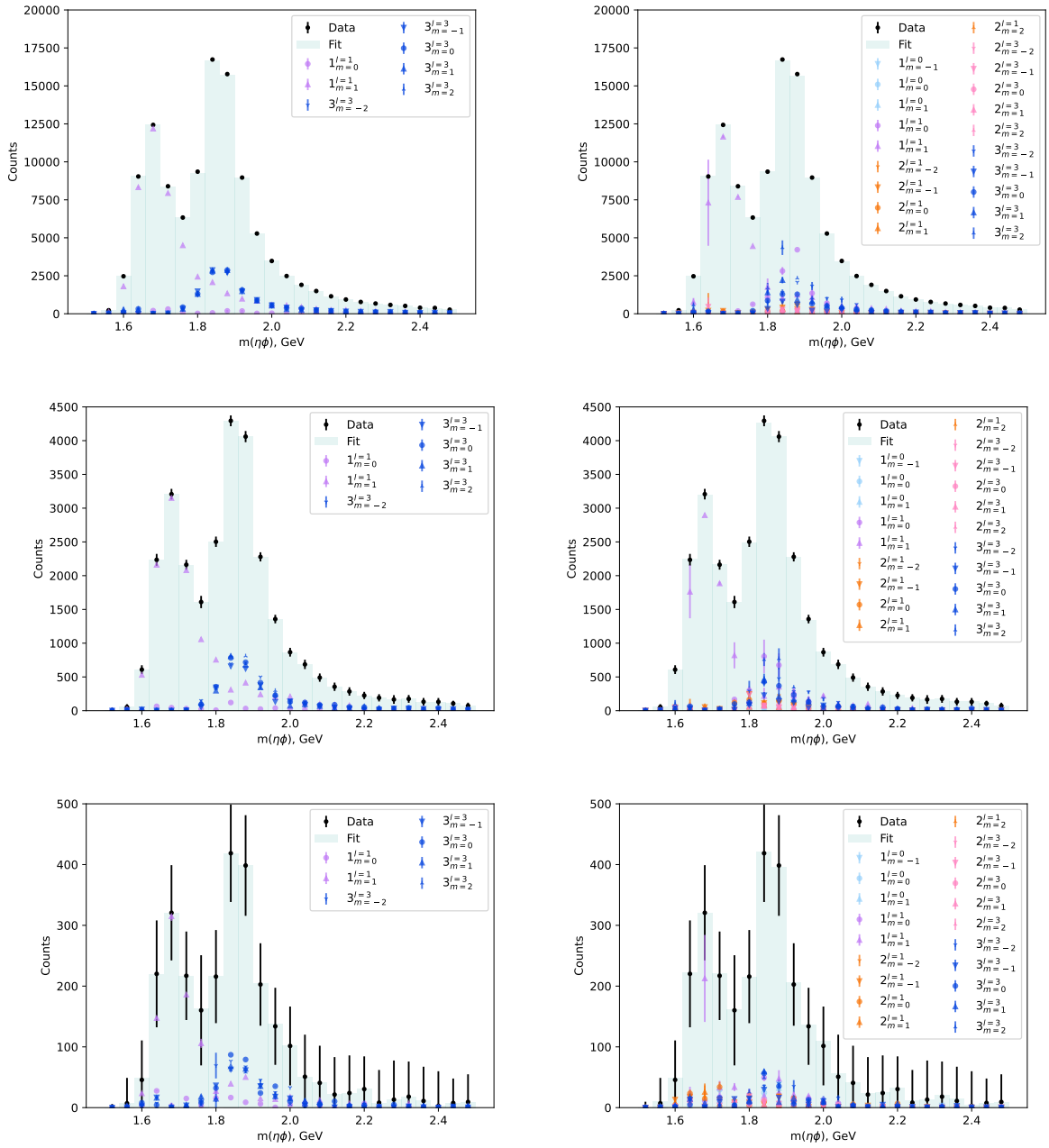

Figure 5.15: Mass independent partial wave fits by m-projection to the simulated study data with two larger wavesets for all three datasets. Both wavesets manage to reproduce the expected amplitudes well.

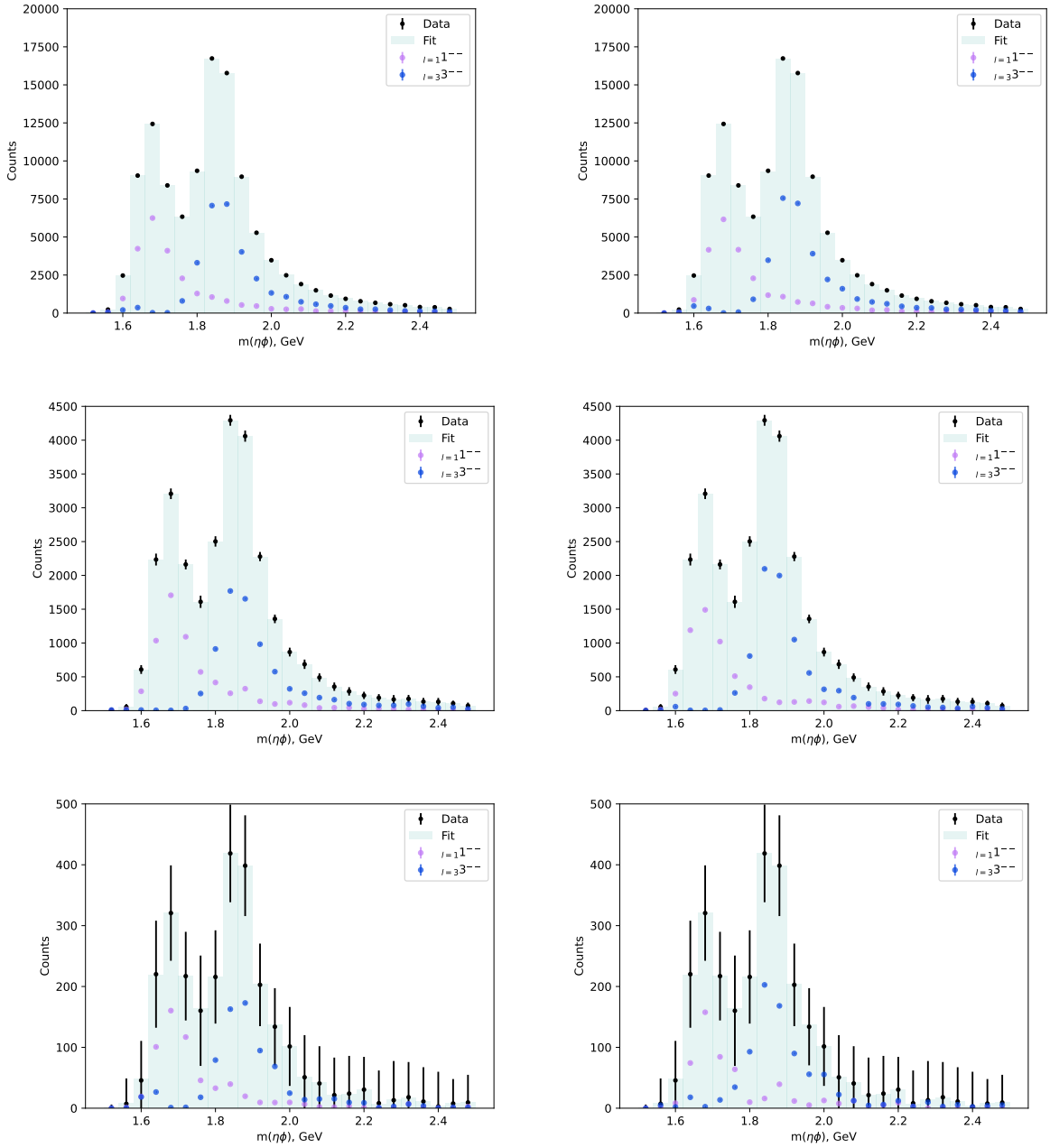

(a) Positive reflectivity.

(b) Negative reflectivity.

Figure 5.16: Mass independent partial wave fits by m-projection and reflectivity to the simulated study data with the true waveset for all three datasets. Both wavesets manage to reproduce the 50:50 split of reflectivities well when statistics are high, but start to see fairly significant deviations in the second mass peak for the two smaller datasets.

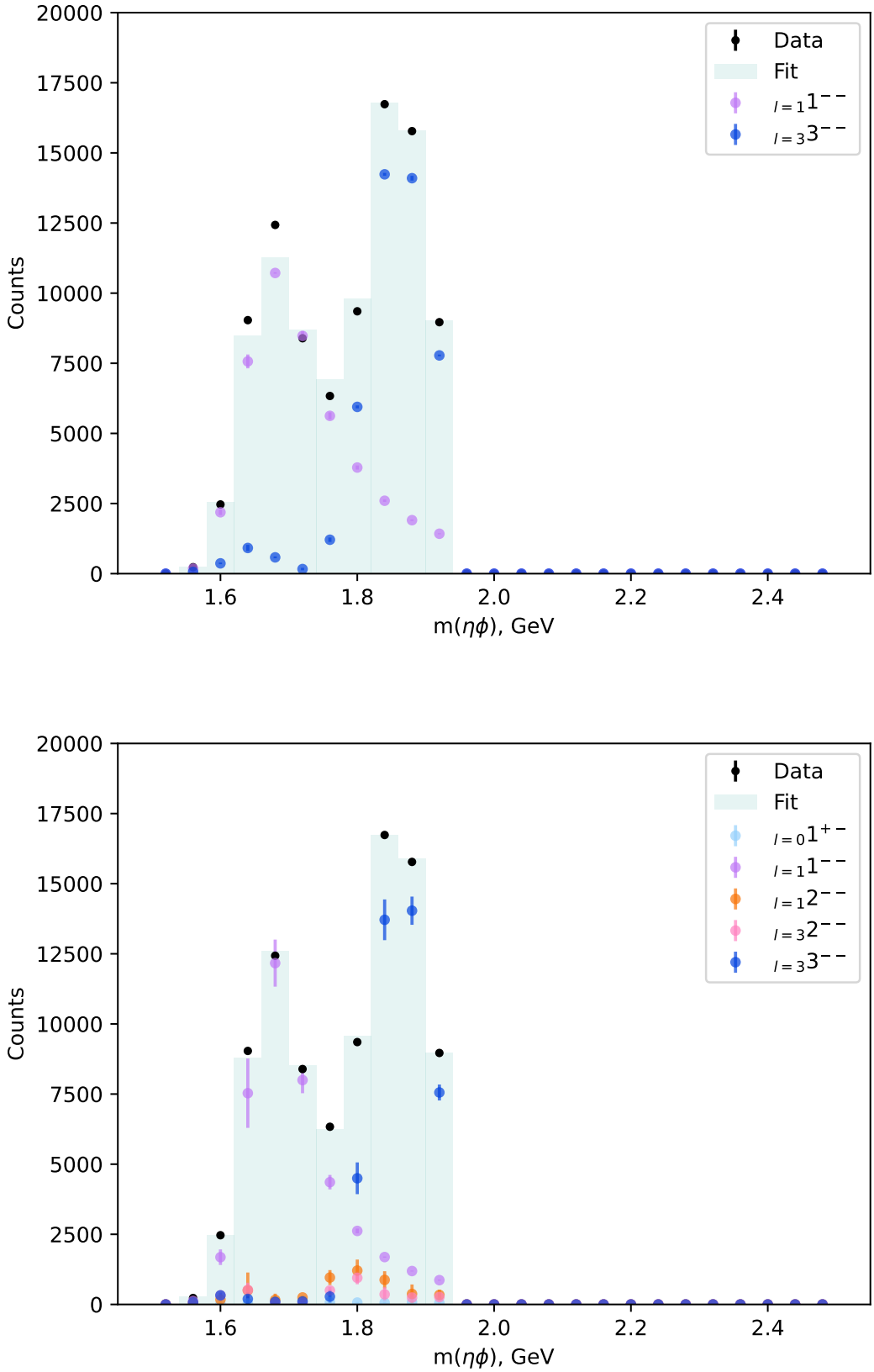

Figure 5.17: Hybrid fits to the large simulated dataset using the true and the reference wavesets. Both reproduce the invariant mass spectrum relatively well, though the first mass peak is underestimated. The reference waveset performs better than the true waveset, contrary to what is seen in mass independent fits. Error bars on partial waves indicate standard deviation of the top 10 solutions by likelihood.

in the input-output studies. Both criteria exhibited very similar lineshapes over the mass range. They followed the expected order for all three datasets, with the true waveset being preferred to the other two, and the reference waveset being preferred to the waveset with all waves up to J = 3. This was consistent for all mass bins, shown in Figure 5.18 for the large dataset.

The input-output studies indicate that partial wave fits to Monte Carlo data in the presence of resolution and detector effects are not always able to recover the true parameters for the amplitudes used to generate the data. The ability to do so depends on both the partial waves used in the generation and the waveset used to fit the simulated data. The 3^{--} resonance seems somewhat more susceptible to leaking intensity to other waves, especially when a number of higher momentum amplitudes are included, but the 1^{--} resonance eventually suffers from the same phenomenon. Individual properties, such as reflectivities, are usually recovered accurately. The AIC and BIC model selection criteria function as expected, with the wavesets closer to the data generating process being preferred. As in data fits, the hybrid and mass independent fit results are similar.

This Chapter covered the exploratory data analysis that was required to decide on the nominal waveset and the associated challenges. The analysis of fits to real data showed that a 1^{--} component seems to be dominant in the mass peak around 1.68 GeV, while no clear structures could be discerned at higher mass. No obvious signs of a 3^{--} resonance or a $\phi(2170)$ signal were observed. The coherent sums over the m-projections and reflectivities that represent the waves denoted by the J^{PC} notation seem continuous and relatively stable over the mass range, though the individual m-projections were not always so. Although model selection techniques did not indicate that any particular waveset should be preferred, the exploratory analysis allowed the selection of a model that describes the angular distributions well in all mass bins of interest and incorporates expected physics. The input-output study on simulated data showed that it was able to reproduce the signal well when the waveset used in fitting was identical to the generator model, but could sometimes fail if that was not the case. The following Chapter will present the results of fits using the nominal waveset.

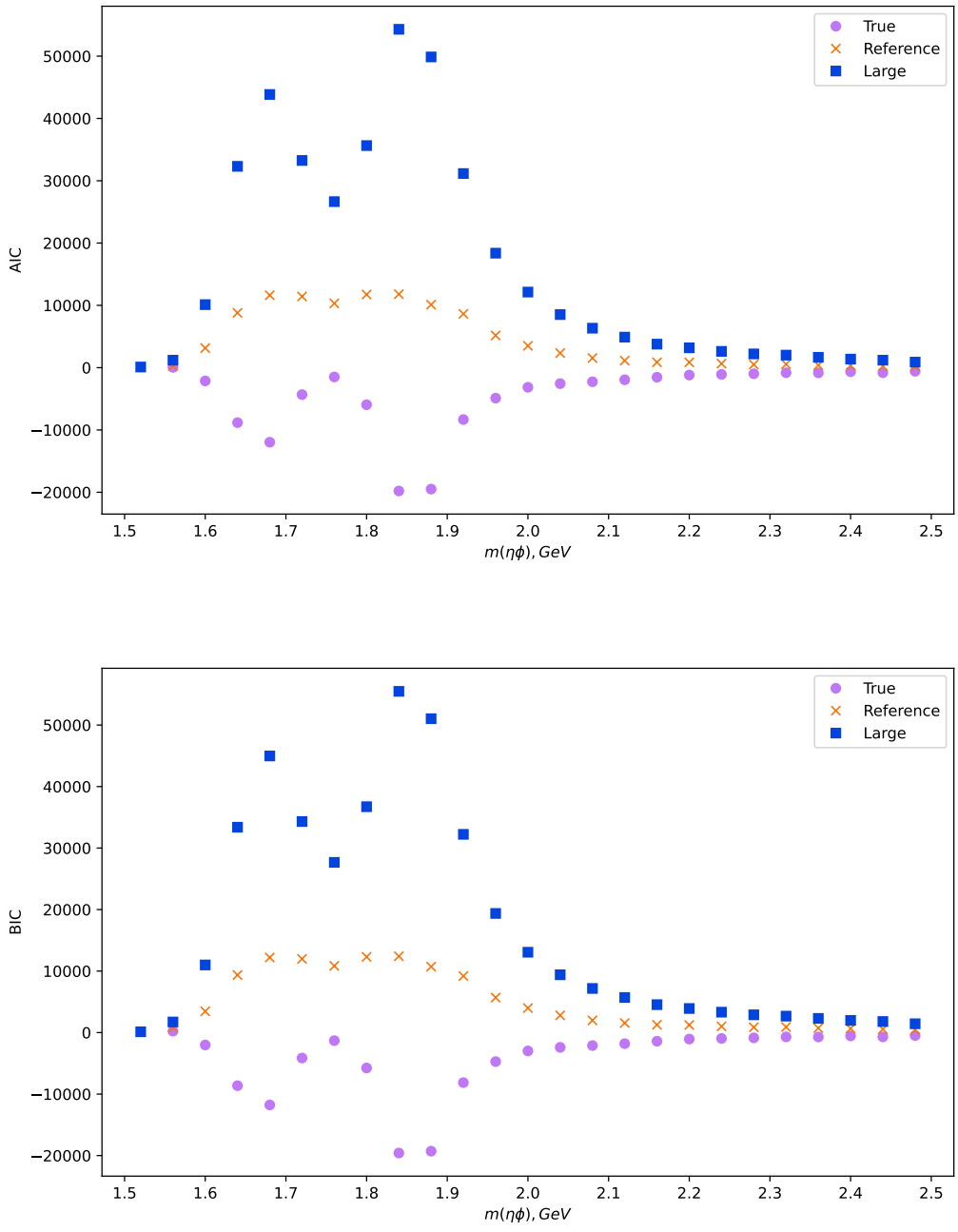

Figure 5.18: The AIC and the BIC metrics for the three wavesets tested in the input-output studies – lower is better. Both criteria show the same trend and the expected ordering of models. The true waveset did best through the mass range, with less similar wavesets doing worse.

Chapter 6

Results

The final results of the partial wave analysis for the nominal waveset described in the previous Chapter are presented below. Section 6.1 presents the fit projections for a number of variables of interest, such as invariant mass and the angular decay distributions in different mass bins. Section 6.2 discusses what information about resonance content can be obtained from the phase motion of the partial wave amplitudes. Section 6.3 contains the extraction of Breit-Wigner resonance parameters for the state identified as the $\phi(1680)$ from both mass independent and hybrid fits; the mass dependent cross-section for the same state is obtained in Section 6.4.

6.1 Projections of the partial wave fits

The invariant mass projection for the nominal waveset is shown in Figure 6.1a, while Figure 6.1b contains the spectrum after acceptance correction has been performed. Primary features observed in the exploratory fits of Subsection 5.2.1 are present: the 1^{--} wave peaks strongly around 1.68 GeV, but no obvious dominance of any individual wave can be determined around the higher mass structure at 1.85 GeV. Though some of the waves, e.g. the 1^{+-}, appear to peak there, it must be remembered that the extended likelihood formulation constrains the per-bin yield. This means that if the invariant mass spectrum contains an enhancement, then some combination of the partial waves must reproduce that. Even if resonances are not present in the data, we would still expect waves around a peak to rise in unison within statistical uncertainty. This is consistent with the results.

Figure 6.2 shows the angular distributions for the two mass bins that cover the peaks of the $\phi(1680)$ and $\phi_3(1850)$ resonances reported by the PDG. All of the distributions are reproduced well within statistical uncertainty in both bins. Angular plots for the other mass bins up to 2.02 GeV can be found in Appendix E. Looking at the acceptance corrected invariant mass spectrum separated by m-projection in Figure 6.3, results are again consistent with previous fits – for the 1^{--} wave, the m = 1 projection is dominant while other waves do not show any strong patterns. Figure 6.4 contains the acceptance corrected invariant mass spectrum separated by

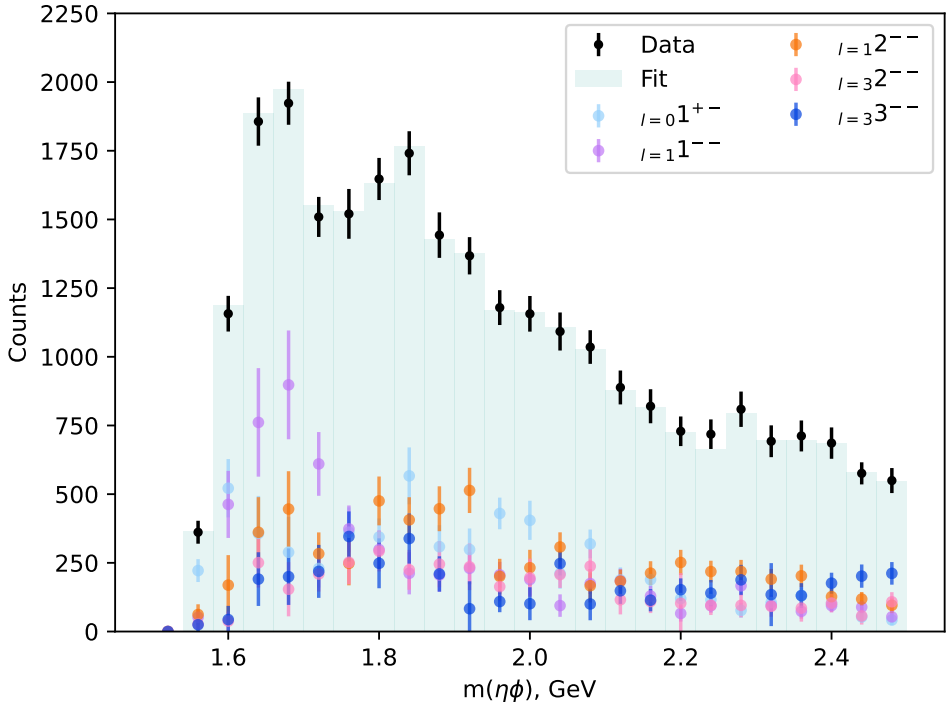

(a) Without acceptance correction.

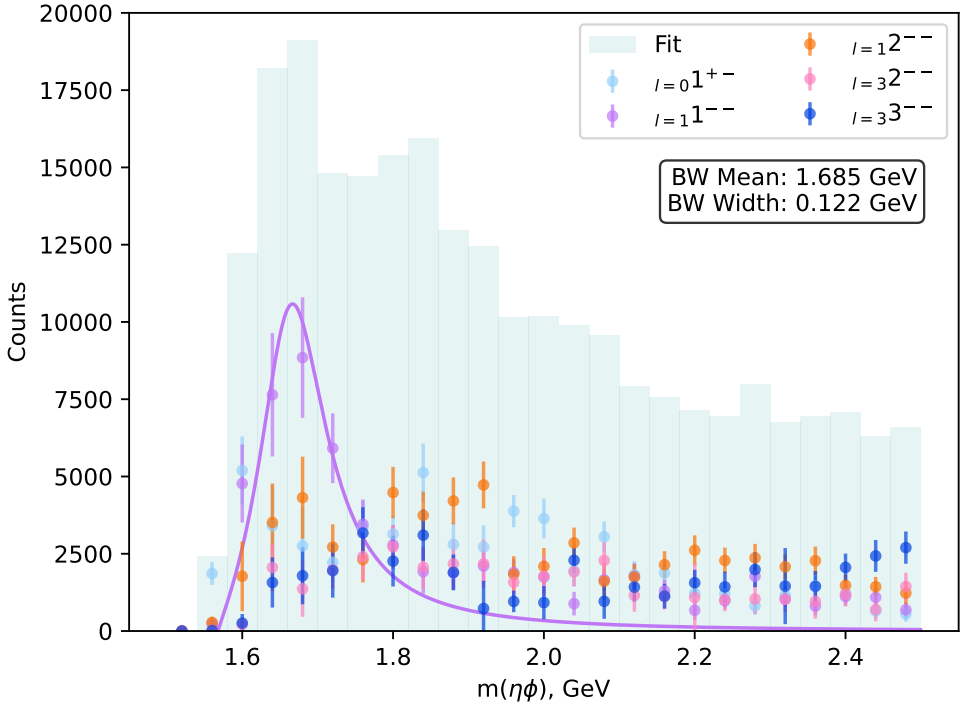

(b) With acceptance correction.

Figure 6.1: Observed and acceptance corrected $\eta\phi$ invariant mass spectra obtained from mass independent fits of the nominal waveset. The 1^{--} wave is dominant around the first peak in the spectrum and is identified as the $\phi(1680)$. The Breit-Wigner obtained from fitting to the 1^{--} intensity is superimposed on the acceptance corrected plot.

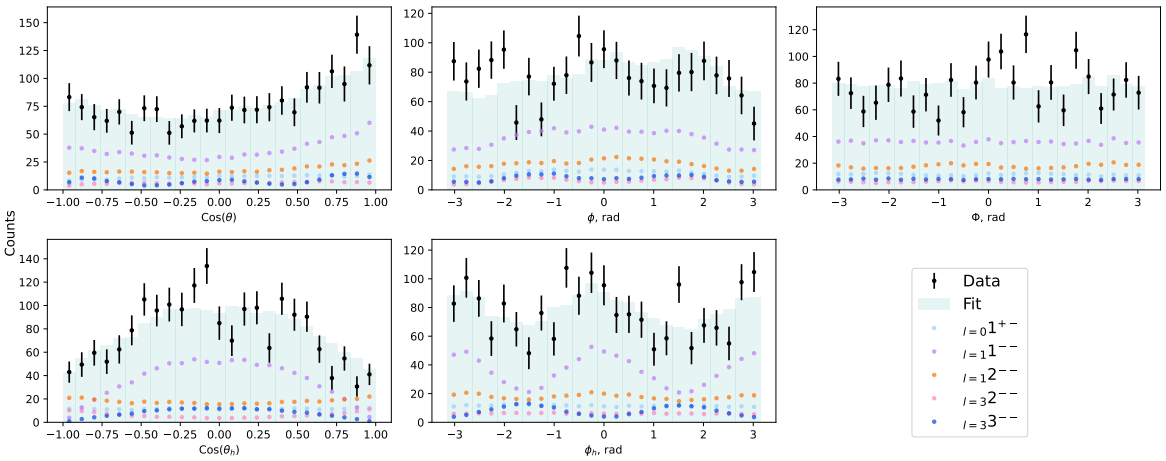

(a) Mass bin 1.66 GeV - 1.7 GeV.

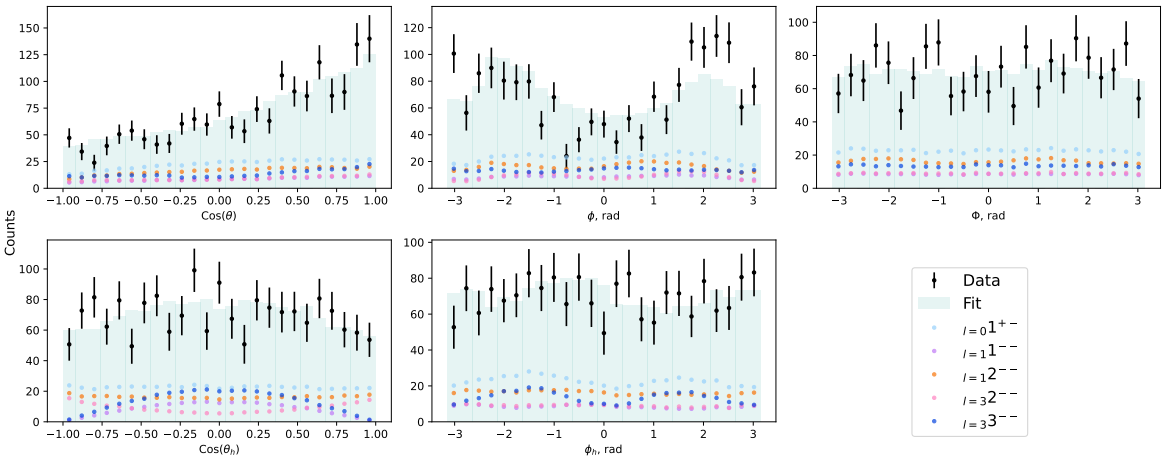

(b) Mass bin 1.82 GeV - 1.86 GeV.

Figure 6.2: The angular distributions for the $\eta\phi$ invariant mass bins 1.66 GeV - 1.7 GeV (a) and 1.82 GeV - 1.86 GeV (b). All distributions are generally reproduced well within uncertainty.

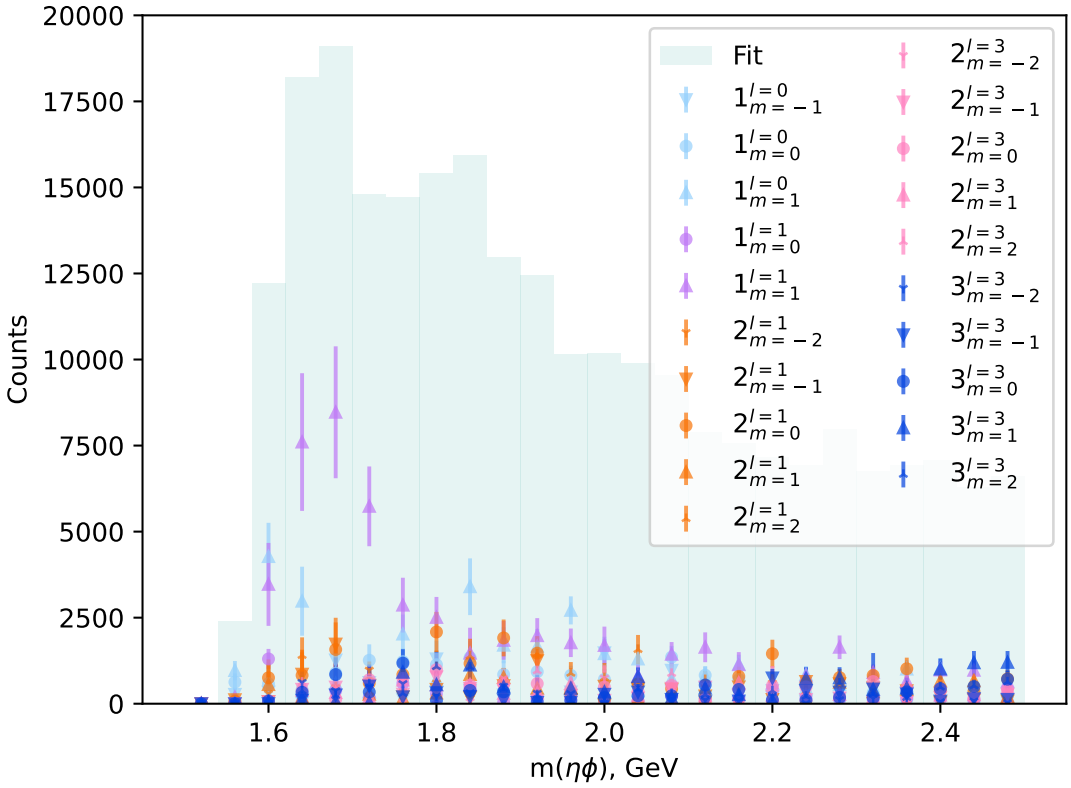

Figure 6.3: The acceptance corrected $\eta\phi$ invariant mass spectrum with amplitudes separated by m-projection for the nominal waveset. As with other wavesets, the m = 1 projection is dominant in the 1^{--} wave, but no strong patterns are obvious in the other waves.

reflectivity. There is a strong bias for the 1^{--} amplitudes towards positive reflectivity at a ratio of approximately 75:25, yet again agreeing with results from other wavesets. This may indicate a preference for natural exchange in the production mechanism.

The same cross-check of the mass independent fit as before is done by performing a hybrid fit with the nominal waveset. The invariant mass spectra from this fit are shown in Figure 6.5. Like before, the 1^{--} amplitudes are constrained using Breit-Wigner terms while the other waves are implemented as piecewise mass independent amplitudes. To reduce the influence of local minima on the results, the first fit iteration was initialised using the fit parameters obtained from the mass independent fit. The Breit-Wigner parameters were left floating within limits of 1.68 GeV - 1.72 GeV for the mass and 0.1 GeV - 0.2 GeV for the width. As expected, the 1^{--} wave is dominant around the first peak while amplitudes around the second peak share comparable fractions of the total intensity. The fit reproduces the spectrum well and generally agrees with the mass independent fit, although there is a discrepancy in the intensities of the 1^{--} wave that are discussed as part of the systematic studies in Chapter 7.

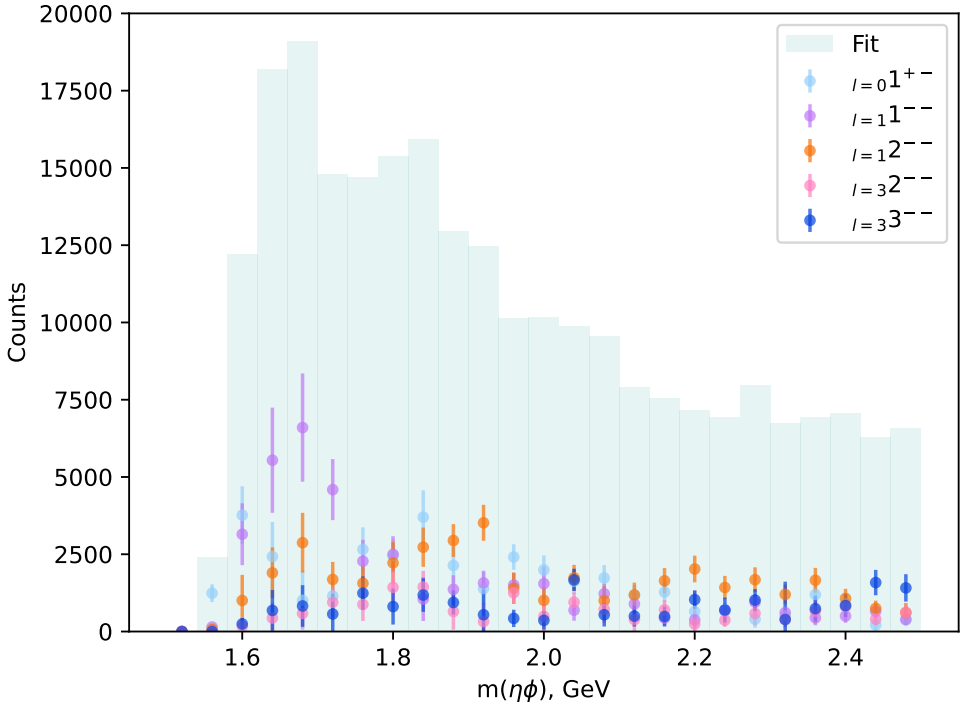

(a) Positive reflectivity.

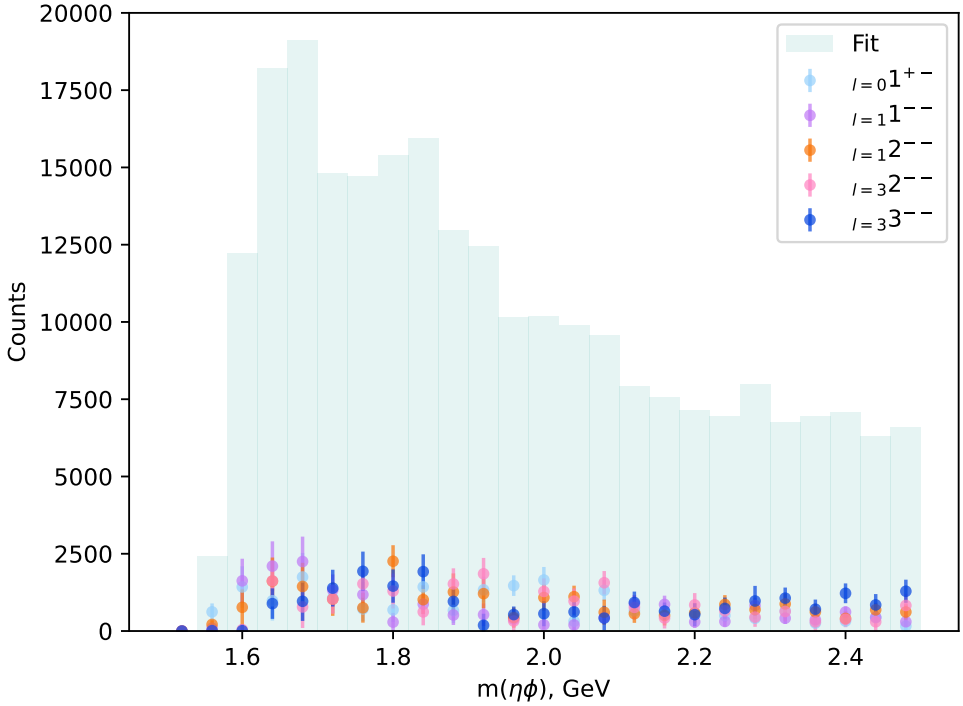

(b) Negative reflectivity.

Figure 6.4: Acceptance corrected $\eta\phi$ invariant mass spectra separated by positive (a) and negative (b) reflectivity for the nominal waveset. The positive reflectivity 1^{--} wave is dominant, with approximately three times the intensity of the negative reflectivity. This may indicate preference for natural exchange production in the $\phi(1680)$.

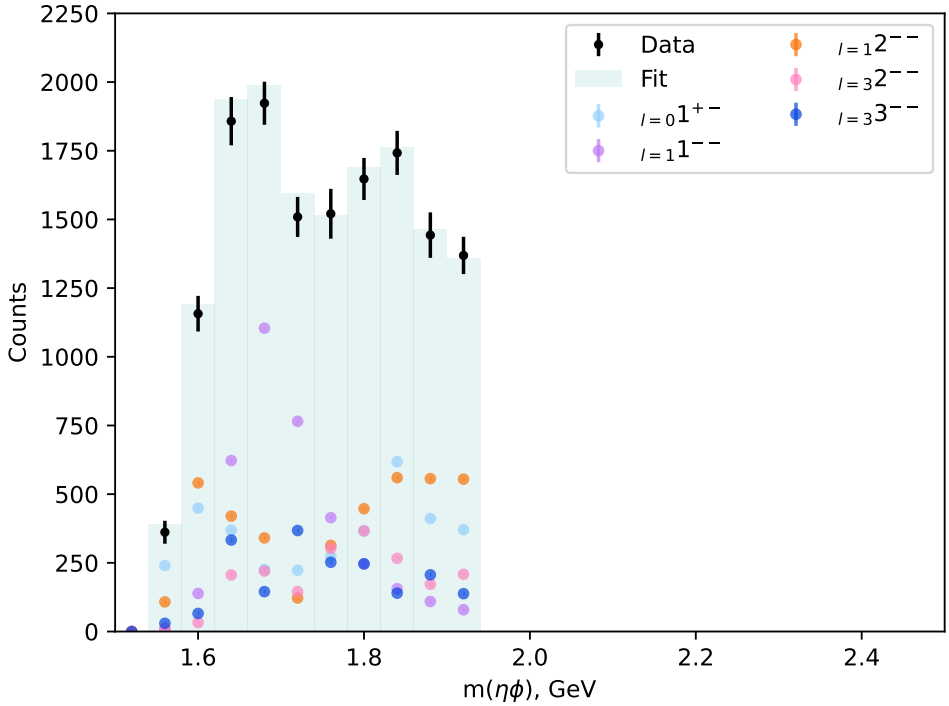

(a) Without acceptance correction.

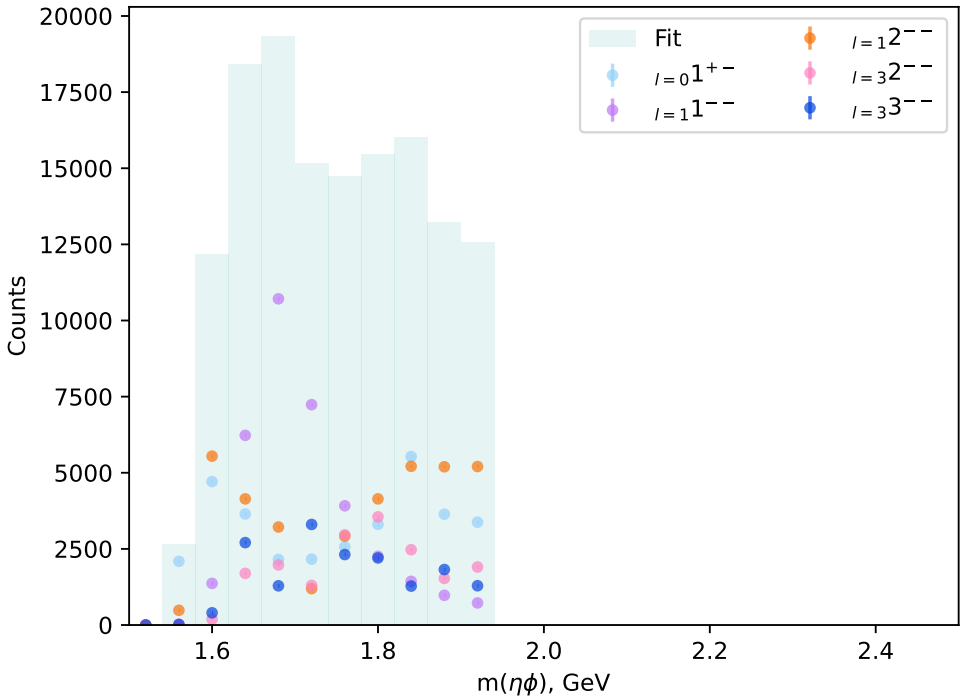

(b) With acceptance correction.

Figure 6.5: The observed (a) and acceptance corrected (b) $\eta\phi$ invariant mass spectra for a hybrid fit using the nominal waveset, with the 1^{--} amplitudes constrained with Breit-Wigner terms. The spectrum is reproduced well and the obtained amplitudes are very similar to the mass independent fit, though intensity in the 1^{--} wave is higher. Statistical uncertainty not shown.

6.2 Phase and phase motion

The complex partial wave amplitudes, as any complex number, can be written in terms of a magnitude and a phase factor. A choice of an arbitrary global phase has to be made in order to uniquely fix all phases in the fit – in fact, the actual observable quantity is the difference of two phases. The conventional choice is to set a reference wave to have zero phase, i.e. have a purely real coefficient. In the reflectivity model, this has to be done for both a positive and a negative reflectivity wave, as the two sets of amplitudes do not interfere with each other. Motion in the phase differences between two waves can provide evidence for the existence of resonant behaviour. If an enhancement in the invariant mass spectrum is caused by a resonance, one would expect the phase of the amplitudes of the resonance to undergo a shift from -90° to 90° with respect to a non-resonant amplitude over the width of the resonance. The crossing point at 0° will coincide with the resonance peak.

Difficulties can arise when trying to interpret phase differences. First, one must decide which pairs of waves to take the phase difference of – although waves are often spoken about in terms of integration over m-projections and reflectivities and projection of the resulting J^{PC} components, the phases are only defined for the individual amplitudes. Based on the fits analysed in Chapter 5, it is assumed that resonances in the 1^{--} wave would be present in either the m = 1 or m = -1 projections in the positive reflectivity. As the latter is not included in the nominal waveset, the m = 1 amplitude is chosen. Regardless of the waves used to compute the phase difference, it is not trivial to deduce what kind of motion is present. Figure 6.6 contains plots for the phase difference between the 1^{--}, m = 1 wave and two other select amplitudes. Both the nominal phase differences obtained from the fits and their negative are shown in different colours to account for discrete ambiguities arising from complex conjugation – as both solutions are valid, both must be visualised. Red curves show an example of what phase motion could be expected in case of a resonance.

Focusing on the mass region from 1.5 GeV to 2 GeV where the $\phi(1680)$ and $\phi_3(1850)$ are expected, hints of resonant phase motion can be seen in some of the subplots. For example, phase differences in Figures 6.6b and 6.6c come close to crossing through 0 at 1.85 GeV, while the outlines of the phase movement in Figures 6.6b and 6.6d look reminiscent of motion that would be produced by a resonance around 1.7 GeV if the phase difference did not jump discontinuously. Such bin-to-bin jumps are especially obvious in 6.6b, where every other bin until 1.85 GeV differs by about 0.7 rad. One could imagine that if these jumps did not happen, or happened in the opposite direction, i.e. instead of moving up the phase difference stayed constrained below 0.4 rad, a fairly smooth resonant signature could be recovered. It can be assumed that this behaviour has similar causes to the e.g. variation in partial wave intensity due to local minima. Study of phase motion thus remains inconclusive for the moment, with it not being incompatible with a resonance between 1.6 GeV and 1.7 GeV but not providing strong positive evidence.

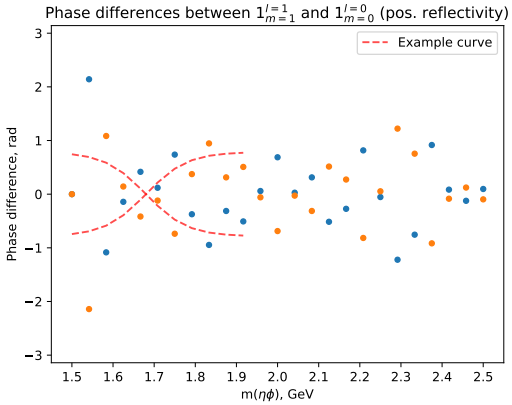

(a) Phase motion of J = 1, L = 1, m = 1 amplitude versus J = 1, L = 0, m = 0 amplitude, positive reflectivity.

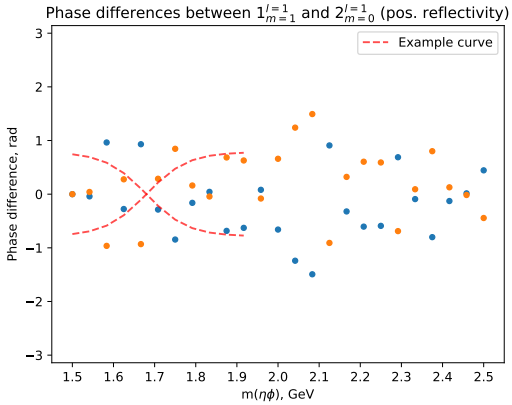

(b) Phase motion of J = 1, L = 1, m = 1 amplitude versus J = 2, L = 1, m = 0 amplitude, positive reflectivity.

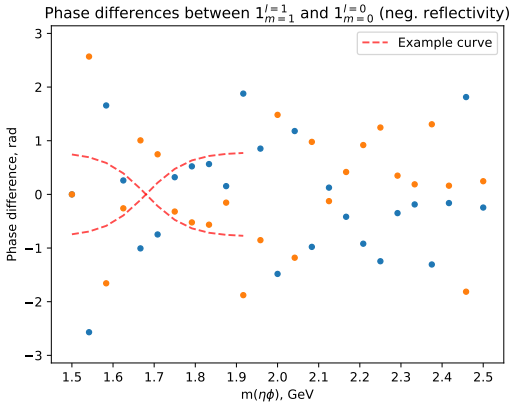

(c) Phase motion of J = 1, L = 1, m = 1 amplitude versus J = 1, L = 0, m = 0 amplitude, negative reflectivity.

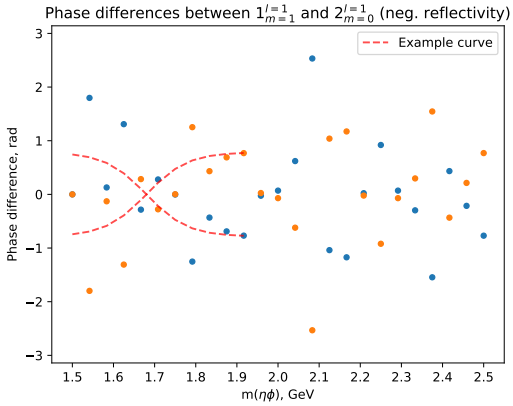

(d) Phase motion of J = 1, L = 1, m = 1 amplitude versus J = 2, L = 1, m = 0 amplitude, negative reflectivity.

Figure 6.6: Plots of phase differences between 1^{--} m = 1 amplitude and (a,c) 1^{+-}, m = 0, (b,d) 2^{--}, m = 1 amplitudes. The top row subplots are for positive reflectivity amplitudes while the bottom row is for negative reflectivity amplitudes. Both the nominal phase difference and its conjugate are plotted, in blue and orange respectively. The red curves demonstrate an example of resonant behaviour. Some potential phase motion might be seen, but discontinuous bin-to-bin jumps prevent strong inferences.

6.3 Breit-Wigner parameters

The partial wave fits strongly indicate that a 1^{--} wave is dominant around the peaking structure at 1.68 GeV. Although evidence from the phase motion is somewhat ambiguous, it is unlikely that the stability of the 1^{--} amplitudes is an unphysical artefact. The wave is thus identified as the $\phi(1680)$ and its mass and width can be obtained from the fit results. These parameters can be extracted from both the hybrid and the mass independent fits. In the former case, there is no more work to do as they are obtained during the fit itself. To obtain the parameters from the mass independent fit, a binned maximum likelihood fit is performed to the acceptance corrected invariant mass distribution. The fit uses a relativistic Breit-Wigner distribution with a Blatt-Weisskopf barrier factor for $L = 1$ [166]. The mass was allowed to float between 1.66 GeV - 1.72 GeV

and the width between 0.1 GeV - 0.2 GeV. The resulting Breit-Wigner is superimposed on the acceptance corrected mass spectrum in Figure 6.1b.

Only the first 11 invariant mass bins were used to find the BW parameters. Their optimal values depend on the range of the fit. The intensity of the 1^{--} wave never goes to 0 in the mass independent fit, even in very high mass bins that are far outwith the expected range of the $\phi(1680)$. This could be caused by either unphysical intensity leakage from other waves in the fit or by a different 1^{--} resonance, e.g. the $\phi(2170)$, contributing. Regardless of reason, the same range of 1.5 GeV - 1.94 GeV as in the hybrid fits is used to eliminate the influence of the unrelated 1^{--} contributions. The mass is found to be 1.685 GeV $\pm$0.02 stat. $^{+0.008}_{-0.014}$ syst. and the width 0.122 GeV $\pm$0.028 stat. $\pm$ 0.037 syst.. These are compatible with both the global PDG average and the e^+e^- measurements. The mass and width of the 1^{--} Breit-Wigner obtained in the hybrid fit are similar at 1.69 GeV and 0.11 GeV respectively. Agreement between the two types of fit is good and well within uncertainty. No evidence is found to support the previous findings by photoproduction experiments that put the mass above 1.7 GeV.

6.4 Mass-dependent cross-section

Once the Breit-Wigners have been fit to the invariant mass distribution, the cross-section can be extracted. It is computed as follows:

$$\frac{d\sigma}{dm} = \frac{N_{obs}}{\varepsilon} \frac{1}{\mathscr{L}\mathscr{B}(\phi \to K^+K^-)\mathscr{B}(\eta \to \gamma\gamma)\Delta m} \tag{6.1}$$

Here N_{obs} is the observed number of events, ε is the acceptance factor, $\mathscr{B}(A \to B)$ is a branching ratio in the decay of A to B, $\mathscr{L}$ is the integrated luminosity of the dataset, and Δm is the mass bin width. The acceptance corrected yield is obtained from the fit Breit-Wigners; of the remaining terms, the luminosity is known and the ϕ and η branching fractions are available from the PDG, having been previously measured to a high precision.

As for the resonance parameters, the cross-section can be obtained from either the hybrid or the mass independent fits. The latter were used to obtain the nominal values for this measurement, as more study is still needed to properly understand the behaviour of hybrid fits. The results are shown in Figure 6.7. The mass dependent cross-section can be integrated to get the total $\eta\phi$ cross-section, which was calculated to be 35.7 nb $\pm$3.79 stat. $^{+10.01}_{-11.29}$ syst.. If the branching ratio $\mathscr{B}(\phi(1680) \to \eta\phi)$ is added to the calculation in Eq.(6.1), the cross-section for $\phi(1680)$ can be computed in addition. This branching fraction is not well known – the one reported measurement referenced in Chapter 1 gives it at around 20%, but this has not yet been corroborated. As this is just a single factor it is trivial to include, but based on the error analysis presented in the original paper can be assumed to have a relative systematic uncertainty of around 50% – see the following Chapter for a discussion. The value without it included will

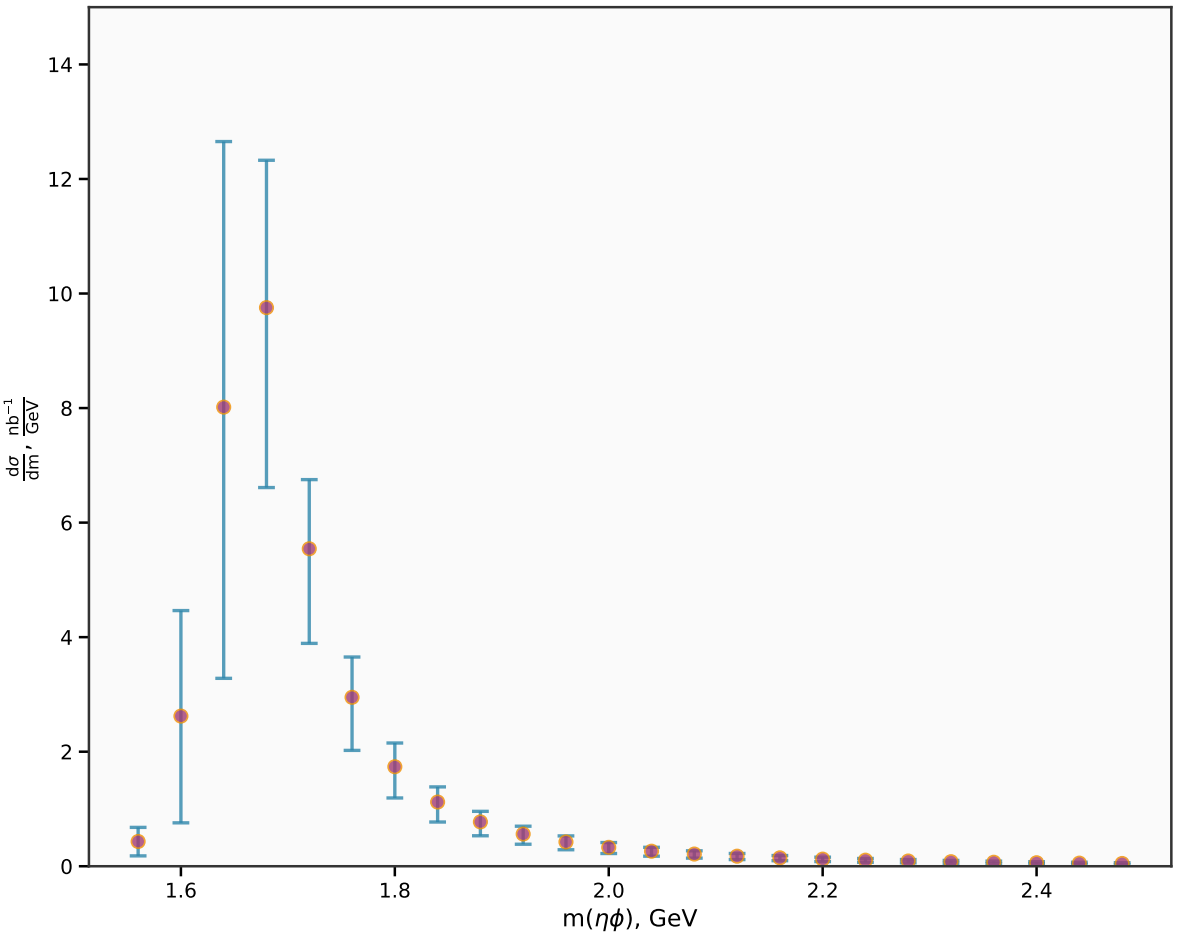

Figure 6.7: The mass dependent cross-section for the $\eta\phi$ final state. Error bars indicate combined statistical and systematic uncertainties. The cross-section for $\phi(1680)$ can be obtained from this curve by dividing through by the branching ratio $\mathscr{B}(\phi(1680) \to \eta\phi)$.

hence be more precise but will only provide a cross-section for this particular final state. The total integrated cross-section with the branching ratio is 178 nb $\pm$19 stat. $^{+102}_{-106}$ syst..

Numerical results in the form of Breit-Wigner parameters and a mass dependent cross-section have been extracted for the state provisionally identified as the $\phi(1680)$. These are collated in Table 6.1. The full list of values for $\frac{d\sigma}{dm}$ is tabulated in Appendix F. The way that systematic uncertainties have been obtained on the measurements will now be discussed in Chapter 7. Further discussion of how to interpret these results beyond the brief remarks already made will be found in Chapter 8, as well as their relation to existing literature and similar analyses.

Table 6.1: The collated results which include Breit-Wigner parameters and cross-sections. Values in the table obtained from a mass independent fit using the nominal waveset.

Results	Values
Mass	$1.685\,\text{GeV} \pm 0.02$ stat. $^{+0.008}_{-0.014}$ syst.
Width	$0.122\,\text{GeV} \pm 0.028$ stat. $\pm\, 0.037$ syst.
Cross-section ($\phi(1680)$)	$178\,\text{nb} \pm 19$ stat. $^{+102}_{-106}$ syst.
Cross-section ($\eta\phi$)	$35.7\,\text{nb} \pm 3.79$ stat. $^{+10.01}_{-11.29}$ syst.

Chapter 7

Systematic uncertainties

The Breit-Wigner parameters of the 1^{--} corresponding to the $\phi(1680)$ and its cross-section have been extracted. This Chapter details the determination of the systematic uncertainties on these values.

7.1 Sources of systematic uncertainty

Besides the statistical errors associated with the measurements, various factors can contribute to further uncertainty on the results. Examples include systematic effects in detector responses; variance of results due to event selection cut values and model selection; uncertainty associated with theoretical calculations; errors on observables or theoretical parameters required to compute the results, and many others. In particle and hadron physics these are all categorised as systematic uncertainties, sometimes also referred to as systematic errors.

These errors can be a major portion of the total uncertainty on the final result – this happens to be the case in the present thesis. From the analysis in Chapter 5 it is easy to infer that the cross-section measurements will be heavily impacted by model selection. As already noted, this is a quantity that is directly proportional on the acceptance corrected yields obtained from the partial wave fits. The observed yields could be seen to vary by as much as 50% between different wavesets, which implies similar differences in corrected yields due to the relatively flat acceptance profile over $\eta\phi$ invariant mass. Similar size of effect could be observed when comparing the mass independent and hybrid fit results for the nominal waveset as well.

Another likely major source of systematic uncertainty on the cross-sections was the choice of Confidence Level cut during event selection. This was the primary exclusivity cut used and as demonstrated by the study performed to optimise this value in Chapter 4, different selections can have strong impacts on the background subtracted yields. Although this does not necessarily translate directly to differences in the yield of the 1^{--} wave, the effect is still likely to be significant. The final two sources of systematics considered were the uncertainty associated with fits reaching different local minima and the choice of mass range used to fit the Breit-

Wigner to the 1^{--} wave intensity distribution. While the effect of local minima, as shown in Chapter 5, did not have major implications on the qualitative interpretation of the results, certain mass bins saw variance in the partial wave intensities on the level of 5-10% and this could have an impact on the overall shape of the 1^{--} amplitudes. It is expected that the choice of mass range will also have some impact on the resonance parameters, especially on the estimate of the Breit-Wigner width.

Systematic errors were obtained from results computed after varying the relevant variable or model, usually given by the standard deviation of the results over all variations including the nominal. In general, variations are chosen by considering 'reasonable' limits for the variable or model in question. This may sometimes be a strict limit dictated by the data, or may rely on scientific judgement. Choosing ranges that are too broad or dissimilar to the nominal variation can artificially inflate the error, while choosing ranges that are too narrow can artificially shrink them. The choices for each systematic are discussed in the following Subsections. The variational procedure was performed separately for each source of systematic uncertainty. The combined uncertainties on all measurements were obtained by adding the relevant individual systematic contributions in quadrature:

$$\sigma_{\text{syst}} = \sqrt{\sum_i \sigma_i^2}, \tag{7.1}$$

where the σ_i is the i-ith source of systematic uncertainty. Strictly speaking, this assumes that the uncertainties are independent and no correlation factors have to be introduced in the above calculation. If they are correlated, then this method will overestimate the total uncertainty. However, as no practical method exists to determine such correlations in high dimensional cases, the standard approach in particle and hadron physics analyses is to add in quadrature.

The following Subsections will present studies performed on the four outlined systematics. While this not an exhaustive list of potential sources of uncertainty that may warrant investigation, these were assumed to be dominant. Brief studies of other cuts and background subtraction models did not suggest that any of these would have impacts much beyond the 2-3% range on the results and were not included in the final systematic uncertainty. The Mandelstam t and beam energy cuts were not investigated as they were considered to be fiducial.

7.1.1 Model selection

Model selection had a major impact on partial wave intensities – depending on the waveset, a wave could go from saturating a mass bin to having almost no intensity in it. Despite this, deciding on how to estimate the resulting uncertainty is not trivial, as it is not obvious what is included in the 'reasonable' subset of all feasible wavesets. Even if the partial waves used are truncated at J = 3 as previously, that still leaves dozens of potential amplitudes and a factorial number of possible models. Considering hybrid fits, which had systematically higher 1^{--} yields, alongside

mass independent fits doubles the possibilities yet again.

In the end, hybrid fits were not included in the uncertainty calculations as they were not studied to the same extent as the mass independent fits. For the latter, following the approach taken in Chapter 5, the simplifying choice of keeping all m-projections was made. Besides the 1^{--} wave, it was assumed that the 3^{--} wave should also be kept in. Finally, other J = 3 waves were left out as there are no theoretical reasons to expect them and no practical results from the exploratory fits to suggest their presence. This left the decision of what combination of wavesets to consider that do or do not include the 1^{+-} and the three J = 2 waves.

Taking these considerations into account, the following wavesets were used to compute the uncertainty on model selection:

- The PDG waveset – the 1^{--} and 3^{--} amplitudes only.
- The PDG waveset with the 1^{+-} amplitudes added.
- The PDG waveset with the 2^{--} amplitudes added.
- The nominal waveset with the removed m-projections added back in.

These four combinations represent possibilities that would not have been surprising to see emerge as the nominal waveset. Although the actual analysis showed that some permutation 1^{+-} and 2^{--} waves were required for good angular fits in certain mass bins, this could have been otherwise. The same holds true for the 2^{--} waves; conversely, it would have been unexpected to see a strong 0^{-+} or 2^{+-} component, which would have indicated exotic state candidates. Finally, as discussed previously, though some m-projections were removed after exploratory studies, there were no strong priors on these beforehand.

Mass independent partial wave fits were performed for each of the listed wavesets using the same event selection and phase space Monte Carlo data as for the main analysis. The Breit-Wigner parameters are plotted against each other in Figure 7.1a, while the cross-section for all variations is shown in Figure 7.1b. The Breit-Wigners for all variations are clustered closely to the nominal values, with the only relative outlier being the mass from the PDG waveset, which is lower at 1.67 GeV. The uncertainty on the Breit-Wigner mass was used asymmetrically, as the values for all non-nominal variations were systematically lower. This gives an uncertainty of -7 MeV on the mass and ± 6 MeV on the width. Like expected, the uncertainty on the cross-section driven by the PDG waveset saturating the first invariant mass peak in a way the other wavesets do not. The uncertainty on the total cross-section is ± 9.35 nb.

7.1.2 Confidence Level cut

The systematic uncertainty on the choice of Confidence Level cut was obtained by varying it around the nominal choice of 10^{-2}. One value below and three above were inspected – 10^{-1},

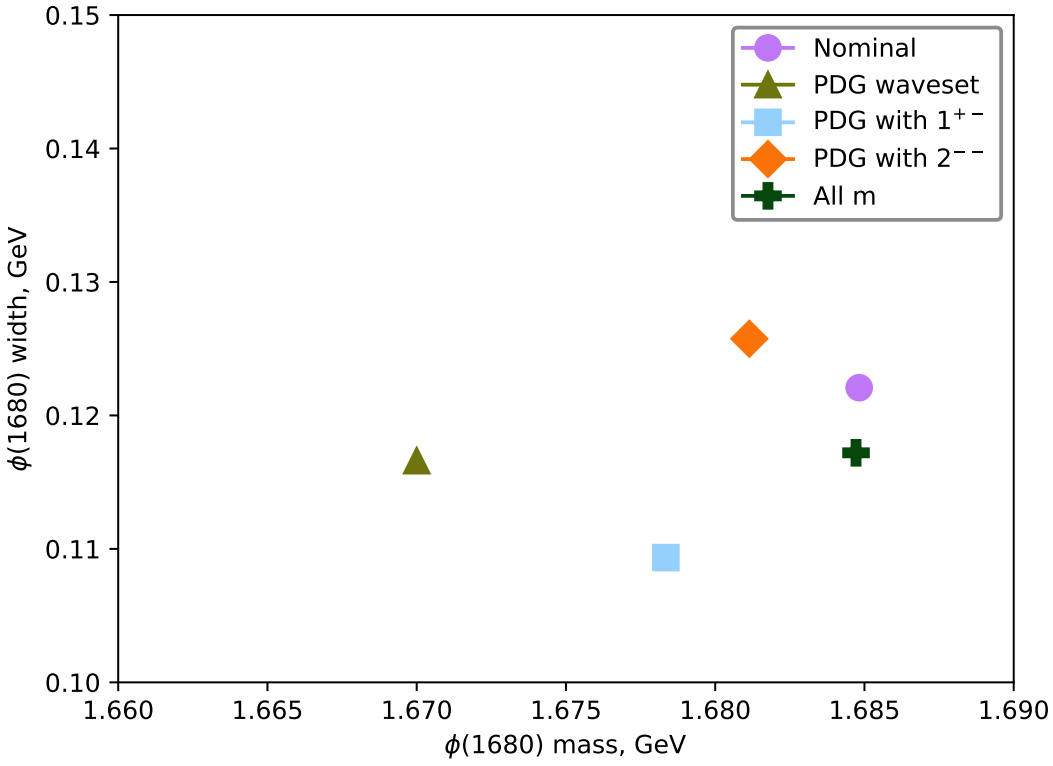

(a)

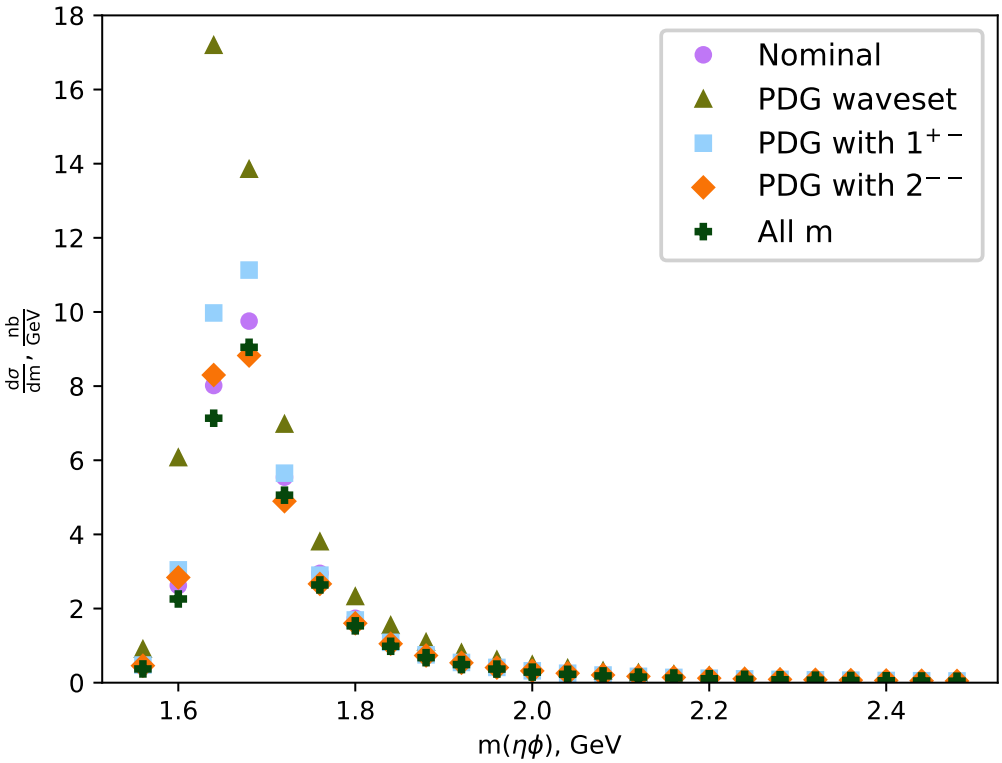

(b)

Figure 7.1: Breit-Wigner parameters (a) and $\frac{d\sigma}{dm}$ (b) for all four systematic model variations plus the nominal waveset.

10^{-3}, 10^{-4}, and 10^{-5}. Like for the model selection study, the same selection cuts besides the Confidence Level and the same phase space Monte Carlo data was used to perform the partial wave fits for each variation. The Breit-Wigner parameters and the cross-section for all variations are shown in Figures 7.2a and 7.2b respectively.

The BW mass was again consistently lower, meaning the uncertainty is asymmetric. Three of the four variations resulted in a lower end estimate around 1.67 GeV. The widths are clustered between 0.1 GeV and 0.12 GeV except for the CL $> 10^{-1}$ setting, which is an outlier at 0.159 GeV. The uncertainties are -9 MeV and ± 22 MeV respectively. An asymmetry that was not obvious from the invariant mass spectra can be observed in the cross-section – in the systematic variations they are consistently lower than for the nominal cut setting. Accordingly, the uncertainty on the total cross-section from the Confidence Level cut is given as -5.2 nb. Additional study would be required to determine the cause for the asymmetry.

7.1.3 Variations due to local minima

The standard deviation on yields from various local minima in the fit was demonstrated in Chapter 5. Further inspection was necessary to determine whether it is reasonable to straightforwardly use this as a systematic uncertainty. Similar variation could be caused by either all 10 top fits varying around the best fit or by e.g. the worst solution being an outlier result skewing the statistic on an otherwise closely clustered set of solutions. The former was true for the nominal waveset, with all 10 fits appearing relatively similar.

The BW parameters and $\frac{d\sigma}{dm}$ for the top 10 solutions by likelihood are shown in Figures 7.3a and 7.3b. The uncertainty on the Breit-Wigner peak is once again asymmetric at -3 MeV, with the mass ranging from 1.674 GeV to 1.685 GeV. Most are close to the nominal value, with only three putting it below 1.68 GeV. The width is affected more, with a range from 0.1 GeV to 0.148 GeV and an uncertainty of ± 14 MeV. The cross sections are distributed around the best fit with an uncertainty of ± 2.2 nb.

7.1.4 Mass range used for Breit-Wigner fit

The nominal variation used the first 11 bins, i.e. $\eta\phi$ mass from 1.5 GeV to 1.94 GeV, to fit the Breit-Wigner corresponding to the $\phi(1680)$. This range is sufficient to cover the full width of the resonance as given by the PDG, but could bias the results if the real position of the peak was closer to the values above 1.7 GeV measured in previous photoproductions experiments. To account for this, the upper limit was varied by up to two bins in both directions, from 1.86 GeV to 2.02 GeV.

The Breit-Wigner parameters and cross-sections for all variations are shown in Figure 7.4. The mass and width both vary approximately smoothly and linearly with the upper limit of the mass. The mass has a standard deviation of $\pm$ 7.6 MeV while the width is much more sensitive

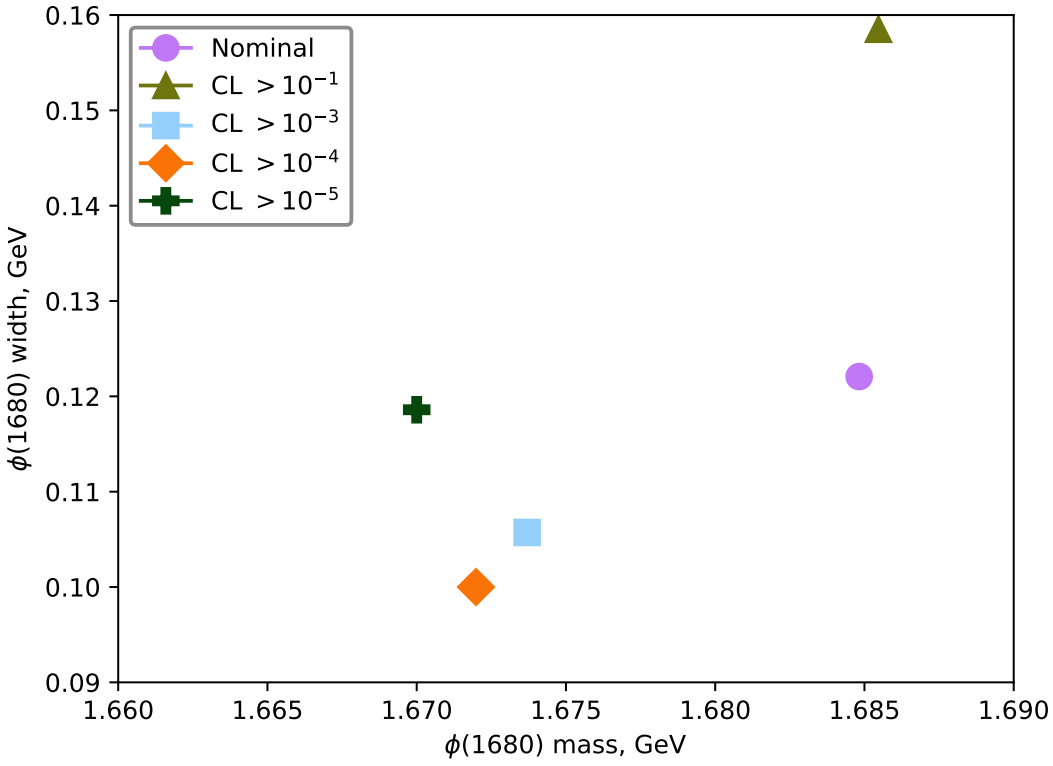

(a)

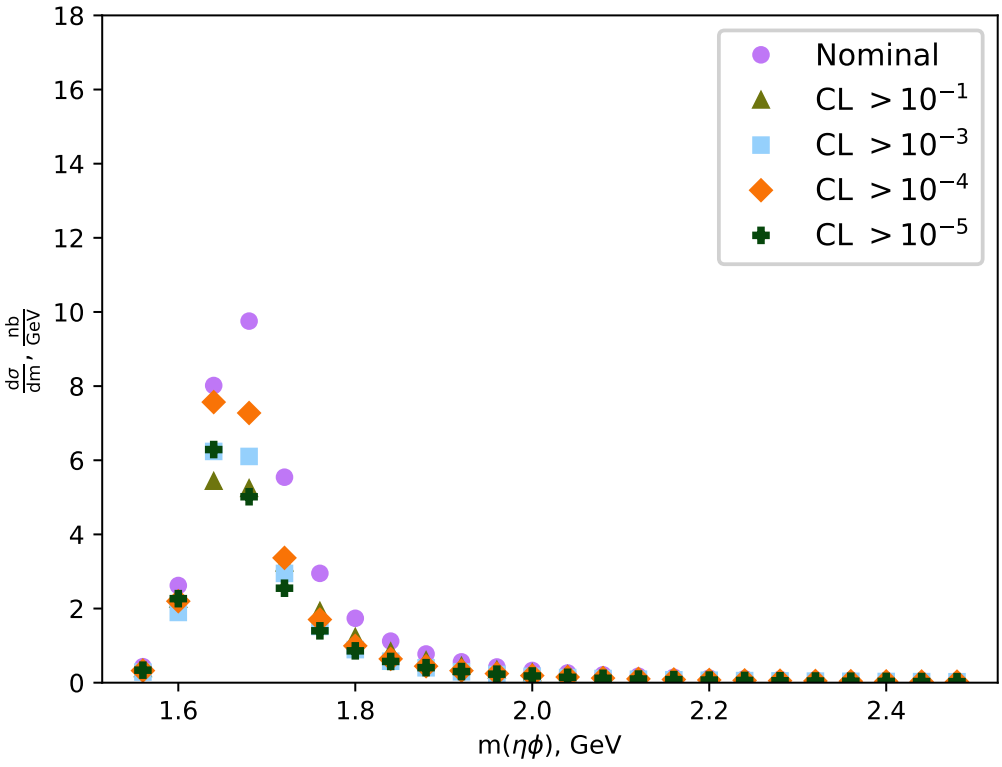

(b)

Figure 7.2: Breit-Wigner parameters (a) and $\frac{d\sigma}{dm}$ (b) for all four systematic CL variations plus the nominal selection.

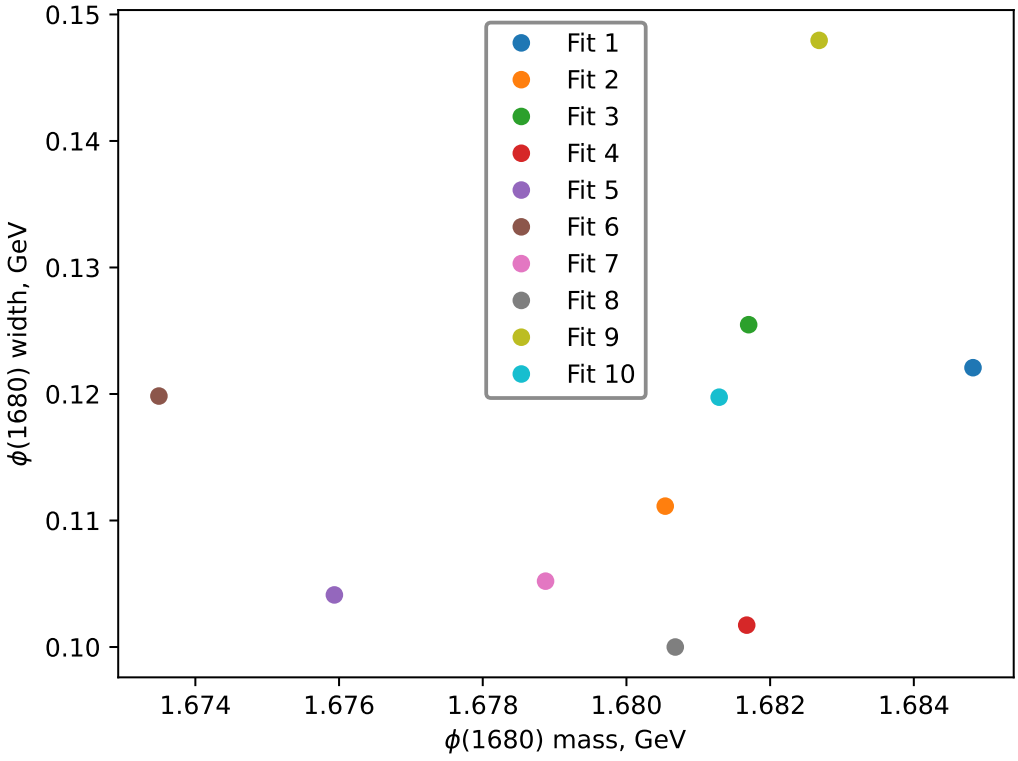

(a)

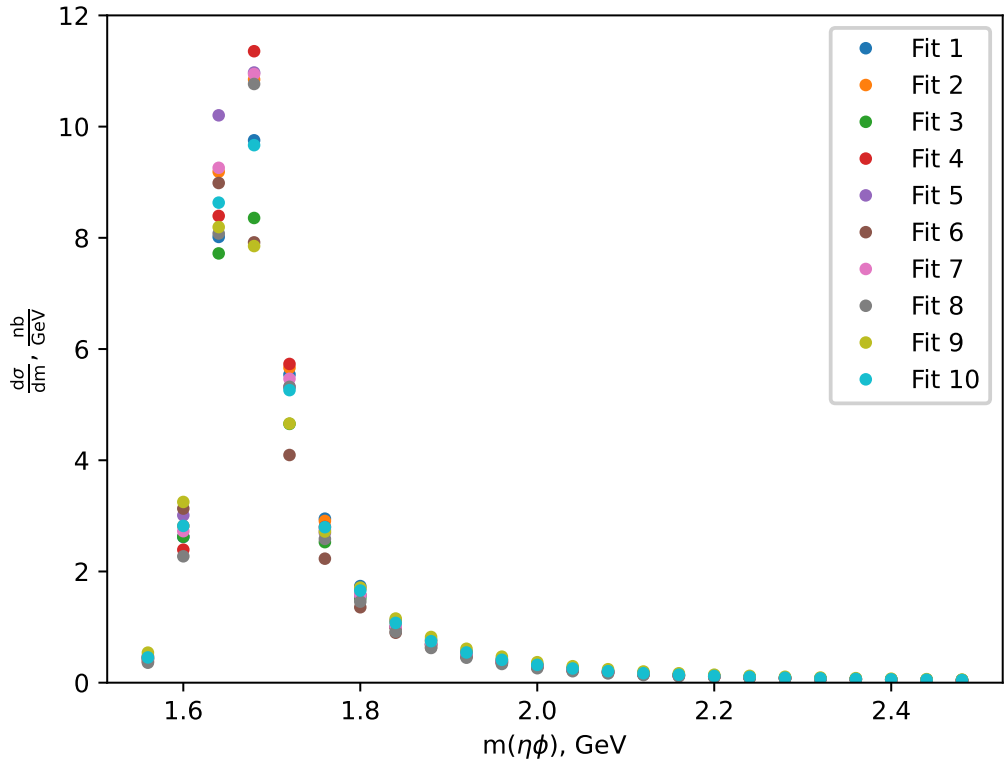

(b)

Figure 7.3: Breit-Wigner parameters (a) and $\frac{d\sigma}{dm}$ (b) for 10 best fits using the nominal waveset according to likelihood.

with an uncertainty of $\pm$ 25 MeV. This drives a difference in Breit-Wigner shape, giving a total cross-section uncertainty of $\pm$ 2.87 nb.

7.1.5 Branching fraction $\mathscr{B}(\phi(1680) \to \eta\phi)$

As mentioned in the previous Chapter, the branching fraction $\mathscr{B}(\phi(1680) \to \eta\phi)$ is not well known, having been reported in 2023 from fits to BELLE and BaBar data [66]. The referenced analysis obtains the fraction by fitting a Breit-Wigner amplitude that includes it as a free parameter, obtaining six separate solutions between two models. Separate systematic errors are reported for each, varying between 1% and 4%. The nominal values themselves range from 19% to 24%. This is not a direct measurement and thus heavily model dependent. Deciding on a precise method to compute an overall systematic uncertainty on the branching fraction would require theory expertise and assistance with fitting data from other collaborations. As such, for the purposes of this thesis, an educated estimate of $20\% \pm 10\%$ is used for the central value and systematic uncertainty. Propagated to the total cross-section, this uncertainty thus dominates the overall error on the measurement at $\pm$ 89 nb.

7.1.6 Combined systematic uncertainties

The combined systematic uncertainties for all measurements are presented in Table 7.1. It also contains the values for statistical, combined systematic, and the total combined uncertainties for ease of comparison. The components from model selection and local minima on the Breit-Wigner mass, as well as the cross-section uncertainty from the Confidence Level, are given as asymmetric due to reasons discussed above. The first two may be correlated – it appears that the BW peak does not move outwith the range of 1.66 GeV to 1.685 GeV regardless of how the models and local minima are varied, if the mass range of the fit is kept the same. However, as the statistical error on the mass is comparable to the total combined errors, any overestimation of the systematic uncertainty on the peak position should only have a minor impact on the results. The total cross-section would be more sensitive to such issues, as the systematics dominate – compare 3.79 nb statistical versus the approximately 11 nb total uncertainties.

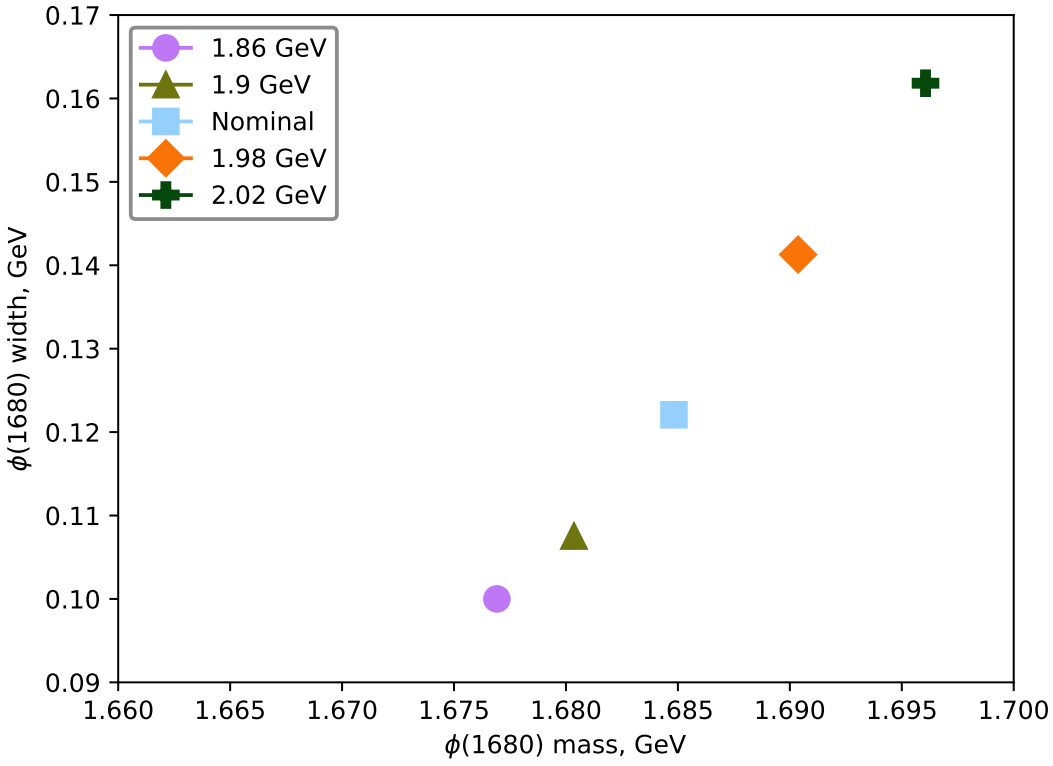

(a)

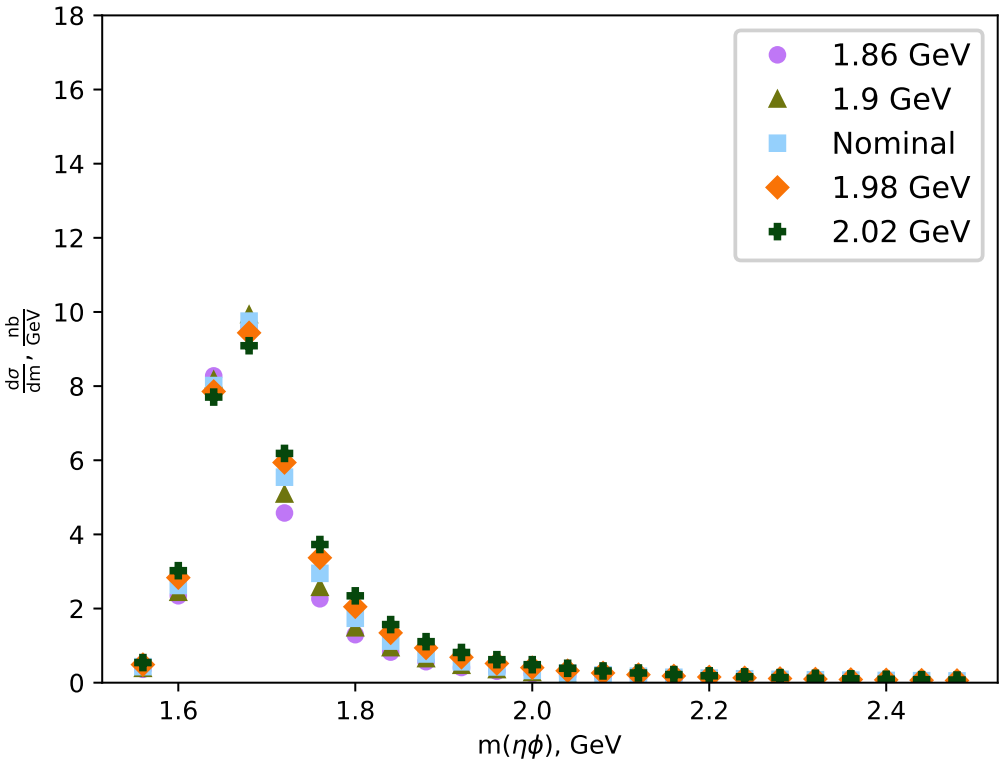

(b)

Figure 7.4: Breit-Wigner parameters (a) and $\frac{d\sigma}{dm}$ (b) for Breit-Wigner fits with different mass ranges using the nominal waveset.

Table 7.1: All major systematic uncertainties applied to the results, tabulated by source and measurement. Statistical, total systematic, and combined uncertainties are provided for comparison. The Breit-Wigner parameters of the $\phi(1680)$ are affected approximately equally by systematic and statistical error, while the cross-section measurements are dominated by systematics.

	$\phi(1680)$ mass	$\phi(1680)$ width	$\eta\phi$ cross-section	$\phi(1680)$ cross-section
Model selection	-7 MeV	± 6 MeV	± 9.35 nb	$\pm$ 47 nb
Confidence Level	-9 MeV	± 22 MeV	-5.2 nb	-26 nb
Local minima	-3 MeV	± 14 MeV	± 2.2nb	± 11 nb
Fit mass range	± 8 MeV	± 25 MeV	± 2.87 nb	± 14 nb
Statistical	$\pm$ 20 MeV	± 28 MeV	$\pm$ 3.79 nb	$\pm$ 19 nb
$\mathscr{B} \to \eta\phi$	-	-	-	$\pm$ 89 nb
Combined systematic	$^{+8}_{-14}$ MeV	± 37 MeV	$^{+10.01}_{-11.29}$ nb	$^{+102}_{-106}$ nb
Total	$^{+22}_{-24}$ MeV	$\pm$ 46 MeV	$^{+10.7}_{-11.9}$ nb	$^{+104}_{-107}$ nb

Chapter 8

Discussion and conclusions

8.1 Strangeonium resonances in $\eta\phi$ decays

This final Chapter will provide some further discussion of the results presented in this thesis and consider next steps for future work. As comments in Chapter 2 established, identifying resonances beyond reasonable doubt is no easy task. However, the partial wave analysis gives good reason to believe that a real 1^{--} signal is present around 1.68 GeV in the $\eta\phi$ invariant mass spectrum. Although model selection and other systematic effects have a strong influence on the per-bin yields in this wave, it peaks at 1.68 GeV consistently regardless of waveset. This can be confirmed visually, but was also demonstrated by the Breit-Wigner fits to the acceptance corrected 1^{--} intensity distributions, with the BW mass reliably between 1.67 and 1.685 GeV. The peak position, and the overall invariant mass projections, was also consistent in hybrid fits performed as cross-check. The variations in Breit-Wigner width were larger, as could be expected from a quantity more sensitive to fluctuations in bins farther away from the peak, with it ranging from 0.1 GeV to 0.158 GeV. It would be surprising to see such consistent results by chance.

Phase motion of the 1^{--} waves was not completely unambiguous due to sometimes large bin-to-bin variations. However, it was compatible with the hypothesis that a resonance was present at 1.68 GeV. Due to this being so close to the $\eta\phi$ mass threshold and the mass binning used, the phases only have a few data points to begin crossing through 0° at the wave peak, meaning the motion would have to be known very precisely in this mass range to rule out a resonant state. As such, the 1^{--} was identified with the $\phi(1680)$, which the PDG classifies as a 1^{--} vector with Breit-Wigner parameters close to ones obtained in this work. More specifically, the parameters can be compared to other measurements collected in the PDG. This is done in Figures 8.1 and 8.1b, with photoproduction and e^+e^- results separated by marker and colour – the tension seen between the two classes of experiment was described in Chapter 1. The present results are very compatible with those from e^+e^- experiments in both mass and width, and equivalently with the PDG average derived from them, showing no sign of the high mass peaks

observed in some of the photoproduction measurements. No signs of any other 1^{--} resonances proposed to explain these outliers, such as the so-called $X(1700)$ or $X(1750)$, were found.

As the partial wave analysis was performed in the reflectivity basis, it can also provide some hints as to the resonance production mechanism. In the high energy and low Mandelstam t limit, which is assumed to apply here, the positive (negative) reflectivity corresponds to a natural (unnatural) parity particle being exchanged. Figure 5.7 showed that the positive reflectivity is dominant for all wavesets, with the ratio of positive to negative ranging from approximately 66:33 to 75:25, implying natural parity exchange, e.g. via pomerons. Such inferences have been made successfully in published GlueX analyses, such as in the extraction of spin density matrix element for the vector $\rho(770)$ [167] and the partial wave analysis of $a_2(1320)$ [168]. Both also showed the prevalence of natural parity exchanges. The latter utilised a hybrid fit like the ones used as a cross-check in this thesis, showing that such partial wave approaches are viable for investigating production mechanisms.

Other than the $\phi(1680)$, two other excited ϕ mesons could have been seen in the partial wave analysis. One is the 3^{--} state called the $\phi_3(1850)$, while the other is the controversial hybrid candidate $\phi(2170)$. Neither were observed – the latter outcome was not surprising, as its production cross-section, as measured or predicted in literature, is quite small, while at the same being located in a mass region that likely has a significant amount of remaining baryon background events. More surprising was the lack of 3^{--} signal around the second $\eta\phi$ invariant mass peak, with it only being obtained using the PDG waveset. Practically all other wavesets saw the 3^{--} amplitudes lose most of their intensity to other waves. Although this does not decisively preclude the existence of the $\phi_3(1850)$, some doubt is cast on its status and quantum number assignment.

In addition to the Breit-Wigner parameters, cross-sections for the $\eta\phi$ final state and the $\phi(1680)$ were extracted. As noted in Chapter 1, there are no photoproduction measurements with which to compare these results. The single currently published paper that attempts to compute the $\phi(1680)$ cross-section for photoproduction [68] can be used as a rough check on the orders of magnitude. The two models used in the paper both give estimates of a cross-section around 100 nb at centre-of-mass energies similar to ones at GlueX. This is compatible with the lower bound of the computed cross-section. The very high uncertainty on the $\phi(1680)$ branching fraction means this is not a very stringent test, but it is hoped that the $\eta\phi$ cross-section will be helpful to further modelling efforts that may be able to obtain a more precise estimate of the branching ratio.

8.2 Future work

Multiple pathways forward are available to continue the analysis of the $\eta\phi$ channel. Firstly, the partial wave fits were performed on GlueX-II data only, leaving an approximately equal amount

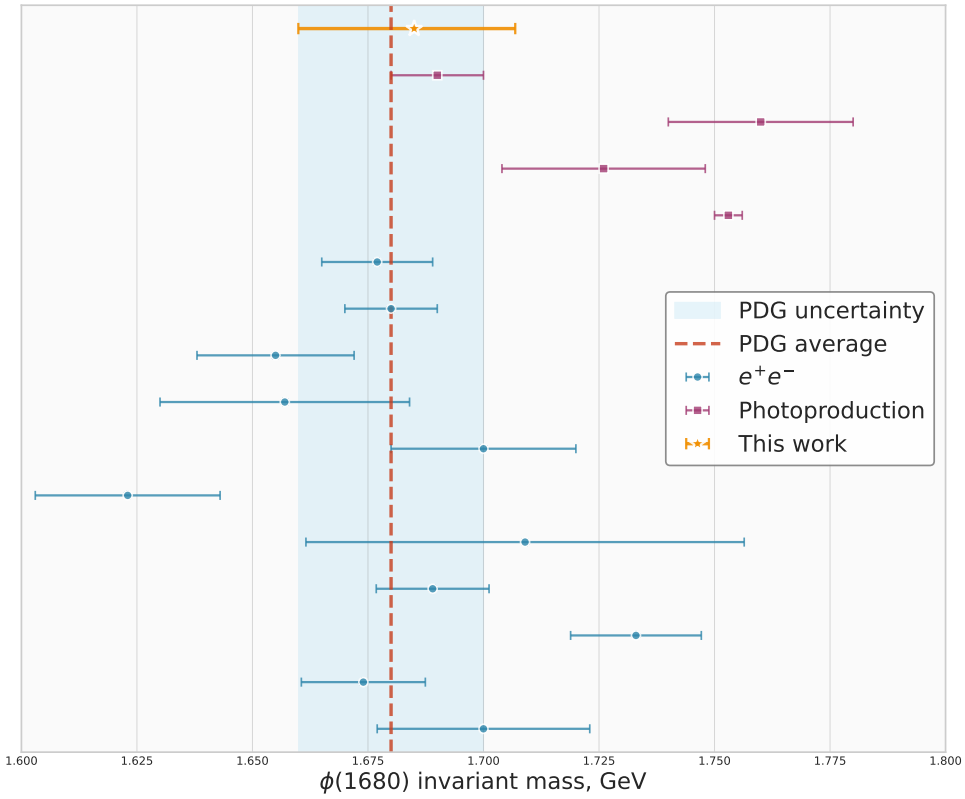

(a)

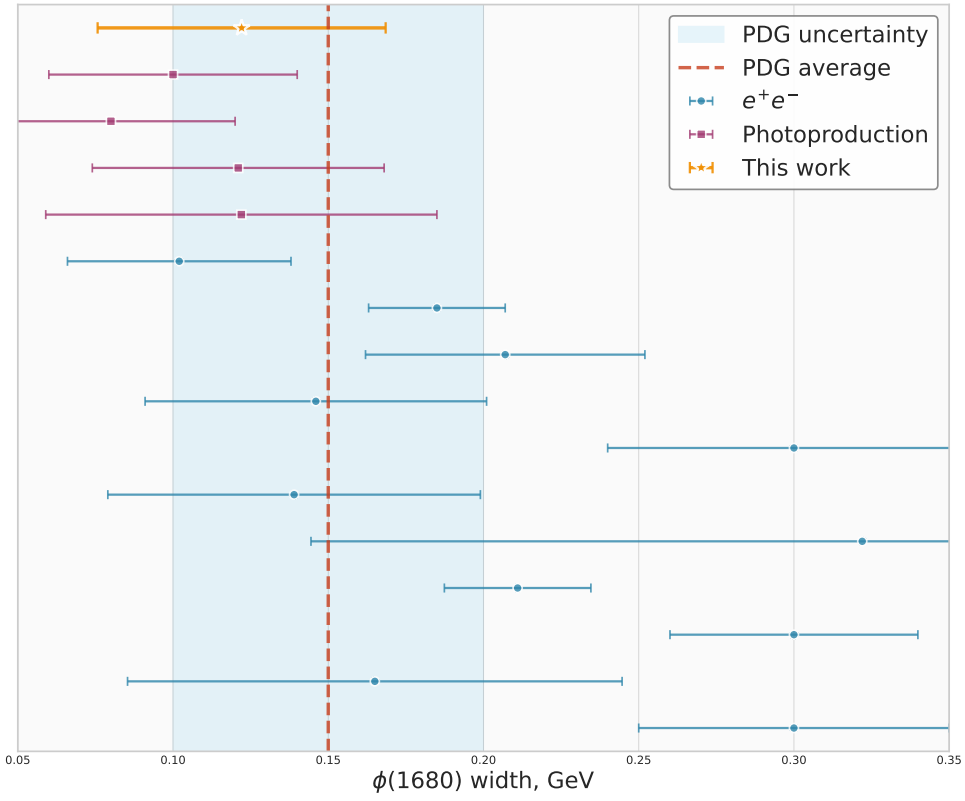

(b)

Figure 8.1: A comparison of $\phi(1680)$ mass (a) and width (b) measurements to the results obtained in the present thesis. Past measurements are taken from the PDG, with the photoproduction results taken from the last edition (2019) that still reported them. If systematic uncertainties are provided, they are added in quadrature with the statistical error to produce the errorbars in the plots.

unused from GlueX-I. Data from recently completed and ongoing data taking is also becoming available, with the final projections seeing another factor of two increase in available events over the current combined GlueX-I + GlueX-II dataset. This should see a significant increase in precision for the measurement of the $\phi(1680)$ resonance parameters, where statistical uncertainty were significant. As shown from the input-output studies, it may also have some effect in stabilising the partial wave fits. The analysis has also focused on a single final state – adding in other final states with large branching fractions, such as ones with the ϕ decaying to $K_S K_L$, could again roughly double the available statistics, although this is less trivial to incorporate.

With all this extra data, more aggressive event selection could be investigated to remove the baryon background that is present at higher $\eta\phi$ invariant mass. Although strict cuts on e.g. ηp mass would still not be possible due to its effect on the decay angular distributions demonstrated in Chapter 4, loss of statistics would no longer be a contributing limiting factor. Alternatively, the model could be modified to incorporate baryonic contributions directly. Regardless of the method, minimising this background could make a search for $\phi(2170)$ in the $\eta\phi$ channel feasible despite its low cross-section. It would also aid in clarifying the nature of the second invariant mass peak seen in the data and allow a more conclusive statement on the status of the $\phi_3(1850)$.

Beyond gathering extra data, further studies on the partial wave model will be required. The continuous ambiguities in the model have been analysed before, but it is not entirely clear how this relates to the fits in practice for more complicated wavesets. The systematic uncertainty arising from model selection drives the overall uncertainty on the cross-section of the $\phi(1680)$, alongside the currently poorly understood branching fractions of the $\phi(1680)$, and a better understanding of how the partial wave fits behave is needed to reduce this. Additional ways to add constraints could help stabilise fits – the hybrid fit, as demonstrated previously, parametrises certain partial waves with mass dependent Breit-Wigners, but it is also possible to constrain variables like the phases between waves. The latter may also limit the apparent instability in the phase motion, bolstering evidence for the presence of $\phi(1680)$.

Another way to more deeply explore partial wave models would be to adopt Bayesian techniques. The fits in this thesis were performed using maximum likelihood fitting with the Minuit minimiser. Changing out Minuit with Markov Chain Monte Carlo samplers may allow more insight, as instead of converging to a limited number of local minima, the sampler can in principle map out the full posterior distribution of the model. Techniques for waveset selection also need to be studied. Metrics like relative likelihoods, AIC, and BIC were considered when picking the nominal model, but none of these were ultimately decisive. More work with both simulated and real data will be required to confirm whether these can be useful in practice with current partial wave techniques. Work at GlueX is also underway to explore the use of regularisation techniques in the fits themselves, which involve the use of penalty terms in the likelihood in order to force spurious free parameters to go down to zero.

Appendix A

Spin dependent correction factors

The amplitudes provided in Chapter 2 require spin correction factors that were omitted from the derivation without loss of generality. These factors are expressed in terms of a function z, with the first four being given below:

$$F_0(q) = 1 \tag{A.1}$$

$$F_1(q) = \sqrt{\frac{2z}{z+1}} \tag{A.2}$$

$$F_2(q) = \sqrt{\frac{13z^2}{(z-3)^2+9z}} \tag{A.3}$$

$$F_3(q) = \sqrt{\frac{277z^3}{z(z-15)^2+9(z-5)^2}} \tag{A.4}$$

The function z is itself defined in terms of the breakup momentum q:

$$z = \left(\frac{q}{0.1973}\right)^2 \tag{A.5}$$

Appendix B

sPlot fits for all invariant mass bins

The sPlot fits for the remaining 24 mass bins were omitted from the main text for the sake of brevity. They are presented here. Histogram ranges differ slightly in some cases to remove visual artefacts caused by the numerical precision of subtracting and dividing numbers close to 0.

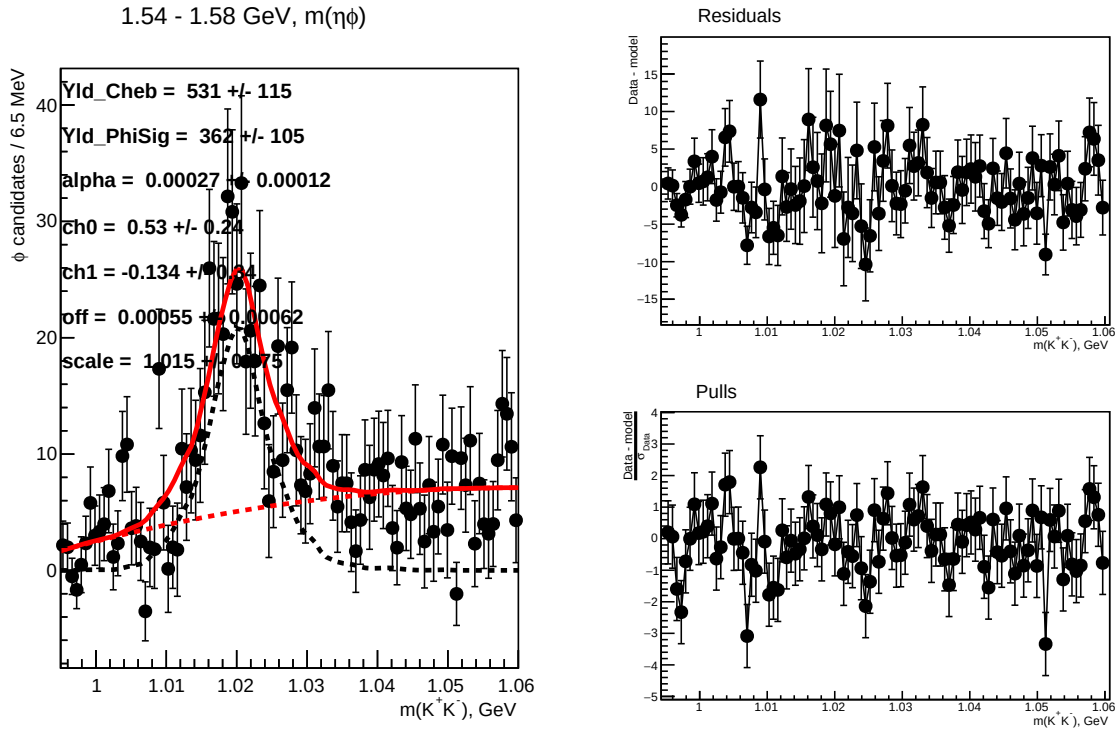
1.54 - 1.58 GeV, m(ηϕ)
Yld_Cheb = 531 +/- 115
Yld_PhiSig = 362 +/- 105
alpha = 0.00027 +/- 0.00012
ch0 = 0.53 +/- 0.24
ch1 = -0.134 +/- 0.134
off = 0.00055 +/- 0.00062
scale = 1.015 +/- 0.075
ϕ candidates / 6.5 MeV
m(K⁺K⁻), GeV
Residuals
Data - model
m(K⁺K⁻), GeV
Pulls
(Data - model) / σ Data
m(K⁺K⁻), GeV

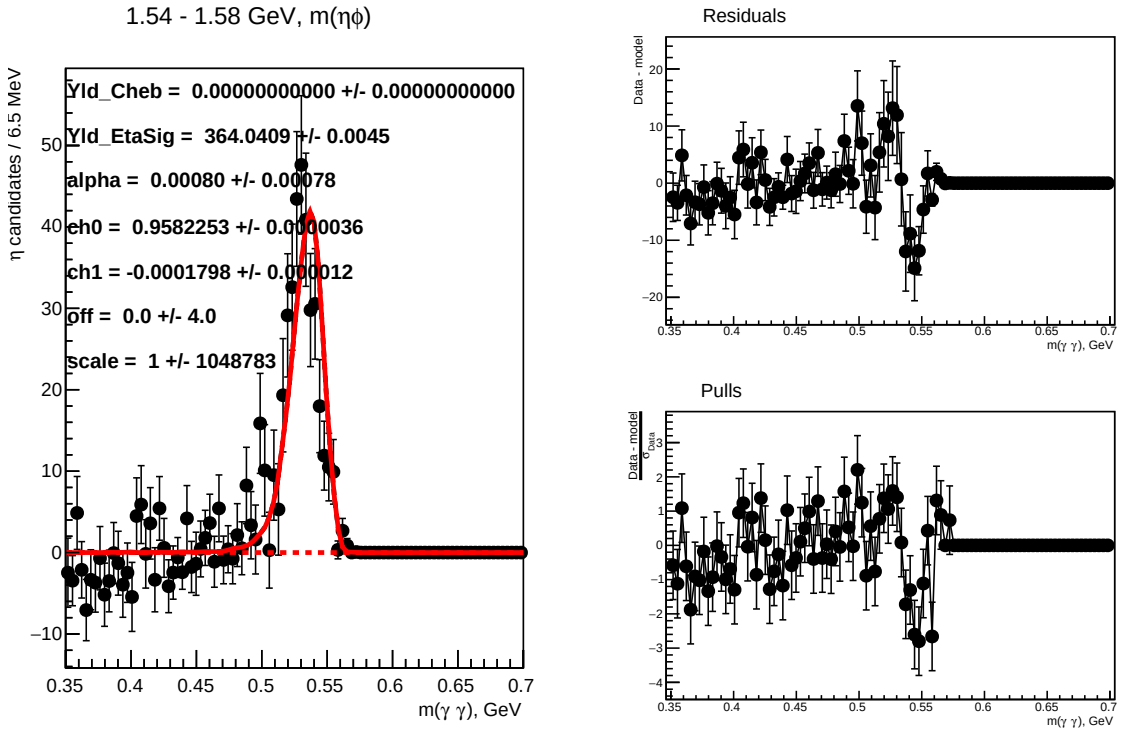
1.54 - 1.58 GeV, m(ηϕ)
Yld_Cheb = 0.00000000000 +/- 0.00000000000
Yld_EtaSig = 364.0409 +/- 0.0045
alpha = 0.00080 +/- 0.00078
ch0 = 0.9582253 +/- 0.0000036
ch1 = -0.0001798 +/- 0.0000012
off = 0.0 +/- 4.0
scale = 1 +/- 1048783
η candidates / 6.5 MeV
m(γ γ), GeV
Residuals
Data - model
m(γ γ), GeV
Pulls
(Data - model) / σ Data
m(γ γ), GeV

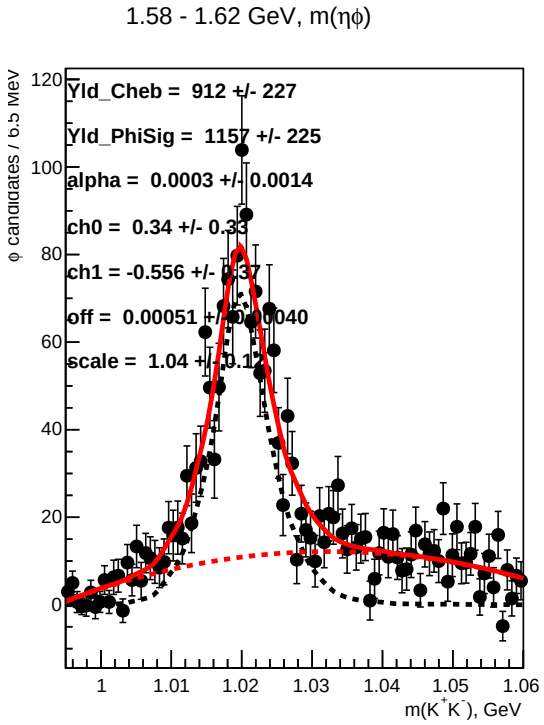
1.58 - 1.62 GeV, m(ηϕ)
Yld_Cheb = 912 +/- 227
Yld_PhiSig = 1157 +/- 225
alpha = 0.0003 +/- 0.0014
ch0 = 0.34 +/- 0.33
ch1 = -0.556 +/- 0.37
off = 0.00051 +/- 0.00040
scale = 1.04 +/- 0.12
ϕ candidates / 0.5 MeV
m(K⁺K⁻), GeV

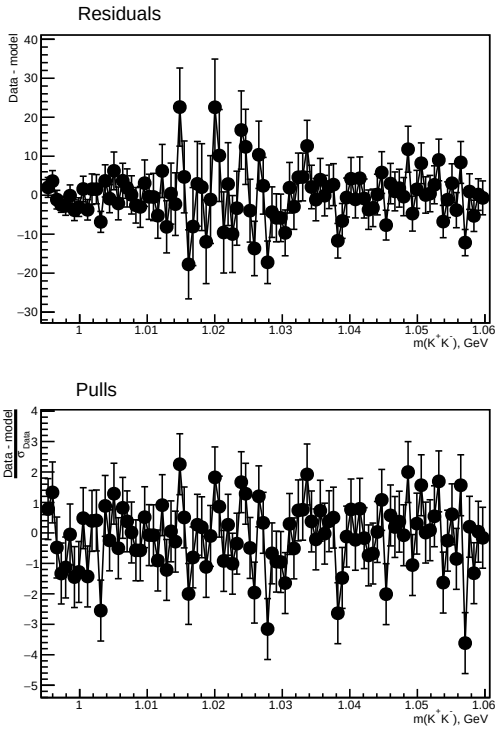
Residuals
Data - model
m(K⁺K⁻), GeV
Pulls
(Data - model) / σ Data
m(K⁺K⁻), GeV

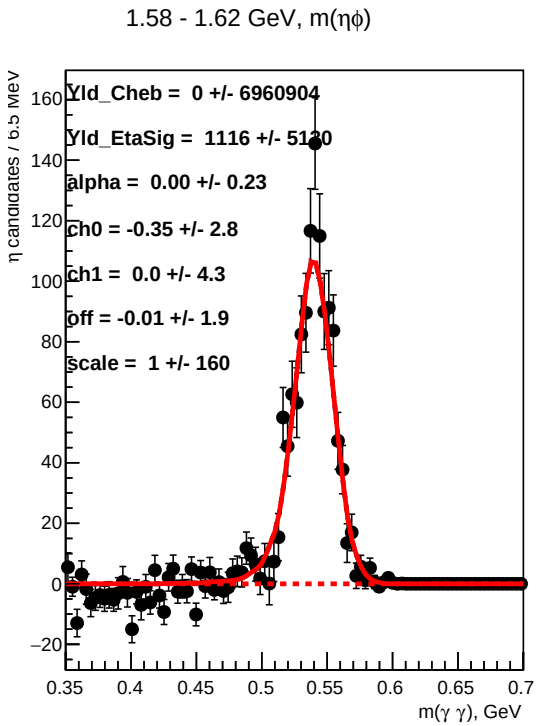
1.58 - 1.62 GeV, m(ηϕ)
Yld_Cheb = 0 +/- 6960904
Yld_EtaSig = 1116 +/- 5130
alpha = 0.00 +/- 0.23
ch0 = -0.35 +/- 2.8
ch1 = 0.0 +/- 4.3
off = -0.01 +/- 1.9
scale = 1 +/- 160
η candidates / 0.5 MeV
m(γ γ), GeV

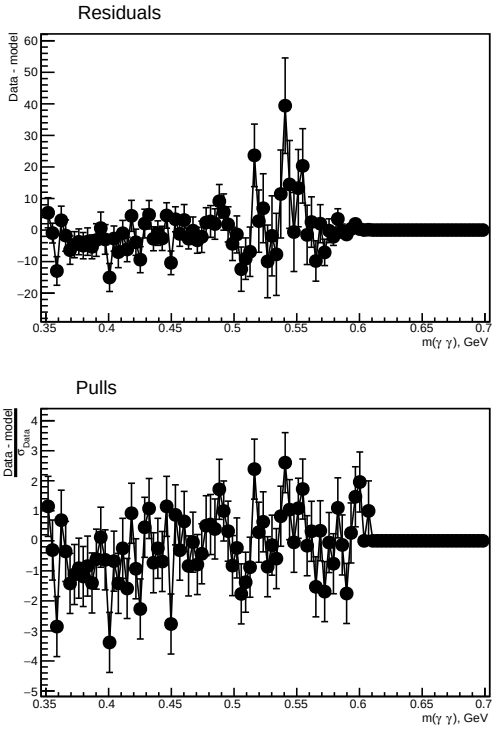
Residuals
Data - model
m(γ γ), GeV
Pulls
(Data - model) / σ Data
m(γ γ), GeV

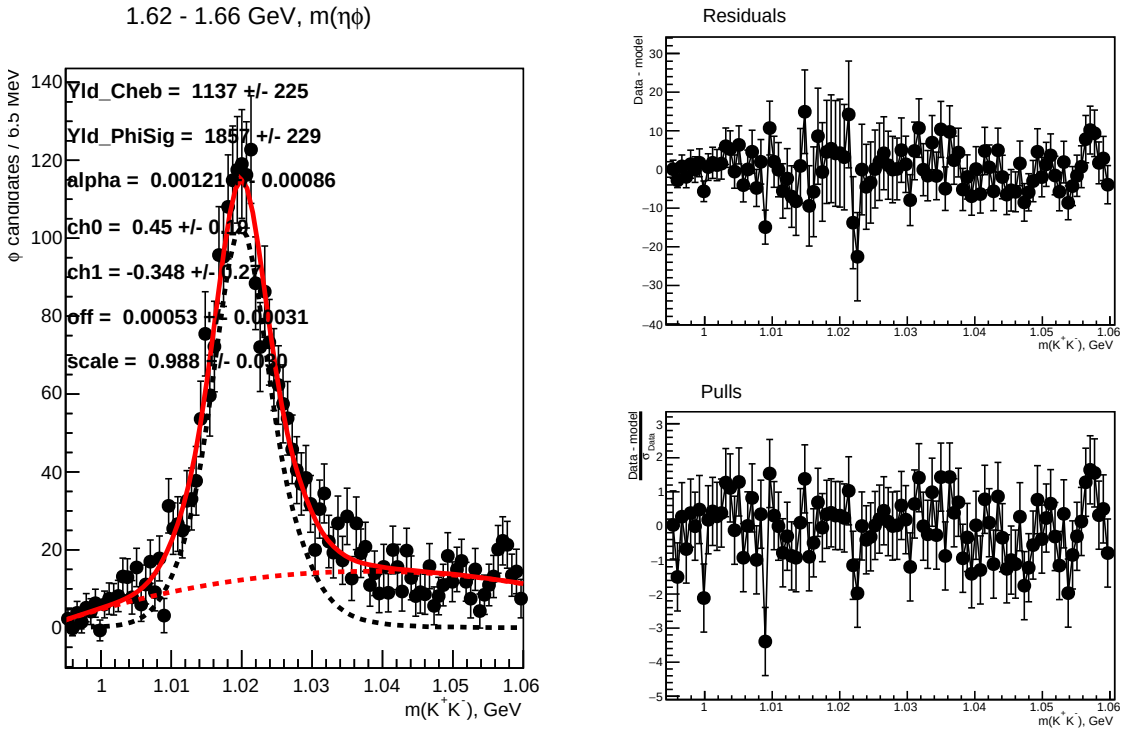
1.62 - 1.66 GeV, m(ηϕ)
Yld_Cheb = 1137 +/- 225
Yld_PhiSig = 1857 +/- 229
alpha = 0.00121 +/- 0.00086
ch0 = 0.45 +/- 0.12
ch1 = -0.348 +/- 0.27
off = 0.00053 +/- 0.00031
scale = 0.988 +/- 0.030
ϕ candidates / 6.5 MeV
m(K⁺K⁻), GeV
Residuals
Data - model
m(K⁺K⁻), GeV
Pulls
Data - model / σ Data
m(K⁺K⁻), GeV

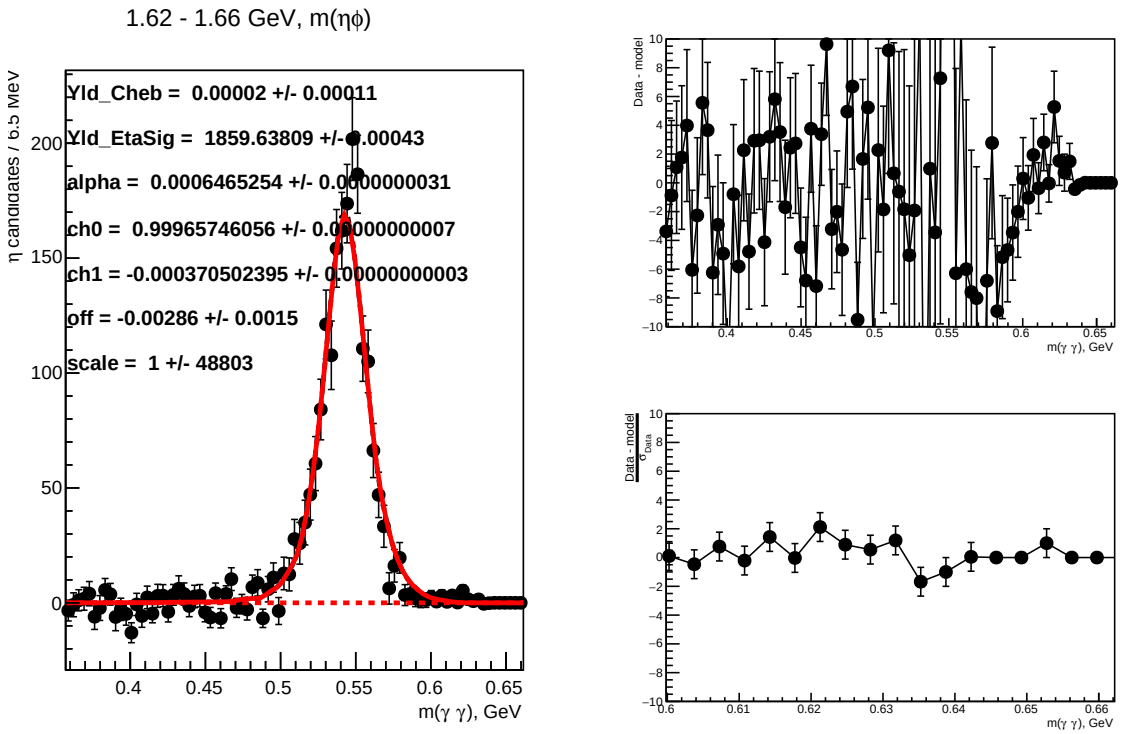
1.62 - 1.66 GeV, m(ηϕ)
Yld_Cheb = 0.00002 +/- 0.00011
Yld_EtaSig = 1859.63809 +/- 0.00043
alpha = 0.0006465254 +/- 0.0000000031
ch0 = 0.99965746056 +/- 0.00000000007
ch1 = -0.000370502395 +/- 0.000000000003
off = -0.00286 +/- 0.0015
scale = 1 +/- 48803
η candidates / 6.5 MeV
m(γ γ), GeV
Data - model
m(γ γ), GeV
Data - model / σ Data
m(γ γ), GeV

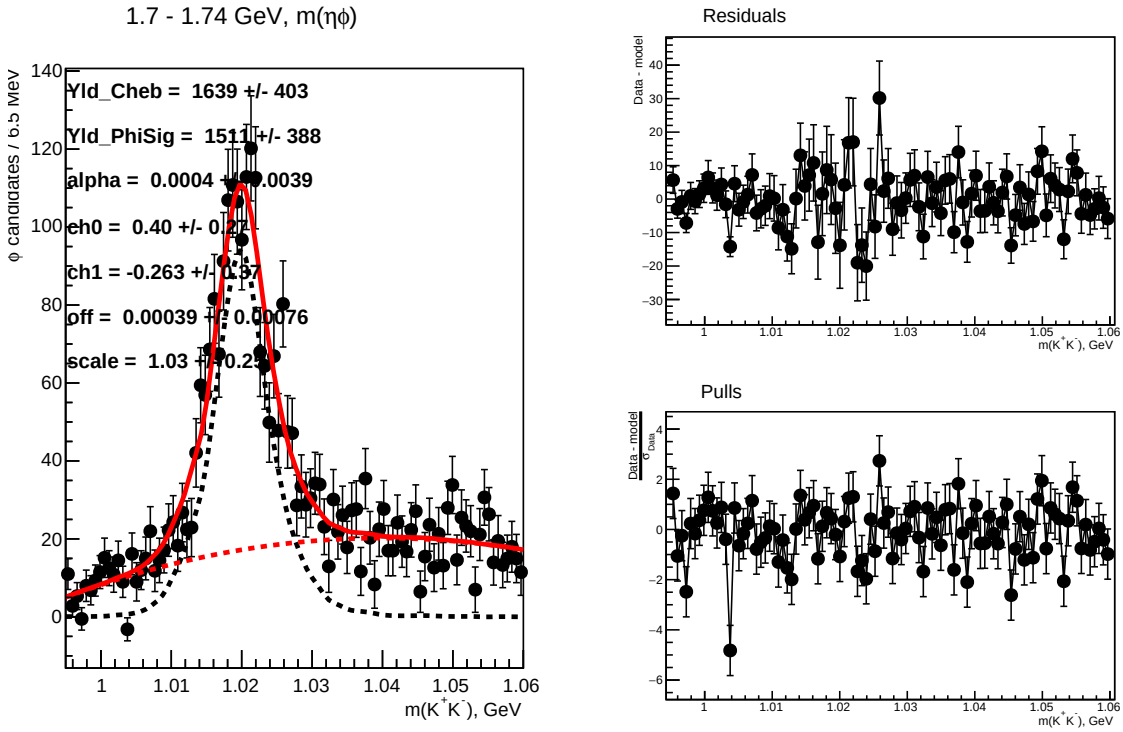
1.7 - 1.74 GeV, m(ηϕ)
Yld_Cheb = 1639 +/- 403
Yld_PhiSig = 1511 +/- 388
alpha = 0.0004 +/- 0.0039
ch0 = 0.40 +/- 0.27
ch1 = -0.263 +/- 0.137
off = 0.00039 +/- 0.00076
scale = 1.03 +/- 0.25
ϕ candidates / 0.5 MeV
m(K⁺K⁻), GeV
Residuals
Data - model
m(K⁺K⁻), GeV
Pulls
(Data - model) / σ Data
m(K⁺K⁻), GeV

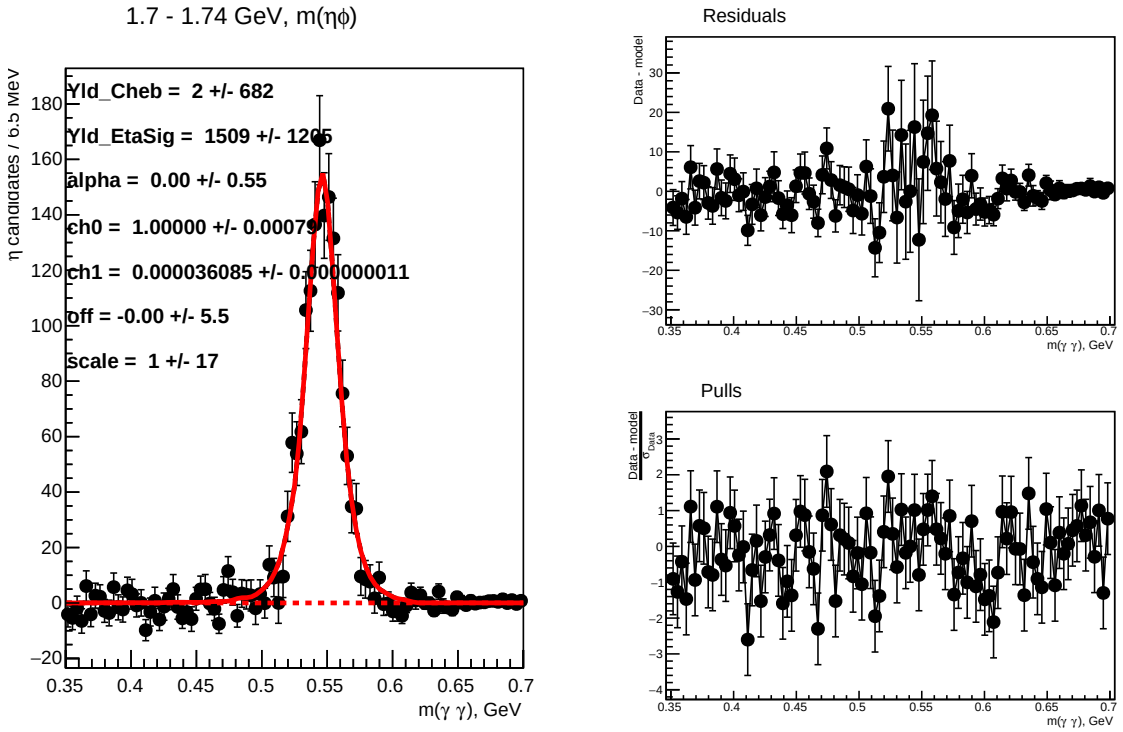
1.7 - 1.74 GeV, m(ηϕ)
Yld_Cheb = 2 +/- 682
Yld_EtaSig = 1509 +/- 1205
alpha = 0.00 +/- 0.55
ch0 = 1.00000 +/- 0.00079
ch1 = 0.000036085 +/- 0.000000011
off = -0.00 +/- 5.5
scale = 1 +/- 17
η candidates / 0.5 MeV
m(γ γ), GeV
Residuals
Data - model
m(γ γ), GeV
Pulls
(Data - model) / σ Data
m(γ γ), GeV

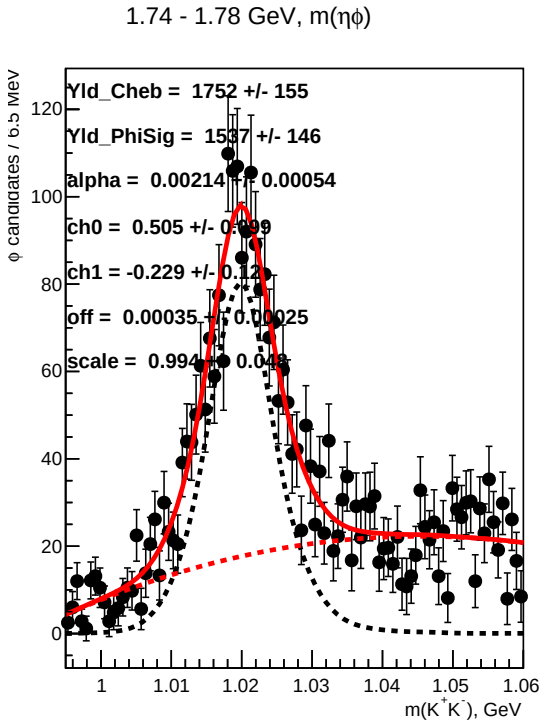
1.74 - 1.78 GeV, m(ηϕ)
Yld_Cheb = 1752 +/- 155
Yld_PhiSig = 1537 +/- 146
alpha = 0.00214 +/- 0.00054
ch0 = 0.505 +/- 0.099
ch1 = -0.229 +/- 0.129
off = 0.00035 +/- 0.00025
scale = 0.994 +/- 0.048
φ candidates / 0.5 MeV
m(K⁺K⁻), GeV

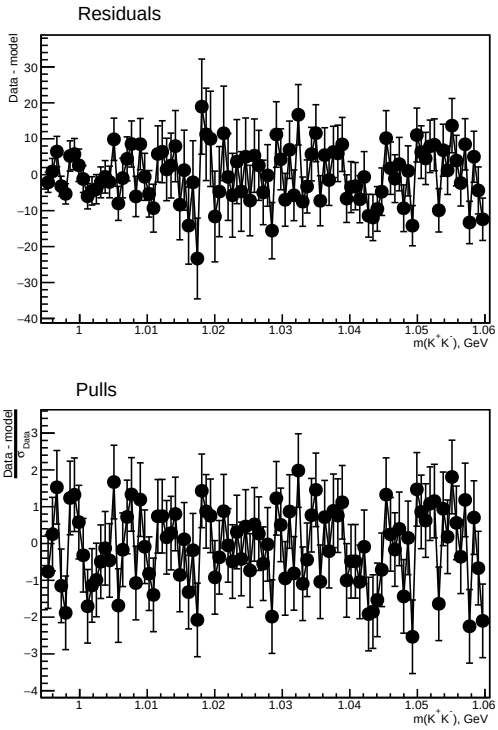
Residuals
Data - model
m(K⁺K⁻), GeV
Pulls
(Data - model) / σ Data
m(K⁺K⁻), GeV

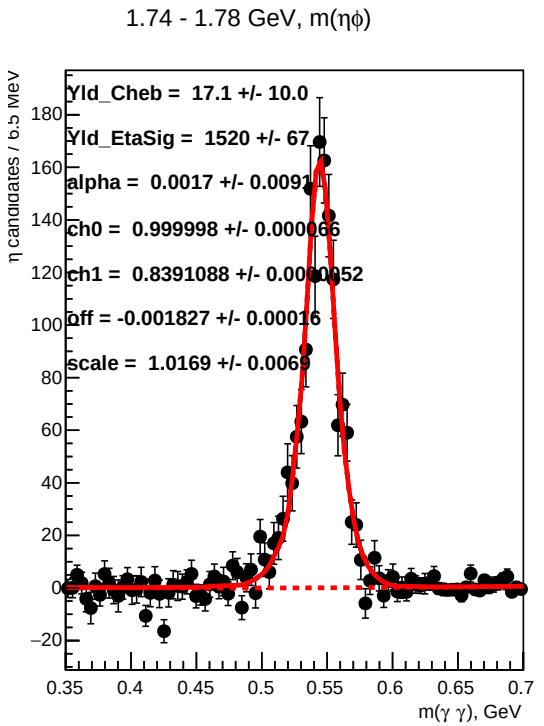
1.74 - 1.78 GeV, m(ηϕ)
Yld_Cheb = 17.1 +/- 10.0
Yld_EtaSig = 1520 +/- 67
alpha = 0.0017 +/- 0.0091
ch0 = 0.999998 +/- 0.000066
ch1 = 0.8391088 +/- 0.0000052
off = -0.001827 +/- 0.00016
scale = 1.0169 +/- 0.0069
η candidates / 0.5 MeV
m(γ γ), GeV

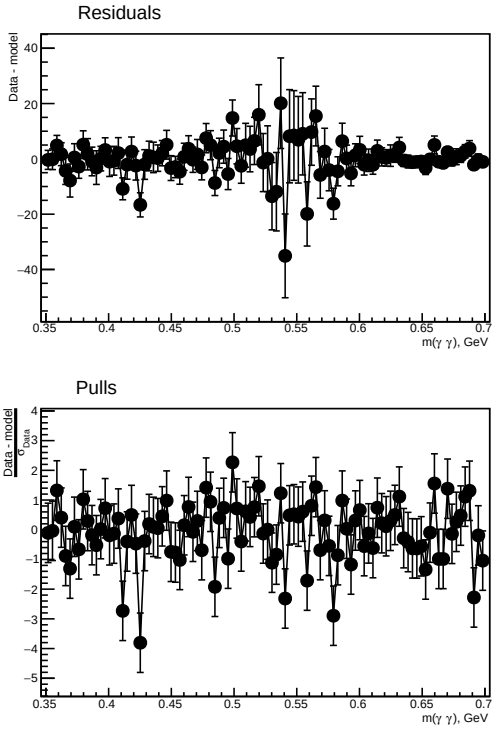
Residuals
Data - model
m(γ γ), GeV
Pulls
(Data - model) / σ Data
m(γ γ), GeV

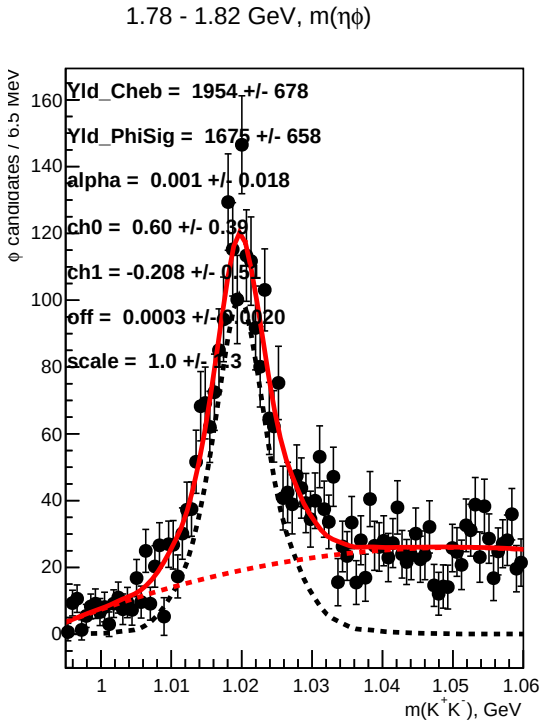
1.78 - 1.82 GeV, m(ηϕ)
Yld_Cheb = 1954 +/- 678
Yld_PhiSig = 1675 +/- 658
alpha = 0.001 +/- 0.018
ch0 = 0.60 +/- 0.39
ch1 = -0.208 +/- 0.51
off = 0.0003 +/- 0.0020
scale = 1.0 +/- 0.3
ϕ candidates / 0.5 MeV
m(K⁺K⁻), GeV

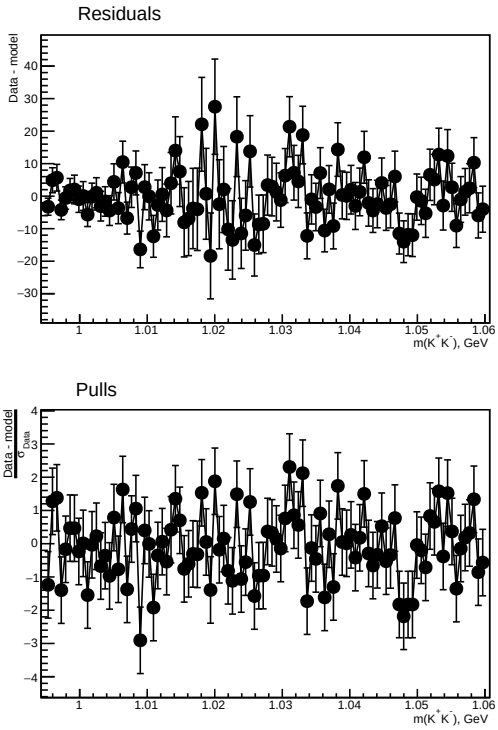
Residuals
Data - model
m(K⁺K⁻), GeV
Pulls
(Data - model) / σ Data
m(K⁺K⁻), GeV

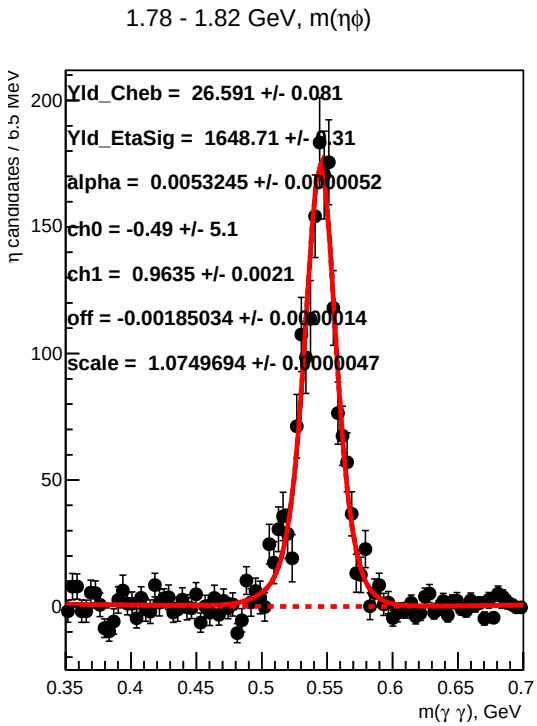
1.78 - 1.82 GeV, m(ηϕ)
Yld_Cheb = 26.591 +/- 0.081
Yld_EtaSig = 1648.71 +/- 0.31
alpha = 0.0053245 +/- 0.0000052
ch0 = -0.49 +/- 5.1
ch1 = 0.9635 +/- 0.0021
off = -0.00185034 +/- 0.0000014
scale = 1.0749694 +/- 0.0000047
η candidates / 0.5 MeV
m(γ γ), GeV

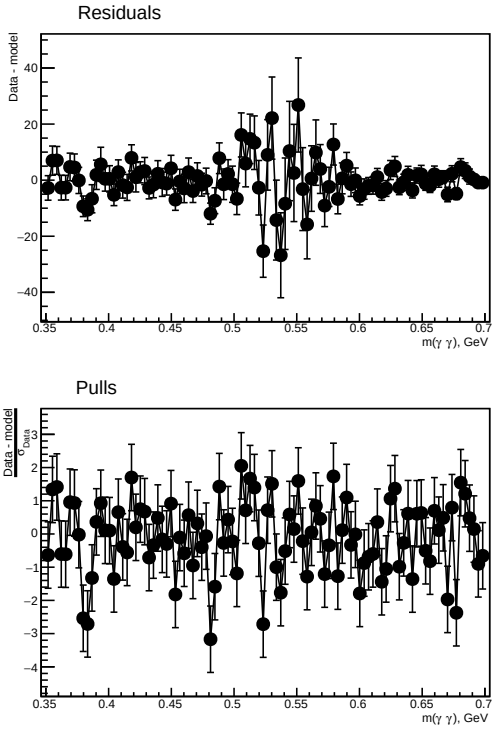
Residuals
Data - model
m(γ γ), GeV
Pulls
(Data - model) / σ Data
m(γ γ), GeV

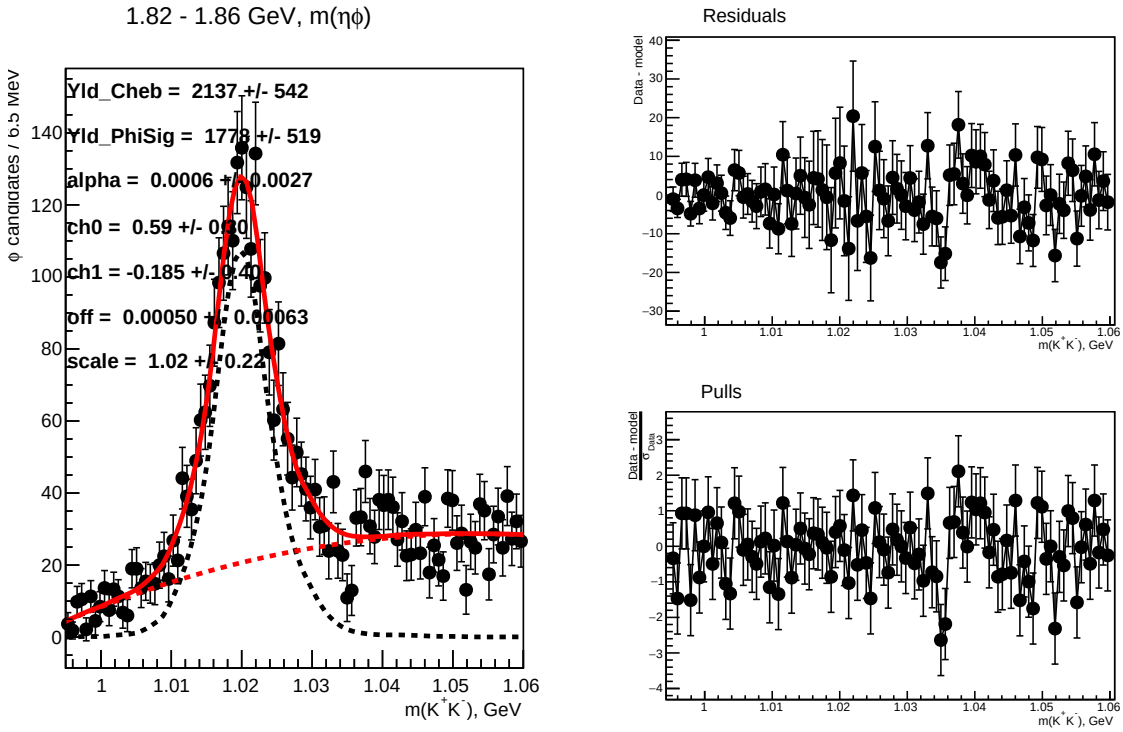
1.82 - 1.86 GeV, m(ηϕ)
Yld_Cheb = 2137 +/- 542
Yld_PhiSig = 1773 +/- 519
alpha = 0.0006 +/- 0.0027
ch0 = 0.59 +/- 0.30
ch1 = -0.185 +/- 0.40
off = 0.00050 +/- 0.00063
scale = 1.02 +/- 0.22
ϕ candidates / 6.5 MeV
m(K⁺K⁻), GeV
Residuals
Data - model
m(K⁺K⁻), GeV
Pulls
(Data - model) / σData
m(K⁺K⁻), GeV

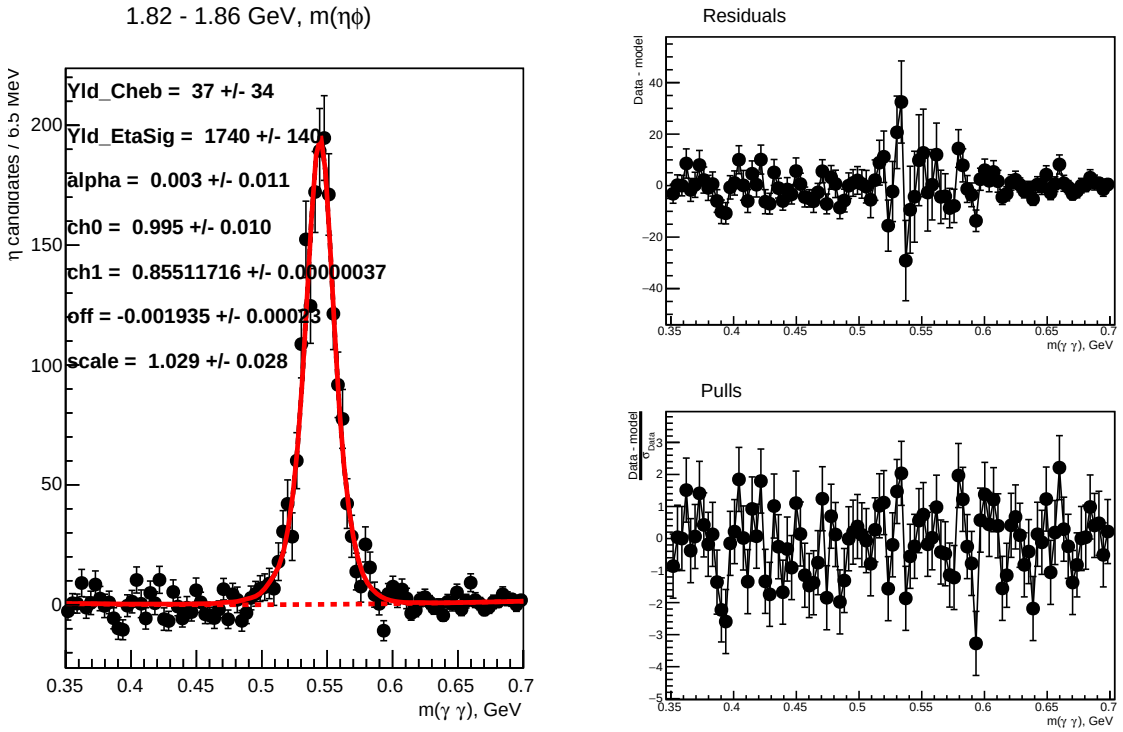
1.82 - 1.86 GeV, m(ηϕ)
Yld_Cheb = 37 +/- 34
Yld_EtaSig = 1740 +/- 140
alpha = 0.003 +/- 0.011
ch0 = 0.995 +/- 0.010
ch1 = 0.85511716 +/- 0.00000037
off = -0.001935 +/- 0.000023
scale = 1.029 +/- 0.028
η candidates / 6.5 MeV
m(γ γ), GeV
Residuals
Data - model
m(γ γ), GeV
Pulls
(Data - model) / σData
m(γ γ), GeV

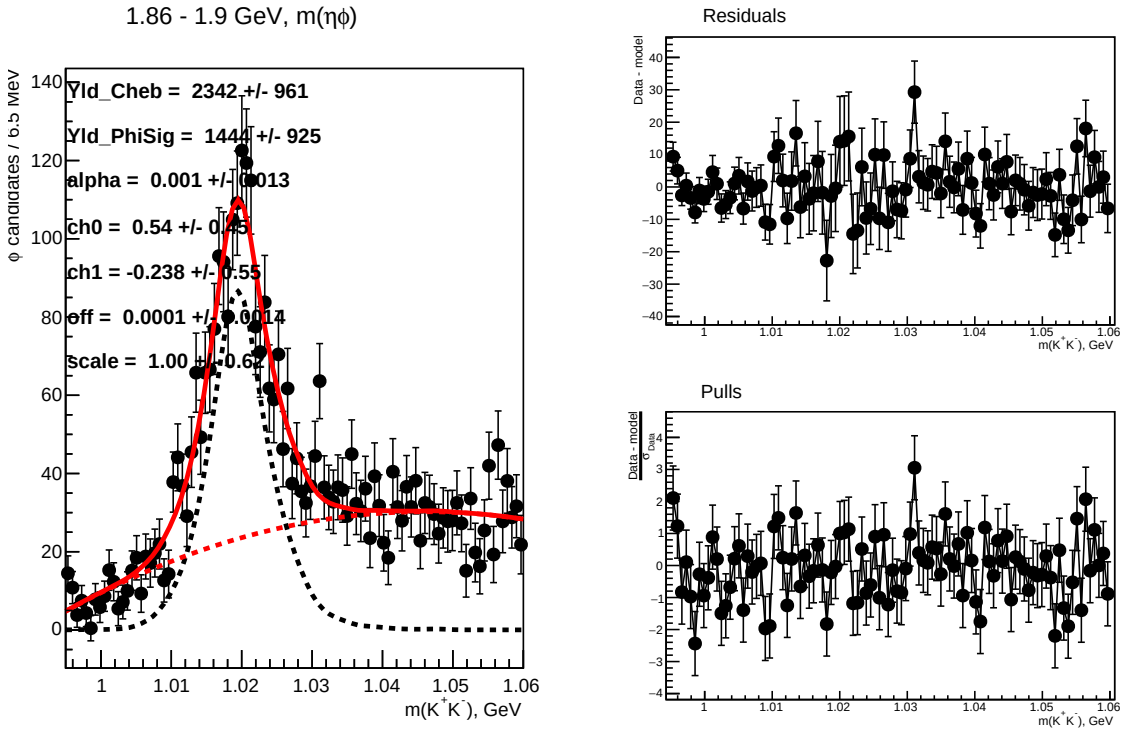
1.86 - 1.9 GeV, m(ηϕ)
Yld_Cheb = 2342 +/- 961
Yld_PhiSig = 1444 +/- 925
alpha = 0.001 +/- 0.0013
ch0 = 0.54 +/- 0.45
ch1 = -0.238 +/- 0.55
off = 0.0001 +/- 0.0014
scale = 1.00 +/- 0.62
φ candidates / 6.5 MeV
m(K⁺K⁻), GeV
Residuals
Data - model
m(K⁺K⁻), GeV
Pulls
Data - model / σ Data
m(K⁺K⁻), GeV

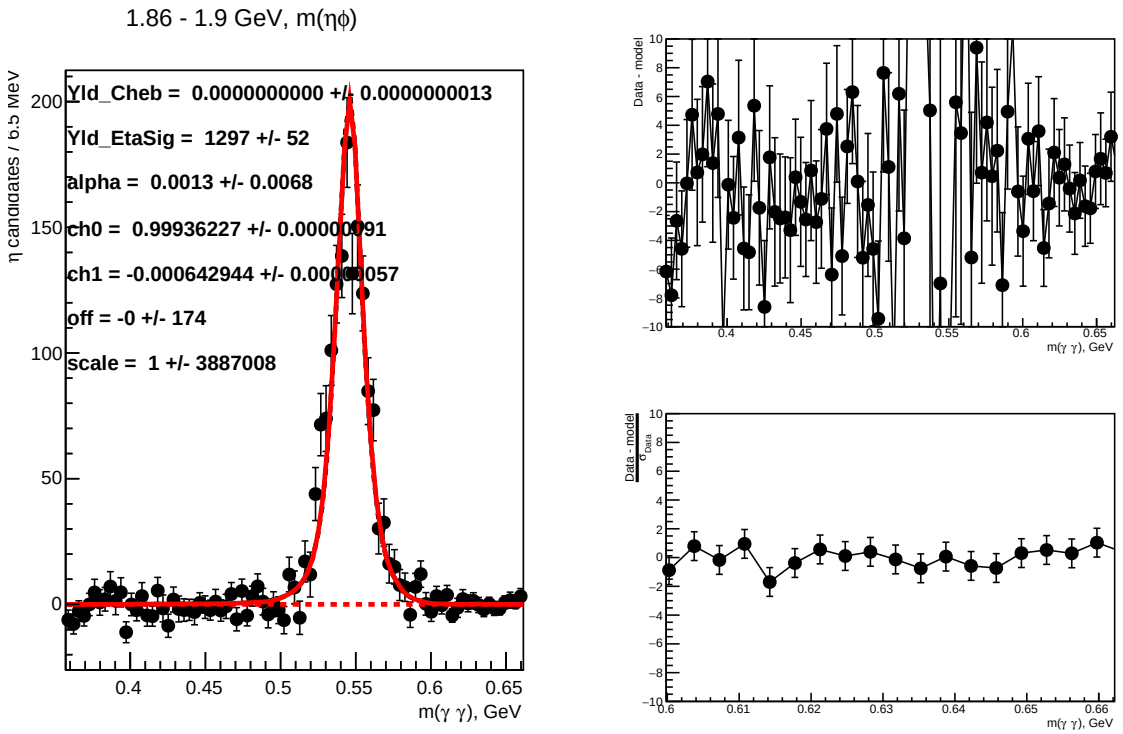
1.86 - 1.9 GeV, m(ηϕ)
Yld_Cheb = 0.0000000000 +/- 0.0000000013
Yld_EtaSig = 1297 +/- 52
alpha = 0.0013 +/- 0.0068
ch0 = 0.99936227 +/- 0.00000091
ch1 = -0.000642944 +/- 0.000000057
off = -0 +/- 174
scale = 1 +/- 3887008
η candidates / 6.5 MeV
m(γ γ), GeV
Data - model
m(γ γ), GeV
Data - model / σ Data
m(γ γ), GeV

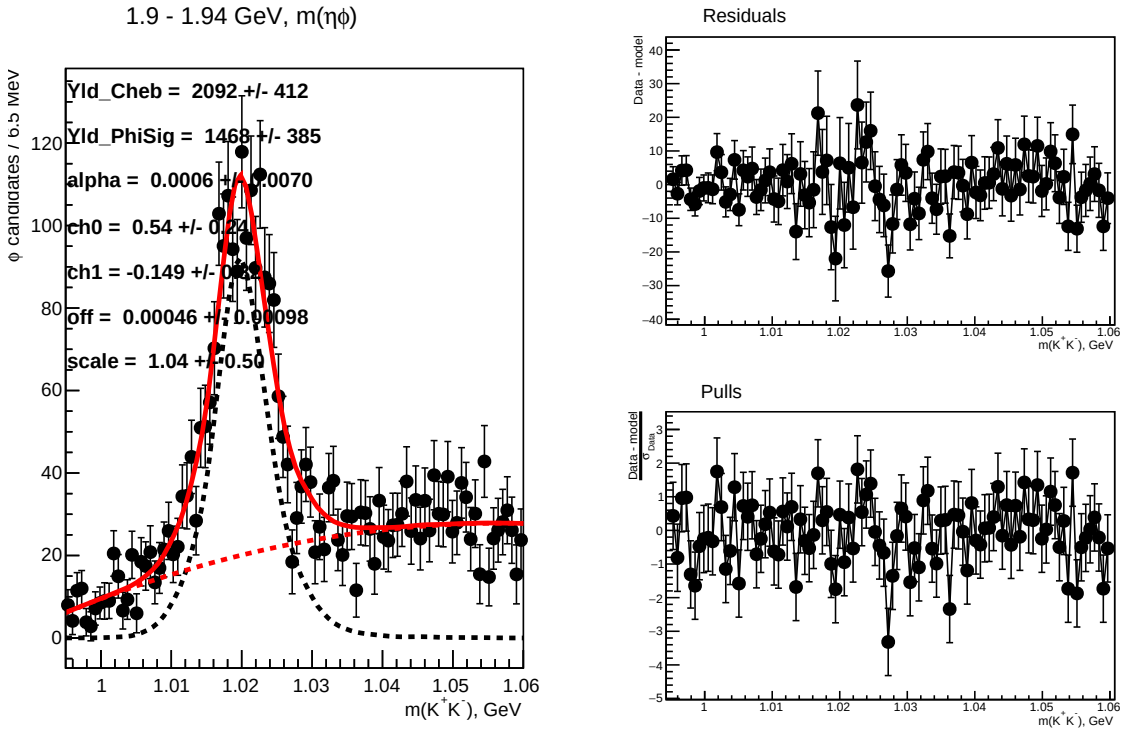
1.9 - 1.94 GeV, m(ηϕ)
Yld_Cheb = 2092 +/- 412
Yld_PhiSig = 1468 +/- 385
alpha = 0.0006 +/- 0.0070
ch0 = 0.54 +/- 0.24
ch1 = -0.149 +/- 0.083
off = 0.00046 +/- 0.00098
scale = 1.04 +/- 0.50
ϕ candidates / 0.5 MeV
m(K⁺K⁻), GeV
Residuals
Data - model
m(K⁺K⁻), GeV
Pulls
(Data - model) / σ Data
m(K⁺K⁻), GeV

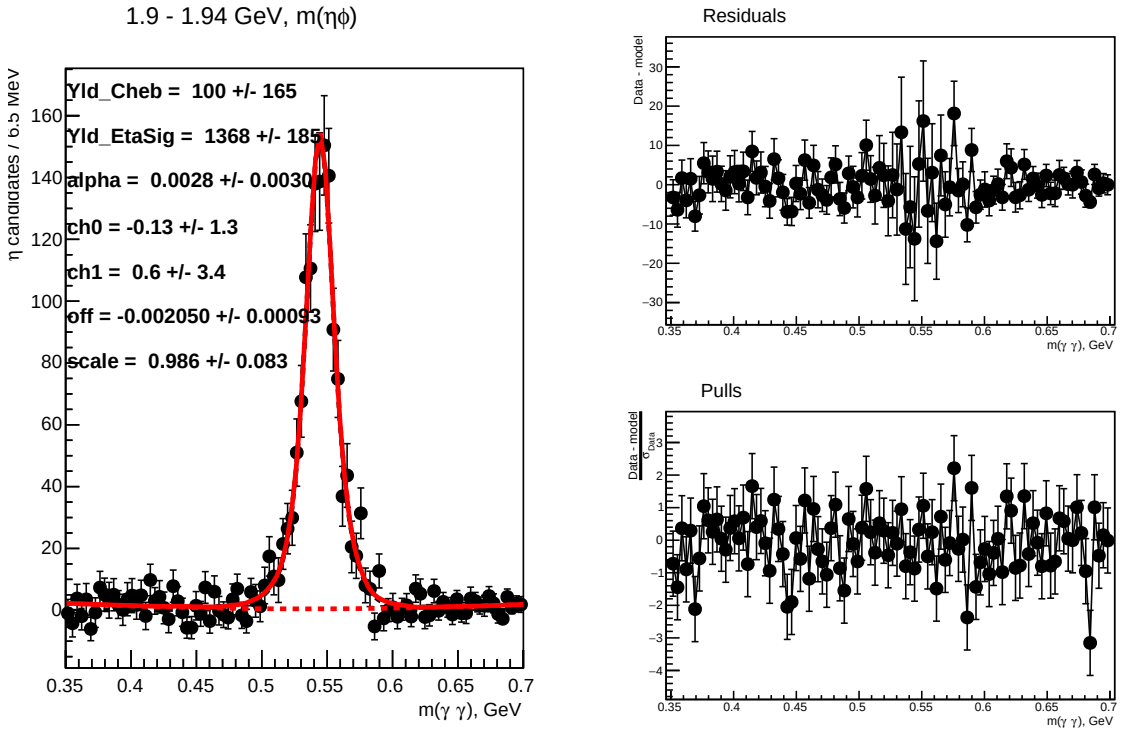
1.9 - 1.94 GeV, m(ηϕ)
Yld_Cheb = 100 +/- 165
Yld_EtaSig = 1368 +/- 185
alpha = 0.0028 +/- 0.0030
ch0 = -0.13 +/- 1.3
ch1 = 0.6 +/- 3.4
off = -0.002050 +/- 0.00093
scale = 0.986 +/- 0.083
η candidates / 0.5 MeV
m(γ γ), GeV
Residuals
Data - model
m(γ γ), GeV
Pulls
(Data - model) / σ Data
m(γ γ), GeV

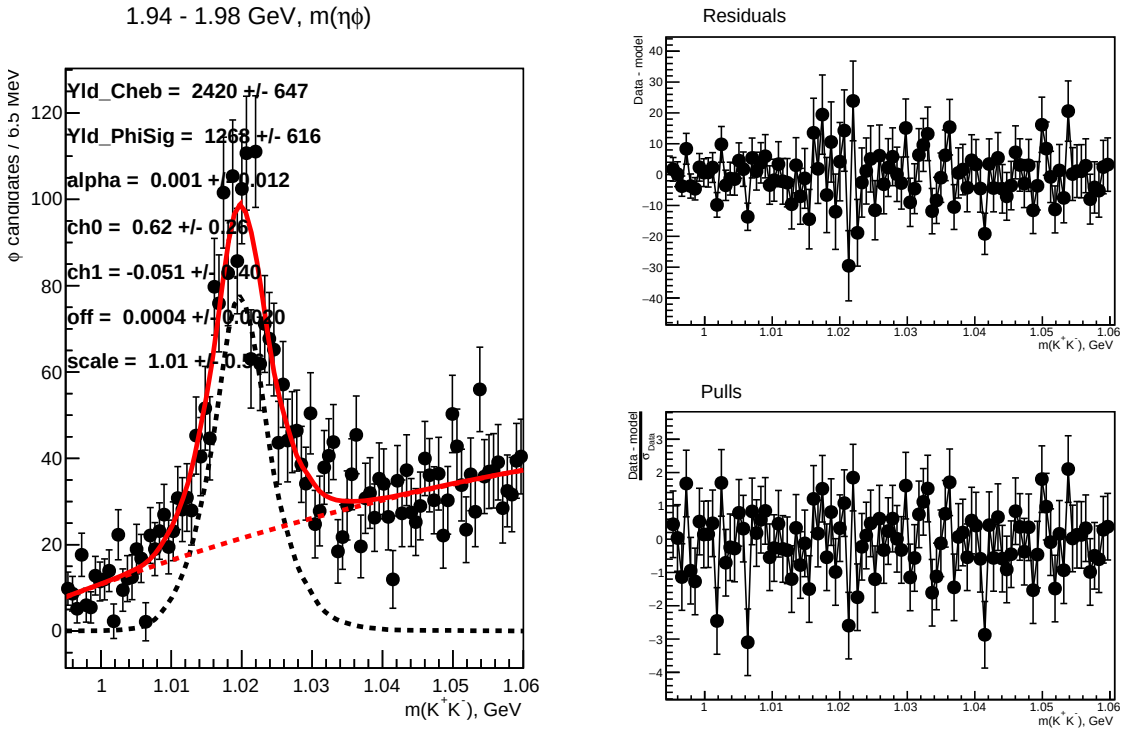
1.94 - 1.98 GeV, m(ηϕ)
Yld_Cheb = 2420 +/- 647
Yld_PhiSig = 1268 +/- 616
alpha = 0.001 +/- 0.012
ch0 = 0.62 +/- 0.26
ch1 = -0.051 +/- 0.040
off = 0.0004 +/- 0.0020
scale = 1.01 +/- 0.
φ candidates / 6.5 MeV
m(K⁺K⁻), GeV
Residuals
Data - model
m(K⁺K⁻), GeV
Pulls
(Data - model) / σ Data
m(K⁺K⁻), GeV

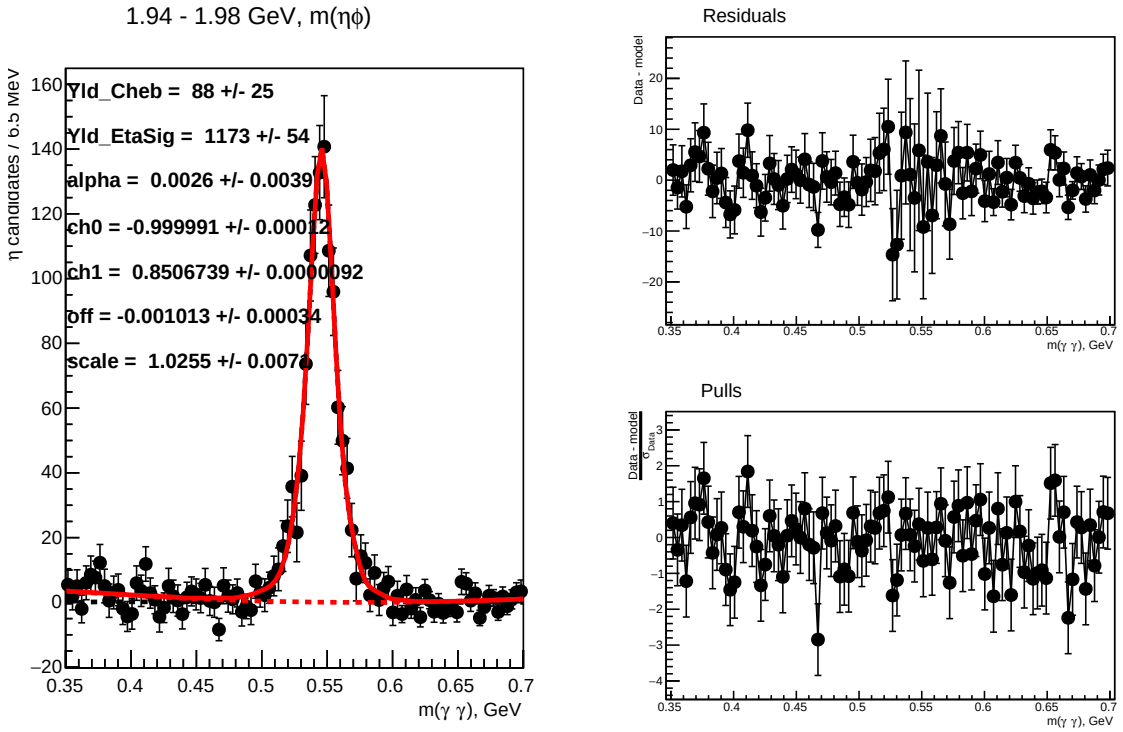
1.94 - 1.98 GeV, m(ηϕ)
Yld_Cheb = 88 +/- 25
Yld_EtaSig = 1173 +/- 54
alpha = 0.0026 +/- 0.0039
ch0 = -0.999991 +/- 0.00012
ch1 = 0.8506739 +/- 0.0000092
off = -0.001013 +/- 0.00034
scale = 1.0255 +/- 0.007
η candidates / 6.5 MeV
m(γ γ), GeV
Residuals
Data - model
m(γ γ), GeV
Pulls
(Data - model) / σ Data
m(γ γ), GeV

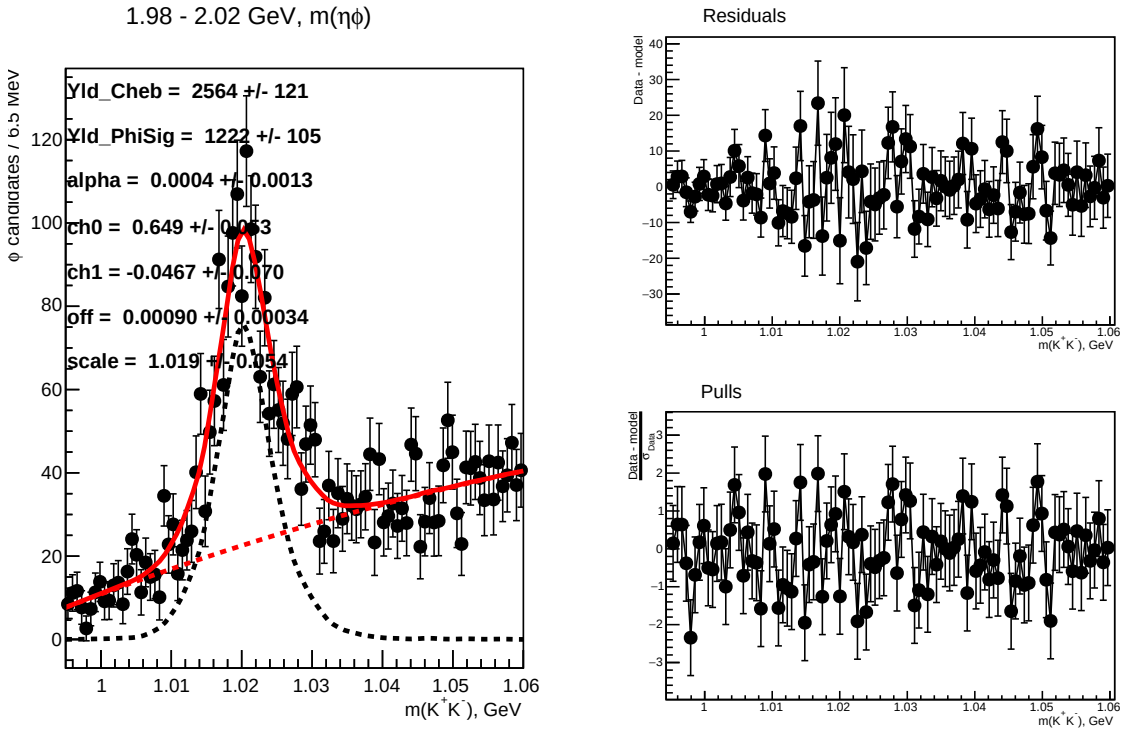
1.98 - 2.02 GeV, m(ηϕ)
Yld_Cheb = 2564 +/- 121
Yld_PhiSig = 1222 +/- 105
alpha = 0.0004 +/- 0.0013
ch0 = 0.649 +/- 0.063
ch1 = -0.0467 +/- 0.070
off = 0.00090 +/- 0.00034
scale = 1.019 +/- 0.054
ϕ candidates / 0.5 MeV
m(K⁺K⁻), GeV
Residuals
Data - model
m(K⁺K⁻), GeV
Pulls
(Data - model)/σ_Data
m(K⁺K⁻), GeV

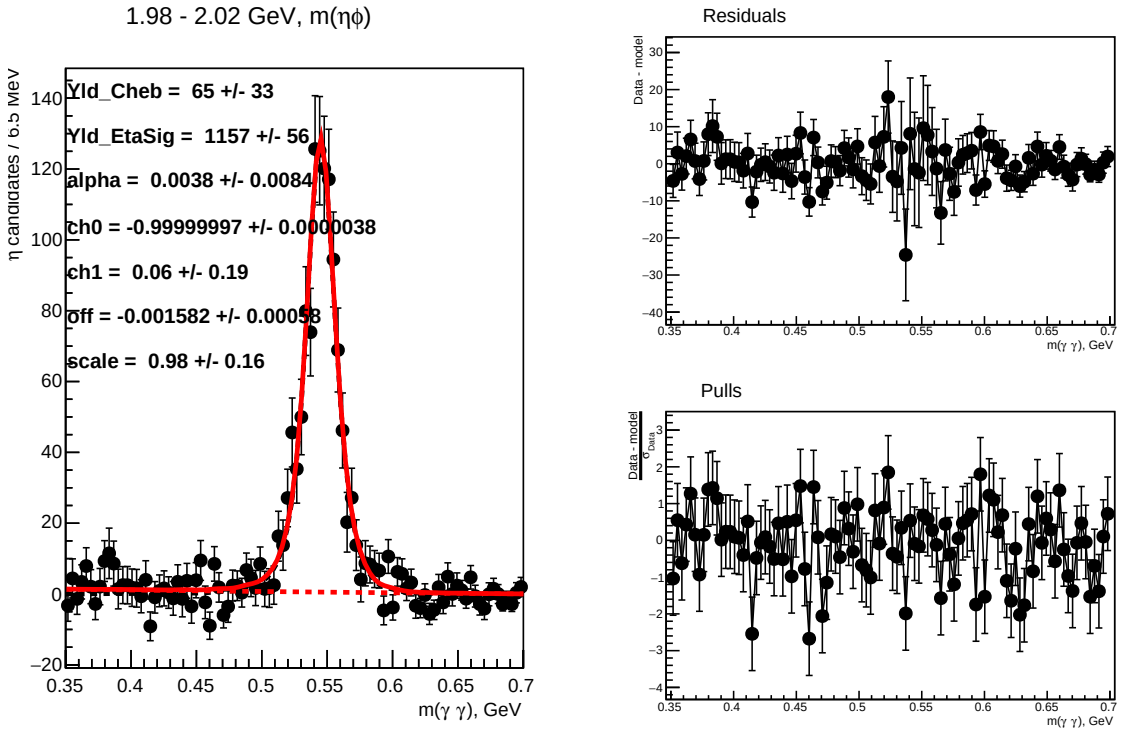
1.98 - 2.02 GeV, m(ηϕ)
Yld_Cheb = 65 +/- 33
Yld_EtaSig = 1157 +/- 56
alpha = 0.0038 +/- 0.0084
ch0 = -0.99999997 +/- 0.0000038
ch1 = 0.06 +/- 0.19
off = -0.001582 +/- 0.00058
scale = 0.98 +/- 0.16
η candidates / 0.5 MeV
m(γ γ), GeV
Residuals
Data - model
m(γ γ), GeV
Pulls
(Data - model)/σ_Data
m(γ γ), GeV

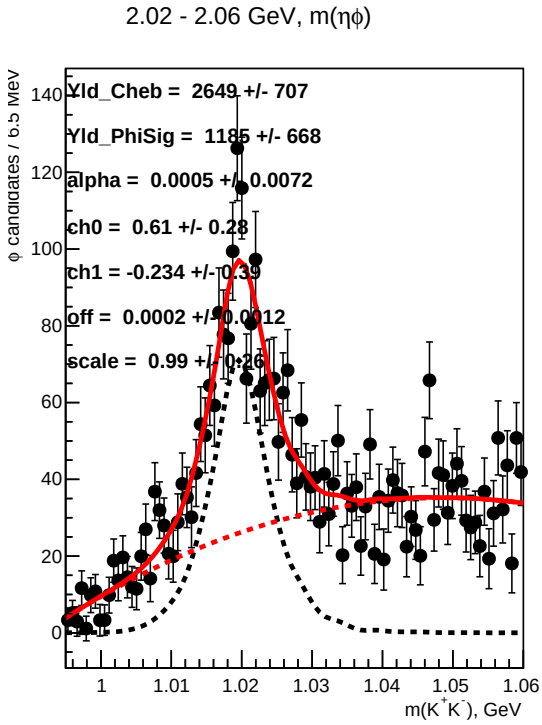
2.02 - 2.06 GeV, m(ηϕ)
Yld_Cheb = 2649 +/- 707
Yld_PhiSig = 1185 +/- 668
alpha = 0.0005 +/- 0.0072
ch0 = 0.61 +/- 0.28
ch1 = -0.234 +/- 0.39
off = 0.0002 +/- 0.0012
scale = 0.99 +/- 0.26
ϕ candidates / 6.5 MeV
m(K⁺K⁻), GeV

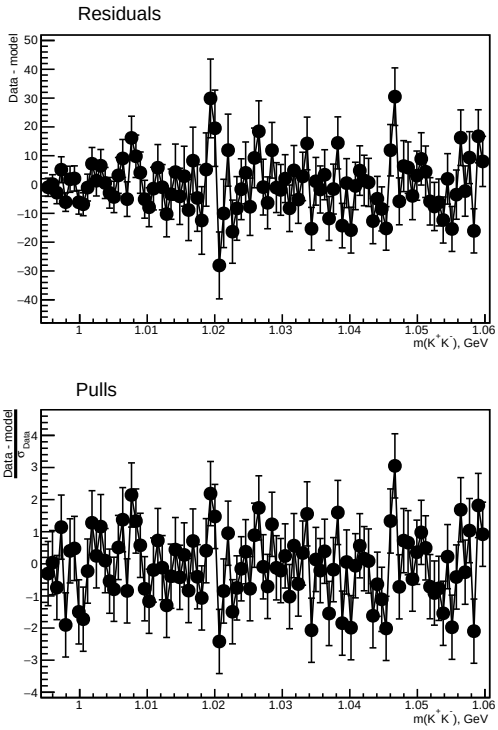
Residuals
Data - model
m(K⁺K⁻), GeV
Pulls
(Data - model) / σ Data
m(K⁺K⁻), GeV

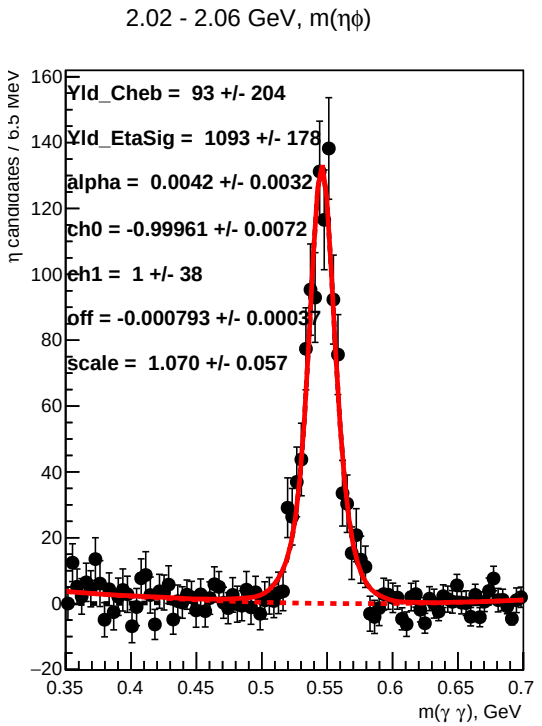
2.02 - 2.06 GeV, m(ηϕ)
Yld_Cheb = 93 +/- 204
Yld_EtaSig = 1093 +/- 178
alpha = 0.0042 +/- 0.0032
ch0 = -0.99961 +/- 0.0072
ch1 = 1 +/- 38
off = -0.000793 +/- 0.00037
scale = 1.070 +/- 0.057
η candidates / 6.5 MeV
m(γ γ), GeV

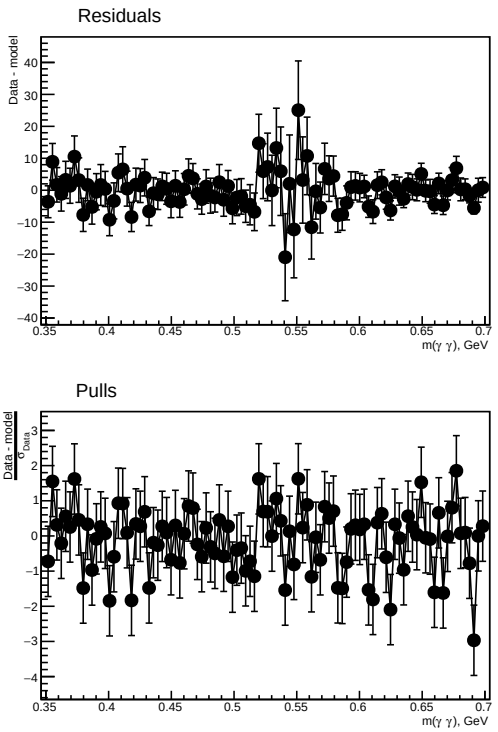
Residuals
Data - model
m(γ γ), GeV
Pulls
(Data - model) / σ Data
m(γ γ), GeV

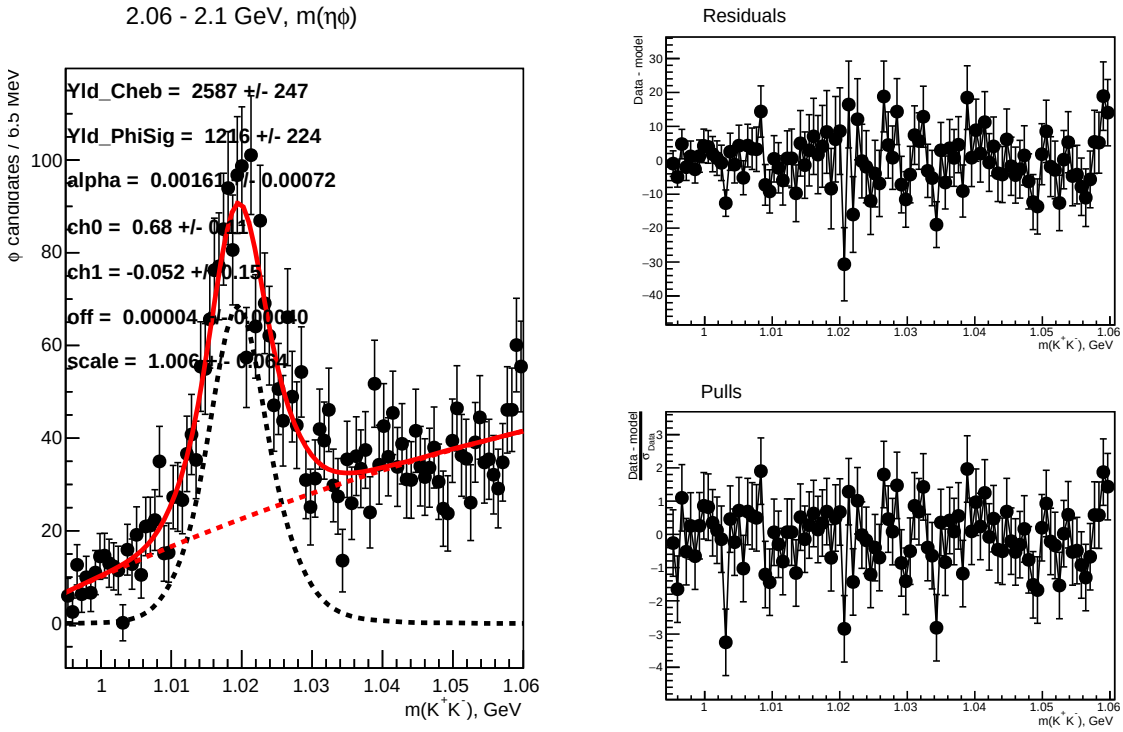
2.06 - 2.1 GeV, m(ηϕ)
Yld_Cheb = 2587 +/- 247
Yld_PhiSig = 1216 +/- 224
alpha = 0.00161 +/- 0.00072
ch0 = 0.68 +/- 0.11
ch1 = -0.052 +/- 0.15
off = 0.00004 +/- 0.00010
scale = 1.006 +/- 0.064
φ candidates / 6.5 MeV
m(K⁺K⁻), GeV
Residuals
Data - model
m(K⁺K⁻), GeV
Pulls
(Data - model) / σ Data
m(K⁺K⁻), GeV

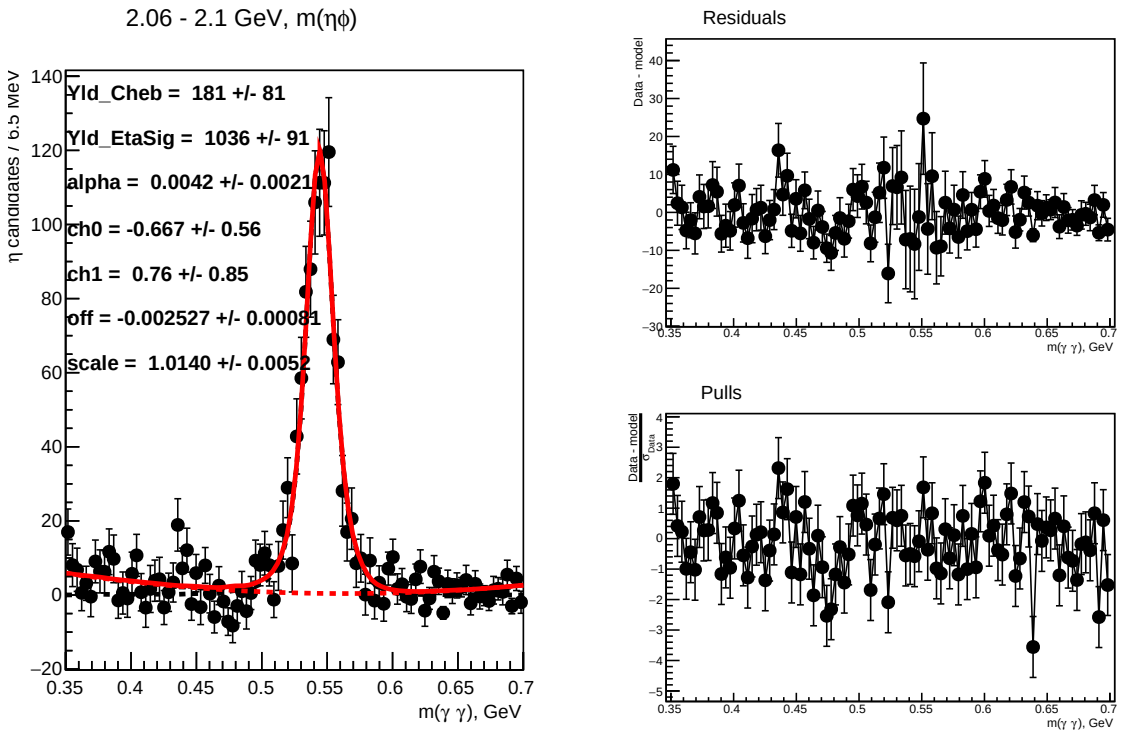
2.06 - 2.1 GeV, m(ηϕ)
Yld_Cheb = 181 +/- 81
Yld_EtaSig = 1036 +/- 91
alpha = 0.0042 +/- 0.0021
ch0 = -0.667 +/- 0.56
ch1 = 0.76 +/- 0.85
off = -0.002527 +/- 0.00081
scale = 1.0140 +/- 0.0052
η candidates / 6.5 MeV
m(γ γ), GeV
Residuals
Data - model
m(γ γ), GeV
Pulls
(Data - model) / σ Data
m(γ γ), GeV

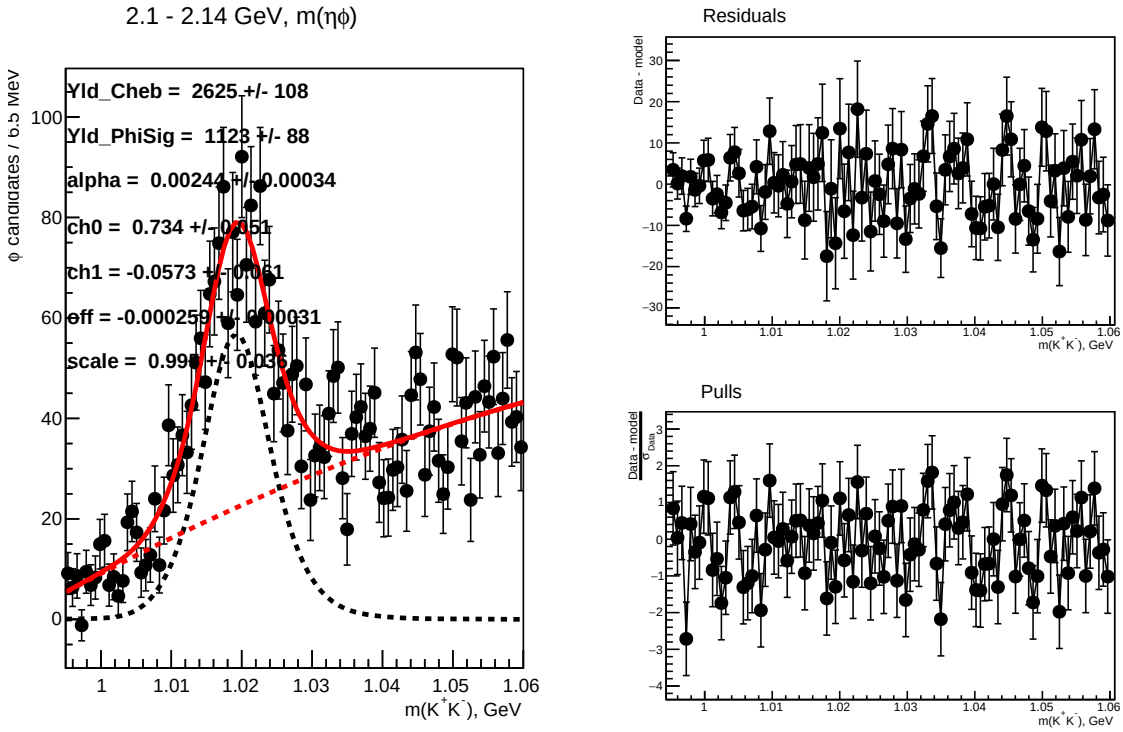
2.1 - 2.14 GeV, m(ηϕ)
Yld_Cheb = 2625 +/- 108
Yld_PhiSig = 1123 +/- 88
alpha = 0.00244 +/- 0.00034
ch0 = 0.734 +/- 0.051
ch1 = -0.0573 +/- 0.061
off = -0.000259 +/- 0.00031
scale = 0.998 +/- 0.036
φ candidates / 6.5 MeV
m(K⁺K⁻), GeV
Residuals
Data - model
m(K⁺K⁻), GeV
Pulls
(Data - model) / σ Data
m(K⁺K⁻), GeV

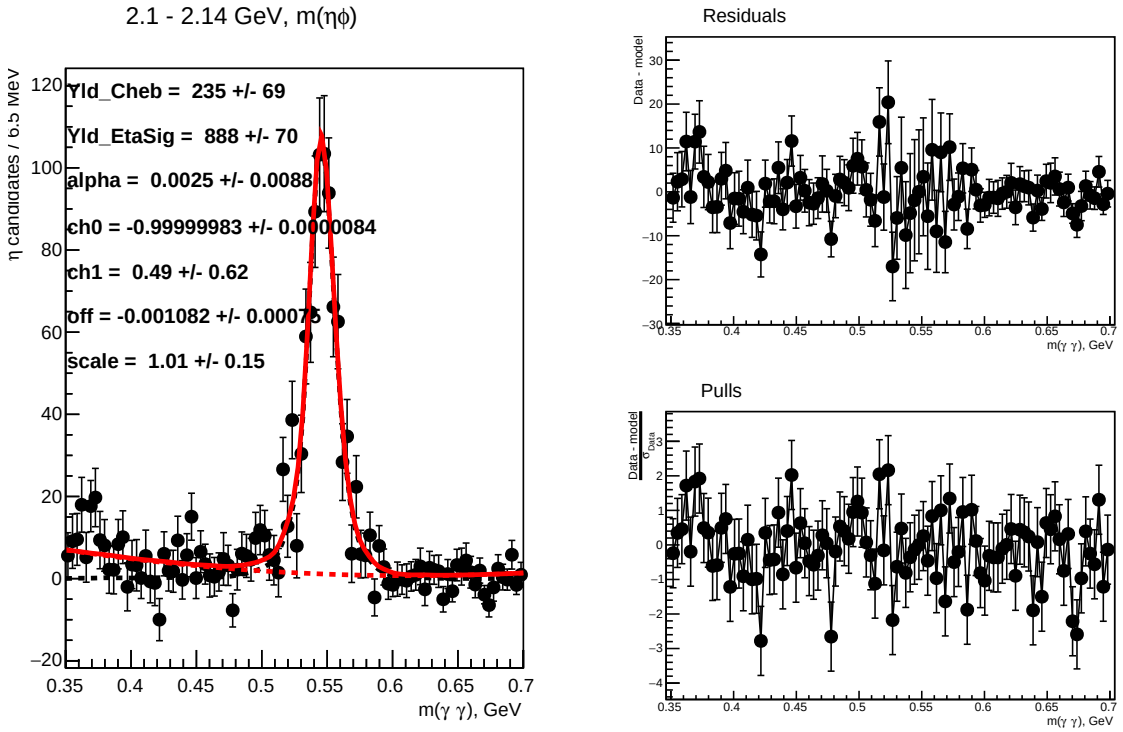
2.1 - 2.14 GeV, m(ηϕ)
Yld_Cheb = 235 +/- 69
Yld_EtaSig = 888 +/- 70
alpha = 0.0025 +/- 0.0088
ch0 = -0.99999983 +/- 0.0000084
ch1 = 0.49 +/- 0.62
off = -0.001082 +/- 0.00075
scale = 1.01 +/- 0.15
η candidates / 6.5 MeV
m(γ γ), GeV
Residuals
Data - model
m(γ γ), GeV
Pulls
(Data - model) / σ Data
m(γ γ), GeV

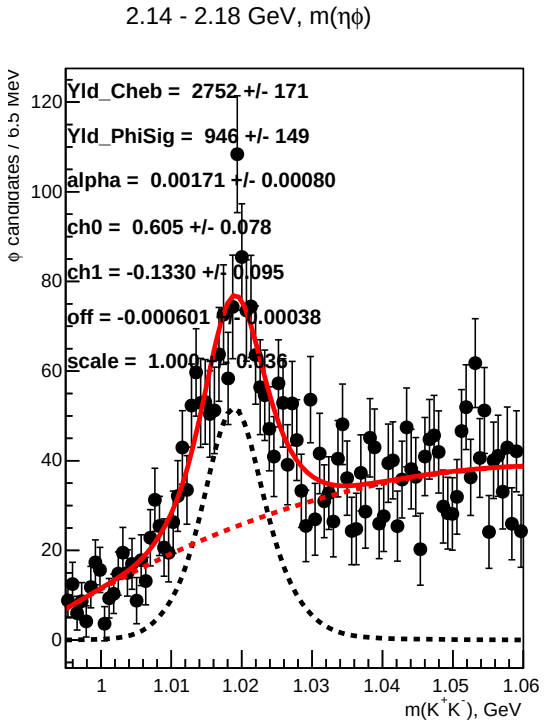
2.14 - 2.18 GeV, m(ηϕ)
Yld_Cheb = 2752 +/- 171
Yld_PhiSig = 946 +/- 149
alpha = 0.00171 +/- 0.00080
ch0 = 0.605 +/- 0.078
ch1 = -0.1330 +/- 0.095
off = -0.000601 +/- 0.00038
scale = 1.000 +/- 0.036
ϕ candidates / 6.5 MeV
m(K⁺K⁻), GeV

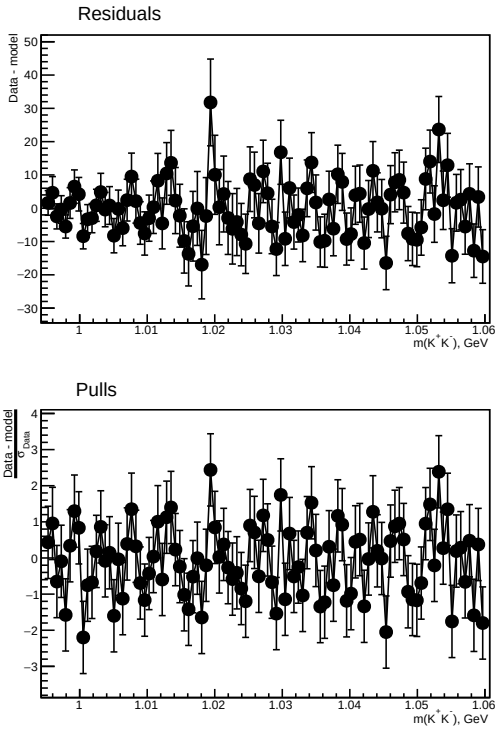
Residuals
Data - model
m(K⁺K⁻), GeV
Pulls
(Data - model) / σ Data
m(K⁺K⁻), GeV

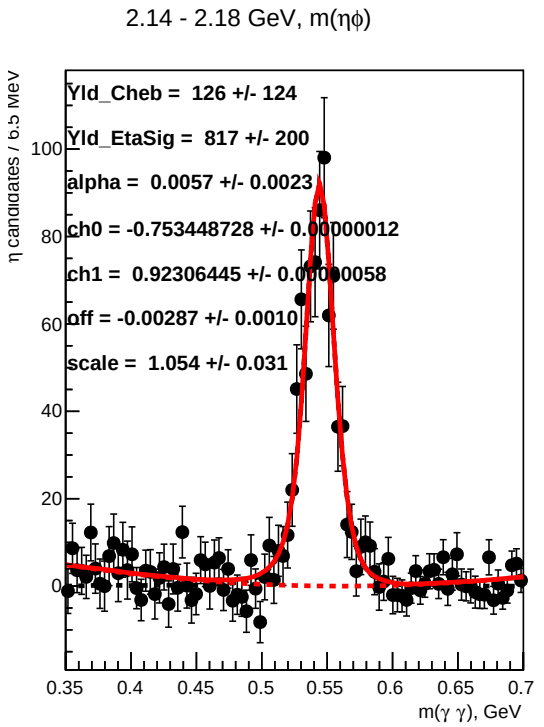
2.14 - 2.18 GeV, m(ηϕ)
Yld_Cheb = 126 +/- 124
Yld_EtaSig = 817 +/- 200
alpha = 0.0057 +/- 0.0023
ch0 = -0.753448728 +/- 0.000000012
ch1 = 0.92306445 +/- 0.00000058
off = -0.00287 +/- 0.0010
scale = 1.054 +/- 0.031
η candidates / 6.5 MeV
m(γ γ), GeV

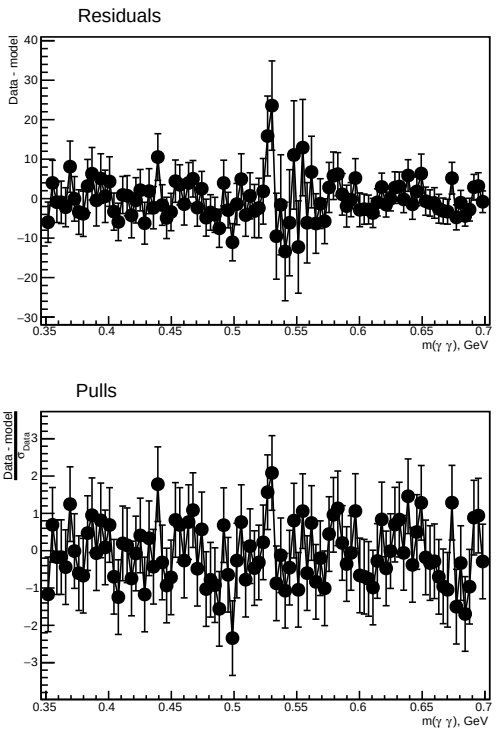
Residuals
Data - model
m(γ γ), GeV
Pulls
(Data - model) / σ Data
m(γ γ), GeV

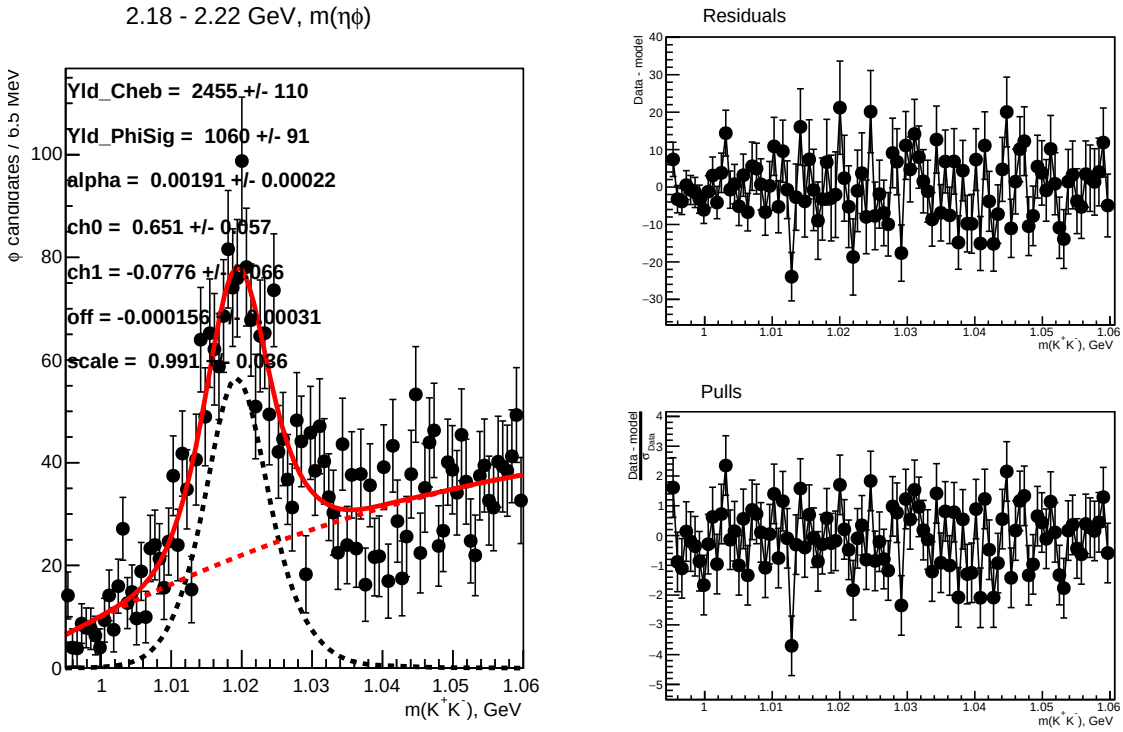
2.18 - 2.22 GeV, m(ηϕ)
Yld_Cheb = 2455 +/- 110
Yld_PhiSig = 1060 +/- 91
alpha = 0.00191 +/- 0.00022
ch0 = 0.651 +/- 0.057
ch1 = -0.0776 +/- 0.066
off = -0.000156 +/- 0.00031
scale = 0.991 +/- 0.036
φ candidates / 6.5 MeV
m(K⁺K⁻), GeV
Residuals
Data - model
m(K⁺K⁻), GeV
Pulls
(Data - model) / σ Data
m(K⁺K⁻), GeV

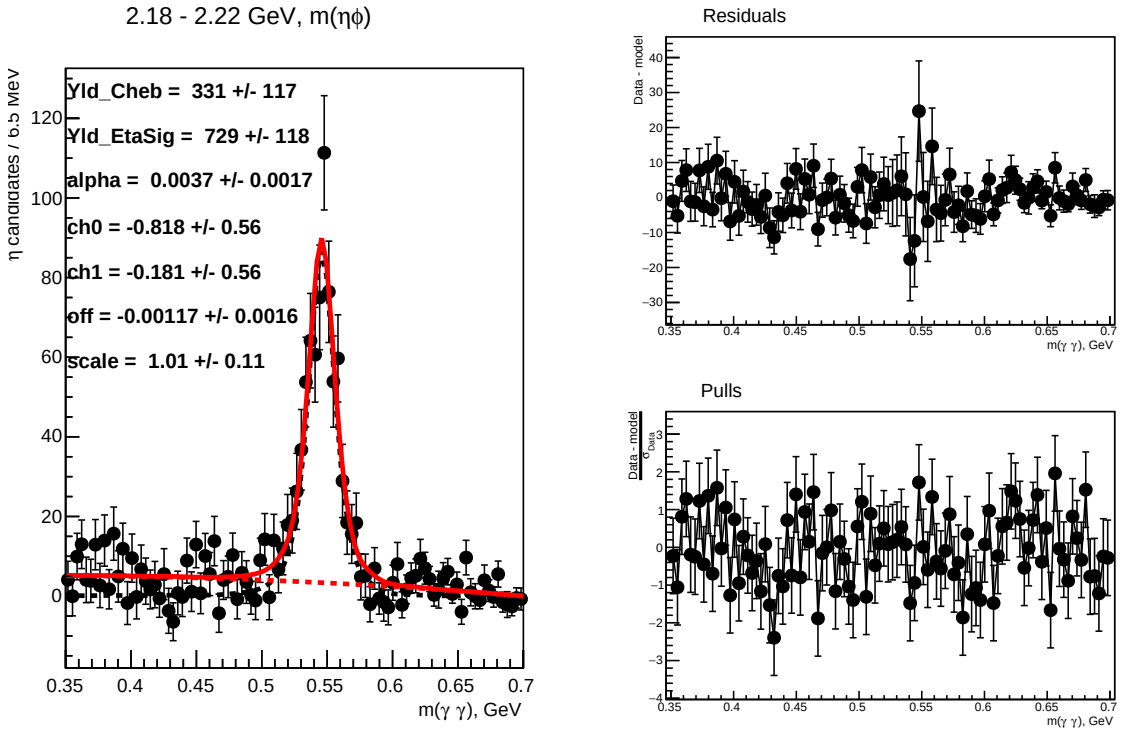
2.18 - 2.22 GeV, m(ηϕ)
Yld_Cheb = 331 +/- 117
Yld_EtaSig = 729 +/- 118
alpha = 0.0037 +/- 0.0017
ch0 = -0.818 +/- 0.56
ch1 = -0.181 +/- 0.56
off = -0.00117 +/- 0.0016
scale = 1.01 +/- 0.11
η candidates / 6.5 MeV
m(γ γ), GeV
Residuals
Data - model
m(γ γ), GeV
Pulls
(Data - model) / σ Data
m(γ γ), GeV

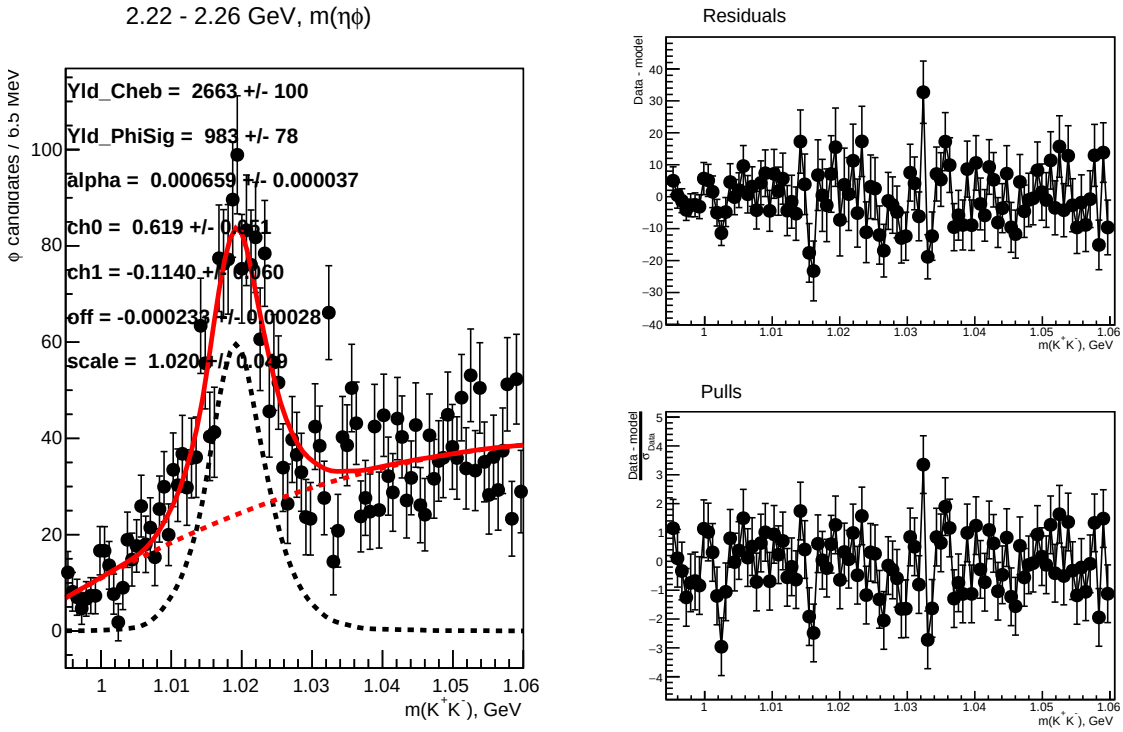
2.22 - 2.26 GeV, m(ηϕ)
Yld_Cheb = 2663 +/- 100
Yld_PhiSig = 983 +/- 78
alpha = 0.000659 +/- 0.000037
ch0 = 0.619 +/- 0.061
ch1 = -0.1140 +/- 0.0060
off = -0.000233 +/- 0.00028
scale = 1.020 +/- 0.049
ϕ candidates / 6.5 MeV
m(K⁺K⁻), GeV
Residuals
Data - model
m(K⁺K⁻), GeV
Pulls
(Data - model) / σData
m(K⁺K⁻), GeV

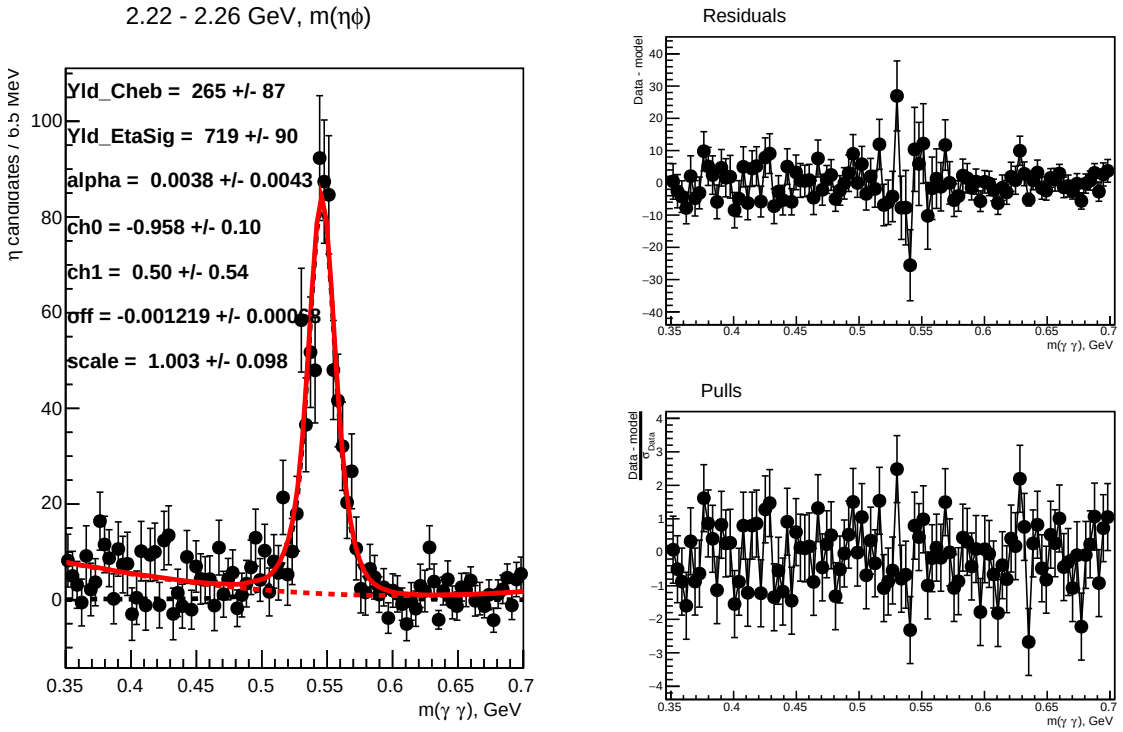
2.22 - 2.26 GeV, m(ηϕ)
Yld_Cheb = 265 +/- 87
Yld_EtaSig = 719 +/- 90
alpha = 0.0038 +/- 0.0043
ch0 = -0.958 +/- 0.10
ch1 = 0.50 +/- 0.54
off = -0.001219 +/- 0.00068
scale = 1.003 +/- 0.098
η candidates / 6.5 MeV
m(γ γ), GeV
Residuals
Data - model
m(γ γ), GeV
Pulls
(Data - model) / σData
m(γ γ), GeV

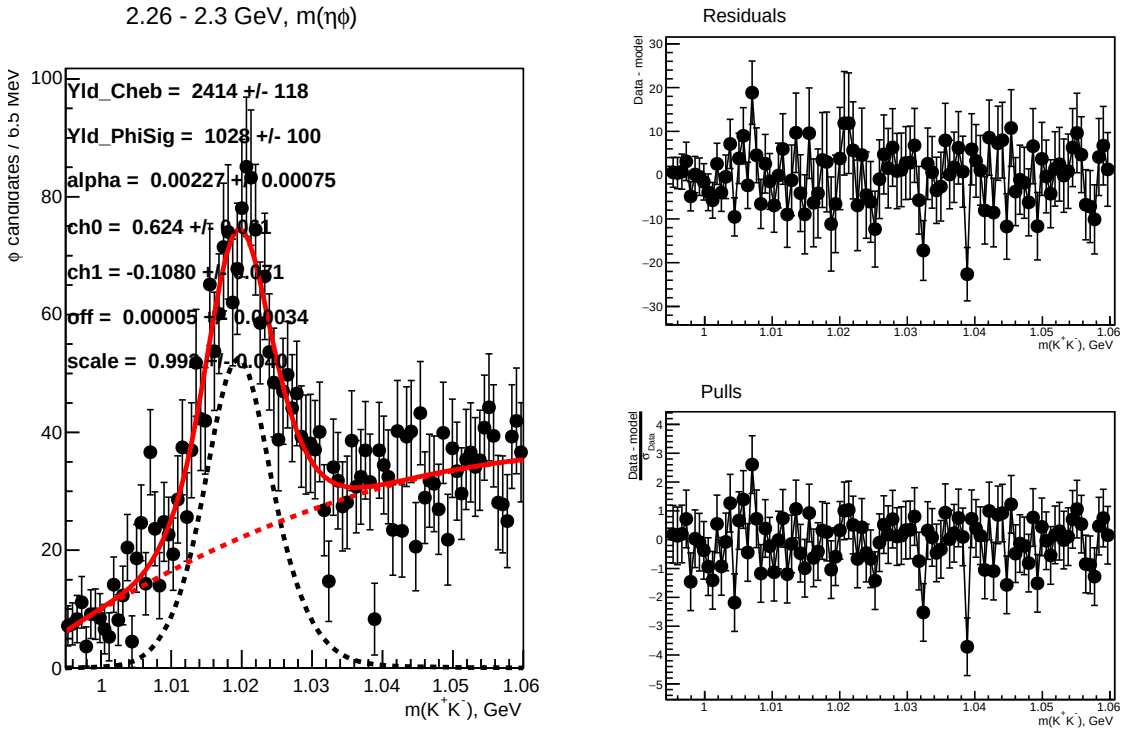
2.26 - 2.3 GeV, m(ηϕ)
Yld_Cheb = 2414 +/- 118
Yld_PhiSig = 1028 +/- 100
alpha = 0.00227 +/- 0.00075
ch0 = 0.624 +/- 0.061
ch1 = -0.1080 +/- 0.071
off = 0.00005 +/- 0.00034
scale = 0.993 +/- 0.040
ϕ candidates / 6.5 MeV
m(K⁺K⁻), GeV
Residuals
Data - model
m(K⁺K⁻), GeV
Pulls
(Data - model) / σ Data
m(K⁺K⁻), GeV

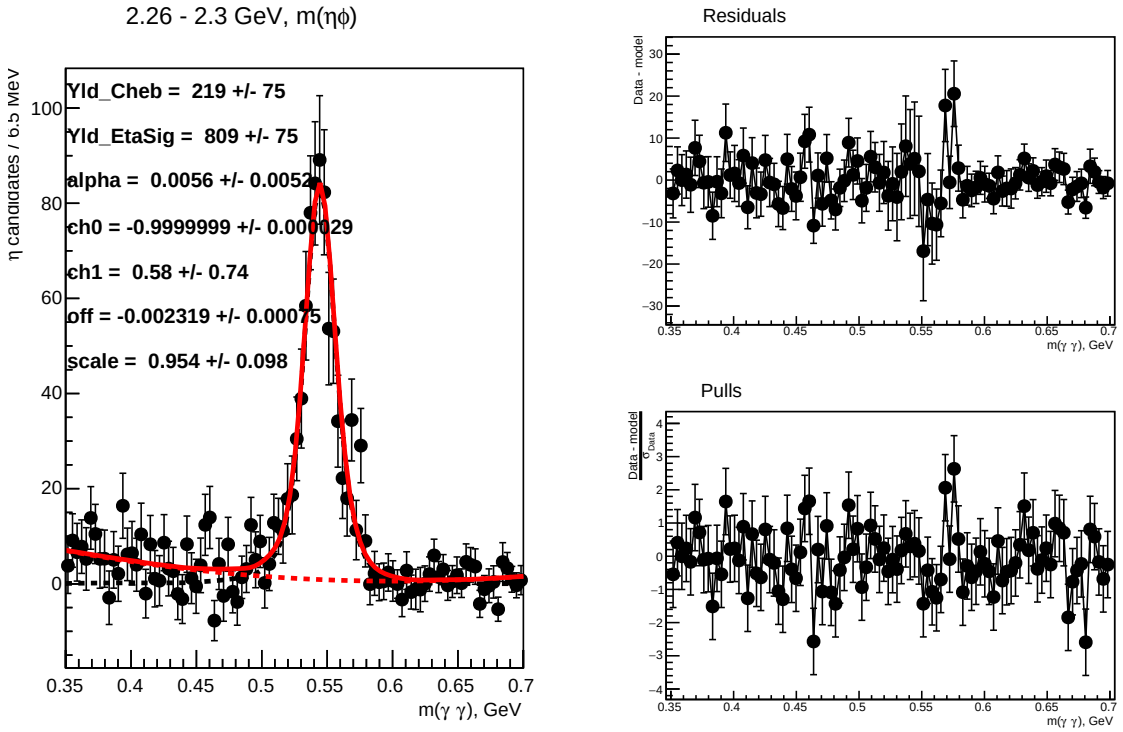
2.26 - 2.3 GeV, m(ηϕ)
Yld_Cheb = 219 +/- 75
Yld_EtaSig = 809 +/- 75
alpha = 0.0056 +/- 0.0052
ch0 = -0.9999999 +/- 0.000029
ch1 = 0.58 +/- 0.74
off = -0.002319 +/- 0.00075
scale = 0.954 +/- 0.098
η candidates / 6.5 MeV
m(γ γ), GeV
Residuals
Data - model
m(γ γ), GeV
Pulls
(Data - model) / σ Data
m(γ γ), GeV

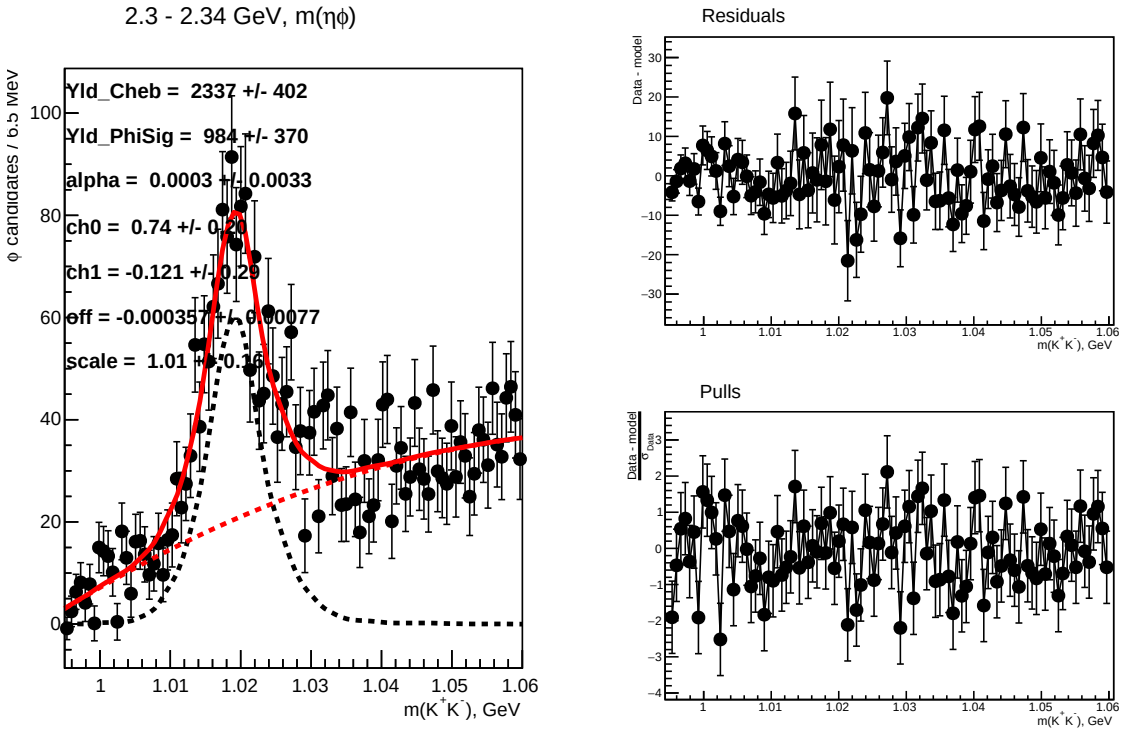
2.3 - 2.34 GeV, m(ηϕ)
Yld_Cheb = 2337 +/- 402
Yld_PhiSig = 984 +/- 370
alpha = 0.0003 +/- 0.0033
ch0 = 0.74 +/- 0.20
ch1 = -0.121 +/- 0.29
off = -0.000357 +/- 0.00077
scale = 1.01 +/- 0.16
ϕ candidates / 6.5 MeV
m(K⁺K⁻), GeV
Residuals
Data - model
m(K⁺K⁻), GeV
Pulls
(Data - model) / σData
m(K⁺K⁻), GeV

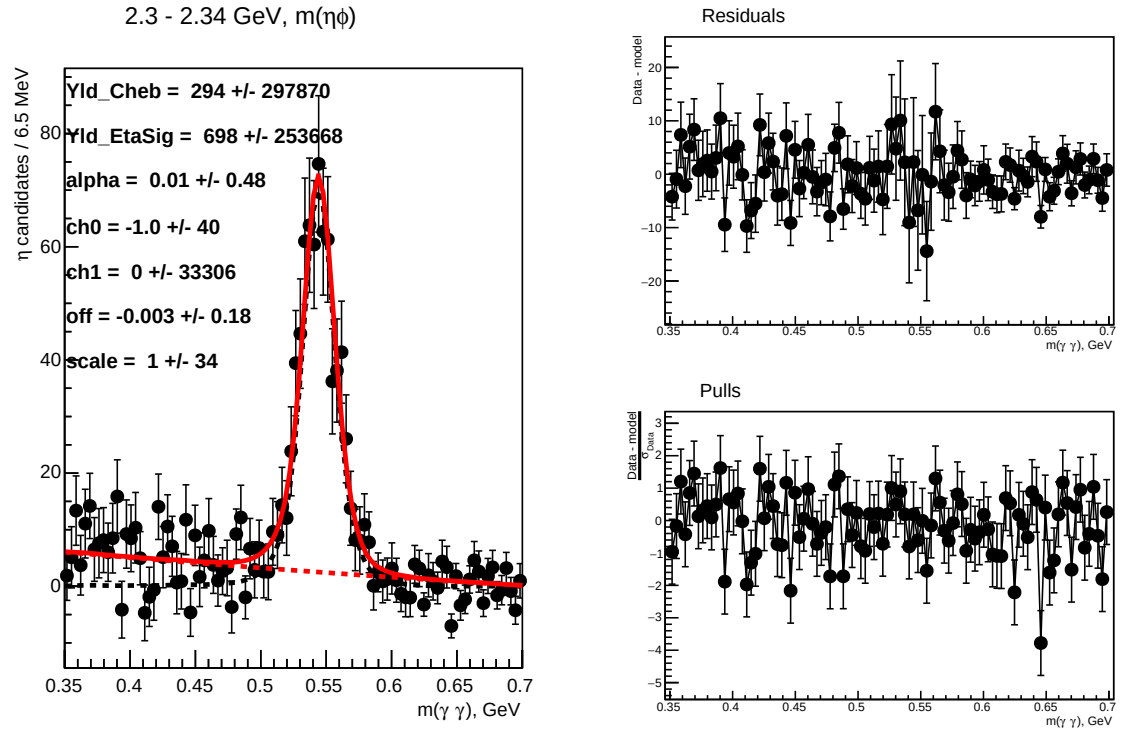
2.3 - 2.34 GeV, m(ηϕ)
Yld_Cheb = 294 +/- 297870
Yld_EtaSig = 698 +/- 253668
alpha = 0.01 +/- 0.48
ch0 = -1.0 +/- 40
ch1 = 0 +/- 33306
off = -0.003 +/- 0.18
scale = 1 +/- 34
η candidates / 6.5 MeV
m(γ γ), GeV
Residuals
Data - model
m(γ γ), GeV
Pulls
(Data - model) / σData
m(γ γ), GeV

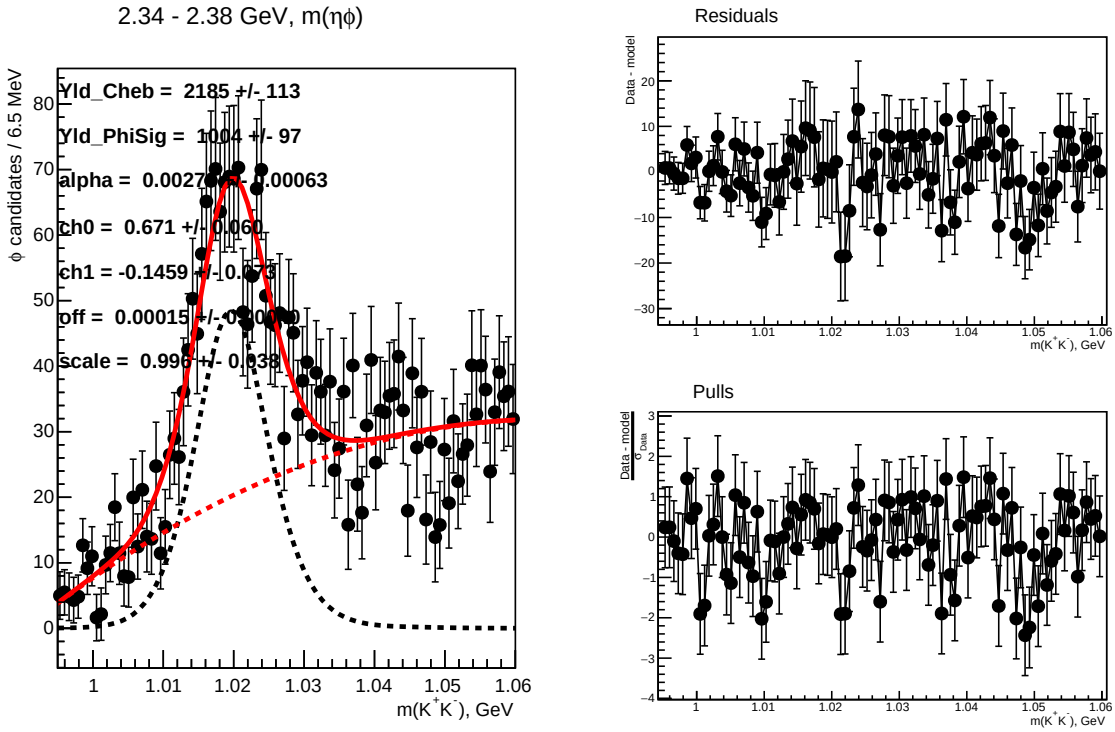
2.34 - 2.38 GeV, m(ηϕ)
Yld_Cheb = 2185 +/- 113
Yld_PhiSig = 1004 +/- 97
alpha = 0.0027 +/- 0.00063
ch0 = 0.671 +/- 0.060
ch1 = -0.1459 +/- 0.0
off = 0.00015 +/- 0.0
scale = 0.996 +/- 0.038
ϕ candidates / 6.5 MeV
m(K⁺K⁻), GeV
Residuals
Data - model
m(K⁺K⁻), GeV
Pulls
Data - model / σ Data
m(K⁺K⁻), GeV

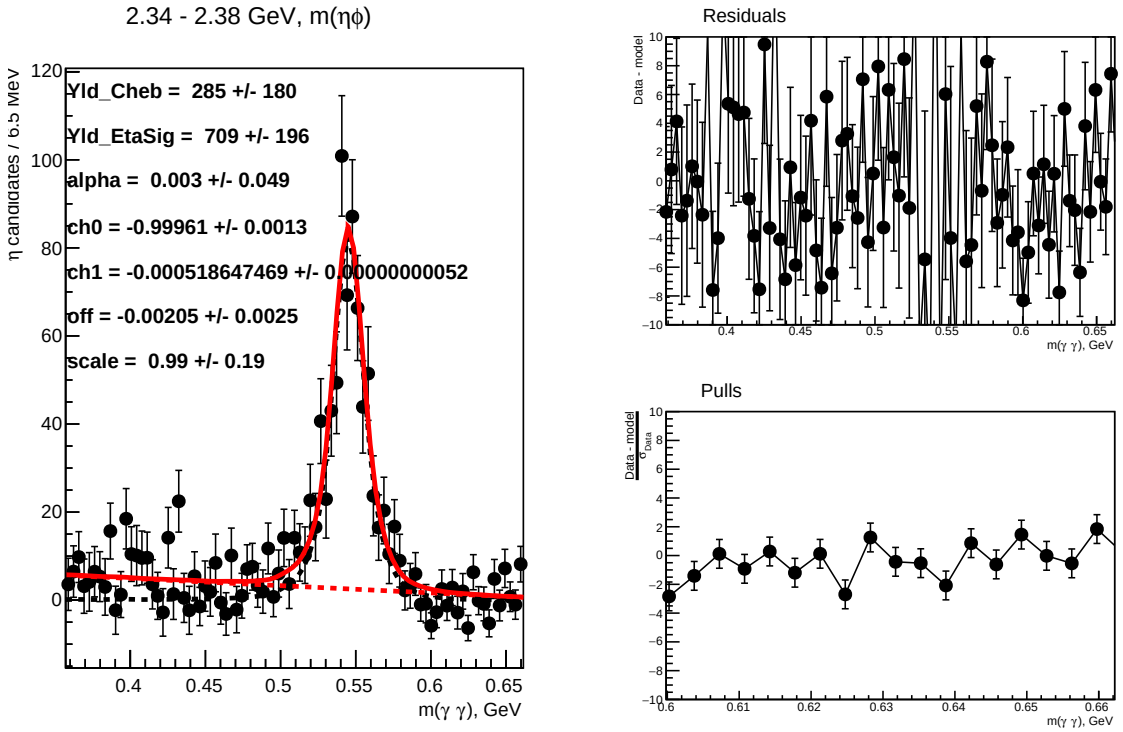
2.34 - 2.38 GeV, m(ηϕ)
Yld_Cheb = 285 +/- 180
Yld_EtaSig = 709 +/- 196
alpha = 0.003 +/- 0.049
ch0 = -0.99961 +/- 0.0013
ch1 = -0.000518647469 +/- 0.000000000052
off = -0.00205 +/- 0.0025
scale = 0.99 +/- 0.19
η candidates / 6.5 MeV
m(γ γ), GeV
Residuals
Data - model
m(γ γ), GeV
Pulls
Data - model / σ Data
m(γ γ), GeV

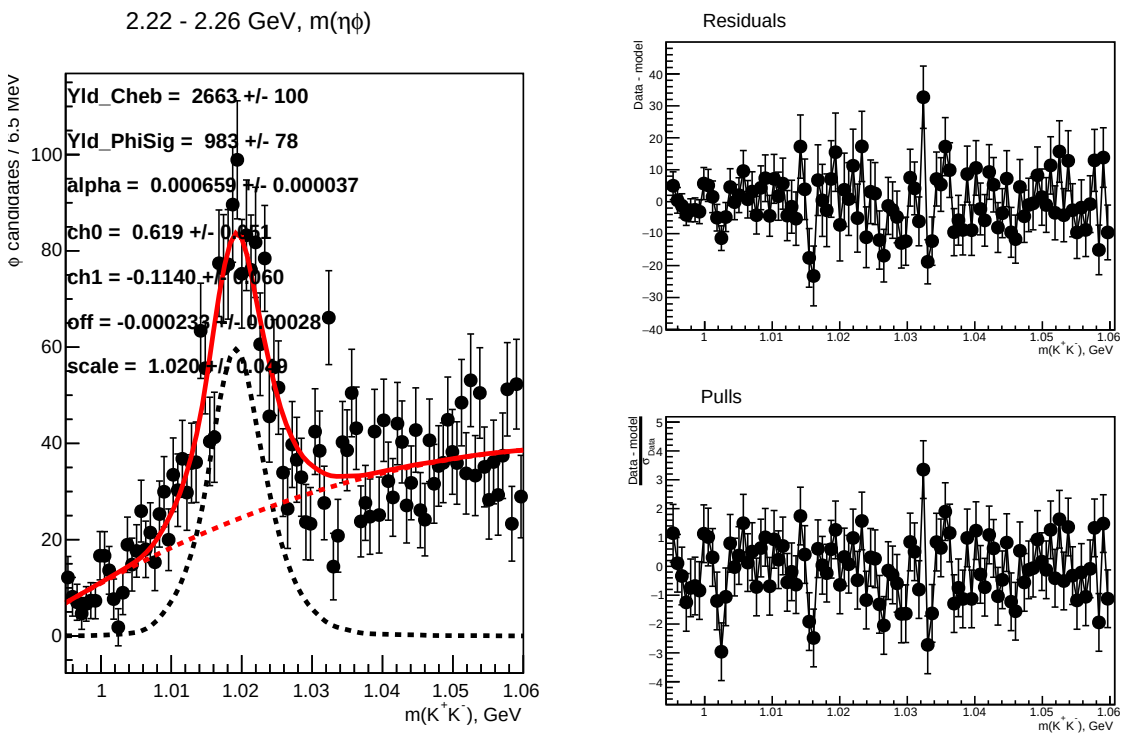
2.22 - 2.26 GeV, m(ηϕ)
Yld_Cheb = 2663 +/- 100
Yld_PhiSig = 983 +/- 78
alpha = 0.000659 +/- 0.000037
ch0 = 0.619 +/- 0.061
ch1 = -0.1140 +/- 0.0060
off = -0.000233 +/- 0.00028
scale = 1.020 +/- 0.049
ϕ candidates / 6.5 MeV
m(K⁺K⁻), GeV
Residuals
Data - model
m(K⁺K⁻), GeV
Pulls
(Data - model) / σData
m(K⁺K⁻), GeV

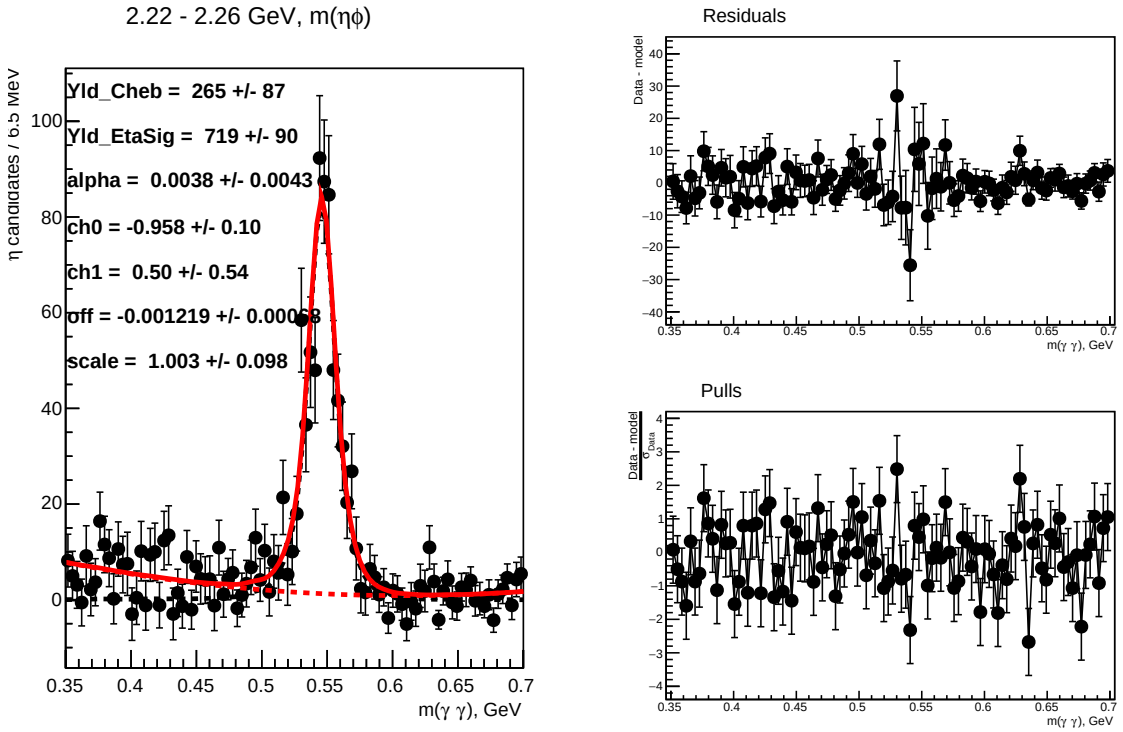
2.22 - 2.26 GeV, m(ηϕ)
Yld_Cheb = 265 +/- 87
Yld_EtaSig = 719 +/- 90
alpha = 0.0038 +/- 0.0043
ch0 = -0.958 +/- 0.10
ch1 = 0.50 +/- 0.54
off = -0.001219 +/- 0.00068
scale = 1.003 +/- 0.098
η candidates / 6.5 MeV
m(γ γ), GeV
Residuals
Data - model
m(γ γ), GeV
Pulls
(Data - model) / σData
m(γ γ), GeV

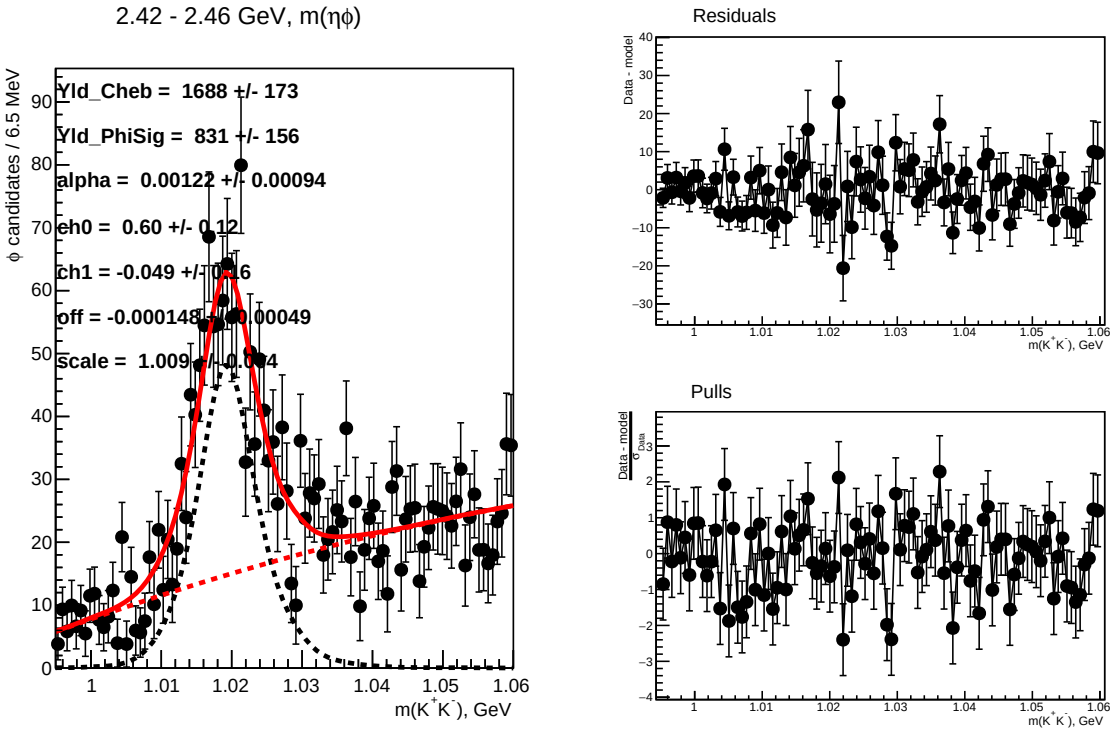
2.42 - 2.46 GeV, m(ηϕ)
Yld_Cheb = 1688 +/- 173
Yld_PhiSig = 831 +/- 156
alpha = 0.00122 +/- 0.00094
ch0 = 0.60 +/- 0.12
ch1 = -0.049 +/- 0.016
off = -0.000148 +/- 0.00049
scale = 1.009 +/- 0.004
ϕ candidates / 6.5 MeV
m(K⁺K⁻), GeV
Residuals
Data - model
m(K⁺K⁻), GeV
Pulls
(Data - model) / σ Data
m(K⁺K⁻), GeV

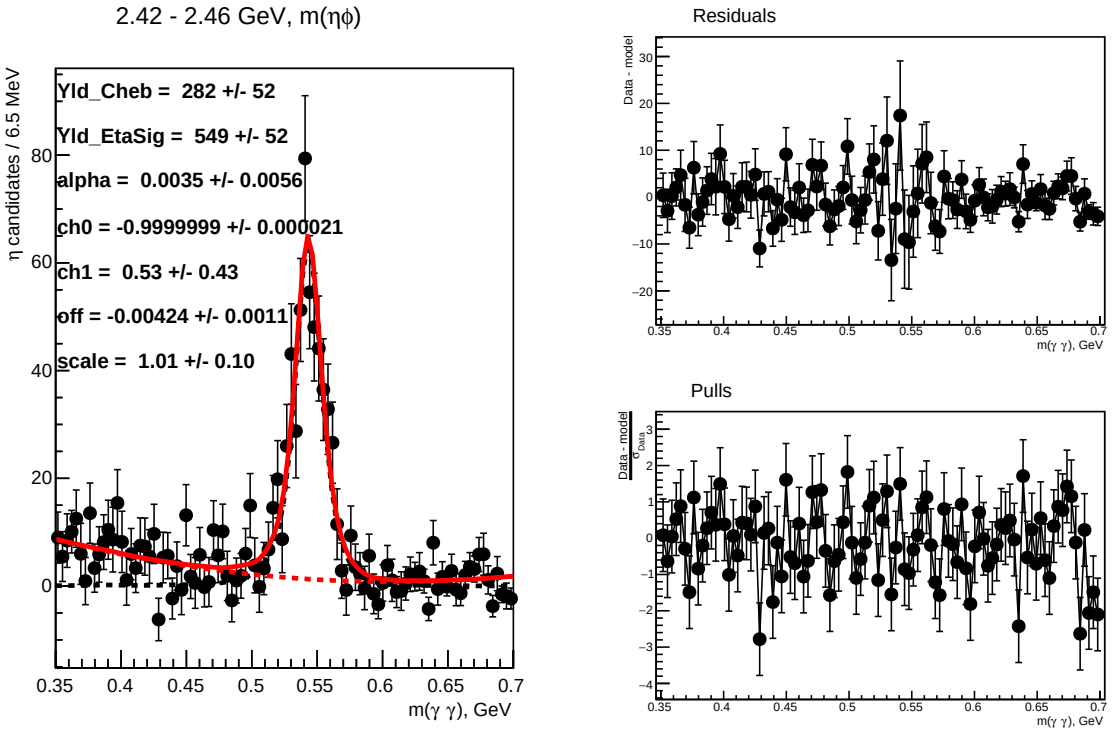
2.42 - 2.46 GeV, m(ηϕ)
Yld_Cheb = 282 +/- 52
Yld_EtaSig = 549 +/- 52
alpha = 0.0035 +/- 0.0056
ch0 = -0.9999999 +/- 0.000021
ch1 = 0.53 +/- 0.43
off = -0.00424 +/- 0.0011
scale = 1.01 +/- 0.10
η candidates / 6.5 MeV
m(γ γ), GeV
Residuals
Data - model
m(γ γ), GeV
Pulls
(Data - model) / σ Data
m(γ γ), GeV

Appendix C

Best fits according to AIC and BIC metrics

Table C.1: Best 3 models per mass bin by AIC (bins 1-13).

Mass bin (GeV)	Best models
1.50 GeV - 1.54 GeV	1. J=1 (L=0, 1); J=2 (L=1) 2. J=1 (L=0, 1); J=2 (L=1, 3); J=3 (L=3) (pos. refl.) 3. J=1 (L=0, 1); J=2 (L=2)
1.54 GeV - 1.58 GeV	1. J=1 (L=0, 1); J=2 (L=1) 2. J=1 (L=0, 1); J=2 (L=1, 3); J=3 (L=3) (neg. refl.) 3. J=1 (L=0); J=2 (L=1, 3); J=3 (L=3)
1.58 GeV - 1.62 GeV	1. J=1 (L=1); J=2 (L=1, 2, 3); J=3 (L=3) 2. J=1 (L=0, 1); J=3 (L=3) 3. J=1 (L=0, 1, 2); J=2 (L=1, 2, 3); J=3 (L=2, 3, 4)
1.62 GeV - 1.66 GeV	1. J=1 (L=0, 1, 2); J=2 (L=1, 2, 3); J=3 (L=2, 3, 4) 2. J=1 (L=1); J=2 (L=1, 2, 3); J=3 (L=3) 3. J=0 (L=1); J=1 (L=1); J=2 (L=1, 2, 3)
1.66 GeV - 1.70 GeV	1. J=1 (L=0, 1, 2); J=2 (L=1, 2, 3); J=3 (L=2, 3, 4) 2. J=1 (L=1); J=2 (L=1, 2, 3); J=3 (L=3) 3. J=0 (L=1); J=1 (L=1); J=2 (L=1, 2, 3)
1.70 GeV - 1.74 GeV	1. J=1 (L=0, 1, 2); J=2 (L=1, 2, 3); J=3 (L=2, 3, 4) 2. J=1 (L=1); J=2 (L=1, 2, 3); J=3 (L=3) 3. J=0 (L=1); J=1 (L=1); J=2 (L=1, 2, 3)
1.74 GeV - 1.78 GeV	1. J=1 (L=0, 1, 2); J=2 (L=1, 2, 3); J=3 (L=2, 3, 4) 2. J=1 (L=1); J=2 (L=1, 2, 3); J=3 (L=3) 3. J=0 (L=1); J=1 (L=1); J=2 (L=1, 3); J=3 (L=3)
1.78 GeV - 1.82 GeV	1. J=1 (L=0, 1, 2); J=2 (L=1, 2, 3); J=3 (L=2, 3, 4) 2. J=1 (L=1); J=2 (L=1, 2, 3); J=3 (L=3) 3. J=1 (L=0); J=2 (L=1, 3); J=3 (L=3)
1.82 GeV - 1.86 GeV	1. J=1 (L=0, 1, 2); J=2 (L=1, 2, 3); J=3 (L=2, 3, 4) 2. J=1 (L=1); J=2 (L=1, 2, 3); J=3 (L=3) 3. J=1 (L=0); J=2 (L=1, 3); J=3 (L=3)
1.86 GeV - 1.90 GeV	1. J=1 (L=0, 1, 2); J=2 (L=1, 2, 3); J=3 (L=2, 3, 4) 2. J=1 (L=1); J=2 (L=1, 2, 3); J=3 (L=3) 3. J=2 (L=1, 2, 3); J=3 (L=3)
1.90 GeV - 1.94 GeV	1. J=1 (L=0, 1, 2); J=2 (L=1, 2, 3); J=3 (L=2, 3, 4) 2. J=1 (L=1); J=2 (L=1, 2, 3); J=3 (L=3) 3. J=0 (L=1); J=1 (L=1); J=2 (L=1, 2, 3)
1.94 GeV - 1.98 GeV	1. J=1 (L=0, 1, 2); J=2 (L=1, 2, 3); J=3 (L=2, 3, 4) 2. J=1 (L=0, 1); J=2 (L=1, 3); J=3 (L=3) (pos. refl.) 3. J=1 (L=1); J=2 (L=1, 2, 3); J=3 (L=3)
1.98 GeV - 2.02 GeV	1. J=1 (L=0, 1, 2); J=2 (L=1, 2, 3); J=3 (L=2, 3, 4) 2. J=1 (L=1); J=2 (L=1, 2, 3); J=3 (L=3) 3. J=0 (L=1); J=1 (L=1); J=2 (L=1, 2, 3)

Table C.2: Best 3 models per mass bin by AIC (bins 14-25).

Mass bin (GeV)	Best models
2.02 GeV - 2.06 GeV	1. J=1 (L=0, 1, 2); J=2 (L=1, 2, 3); J=3 (L=2, 3, 4) 2. J=1 (L=1); J=2 (L=1, 2, 3); J=3 (L=3) 3. J=1 (L=0); J=2 (L=1, 3); J=3 (L=3)
2.06 GeV - 2.10 GeV	1. J=1 (L=0, 1, 2); J=2 (L=1, 2, 3); J=3 (L=2, 3, 4) 2. J=1 (L=1); J=2 (L=1, 2, 3); J=3 (L=3) 3. J=1 (L=0); J=2 (L=1, 3); J=3 (L=3)
2.10 GeV - 2.14 GeV	1. J=1 (L=0, 1, 2); J=2 (L=1, 2, 3); J=3 (L=2, 3, 4) 2. J=1 (L=1); J=2 (L=1, 2, 3); J=3 (L=3) 3. J=2 (L=1, 2, 3); J=3 (L=3)
2.14 GeV - 2.18 GeV	1. J=1 (L=0, 1, 2); J=2 (L=1, 2, 3); J=3 (L=2, 3, 4) 2. J=1 (L=1); J=2 (L=1, 2, 3); J=3 (L=3) 3. J=1 (L=0, 1); J=2 (L=1, 3); J=3 (L=3) (pos. refl.)
2.18 GeV - 2.22 GeV	1. J=1 (L=1); J=2 (L=1, 2, 3); J=3 (L=3) 2. J=1 (L=0, 1, 2); J=2 (L=1, 2, 3); J=3 (L=2, 3, 4) 3. J=0 (L=1); J=1 (L=1); J=2 (L=1, 2, 3)
2.22 GeV - 2.26 GeV	1. J=1 (L=1); J=2 (L=1, 2, 3); J=3 (L=3) 2. J=1 (L=0, 1); J=2 (L=1, 3); J=3 (L=3) (pos. refl.) 3. J=1 (L=0, 1, 2); J=2 (L=1, 2, 3); J=3 (L=2, 3, 4)
2.26 GeV - 2.30 GeV	1. J=1 (L=1); J=2 (L=1, 2, 3); J=3 (L=3) 2. J=1 (L=0, 1, 2); J=2 (L=1, 2, 3); J=3 (L=2, 3, 4) 3. J=0 (L=1); J=1 (L=1); J=2 (L=1, 3); J=3 (L=3)
2.30 GeV - 2.34 GeV	1. J=1 (L=0, 1, 2); J=2 (L=1, 2, 3); J=3 (L=2, 3, 4) 2. J=1 (L=1); J=2 (L=1, 2, 3); J=3 (L=3) 3. J=1 (L=0, 1); J=2 (L=1, 3); J=3 (L=3) (neg. refl.)
2.34 GeV - 2.38 GeV	1. J=1 (L=0, 1, 2); J=2 (L=1, 2, 3); J=3 (L=2, 3, 4) 2. J=1 (L=0, 1); J=2 (L=1, 3); J=3 (L=3) (pos. refl.) 3. J=1 (L=1); J=2 (L=1, 2, 3); J=3 (L=3)
2.38 GeV - 2.42 GeV	1. J=1 (L=0, 1, 2); J=2 (L=1, 2, 3); J=3 (L=2, 3, 4) 2. J=1 (L=1); J=2 (L=1, 2, 3); J=3 (L=3) 3. J=1 (L=1); J=2 (L=1, 3); J=3 (L=3)
2.42 GeV - 2.46 GeV	1. J=1 (L=0, 1, 2); J=2 (L=1, 2, 3); J=3 (L=2, 3, 4) 2. J=1 (L=1); J=2 (L=1, 2, 3); J=3 (L=3) 3. J=0 (L=1); J=1 (L=1); J=2 (L=1, 3); J=3 (L=3)
2.46 GeV - 2.50 GeV	1. J=1 (L=1); J=2 (L=1, 2, 3); J=3 (L=3) 2. J=1 (L=0, 1, 2); J=2 (L=1, 2, 3); J=3 (L=2, 3, 4) 3. J=0 (L=1); J=1 (L=1); J=2 (L=1, 3); J=3 (L=3)

Table C.3: Best 3 models per mass bin by BIC (bins 1-13).

Mass bin (GeV)	Best models
1.50 GeV - 1.54 GeV	1. J=1 (L=0, 1); J=2 (L=1) 2. J=1 (L=0, 1); J=2 (L=1, 3); J=3 (L=3) (pos. refl.) 3. J=1 (L=0, 1); J=2 (L=2)
1.54 GeV - 1.58 GeV	1. J=1 (L=0, 1); J=2 (L=1) 2. J=1 (L=0, 1); J=2 (L=3) 3. J=1 (L=0, 1); J=2 (L=1, 3); J=3 (L=3) (pos. refl.)
1.58 GeV - 1.62 GeV	1. J=1 (L=0, 1); J=3 (L=3) 2. J=1 (L=0, 1); J=2 (L=2) 3. J=1 (L=0, 1); J=2 (L=1)
1.62 GeV - 1.66 GeV	1. J=1 (L=0, 1); J=2 (L=1) 2. J=1 (L=0, 1); J=2 (L=2) 3. J=1 (L=0, 1); J=3 (L=3)
1.66 GeV - 1.70 GeV	1. J=1 (L=0, 1); J=2 (L=1) 2. J=1 (L=0, 1); J=2 (L=2) 3. J=1 (L=0, 1); J=2 (L=3)
1.70 GeV - 1.74 GeV	1. J=1 (L=0, 1); J=2 (L=1) 2. J=1 (L=0, 1); J=2 (L=2) 3. J=1 (L=0, 1); J=2 (L=3)
1.74 GeV - 1.78 GeV	1. J=1 (L=0, 1); J=2 (L=1) 2. J=1 (L=0, 1); J=2 (L=2) 3. J=1 (L=0, 1); J=2 (L=1, 3); J=3 (L=3) (pos. refl.)
1.78 GeV - 1.82 GeV	1. J=1 (L=0, 1); J=2 (L=1) 2. J=1 (L=0); J=2 (L=1, 3); J=3 (L=3) 3. J=1 (L=1); J=2 (L=1, 2, 3); J=3 (L=3)
1.82 GeV - 1.86 GeV	1. J=1 (L=0, 1); J=2 (L=1) 2. J=1 (L=0); J=2 (L=1, 3); J=3 (L=3) 3. J=1 (L=0, 1); J=2 (L=1, 3); J=3 (L=3) (pos. refl.)
1.86 GeV - 1.90 GeV	1. J=1 (L=0, 1); J=2 (L=1) 2. J=1 (L=0, 1); J=2 (L=1, 3); J=3 (L=3) (pos. refl.) 3. J=1 (L=1); J=2 (L=1, 2, 3); J=3 (L=3)
1.90 GeV - 1.94 GeV	1. J=1 (L=0, 1); J=2 (L=1) 2. J=0 (L=1); J=1 (L=1); J=2 (L=1, 2, 3) 3. J=1 (L=0, 1); J=2 (L=3)
1.94 GeV - 1.98 GeV	1. J=1 (L=0, 1); J=2 (L=1, 3); J=3 (L=3) (pos. refl.) 2. J=1 (L=0, 1); J=2 (L=1) 3. J=1 (L=0, 1); J=2 (L=3)
1.98 GeV - 2.02 GeV	1. J=1 (L=0, 1); J=2 (L=1) 2. J=0 (L=1); J=1 (L=1); J=2 (L=1, 2, 3) 3. J=1 (L=0, 1); J=2 (L=1, 3); J=3 (L=3) (pos. refl.)

Table C.4: Best 3 models per mass bin by BIC (bins 14-25).

Mass bin (GeV)	Best models
2.02 GeV - 2.06 GeV	1. J=1 (L=0, 1); J=2 (L=1, 3); J=3 (L=3) (pos. refl.) 2. J=1 (L=0, 1); J=2 (L=1) 3. J=1 (L=0); J=2 (L=1, 3); J=3 (L=3)
2.06 GeV - 2.10 GeV	1. J=1 (L=0, 1); J=2 (L=1) 2. J=1 (L=0, 1); J=2 (L=3) 3. J=1 (L=1); J=2 (L=1, 2, 3); J=3 (L=3)
2.10 GeV - 2.14 GeV	1. J=1 (L=0, 1); J=2 (L=1) 2. J=1 (L=0, 1); J=2 (L=1, 3); J=3 (L=3) (pos. refl.) 3. J=1 (L=0, 1); J=2 (L=3)
2.14 GeV - 2.18 GeV	1. J=1 (L=0, 1); J=2 (L=1, 3); J=3 (L=3) (pos. refl.) 2. J=1 (L=0, 1); J=2 (L=1) 3. J=1 (L=1); J=2 (L=1, 2, 3); J=3 (L=3)
2.18 GeV - 2.22 GeV	1. J=1 (L=0, 1); J=2 (L=1, 3); J=3 (L=3) (pos. refl.) 2. J=1 (L=0, 1); J=2 (L=1) 3. J=1 (L=1); J=2 (L=1, 2, 3); J=3 (L=3)
2.22 GeV - 2.26 GeV	1. J=1 (L=0, 1); J=2 (L=1, 3); J=3 (L=3) (pos. refl.) 2. J=1 (L=0, 1); J=2 (L=1, 3); J=3 (L=3) (neg. refl.) 3. J=1 (L=0, 1); J=2 (L=1)
2.26 GeV - 2.30 GeV	1. J=1 (L=0, 1); J=2 (L=1, 3); J=3 (L=3) (neg. refl.) 2. J=1 (L=1); J=2 (L=1, 2, 3); J=3 (L=3) 3. J=1 (L=0, 1); J=2 (L=1, 3); J=3 (L=3) (pos. refl.)
2.30 GeV - 2.34 GeV	1. J=1 (L=0, 1); J=2 (L=1, 3); J=3 (L=3) (neg. refl.) 2. J=1 (L=0, 1); J=2 (L=1, 3); J=3 (L=3) (pos. refl.) 3. J=1 (L=0, 1); J=2 (L=1)
2.34 GeV - 2.38 GeV	1. J=1 (L=0, 1); J=2 (L=1, 3); J=3 (L=3) (pos. refl.) 2. J=1 (L=0, 1); J=2 (L=1) 3. J=1 (L=1); J=2 (L=1, 2, 3); J=3 (L=3)
2.38 GeV - 2.42 GeV	1. J=1 (L=0, 1); J=2 (L=1, 3); J=3 (L=3) (pos. refl.) 2. J=1 (L=1); J=2 (L=1, 2, 3); J=3 (L=3) 3. J=1 (L=1); J=2 (L=1, 3); J=3 (L=3)
2.42 GeV - 2.46 GeV	1. J=1 (L=0, 1); J=2 (L=1, 3); J=3 (L=3) (pos. refl.) 2. J=1 (L=1); J=2 (L=1, 2, 3); J=3 (L=3) 3. J=0 (L=1); J=1 (L=1); J=2 (L=1, 3); J=3 (L=3)
2.46 GeV - 2.50 GeV	1. J=1 (L=0, 1); J=2 (L=1, 3); J=3 (L=3) (pos. refl.) 2. J=1 (L=0, 1); J=2 (L=1, 3); J=3 (L=3) (neg. refl.) 3. J=1 (L=1); J=2 (L=1, 2, 3); J=3 (L=3)

Appendix D

Additional partial wave fit plots

Plots for additional mass independent partial wave fits that did not make it to the main body of the thesis are presented here. Statistical errors on the partial waves are not included.

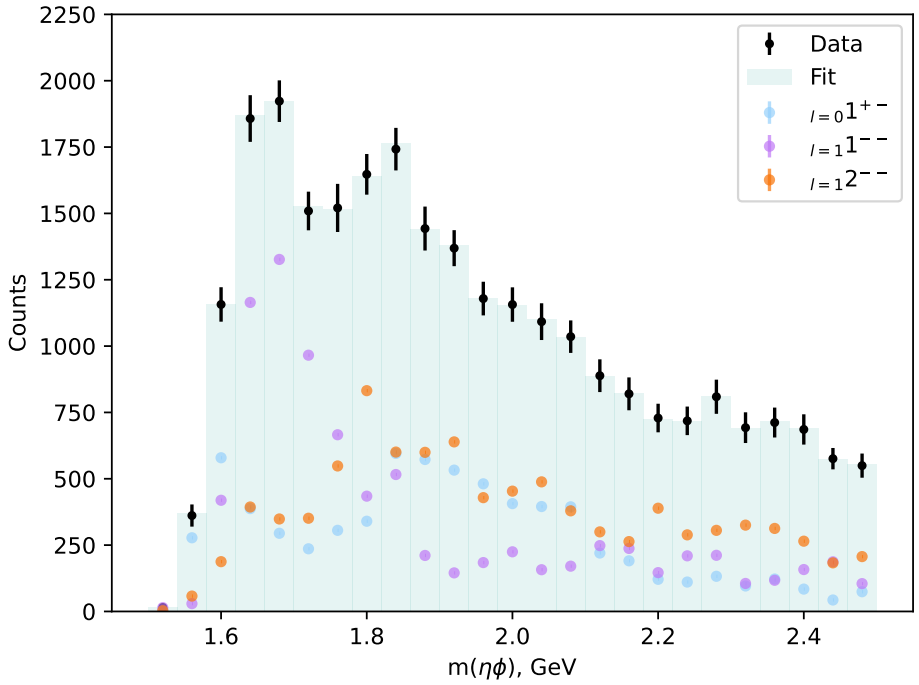

Figure D.1: Invariant mass spectrum projection with 1^{+-}, 1^{--}, and $2^{--}_{L=1}$ waves.

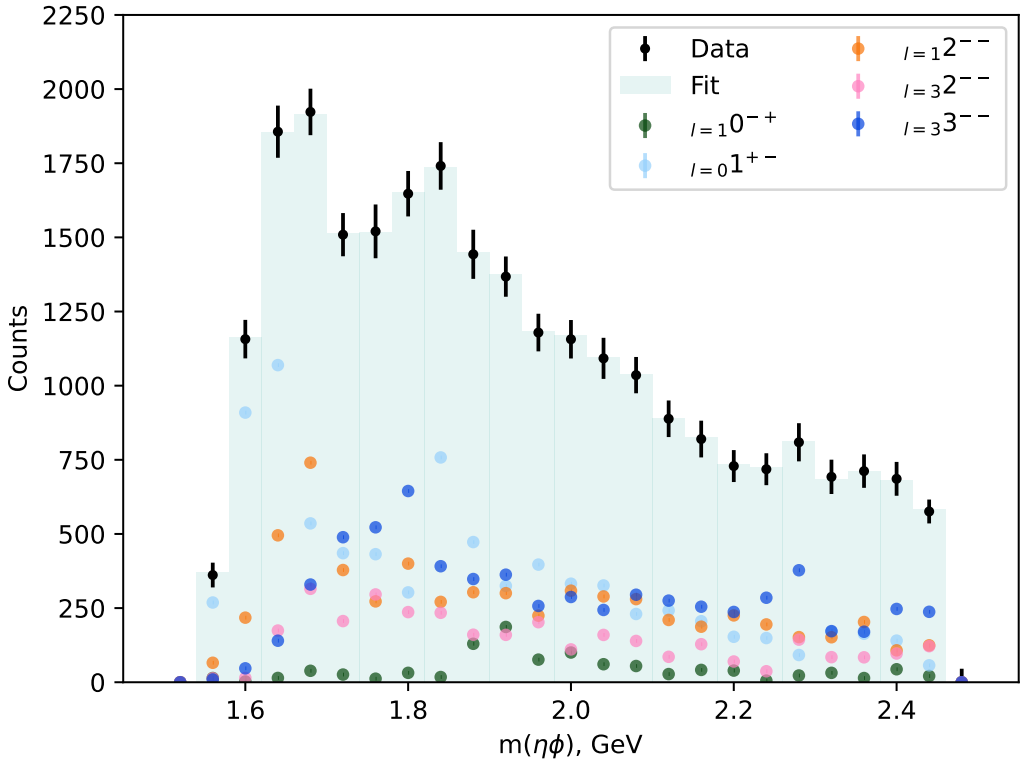

Figure D.2: Invariant mass spectrum projection without 1^{--} waves.

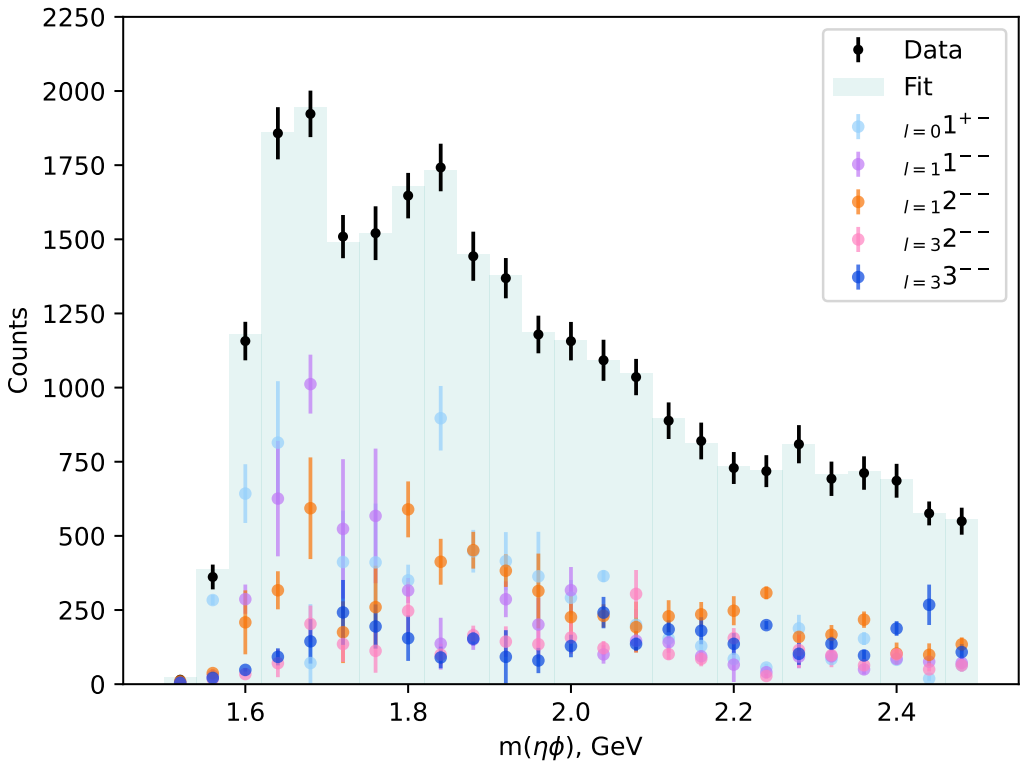

Figure D.3: Invariant mass spectrum projection for waveset with $1^{+-}, 1^{--}, 2^{--}, 3^{--}$ waves with only positive reflectivity amplitudes. Error bars indicate variation between local minima.

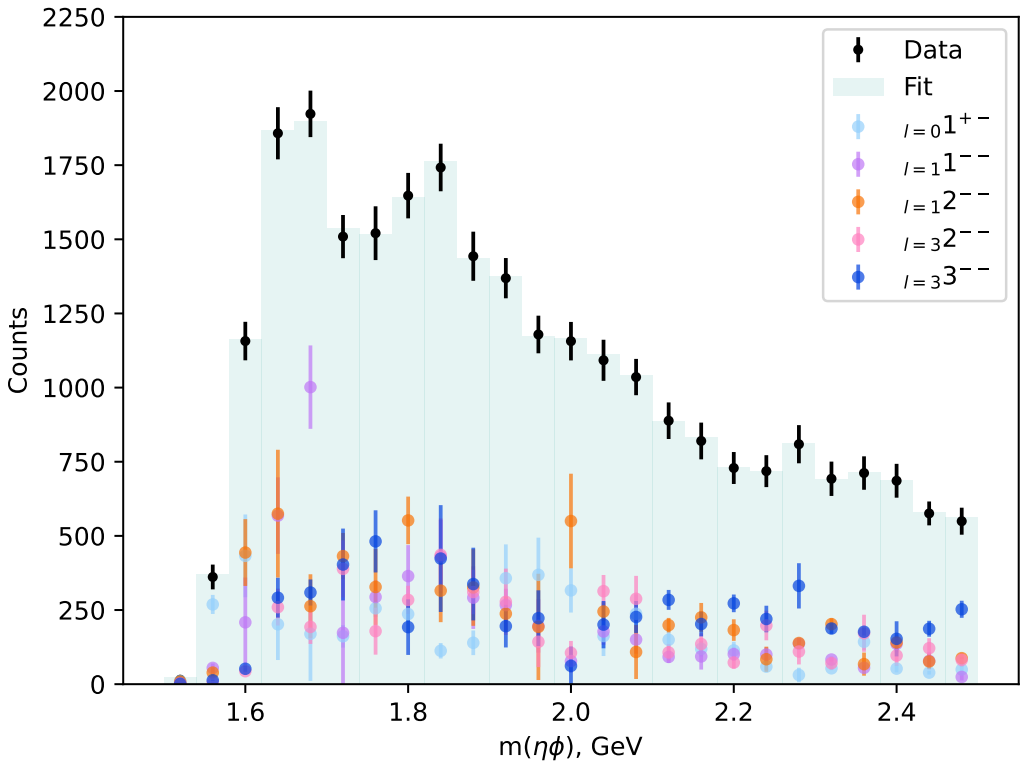

Figure D.4: Invariant mass spectrum projection for waveset with $1^{+-}, 1^{--}, 2^{--}, 3^{--}$ waves with only negative reflectivity amplitudes. Error bars indicate variation between local minima.

Appendix E

Angular distributions for nominal fit

Fits to the angular distributions using the nominal waveset for invariant mass bins up to 2.02 GeV are provided below.

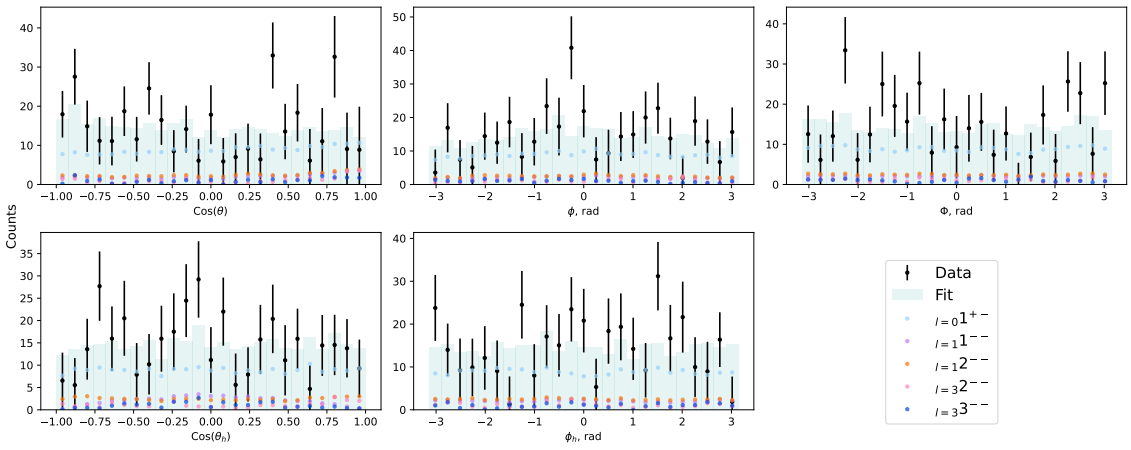

Figure E.1: 1.54 GeV - 1.58 GeV.

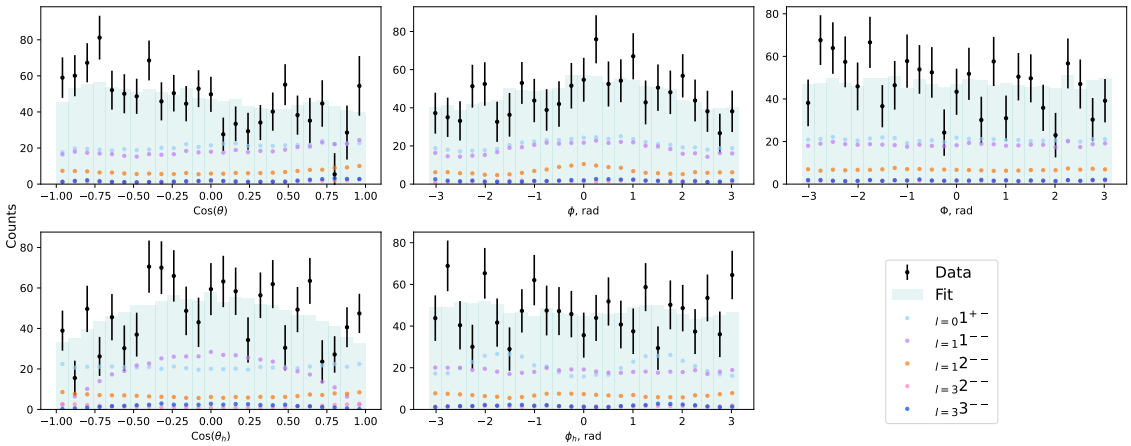

Figure E.2: 1.58 GeV - 1.62 GeV.

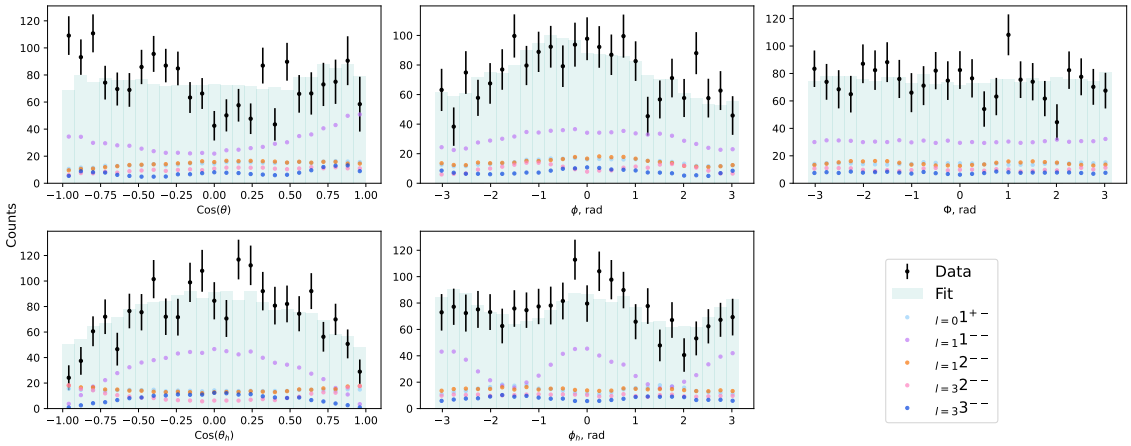

Figure E.3: 1.62 GeV - 1.66 GeV.

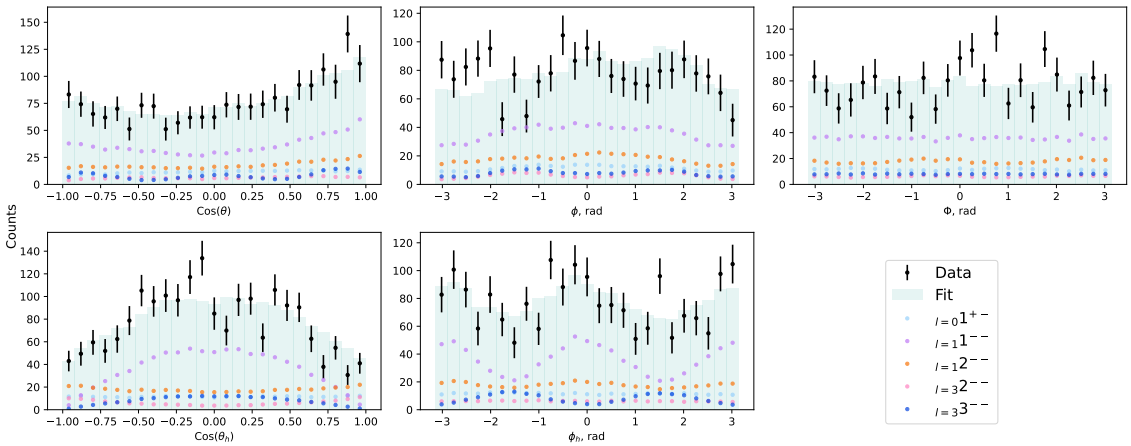

Figure E.4: 1.66 GeV - 1.7 GeV.

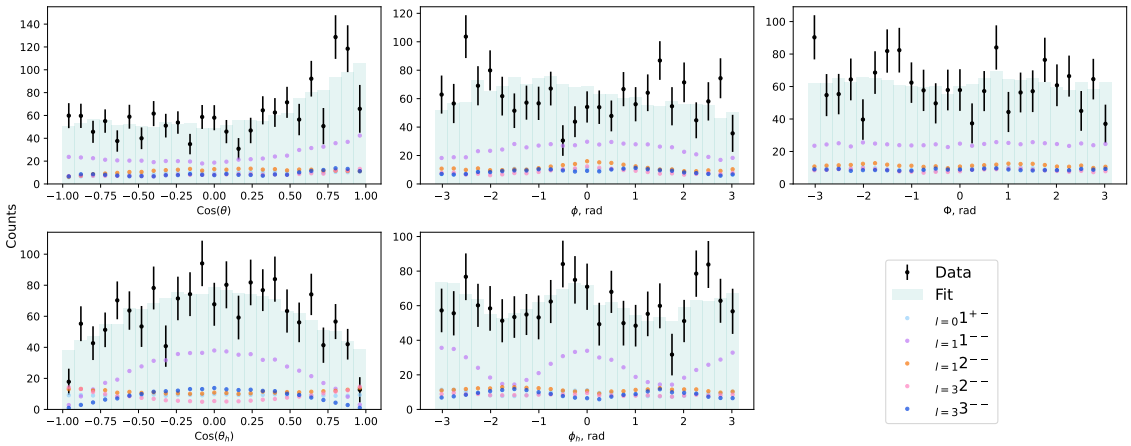

Figure E.5: 1.7 GeV - 1.74 GeV.

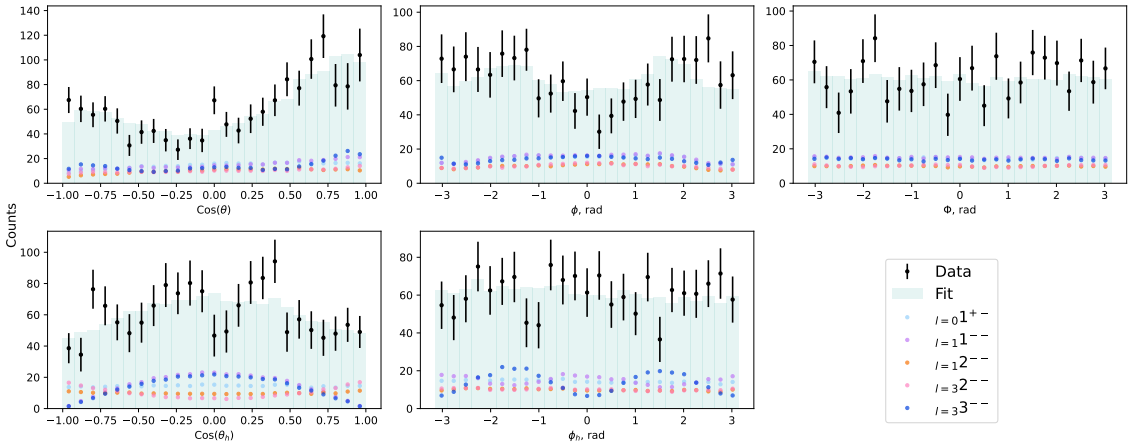

Figure E.6: 1.74 GeV - 1.78 GeV.

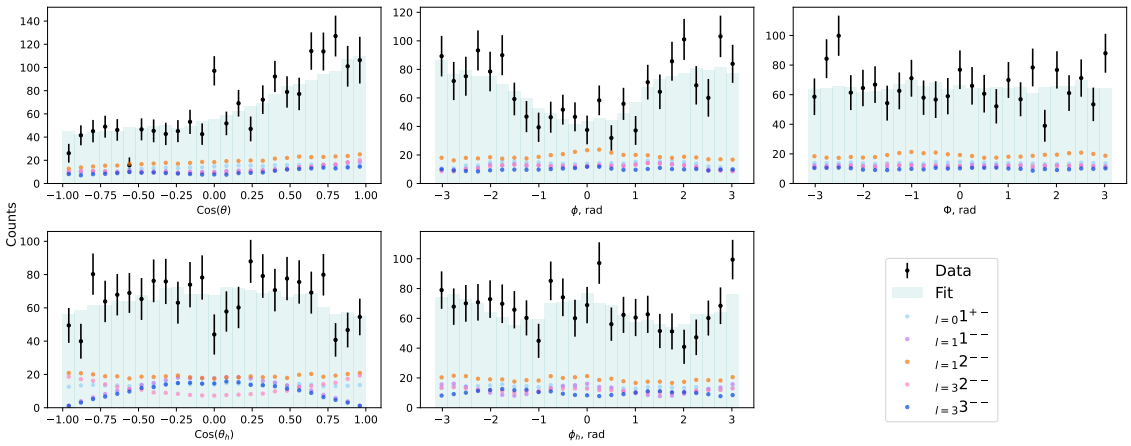

Figure E.7: 1.78 GeV - 1.82 GeV.

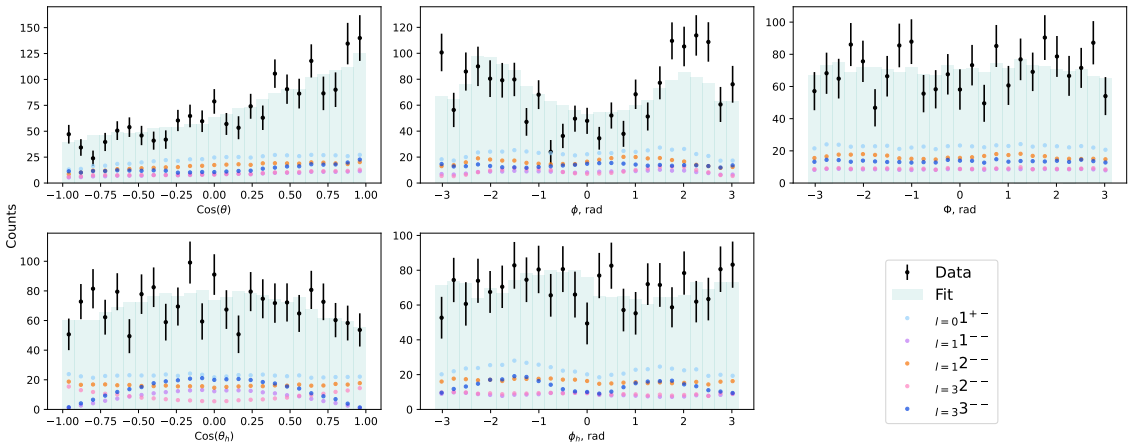

Figure E.8: 1.82 GeV - 1.86 GeV.

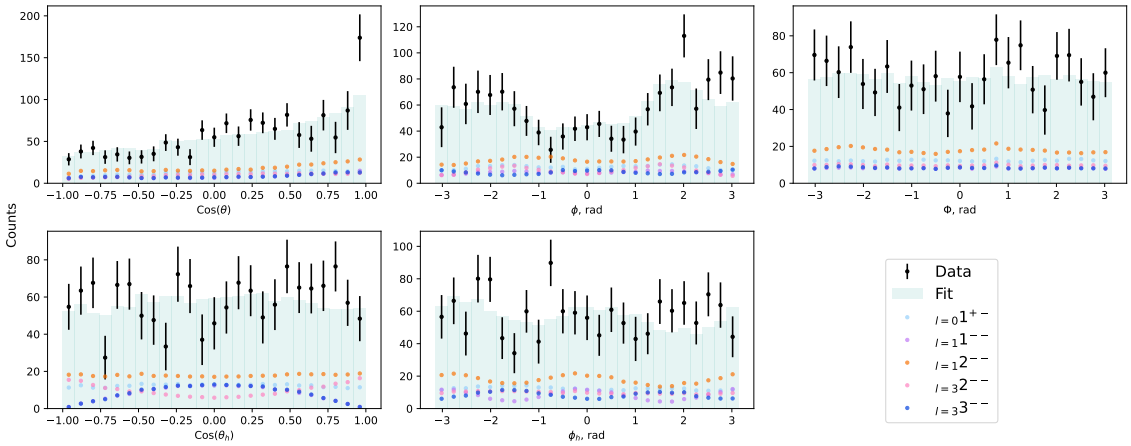

Figure E.9: 1.86 GeV - 1.9 GeV.

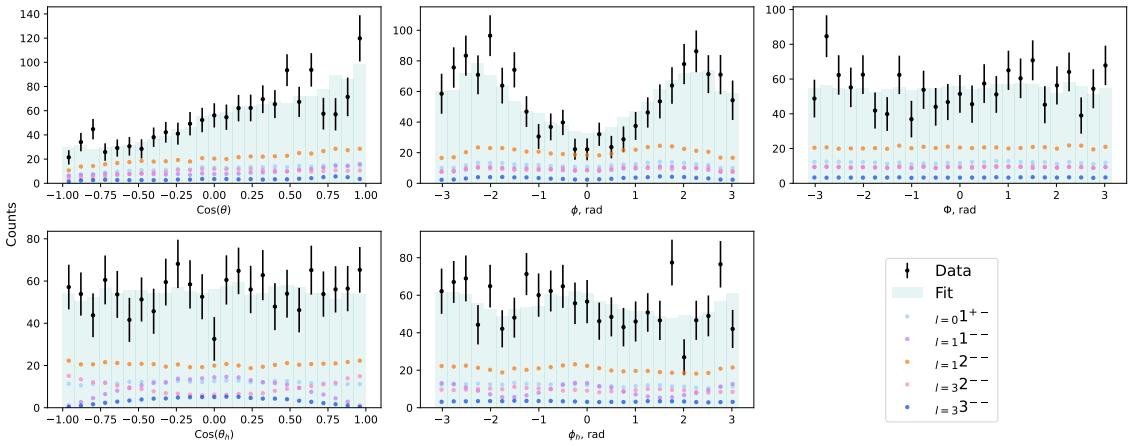

Figure E.10: 1.9 GeV - 1.94 GeV.

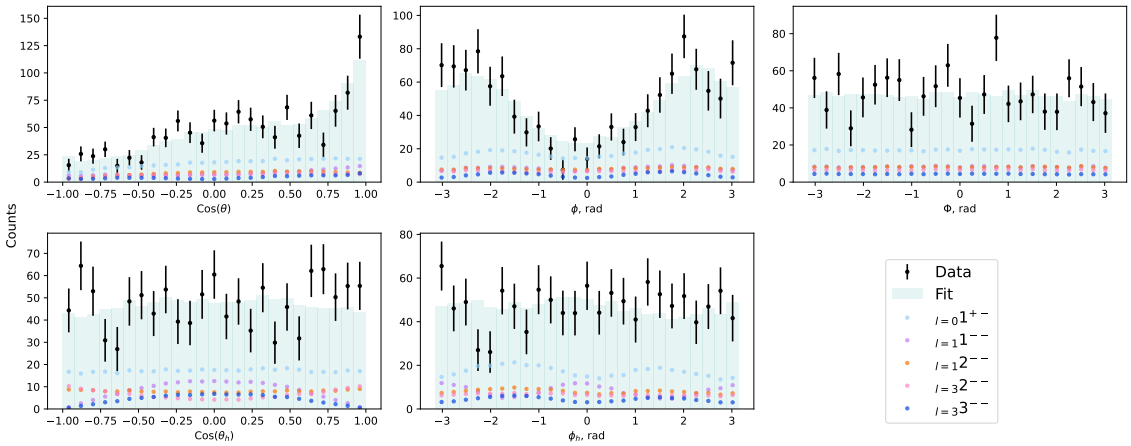

Figure E.11: 1.94 GeV - 1.98 GeV.

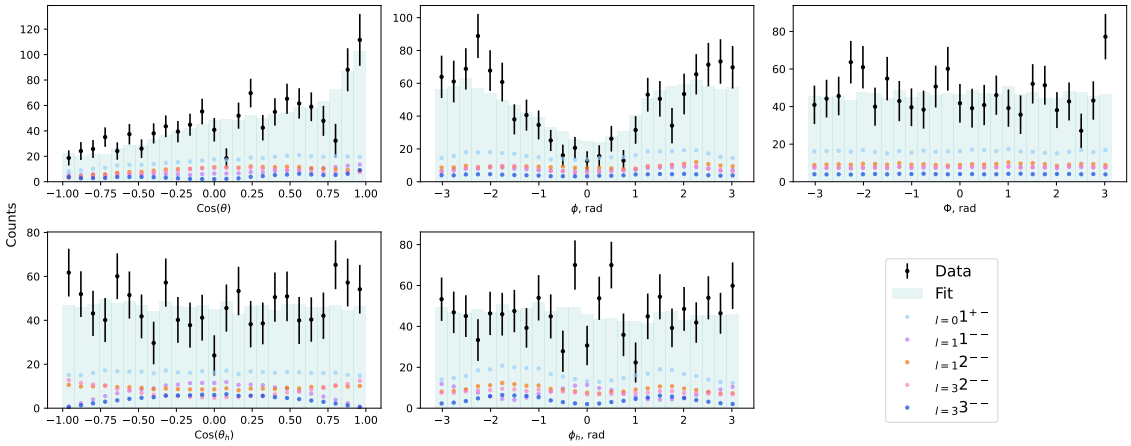

Figure E.12: 1.98 GeV - 2.02 GeV.

Appendix F

Numeric cross-section results

Table F.1: Mass-dependent cross sections $\frac{\mathrm{d}\sigma}{\mathrm{dm}}$.

Mass bin (GeV)	$\frac{\mathrm{d}\sigma}{\mathrm{d}m}$
1.50 GeV - 1.54 GeV	0.0
1.54 GeV - 1.58 GeV	0.432132
1.58 GeV - 1.62 GeV	2.621577
1.62 GeV - 1.66 GeV	8.016326
1.66 GeV - 1.70 GeV	9.753698
1.70 GeV - 1.74 GeV	5.543202
1.74 GeV - 1.78 GeV	2.949543
1.78 GeV - 1.82 GeV	1.737230
1.82 GeV - 1.86 GeV	1.121139
1.86 GeV - 1.90 GeV	0.774295
1.90 GeV - 1.94 GeV	0.562244
1.94 GeV - 1.98 GeV	0.424091
1.98 GeV - 2.02 GeV	0.329517
2.02 GeV - 2.06 GeV	0.262184
2.06 GeV - 2.10 GeV	0.212696
2.10 GeV - 2.14 GeV	0.175359
2.14 GeV - 2.18 GeV	0.146564
2.18 GeV - 2.22 GeV	0.123940
2.22 GeV - 2.26 GeV	0.105876
2.26 GeV - 2.30 GeV	0.091252
2.30 GeV - 2.34 GeV	0.079267
2.34 GeV - 2.38 GeV	0.069339
2.38 GeV - 2.42 GeV	0.061034
2.42 GeV - 2.46 GeV	0.054028
2.46 GeV - 2.50 GeV	0.048071

Table F.2: Mass-dependent cross sections $\frac{d\sigma}{dm}$ total combined uncertainties.

Mass bin (GeV)	Lower error	Upper error
1.50 GeV - 1.54 GeV	0.0	0.0
1.54 GeV - 1.58 GeV	0.261848	0.257087
1.58 GeV - 1.62 GeV	1.884455	1.863395
1.62 GeV - 1.66 GeV	4.741117	4.642751
1.66 GeV - 1.70 GeV	3.156196	2.590869
1.70 GeV - 1.74 GeV	1.773897	1.369415
1.74 GeV - 1.78 GeV	1.098542	0.918091
1.78 GeV - 1.82 GeV	0.689574	0.591667
1.82 GeV - 1.86 GeV	0.459742	0.399223
1.86 GeV - 1.90 GeV	0.325756	0.285304
1.90 GeV - 1.94 GeV	0.241667	0.213062
1.94 GeV - 1.98 GeV	0.185559	0.164443
1.98 GeV - 2.02 GeV	0.146319	0.130201
2.02 GeV - 2.06 GeV	0.117855	0.105218
2.06 GeV - 2.10 GeV	0.096595	0.086470
2.10 GeV - 2.14 GeV	0.080329	0.072069
2.14 GeV - 2.18 GeV	0.067632	0.060792
2.18 GeV - 2.22 GeV	0.057552	0.051813
2.22 GeV - 2.26 GeV	0.049430	0.044561
2.26 GeV - 2.30 GeV	0.042801	0.038631
2.30 GeV - 2.34 GeV	0.037331	0.033729
2.34 GeV - 2.38 GeV	0.032771	0.029636
2.38 GeV - 2.42 GeV	0.028937	0.026189
2.42 GeV - 2.46 GeV	0.025686	0.023263
2.46 GeV - 2.50 GeV	0.022909	0.020762

Bibliography

[1] Alan Chalmers. “Atomism from the 17th to the 20th Century”. In: *The Stanford Encyclopedia of Philosophy*. Ed. by Edward N. Zalta. Spring 2019. Metaphysics Research Lab, Stanford University, 2019.

[2] J. J. Thomson and. “XL. Cathode Rays”. In: *The London, Edinburgh, and Dublin Philosophical Magazine and Journal of Science* 44.269 (1897), pp. 293–316. DOI: 10.1080/14786449708621070.

[3] J.J. Thomson and. “XXIV. On the structure of the atom: an investigation of the stability and periods of oscillation of as number of corpuscles arranged at equal intervals around the circumference of a circle; with application of the results to the theory of atomic structure”. In: *The London, Edinburgh, and Dublin Philosophical Magazine and Journal of Science* 7.39 (1904), pp. 237–265. DOI: 10.1080/14786440409463107.

[4] B.R. Webber and E.A. Davis. “Commentary on ‘The scattering of and particles by matter and the structure of the atom’ by E. Rutherford (Philosophical Magazine 21 (1911) 669–688)”. In: *Philosophical Magazine* 92.4 (2012), pp. 399–405. DOI: 10.1080/14786435.2011.614643.

[5] E. Rutherford and. “LXXIX. The scattering of and particles by matter and the structure of the atom”. In: *The London, Edinburgh, and Dublin Philosophical Magazine and Journal of Science* 21.125 (1911), pp. 669–688. DOI: 10.1080/14786440508637080.

[6] N. Bohr and. “XXXVII. On the constitution of atoms and molecules”. In: *The London, Edinburgh, and Dublin Philosophical Magazine and Journal of Science* 26.153 (1913), pp. 476–502. DOI: 10.1080/14786441308634993.

[7] E. Rutherford and. “LIV. Collision of particles with light atoms. IV. An anomalous effect in nitrogen”. In: *The London, Edinburgh, and Dublin Philosophical Magazine and Journal of Science* 37.222 (1919), pp. 581–587. DOI: 10.1080/14786440608635919.

[8] James Chadwick. “The existence of a neutron”. In: *Proceedings of the Royal Society of London. Series A, Containing Papers of a Mathematical and Physical Character* 136.830 (1932), pp. 692–708. DOI: 10.1098/rspa.1932.0112.

[9] George Gamow. “Mass defect curve and nuclear constitution”. In: *Proceedings of the Royal Society of London. Series A, Containing Papers of a Mathematical and Physical Character* 126.803 (1930), pp. 632–644.

[10] E Gapon and D Iwanenko. “Zur Bestimmung der isotopenzahl”. In: *Naturwissenschaften* 20.43 (1932), pp. 792–793.

[11] Lise Meitner and Otto Robert Frisch. “Disintegration of uranium by neutrons: a new type of nuclear reaction”. In: *Nature* 143.3615 (1939), pp. 239–240.

[12] Otto Robert Frisch. “Physical evidence for the division of heavy nuclei under neutron bombardment”. In: *Nature* 143.3616 (1939), pp. 276–276.

[13] NN Das Gupta and Surya K Ghosh. “A report on the Wilson cloud chamber and its applications in physics”. In: *Reviews of Modern Physics* 18.2 (1946), p. 225.

[14] Carl D Anderson. “The positive electron”. In: *Physical review* 43.6 (1933), p. 491.

[15] Carl D Anderson and Seth H Neddermeyer. “Cloud chamber observations of cosmic rays at 4300 meters elevation and near sea-level”. In: *Physical Review* 50.4 (1936), p. 263.

[16] R BrownMiss et al. “Observations with electron-sensitive plates exposed to cosmic radiation”. In: *Nature* 163.4133 (1949), pp. 82–87.

[17] Aaron Jay Seriff et al. “Cloud-chamber observations of the new unstable cosmic-ray particles”. In: *Physical Review* 78.3 (1950), p. 290.

[18] VE Barnes et al. “Observation of a hyperon with strangeness minus three”. In: *The Eightfold Way*. CRC Press, 2018, pp. 88–90.

[19] Murray Gell-Mann. “Isotopic spin and new unstable particles”. In: *Physical Review* 92.3 (1953), p. 833.

[20] Abraham Pais. “On the baryon-meson-photon system”. In: *Progress of Theoretical Physics* 10.4 (1953), pp. 457–469.

[21] Kazuhiko Nishijima. “Charge independence theory of V particles”. In: *Progress of Theoretical Physics* 13.3 (1955), pp. 285–304.

[22] Thomas Roser and Ernest Courant. “The cosmotron and the bevatron: the first GeV accelerators”. In: *IN THE XXI CENTURY* (2016), p. 117.

[23] Bruce Cork et al. “Antineutrons produced from antiprotons in charge-exchange collisions”. In: *Physical Review* 104.4 (1956), p. 1193.

[24] M. Stanley Livingston. “Early History of Particle Accelerators”. In: *Advances in Electronics and Electron Physics* 50 (1980). Ed. by L. Marton and C. Marton, pp. 1–88. ISSN: 0065-2539. DOI: https://doi.org/10.1016/S0065-2539(08)61061-6.

[25] Hans Paetz gen. Schieck. "The particle zoo". In: *Key Nuclear Reaction Experiments*. 2053-2563. IOP Publishing, 2015, 6-1 to 6–16. ISBN: 978-0-7503-1173-1. DOI: 10.1088/978-0-7503-1173-1ch6.

[26] Murray Gell-Mann. "The Eightfold Way: A Theory of strong interaction symmetry". In: *The Eightfold Way*. CRC Press, 2018, pp. 11–57.

[27] Laurascudder. *Meson octet*. 2007. URL: https://commons.wikimedia.org/wiki/File:Meson_octet.png.

[28] Murray Gell-Mann. "A Schematic Model of Baryons and Mesons 1". In: *The Eightfold Way*. CRC Press, 2018, pp. 168–169.

[29] George Zweig. *An SU(3) model for strong interaction symmetry and its breaking*. Tech. rep. CM-P00042884, 1964.

[30] Elliott D Bloom et al. "High-Energy Inelastic e- p Scattering at 6 and 10". In: *Physical Review Letters* 23.16 (1969), p. 930.

[31] J. -E. Augustin et al. "Discovery of a Narrow Resonance in e^+e^- Annihilation". In: *Phys. Rev. Lett.* 33 (23 Dec. 1974), pp. 1406–1408. DOI: 10.1103/PhysRevLett.33.1406.

[32] J. J. Aubert et al. "Experimental Observation of a Heavy Particle *J*". In: *Phys. Rev. Lett.* 33 (23 Dec. 1974), pp. 1404–1406. DOI: 10.1103/PhysRevLett.33.1404.

[33] S. W. Herb et al. "Observation of a Dimuon Resonance at 9.5 GeV in 400-GeV Proton-Nucleus Collisions". In: *Phys. Rev. Lett.* 39 (5 Aug. 1977), pp. 252–255. DOI: 10.1103/PhysRevLett.39.252.

[34] F. Abe et al. "Observation of Top Quark Production in $\overline{p}p$ Collisions with the Collider Detector at Fermilab". In: *Phys. Rev. Lett.* 74 (14 Apr. 1995), pp. 2626–2631. DOI: 10.1103/PhysRevLett.74.2626.

[35] S. Abachi et al. "Observation of the Top Quark". In: *Phys. Rev. Lett.* 74 (14 Apr. 1995), pp. 2632–2637. DOI: 10.1103/PhysRevLett.74.2632.

[36] Hua-Xing Chen et al. "The hidden-charm pentaquark and tetraquark states". In: *Physics Reports* 639 (2016), pp. 1–121.

[37] Moskov Amaryan. "History and geography of light pentaquark searches: challenges and pitfalls". In: *The European Physical Journal Plus* 137.6 (2022), p. 684.

[38] Eberhard Klempt and Alexander Zaitsev. "Glueballs, hybrids, multiquarks: Experimental facts versus QCD inspired concepts". In: *Physics Reports* 454.1-4 (2007), pp. 1–202.

[39] AJRL Chodos et al. "New extended model of hadrons". In: *Physical Review D* 9.12 (1974), p. 3471.

[40] Nathan Isgur and Jack Paton. "Flux-tube model for hadrons in QCD". In: *Physical Review D* 31.11 (1985), p. 2910.

[41] Michael E Peskin. *An Introduction to quantum field theory*. CRC press, 2018.

[42] Kenneth G Wilson. "Confinement of quarks". In: *Physical review D* 10.8 (1974), p. 2445.

[43] Jeff Greensite. *An introduction to the confinement problem*. Vol. 821. Springer, 2011.

[44] David J Gross and Frank Wilczek. "Ultraviolet behavior of non-abelian gauge theories". In: *Physical Review Letters* 30.26 (1973), p. 1343.

[45] S. Navas et al. "Review of Particle Physics". In: *Phys. Rev. D* 110 (3 Aug. 2024), p. 030001. DOI: 10.1103/PhysRevD.110.030001.

[46] Pei-Lian Liu, Shuang-Shi Fang, and Xin-Chou Lou. "Strange quarkonium states at BESIII". In: *Chinese Physics C* 39.8 (2015), p. 082001.

[47] T Barnes, N Black, and PR Page. "Strong decays of strange quarkonia". In: *Physical Review D* 68.5 (2003), p. 054014.

[48] Gui-Jun Ding and Mu-lin Yan. "A candidate for 1– strangeonium hybrid". In: *Physics letters B* 650.5-6 (2007), pp. 390–400.

[49] Gui-Jun Ding and Mu-Lin Yan. "Y (2175): Distinguish hybrid state from higher quarkonium". In: *Physics Letters B* 657.1-3 (2007), pp. 49–54.

[50] Mario Abud, Franco Buccella, and Francesco Tramontano. "Hints for the existence of hexaquark states in the baryon-antibaryon sector". In: *Physical Review D—Particles, Fields, Gravitation, and Cosmology* 81.7 (2010), p. 074018.

[51] JJ Sakurai. "Possible Existence of a T= 0 Vector Meson at 1020 MeV". In: *Physical Review Letters* 9.11 (1962), p. 472.

[52] PL Connolly et al. "Existence and properties of the ϕ meson". In: *Physical Review Letters* 10.8 (1963), p. 371.

[53] Susumu Okubo. "φ-meson and unitary symmetry model". In: *Physics Letters* 5.2 (1963), pp. 165–168.

[54] G Zweig. "CERN report no. 8419". In: *TH412* (1964).

[55] Jugoro Iizuka. "A systematics and phenomenology of meson family". In: *Progress of Theoretical Physics Supplement* 37 (1966), pp. 21–34.

[56] David J Griffiths and Darrell F Schroeter. *Introduction to quantum mechanics*. Cambridge university press, 2018.

[57] Griffiths, David J and Krishnavedala. *Feynmann diagram of OZI suppressed ϕ decay*. 2016. URL: https://commons.wikimedia.org/wiki/File:OZI_rule_-_Feynmann_diagram2.svg.

[58] D. Frame et al. "A spin-parity analysis of the K+ system produced in the reaction K+p $\rightarrow$ K+p, $\rightarrow$ K+K at 13 GeV / c". In: *Nuclear Physics B* 276.3 (1986), pp. 667–705. ISSN: 0550-3213. DOI: https://doi.org/10.1016/0550-3213(86)90071-4.

[59] J. A. J. Matthews et al. "Production and Decay of the $\varphi(1680)$ in $\pi^+ d \rightarrow pp\pi^+\pi^-\pi^0$ at 6.95 $\frac{\text{GeV}}{c}$". In: *Phys. Rev. D* 3 (11 June 1971), pp. 2561–2572. DOI: 10.1103/PhysRevD.3.2561.

[60] J. Buon. "Recent Results from DCI and elsewhere on Vector Meson Production between 1.4 and 2.2 GeV". In: *J. Phys. Colloq.* 43.C3 (1982). Ed. by Pierre Petiau and M. Porneuf, pp. 77–80. DOI: 10.1051/jphyscol:1982315.

[61] D. Aston et al. "Evidence for a High Mass Enhancement in K^+K^- Photoproduction". In: *Phys. Lett. B* 104 (1981), pp. 231–234. DOI: 10.1016/0370-2693(81)90597-9.

[62] M. Atkinson et al. "Photoproduction of ϕ Mesons by Linearly Polarized Photons of Energy 20-GeV to 40-GeV and Further Evidence for a Photoproduced High Mass KK Enhancement". In: *Z. Phys. C* 27 (1985), p. 233. DOI: 10.1007/BF01556612.

[63] J. Busenitz et al. "High-energy photoproduction of $\pi^+\pi^-\pi^0$, K^+K^-, and $p\bar{p}$ states". In: *Phys. Rev. D* 40 (1 July 1989), pp. 1–21. DOI: 10.1103/PhysRevD.40.1.

[64] J.M Link et al. "Observation of a 1750 MeV/c2 enhancement in the diffractive photoproduction of K+K". In: *Physics Letters B* 545.1 (2002), pp. 50–56. ISSN: 0370-2693. DOI: https://doi.org/10.1016/S0370-2693(02)02561-3.

[65] M. Ablikim et al. "Partial wave analysis of $\psi(3686) \rightarrow K^+K^-\eta$". In: *Phys. Rev. D* 101 (3 Feb. 2020), p. 032008. DOI: 10.1103/PhysRevD.101.032008.

[66] Wenjing Zhu and XiaoLong Wang. "Determination of the resonant parameters of excited vector strangenia with data". In: *Chin. Phys. C* 47.11 (2023), p. 113003. DOI: 10.1088/1674-1137/acf034.

[67] W. J. Zhu et al. "Study of $e^+e^- \rightarrow \eta\phi$ via Initial State Radiation at Belle". In: *Phys. Rev. D* 107 (2023), p. 012006. DOI: 10.1103/PhysRevD.107.012006.

[68] Chen Dong et al. "Production of strangeonium ϕ (1680) state in electromagnetic probe-driven scatterings and hadron–hadron ultraperipheral collisions". In: *The European Physical Journal C* 83.5 (2023), p. 430.

[69] S. Al- Harran et al. "Observation of a $K\bar{K}$ Enhancement at 1.85-GeV in the Reaction $K^-P \rightarrow K\bar{K}\Lambda$ at 8.25-GeV/c". In: *Phys. Lett. B* 101 (1981), pp. 357–360. DOI: 10.1016/0370-2693(81)90063-0.

[70] T. Armstrong et al. "EVIDENCE FOR A HIGH MASS 'PHI LIKE' STATE". In: *Phys. Lett. B* 110 (1982), pp. 77–81. DOI: 10.1016/0370-2693(82)90956-X.

[71] D. Aston et al. "Spin Parity Determination of the $\phi(J)$ (1850) From $K^- p$ Interactions at 11-GeV/c". In: *Phys. Lett. B* 208 (1988), pp. 324–330. DOI: 10.1016/0370-2693(88)90439-X.

[72] Bernard Aubert et al. "A Structure at 2175-MeV in $e^+e^- \to \phi f_0(980)$ Observed via Initial-State Radiation". In: *Phys. Rev. D* 74 (2006), p. 091103. DOI: 10.1103/PhysRevD.74.091103.

[73] C. P. Shen et al. "Observation of the $\phi(1680)$ and the Y(2175) in $e^+e^- \to \phi\pi^+\pi^-$". In: *Phys. Rev. D* 80 (2009), p. 031101. DOI: 10.1103/PhysRevD.80.031101.

[74] Medina Ablikim et al. "Observation of Y(2175) in J/$\psi \to \eta\phi f_0(980)$". In: *Phys. Rev. Lett.* 100 (2008), p. 102003. DOI: 10.1103/PhysRevLett.100.102003.

[75] M. Ablikim et al. "Measurement of $e^+e^- \to K^+K^-$ cross section at $\sqrt{s} = 2.00 - 3.08$ GeV". In: *Phys. Rev. D* 99.3 (2019), p. 032001. DOI: 10.1103/PhysRevD.99.032001.

[76] M. Ablikim et al. "Observation of a structure in $e^+e^- \to \phi\eta'$ at $\sqrt{s}$ from 2.05 to 3.08 GeV". In: *Phys. Rev. D* 102.1 (2020), p. 012008. DOI: 10.1103/PhysRevD.102.012008.

[77] Medina Ablikim et al. "Cross section measurement of $e^+e^- \to K_S^0 K_L^0$ at $\sqrt{s} = 2.00 - 3.08$ *GeV*". In: *Phys. Rev. D* 104.9 (2021), p. 092014. DOI: 10.1103/PhysRevD.104.092014.

[78] Medina Ablikim et al. "Study of the process $e^+e^- \to \phi\eta$ at center-of-mass energies between 2.00 and 3.08 GeV". In: *Phys. Rev. D* 104.3 (2021), p. 032007. DOI: 10.1103/PhysRevD.104.032007.

[79] M. Ablikim et al. "Measurement of $e^+e^- \to K^+K^-\pi^0$ cross section and observation of a resonant structure". In: *JHEP* 07 (2022), p. 045. DOI: 10.1007/JHEP07(2022)045.

[80] Medina Ablikim et al. "Measurement of the $e^+e^- \to K_S^0 K_L^0 \pi^0$ cross sections from $\sqrt{s}$ = 2.000 to 3.080 GeV". In: *JHEP* 01 (2024), p. 180. DOI: 10.1007/JHEP01(2024)180.

[81] K. Götzen and F. Nerling. "Measurement of the photoproduction cross-section for $\gamma p \to \phi\pi^+\pi^- p$ and search for the Y(2175) at GlueX". In: *Nuovo Cim. C* 47.4 (2024), p. 180. DOI: 10.1393/ncc/i2024-24180-2.

[82] Cheng-Qun Pang. "Excited states of ϕ meson". In: *Physical Review D* 99.7 (Apr. 2019). ISSN: 2470-0029. DOI: 10.1103/physrevd.99.074015.

[83] Gui-Jun Ding and Mu-Lin Yan. "Y(2175): Distinguish hybrid state from higher quarkonium". In: *Physics Letters B* 657.1–3 (Nov. 2007), pp. 49–54. ISSN: 0370-2693. DOI: 10.1016/j.physletb.2007.10.020.

[84] Gui-Jun Ding and Mu-Lin Yan. "A candidate for 1^{--} strangeonium hybrid". In: *Physics Letters B* 650.5–6 (July 2007), pp. 390–400. ISSN: 0370-2693. DOI: 10.1016/j.physletb.2007.05.026.

[85] J. Ho et al. "Is the Y(2175) a strangeonium hybrid meson?" In: *Physical Review D* 100.3 (Aug. 2019). ISSN: 2470-0029. DOI: 10.1103/physrevd.100.034012.

[86] Zhi-Gang Wang. "Analysis of as a tetraquark state with QCD sum rules". In: *Nuclear Physics A* 791.1–2 (July 2007), pp. 106–116. ISSN: 0375-9474. DOI: 10.1016/j.nuclphysa.2007.04.012.

[87] N.V. Drenska, R. Faccini, and A.D. Polosa. "Higher tetraquark particles". In: *Physics Letters B* 669.2 (Nov. 2008), pp. 160–166. ISSN: 0370-2693. DOI: 10.1016/j.physletb.2008.09.038.

[88] Yubing Dong et al. "Selected strong decays of $\eta(2225)$ and $\phi(2170)$ as $\Lambda\bar{\Lambda}$ bound states". In: *Physical Review D* 96.7 (Oct. 2017). ISSN: 2470-0029. DOI: 10.1103/physrevd.96.074027.

[89] Lu Zhao et al. "Meson-exchange model for the $\Lambda\bar{\Lambda}$ interaction". In: *Physical Review D* 87.5 (Mar. 2013). ISSN: 1550-2368. DOI: 10.1103/physrevd.87.054034.

[90] A. Martínez Torres et al. "X(2175) as a resonant state of the $\phi K\bar{K}$ system". In: *Physical Review D* 78.7 (Oct. 2008). ISSN: 1550-2368. DOI: 10.1103/physrevd.78.074031.

[91] L. Alvarez-Ruso, J. A. Oller, and J. M. Alarcón. "$\phi(1020)f_0(980)$ S-wave scattering and the Y(2175) resonance". In: *Physical Review D* 80.5 (Sept. 2009). ISSN: 1550-2368. DOI: 10.1103/physrevd.80.054011.

[92] Yi-Wei Jiang et al. "Strong Decays of the $\phi(2170)$ as a Fully Strange Tetraquark State". In: *Symmetry* 16.8 (2024), p. 1021. DOI: 10.3390/sym16081021.

[93] Carlos W. Salgado and Dennis P. Weygand. "On the partial-wave analysis of mesonic resonances decaying to multiparticle final states produced by polarized photons". In: *Physics Reports* 537.1 (2014). On the Partial-Wave Analysis of Mesonic Resonances Decaying to Multiparticle Final States Produced by Polarized Photons, pp. 1–58. ISSN: 0370-1573. DOI: https://doi.org/10.1016/j.physrep.2013.11.005.

[94] V. V. Anashin et al. "Final analysis of KEDR data on J/ψ and ψ(2S) masses". In: *Phys. Lett. B* 749 (2015), pp. 50–56. DOI: 10.1016/j.physletb.2015.07.057.

[95] J. J. Sakurai and Jim Napolitano. *Modern Quantum Mechanics*. 3rd ed. Cambridge University Press, 2020.

[96] Claude Amsler. *Nuclear and Particle Physics*. 2053-2563. IOP Publishing, 2015. ISBN: 978-0-7503-1140-3. DOI: 10.1088/978-0-7503-1140-3.

[97] V. Mathieu et al. "Moments of angular distribution and beam asymmetries in $\eta\pi^0$ photoproduction at GlueX". In: *Physical Review D* 100.5 (Sept. 2019). ISSN: 2470-0029. DOI: 10.1103/physrevd.100.054017.

[98] M. Jacob and G.C. Wick. "On the General Theory of Collisions for Particles with Spin". In: *Annals of Physics* 281.1 (2000), pp. 774–799. ISSN: 0003-4916. DOI: https://doi.org/10.1006/aphy.2000.6022.

[99] Jeffrey D Richman. *An experimenter's guide to the helicity formalism*. Tech. rep. 1984.

[100] D A Varshalovich, A N Moskalev, and V K Khersonskii. *Quantum theory of angular momentum*. World Scientific Pub. Co.,Teaneck, NJ, Dec. 1986.

[101] Matthew R. Shepherd. *AmpTools implementation of Polarized Photoproduction*. 2019. URL: https://halldweb.jlab.org/doc-private/DocDB/ShowDocument?docid=4094.

[102] Justin Stevens. *Vector-Pseudoscalar Amplitude in Reflectivity Basis*. 2023. URL: https://halldweb.jlab.org/doc-private/DocDB/ShowDocument?docid=4858.

[103] Eugene Levin. "An introduction to Pomerons". In: *arXiv preprint hep-ph/9808486* (1998).

[104] Christoph W. Leemann, David R. Douglas, and Geoffrey A. Krafft. "THE CONTINUOUS ELECTRON BEAM ACCELERATOR FACILITY: CEBAF at the Jefferson Laboratory". In: *Annual Review of Nuclear and Particle Science* 51.Volume 51, 2001 (2001), pp. 413–450. ISSN: 1545-4134. DOI: https://doi.org/10.1146/annurev.nucl.51.101701.132327.

[105] GlueX collaboration. *Diagram collection*. 2016. URL: https://gluexweb.jlab.org/drawings.

[106] S. Adhikari et al. "The GlueX beamline and detector". In: *Nuclear Instruments and Methods in Physics Research Section A: Accelerators, Spectrometers, Detectors and Associated Equipment* 987 (Jan. 2021), p. 164807. ISSN: 0168-9002. DOI: 10.1016/j.nima.2020.164807.

[107] H. Bilokon et al. "Coherent bremsstrahlung in crystals as a tool for producing high energy photon beams to be used in photoproduction experiments at CERN SPS". In: *Nuclear Instruments and Methods in Physics Research* 204.2 (1983), pp. 299–310. ISSN: 0167-5087. DOI: https://doi.org/10.1016/0167-5087(83)90061-3.

[108] Jean-Charles Arnault, Samuel Saada, and Victor Ralchenko. "Chemical Vapor Deposition Single-Crystal Diamond: A Review". In: *physica status solidi (RRL) – Rapid Research Letters* 16.1 (2022), p. 2100354. DOI: https://doi.org/10.1002/pssr.202100354.

[109] D.I. Sober et al. "The bremsstrahlung tagged photon beam in Hall B at JLab". In: *Nuclear Instruments and Methods in Physics Research Section A: Accelerators, Spectrometers, Detectors and Associated Equipment* 440.2 (2000), pp. 263–284. ISSN: 0168-9002. DOI: https://doi.org/10.1016/S0168-9002(99)00784-6.

[110] Eljen Technology. *EJ-228 - Fast Timing Plastic Scintillator*. URL: https://eljentechnology.com/products/plastic-scintillators/ej-228-ej-230.

[111] Alexander Edward Barnes. "Development of the Tagger Microscope & Analysis of Spin Density Matrix Elements in $\gamma p \to \phi p$ for the GlueX Experiment". PhD thesis. Jefferson Lab, 2017. DOI: 10.2172/1411406.

[112] David L. Chichester, Scott M. Watson, and James T. Johnson. "Comparison of bcf-10, bcf-12, and bcf-20 scintillating fibers for use in a 1-dimensional linear sensor". English. In: *IEEE Transactions on Nuclear Science* 60.5 (2013), pp. 4015–4021. ISSN: 0018-9499. DOI: 10.1109/TNS.2013.2277799.

[113] Joshua Ballard et al. "Refurbishment and testing of the 1970's era LASS solenoid coils for Jlab's Hall D". In: *AIP Conference Proceedings* 1434.1 (June 2012), pp. 861–868. ISSN: 0094-243X. DOI: 10.1063/1.4707001.

[114] Guthrie Miller and Dieter R. Walz. "A tungsten pin cushion photon beam monitor". In: *Nuclear Instruments and Methods* 117.1 (1974), pp. 33–37. ISSN: 0029-554X. DOI: https://doi.org/10.1016/0029-554X(74)90380-2.

[115] M. Dugger et al. "Design and construction of a high-energy photon polarimeter". In: *Nuclear Instruments and Methods in Physics Research Section A: Accelerators, Spectrometers, Detectors and Associated Equipment* 867 (2017), pp. 115–127. ISSN: 0168-9002. DOI: https://doi.org/10.1016/j.nima.2017.05.026.

[116] F. Barbosa et al. "Pair spectrometer hodoscope for Hall D at Jefferson Lab". In: *Nuclear Instruments and Methods in Physics Research Section A: Accelerators, Spectrometers, Detectors and Associated Equipment* 795 (2015), pp. 376–380. ISSN: 0168-9002. DOI: https://doi.org/10.1016/j.nima.2015.06.012.

[117] Sober, Daniel. *Calibration of the Tagged Photon Beam: Normalization Methods, Shower Counter and Pair Spectrometer*. 1992. URL: https://www.jlab.org/Hall-B/notes/clas_notes92/note92-014.pdf.

[118] E. Pooser et al. "The GlueX Start Counter Detector". In: *Nuclear Instruments and Methods in Physics Research Section A: Accelerators, Spectrometers, Detectors and Associated Equipment* 927 (2019), pp. 330–342. ISSN: 0168-9002. DOI: https://doi.org/10.1016/j.nima.2019.02.029.

[119] N.S. Jarvis et al. "The Central Drift Chamber for GlueX". In: *Nuclear Instruments and Methods in Physics Research Section A: Accelerators, Spectrometers, Detectors and Associated Equipment* 962 (2020), p. 163727. ISSN: 0168-9002. DOI: https://doi.org/10.1016/j.nima.2020.163727.

[120] L. Pentchev et al. "Studies with cathode drift chambers for the GlueX experiment at Jefferson Lab". In: *Nuclear Instruments and Methods in Physics Research Section A: Accelerators, Spectrometers, Detectors and Associated Equipment* 845 (2017). Proceedings of the Vienna Conference on Instrumentation 2016, pp. 281–284. ISSN: 0168-9002. DOI: https://doi.org/10.1016/j.nima.2016.04.076.

[121] W. Klempt. "Review of particle identification by time of flight techniques". In: *Nuclear Instruments and Methods in Physics Research Section A: Accelerators, Spectrometers, Detectors and Associated Equipment* 433.1 (1999), pp. 542–553. ISSN: 0168-9002. DOI: https://doi.org/10.1016/S0168-9002(99)00323-X.

[122] John Melvin Hardin. "Upgrading particle identification and searching for leptophobic bosons at GlueX". PhD thesis. MIT, 2018.

[123] Ahmed Ali. "Particle identification with the PANDA Barrel DIRC and the GlueX DIRC". PhD thesis. Frankfurt U., 2021.

[124] Yunjie Yang. "Commissioning the DIRC Detector and Searching for Axion-like Particles at GlueX". PhD thesis. MIT, 2021.

[125] T.D. Beattie et al. "Construction and performance of the barrel electromagnetic calorimeter for the GlueX experiment". In: *Nuclear Instruments and Methods in Physics Research Section A: Accelerators, Spectrometers, Detectors and Associated Equipment* 896 (2018), pp. 24–42. ISSN: 0168-9002. DOI: https://doi.org/10.1016/j.nima.2018.04.006.

[126] T.D. Beattie et al. "Light yield of Kuraray SCSF-78MJ scintillating fibers for the Gluex barrel calorimeter". In: *Nuclear Instruments and Methods in Physics Research Section A: Accelerators, Spectrometers, Detectors and Associated Equipment* 767 (2014), pp. 245–251. ISSN: 0168-9002. DOI: https://doi.org/10.1016/j.nima.2014.08.038.

[127] GlueX collaboration. *Photo gallery*. URL: https://gluexweb.jlab.org/photos.

[128] Jefferson Lab. *evio data format*. URL: https://github.com/JeffersonLab/evio.

[129] GlueX collaboration. *halld_recon software suite*. URL: https://github.com/JeffersonLab/halld_recon.

[130] GlueX collaboration. *HDDM data format*. URL: https://github.com/JeffersonLab/HDDM.

[131] GlueX collaboration. *DSelector*. URL: https://github.com/JeffersonLab/gluex_root_analysis/tree/master/libraries/DSelector.

[132] R.T. Jones et al. "A bootstrap method for gain calibration and resolution determination of a lead-glass calorimeter". In: *Nuclear Instruments and Methods in Physics Research Section A: Accelerators, Spectrometers, Detectors and Associated Equipment* 566.2 (2006), pp. 366–374. ISSN: 0168-9002. DOI: https://doi.org/10.1016/j.nima.2006.07.061.

[133] Ahmed Hossam Mohammed et al. *Geometric GNNs for Charged Particle Tracking at GlueX*. 2025. arXiv: 2505.22504 [cs.LG]. URL: https://arxiv.org/abs/2505.22504.

[134] R. Frühwirth, A. Strandlie, and W. Waltenberger. "Helix fitting by an extended Riemann fit". In: *Nuclear Instruments and Methods in Physics Research Section A: Accelerators, Spectrometers, Detectors and Associated Equipment* 490.1 (2002), pp. 366–378. ISSN: 0168-9002. DOI: https://doi.org/10.1016/S0168-9002(02)00911-7.

[135] Curtis Meyer and Yves Van Haarlem. *Hall D Tracking and PID Review – The GlueXD Central Drift Chamber*. 2008. URL: https://halldweb.jlab.org/DocDB/0009/000990/011/cdc_dr.pdf.

[136] R. E. Kalman. "A New Approach to Linear Filtering and Prediction Problems". In: *Journal of Basic Engineering* 82.1 (Mar. 1960), pp. 35–45. ISSN: 0021-9223. DOI: 10.1115/1.3662552.

[137] R. E. Kalman and R. S. Bucy. "New Results in Linear Filtering and Prediction Theory". In: *Journal of Basic Engineering* 83.1 (Mar. 1961), pp. 95–108. ISSN: 0021-9223. DOI: 10.1115/1.3658902.

[138] GlueX collaboration. *gen_vec_ps generator*. URL: https://github.com/JeffersonLab/halld_sim/tree/master/src/programs/Simulation/gen_vec_ps.

[139] Eugene Chudakov. *bggen*. 2008. URL: https://github.com/JeffersonLab/halld_sim/tree/master/src/programs/Simulation/bggen.

[140] Christian Bierlich et al. *A comprehensive guide to the physics and usage of PYTHIA 8.3*. 2022. arXiv: 2203.11601 [hep-ph]. URL: https://arxiv.org/abs/2203.11601.

[141] S. Agostinelli et al. "Geant4—a simulation toolkit". In: *Nuclear Instruments and Methods in Physics Research Section A: Accelerators, Spectrometers, Detectors and Associated Equipment* 506.3 (2003), pp. 250–303. ISSN: 0168-9002. DOI: https://doi.org/10.1016/S0168-9002(03)01368-8.

[142] David J. Lange. "The EvtGen particle decay simulation package". In: *Nuclear Instruments and Methods in Physics Research Section A: Accelerators, Spectrometers, Detectors and Associated Equipment* 462.1 (2001). BEAUTY2000, Proceedings of the 7th Int. Conf. on B-Physics at Hadron Machines, pp. 152–155. ISSN: 0168-9002. DOI: https://doi.org/10.1016/S0168-9002(01)00089-4.

[143] S. Mandelstam. "Determination of the Pion-Nucleon Scattering Amplitude from Dispersion Relations and Unitarity. General Theory". In: *Phys. Rev.* 112 (4 Nov. 1958), pp. 1344–1360. DOI: 10.1103/PhysRev.112.1344.

[144] M. Pivk and F.R. Le Diberder. ": A statistical tool to unfold data distributions". In: *Nuclear Instruments and Methods in Physics Research Section A: Accelerators, Spectrometers, Detectors and Associated Equipment* 555.1–2 (Dec. 2005), pp. 356–369. ISSN: 0168-9002. DOI: 10.1016/j.nima.2005.08.106. URL: http://dx.doi.org/10.1016/j.nima.2005.08.106.

[145] Roel Aaij et al. "Branching fraction measurement of the decay B+$\to\psi$(2S)ϕ(1020)K+". In: *Phys. Rev. D* 111.9 (2025), p. 092008. DOI: 10.1103/PhysRevD.111.092008.

[146] Aram Hayrapetyan et al. "Angular analysis of the B0$\to$K*(892)0μ+$\mu-$ decay in proton-proton collisions at s=13TeV". In: *Phys. Lett. B* 864 (2025), p. 139406. DOI: 10.1016/j.physletb.2025.139406.

[147] S. Adhikari et al. "Measurement of spin density matrix elements in $\Lambda(1520)$ photoproduction at 8.2–8.8 GeV". In: *Phys. Rev. C* 105 (3 Mar. 2022), p. 035201. DOI: 10.1103/PhysRevC.105.035201.

[148] Derek Glazier. *brufit*. URL: https://github.com/dglazier/brufit.

[149] ROOT contributors. *RooFit library*. URL: https://root.cern/manual/roofit/.

[150] P. Pauli et al. "Mass-dependent cuts in longitudinal phase space". In: *Phys. Rev. C* 98 (6 Dec. 2018), p. 065201. DOI: 10.1103/PhysRevC.98.065201.

[151] GlueX collaboration Matthew Shepherd. *AmpTools*. DOI: https://zenodo.org/records/10961168. URL: https://github.com/mashephe/AmpTools/tree/master.

[152] F. James and M. Roos. "Minuit: A System for Function Minimization and Analysis of the Parameter Errors and Correlations". In: *Comput. Phys. Commun.* 10 (1975), pp. 343–367. DOI: 10.1016/0010-4655(75)90039-9.

[153] Roger Barlow. "Extended maximum likelihood". In: *Nuclear Instruments and Methods in Physics Research Section A: Accelerators, Spectrometers, Detectors and Associated Equipment* 297.3 (1990), pp. 496–506. ISSN: 0168-9002. DOI: https://doi.org/10.1016/0168-9002(90)91334-8.

[154] Christoph Langenbruch. "Parameter uncertainties in weighted unbinned maximum likelihood fits". In: *The European Physical Journal C* 82.5 (2022), p. 393.

[155] Robert J Tibshirani and Bradley Efron. "An introduction to the bootstrap". In: *Monographs on statistics and applied probability* 57.1 (1993), pp. 1–436.

[156] Jozef J Dudek et al. "Toward the excited meson spectrum of dynamical QCD". In: *Physical Review D—Particles, Fields, Gravitation, and Cosmology* 82.3 (2010), p. 034508.

[157] Jozef J. Dudek and Christopher T. Johnson. "Coupled-channel J^{--} meson resonances from lattice QCD". In: *Phys. Rev. D* 110 (3 Aug. 2024), p. 034512. DOI: 10.1103/PhysRevD.110.034512.

[158] Edumndo Barriga, Jiawei Guo, and Kevin Scheuer. "Ambiguities in the Partial-Wave Analysis of Meson Photoproduction". In: Presented at the PWA13/ATHOS8 workshop, 2024.

[159] Bing Li and Gutti Jogesh Babu. *A graduate course on statistical inference*. Springer, 2019.

[160] Kenneth P. Burnham and David R. Anderson. "Information and Likelihood Theory: A Basis for Model Selection and Inference". In: *Model Selection and Multimodel Inference: A Practical Information-Theoretic Approach*. New York, NY: Springer New York, 2002, pp. 49–97. ISBN: 978-0-387-22456-5.

[161] Hirotugu Akaike. "Akaike's information criterion". In: *International encyclopedia of statistical science*. Springer, 2025, pp. 41–42.

[162] Andrew A Neath and Joseph E Cavanaugh. "The Bayesian information criterion: background, derivation, and applications". In: *Wiley Interdisciplinary Reviews: Computational Statistics* 4.2 (2012), pp. 199–203.

[163] Joseph E. Cavanaugh and Andrew A. Neath. "The Akaike information criterion: Background, derivation, properties, application, interpretation, and refinements". In: *WIREs Computational Statistics* 11.3 (2019). DOI: https://doi.org/10.1002/wics.1460.

[164] Scott I Vrieze. "Model selection and psychological theory: a discussion of the differences between the Akaike information criterion (AIC) and the Bayesian information criterion (BIC)." In: *Psychological methods* 17.2 (2012), p. 228.

[165] D. R. Anderson, K. P. Burnham, and G. C. White. “Comparison of Akaike information criterion and consistent Akaike information criterion for model selection and statistical inference from capture-recapture studies”. In: *Journal of Applied Statistics* 25.2 (1998), pp. 263–282. DOI: 10.1080/02664769823250.

[166] John Markus Blatt and Victor Frederick Weisskopf. *Theoretical nuclear physics*. Springer Science & Business Media, 2012.

[167] S. Adhikari et al. “Measurement of spin-density matrix elements in $\rho(770)$ production with a linearly polarized photon beam at $E_\gamma = 8.2 - -8.8$GeV”. In: *Phys. Rev. C* 108 (5 Nov. 2023), p. 055204. DOI: 10.1103/PhysRevC.108.055204.

[168] F. Afzal et al. “First measurement of $a_2^0(1320)$ polarized photoproduction cross section”. In: *Phys. Rev. C* 112 (1 July 2025), p. 015204. DOI: 10.1103/jfzb-rfl4.